Kidney stone in a chip
Understanding calcium oxalate kidney stone formation

Ibis, F.

DOI
10.4233/uuid:ca17922a-e6ab-4619-8b81-f92603c848df

Publication date
2022

Document Version
Final published version

Citation (APA)
Ibis, F. (2022). *Kidney stone in a chip: Understanding calcium oxalate kidney stone formation*. [Dissertation (TU Delft), Delft University of Technology]. https://doi.org/10.4233/uuid:ca17922a-e6ab-4619-8b81-f92603c848df

KIDNEY STONE IN A CHIP

UNDERSTANDING CALCIUM OXALATE KIDNEY STONE FORMATION

KIDNEY STONE IN A CHIP

UNDERSTANDING CALCIUM OXALATE KIDNEY STONE FORMATION

Proefschrift

ter verkrijging van de graad van doctor
aan de Technische Universiteit Delft,
op gezag van de Rector Magnificus prof.dr.ir. T.H.J.J. van der Hagen,
voorzitter van het College voor Promoties,
in het openbaar te verdedigen op woensdag 8 juni 2022 om 12:30 uur

door

Fatma IBIS

Master of Science in Biomedical Technology,
Izmir Katip Çelebi University, Turkey,
geboren te Izmir, Turkey.

Dit proefschrift is goedgekeurd door de

promotor: Prof.dr.ir. J.T. Padding
copromotor: Dr. H. B. Eral

Samenstelling promotiecommissie bestaat uit:

Rector Magnificus	voorzitter
Prof.dr.ir. J.T. Padding	Technische Universiteit Delft, promotor
Dr. H.B. Eral	Technische Universiteit Delft, copromotor

Onafhankelijke leden:

Prof.dr. N.F. Shahidzadeh	Universiteit van Amsterdam
Prof.dr. S. Kenjereš	Technische Universiteit Delft
Prof.dr. W.K. Kegel	Universiteit Utrecht
Dr. L. Rossi	Technische Universiteit Delft
Dr.ir. V. van Steijn	Technische Universiteit Delft
Prof.dr. J.H. van Esch.	Technische Universiteit Delft, reservelid

This work was sponsored by TU Delft and The Scientific and Technological Research Council of Turkey (TUBITAK)

Keywords: kidney stone, lab on a chip, calcium oxalate, nucleation, crystallization, solubility

Printed by: Ridderprint

ISBN: 978-94-6458-310-6

An electronic version of this dissertation is available at http://repository.tudelft.nl/.

Author e-mail address: fatmaibiss@gmail.com

Dedicated to my family; Hasan, Satı, Funda, İbrahim İbiş who always support me.

If one day, my words are against science, choose science.

Mustafa Kemal Atatürk

CONTENTS

Summary

Kidney stone formation is a global health problem with increasing prevalence. Stone formation is a physiochemical process involving crystallization of inorganic salts in the presence of biological constituents in the urinary system. To inhibit kidney stone formation, a better understanding of the underlying physicochemical mechanism of stone formation in the kidney is required.

In this thesis, the solubility, nucleation and growth of calcium oxalate (CaOx), the most common inorganic constituent of kidney stones, were studied under different conditions such as ion concentration, pH value, and also the role of inhibitors in water or artificial urine was investigated. The first step towards this work was obtaining the solubility curve of calcium oxalate monohydrate (COM) in the solvent, such as ultrapure water and different buffers, to elucidate the physicochemical conditions which can cause the kidney stone formation (Chapter 2).

Beside the solubility study, advanced technology to observe crystal formation in small scale and a very short time was needed. The volume, structure and flow properties inside the kidney inspired us to use microfluidic technology with comparable volume and flow rate. The developed microfluidic devices that mimic pathways in the human kidney were used to study the nucleation and growth of calcium oxalate crystals. The developed devices rendered an alternate perspective to the study of kidney stone formation and showed that microfluidics can provide precise, simple and fast detection of stone formation under various experimental conditions.

Initially, the designed microfluidic device allowed us to build a testing platform for the study of nucleation kinetics of CaOx inside isolated environments provided by droplets. Preliminary experiments were performed by dissolving calcium chloride and sodium oxalate in ultrapure water. The aqueous solution, containing the ions, forms the droplet phase and oil were used as the continuous phase. Altering the pH values, as well as increasing the concentration of additives such as magnesium (Mg) and osteopontin (OPN), were shown to slow down the nucleation kinetics, or even inhibit nucleation (Chapter 3).

Next, the nucleation kinetics of CaOx was studied in artificial urine with varying concentrations of oxalate and, hyaluronic acid (HA), a biopolysacharide commonly found in urine. The results showed that higher oxalate concentrations favored the formation of calcium oxalate dihydrate (COD), the metastable form, over COM, the most stable form. Additionally, COD was the fastest nucleating form in droplets under the conditions studied. An increasing concentration of HA at fixed calcium and oxalate concentrations favored the nucleation of COM. If COM nucleated first in the droplet, COD was not formed within the experimental time scale. However, in droplets where COD appeared first, COM crystals were observed later (Chapter 4).

Finally, the growth rate of CaOx in a microfluidic device, mimicking the geometry of a kidney collecting duct under flow conditions relevant for kidney stone formation, was studied. Calcium and oxalate ions were brought in contact in artificial urine. The growth rate of CaOx crystals was measured as a function of fluid flow rate, the molar ratio of calcium and oxalate, and the addition of OPN. Mainly COD crystals were found in artificial urine. Flow velocity did not affect the growth rate of crystals. The lower molar ratio of calcium and oxalate caused to see both crystals in the same channel. OPN was shown to slow down the kinetics of COD crystals. Furthermore, the higher OPN concentrations inhibited both crystal types. (Chapter 5).

Chapter 1.

Introduction

1.1. Background of Kidney Stone Formation

The urinary system consists of kidneys, ureters, bladder and urethra (Figure 1.1). The urinary system filters approximately 150-180 L fluid per day from renal blood flow to keep essential compounds in the blood while removing toxins, ions, and metabolic waste products.[1, 2]

The kidneys are regulating the volume of numerous body fluid compartments, acid-base balance, electrolyte concentrations, fluid osmolality and removal of toxins.[3-6] The kidneys are the most crucial element of the urinary system. They are attached to the ureter, which transports the excreted urine into the bladder.[4]

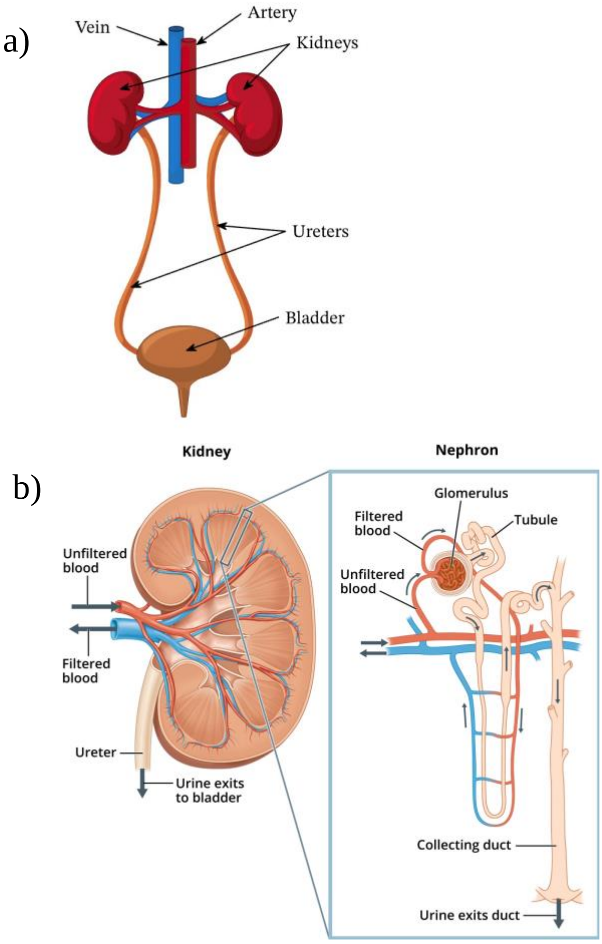

Figure 1.1. a) Urinary system[7] *, b) Structure of the kidney, nephron and collecting duct.*[8]

Kidneys stones appear as a consequence of crystallization of inorganic salts and their aggregation in the presence of biological complexity in the human kidney. Kidney stone disease affects about 12% of the world population, and its prevalence is increasing.[9-11]

Kidney stone formation is a complex process, dependent on numerous physicochemical and biophysical phenomena such as nucleation, crystal growth, aggregation, and retention of stone compounds in the tubular cell. An imbalance between substances that promote or inhibit urine crystallization controls these stages.[1, 2, 9-11]

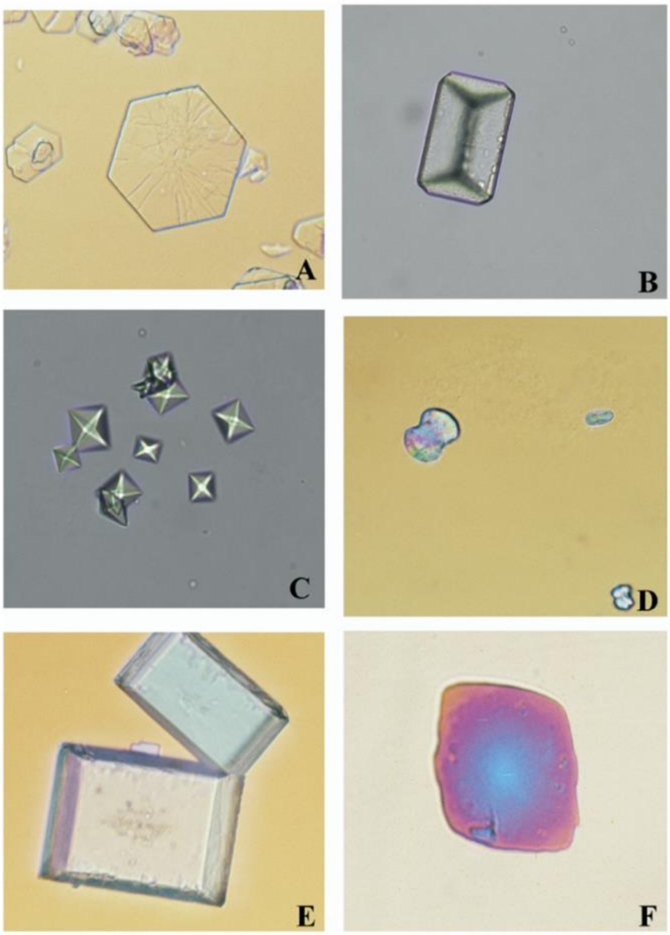

Figure 1.2. Commonly seen kidney stones types as observed with light microscopy. (A) Hexagonal cystine crystals (200X), (B) coffin-lid–shaped struvite crystals (200X), (C) pyramid-shaped calcium oxalate dehydrate crystals (200X), (D) dumbbell-shaped calcium oxalate monohydrate crystal (400X), (E) rectangular uric acid crystals (400X), and (F) rhomboidal uric acid crystals (400X).[12, 13]

Kidney stones are composed of numerous crystals (Figure 1.2) that are found either in a free state or adhering to the renal papillae in the urinary system. It is known as nephrolithiasis or urolithiasis, consisting of crystalline and organic components formed when the urine becomes excessively supersaturated with respect to minerals.[14]

The main compound of kidney stones is calcium oxalate, found in approximately 75-80 % of the stones. The others are struvite (10-20%), uric acid (5%), 5% of the stones contain predominantly brushite or hydroxyapatite, and less than 1% is composed of cystine.[15-17]

1.2. Crystallization

Crystallization is an essential step in the chemical and the pharmaceutical industries.[18, 19] It is a process of solid phase formation in which atoms or molecules are regularly ordered in a unit cell. The crystallization process starts with nucleation, followed by the growth of the crystal. The formation and growth of crystalline particles require a solution that is supersaturated. Solutes will stay dissolved in the solution until a sufficiently high level of supersaturation triggers nucleation.[20-22]

Nucleation can occur by homogeneous nucleation or heterogeneous nucleation, depending on the role of foreign substances.[23] Heterogeneous nucleation is energetically more favorable and it is induced by foreign particles and/or surfaces.[23-25]

There are two widely applied nucleation theories: Classical Nucleation Theory (CNT) and the two-step nucleation theory.[26, 27] CNT is the oldest and analytically simple nucleation theory developed in the 1920s–1940s.[26-28] It suggests that clusters of the solute molecules are formed in a supersaturated solution by an addition mechanism until the cluster reaches a critical size to become a stable nucleus. From this theory, the critical nucleus size in the metastable zone depends on the balance between the surface energy and the chemical potential difference between the solid and solvated form of the component in solution. This theory says that nucleation is one-step process in which density fluctuations and ordering of the solute molecules happen simultaneously.[26-28]

Two-step nucleation theory brings a new perspective to be able to explain a number of experimental observations that could not be explained by CNT.[28, 29] Crystal nucleation is a multiple barrier process in which the first barrier is a disordered cluster formation due to density fluctuations and the second barrier is the transformation of this cluster into an ordered crystalline structure.[28-30] Two-step nucleation theory has been experimentally validated for certain types of interacting molecules such as proteins.[29]

Despite the fact that the fundamental theory behind nucleation remains a mystery, the requirement of surpassing a thermodynamic potential is clear in both.

Both classical and non-classical behaviour has been observed in the literature. For instance, Smeets et al.[30] obtained results from experimental and computational investigations on the precipitation of calcium carbonate ($CaCO_3$) in dilute aqueous solutions. Their assumption is consistent with classical concepts of crystal nucleation and growth with considering of non-classical way.[30]

Banner et al. observed that rhombohedral calcium oxalate monohydrate (COM) can nucleate via a classical pathway, while square COM can nucleate via a non-classical multiphase pathway.[31] Ruiz Agudo et al. considered non-classical pathways during calcium oxalate (CaOx) precipitation in the presence of citrate.[32]

1.3. The Mechanism of Kidney Stone Formation

Stone formation is a multi-step process of nucleation and crystal growth followed by crystal aggregation and crystal retention. Several organic and inorganic compounds present in the urine play either a promoting or an inhibiting role in stone formation.

Low urine volume and high concentration of calcium, sodium, oxalate, and urate in the urine are identified to promote kidney stone formation. On the other hand, various inorganic constituents like citrate, magnesium, and organic substances like nephrocalcin, urinary prothrombin fragment-1, osteopontin, and hyaluronic acid are identified to suppress the formation of kidney stones.[34, 35] Figure 1.3 shows a scheme of the mechanism behind kidney stone formation.

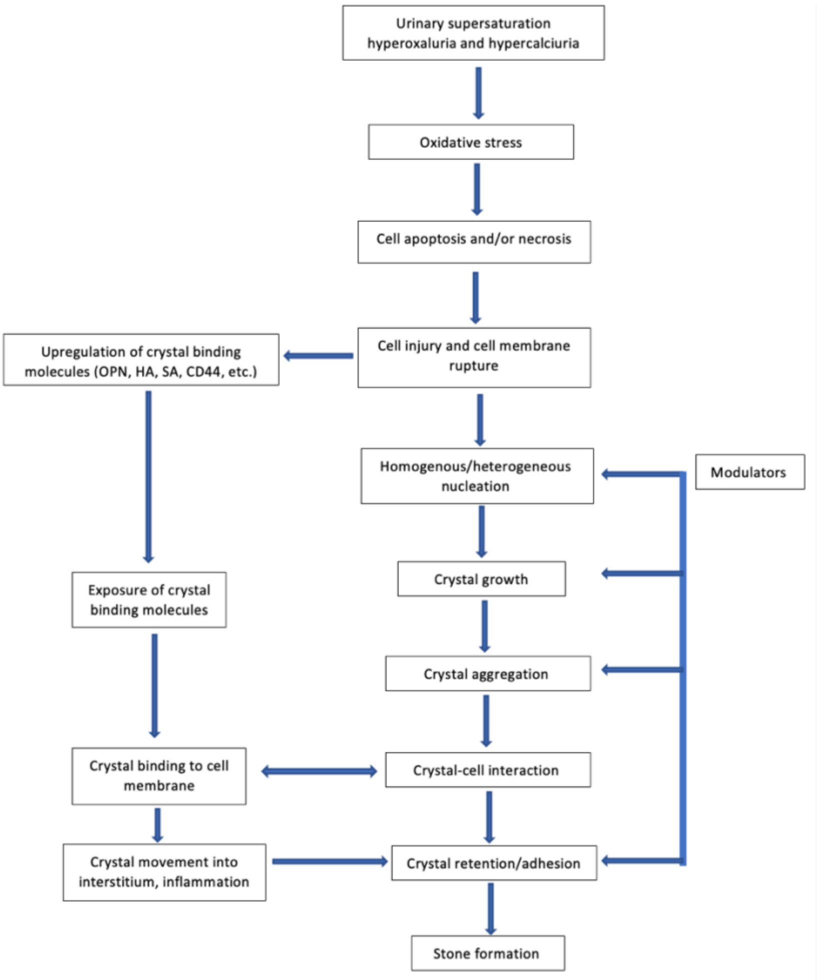

Figure 1.3. The mechanism of kidney stone formation.[33]

Once urinary supersaturation increases, crystal particles are formed. Under most circumstances, these crystals remain small and are easily excreted out of the body. Nevertheless, particles can aggregate and grow when they are retained within the kidney, which causes kidney stones. Importantly, it has been revealed that injured renal tubular (Figure 1.1.b), involves tubules or tube-shaped structures, promote crystal retention and growth of stones on the renal papillary surface.[36, 37] Moreover, crystal nucleation happens even at low supersaturation when the renal tube is injured.[36, 37] Thus, nucleation might occur easier due to increased surface area and in the presence of a rough surface. Another factor is crystal-cell interaction, which is also enhanced by renal tubular injury. Adhesion of urinary crystals to the apical surface of renal tubular cells could be a critical phase in kidney stone formation.[37]

1.4. Calcium Oxalate Crystals (CaOx)

Calcium oxalate stone formation in water or artificial urine conditions with various organic and/or inorganic additives have been reported.[38-44] Calcium oxalate hydrates are well-known biominerals that can crystallize into three different forms (see Figure 1.4 and 1.5), namely calcium oxalate monohydrate (COM) that has a monoclinic shape, calcium oxalate dihydrate (COD) that has a tetragonal shape, and calcium oxalate trihydrate (COT) that has a triclinic shape. COM is thermodynamically the most stable form, while COT is the least stable form and rarely present in kidney stones.[45, 46]

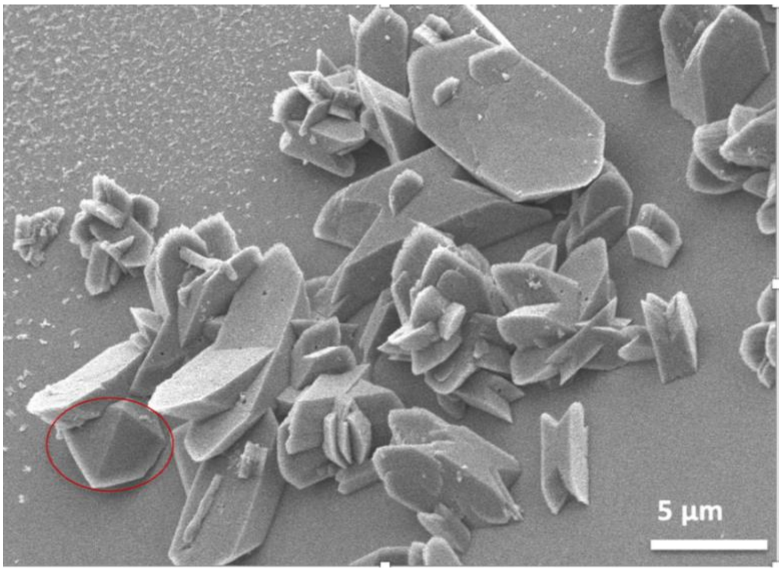

Figure 1.4. CaOx crystals formed in the microfluidic device after two hours, using calcium and oxalate precursor solutions (8.0 mM) at a flow rate of 1 µL/min in ultrapure water. Most crystals are COM with rhomboid and pinacoid shapes, except red encircled COD with bipyramid shape.[47, 48]

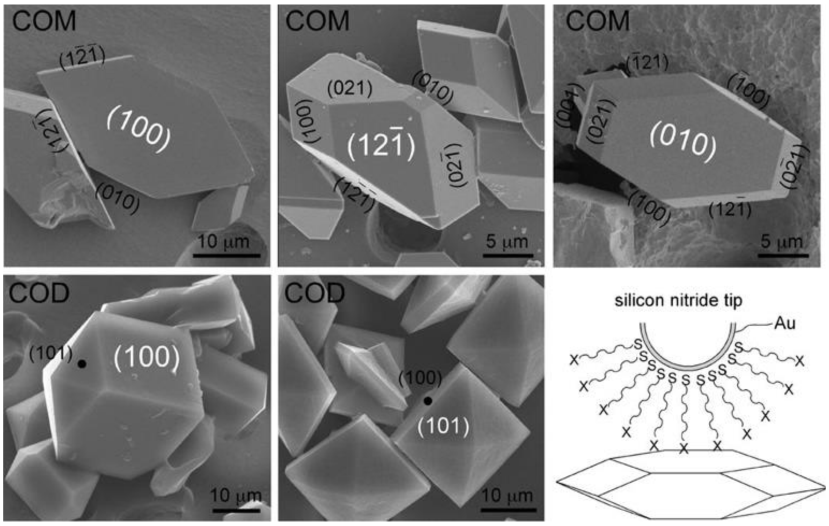

Figure 1.5. Scanning electron micrographs (SEM) of calcium oxalate monohydrate (COM, whewellite) and calcium oxalate dihydrate (COD, weddellite) crystals which were grown in aqueous solutions including 1.0 mM CaOx, 5-10 μg/ml polyacrylic acid, 10 mM HEPES buffer, and 150 mM NaCl.[49]

1.5. Inhibition of Calcium Oxalate Stone formation

The adsorptive nature of COM allows it to bind to macromolecules or attach to epithelial cell surfaces.[50, 51] Because of this attachment the residence time is increased, allowing sufficient crystal growth and aggregation for problematic stone formation.[51] Hyaluronic acid (HA) is a high-molecular-mass polysaccharide that is identified as a significant crystal-binding molecule.[50] The anionic nature of HA allows for complex interaction with cations, calcium ions in particular.[50] Furthermore, the attachment of crystals in the tubules is a result of regenerating cells that express HA at their surfaces.[33, 46, 52]

Experimental environments, such as rat kidneys and human renal tubular cells, have been used to study the adhesion effect. Aside from HA, acidic urine (lower pH) is also considered a major risk factor in stone formation and possibly enhances crystal retention. Moreover, medical studies with renal tubular cells show that citrate is very important for treating COM dominated kidney stones and is capable of inhibiting crystal growth, aggregation, and retention.[36, 37, 50-52]

Osteopontin is an organic inhibitor which is a protein vital in bone mineralization, where it is assumed to provide the connection of osteoblasts to bone.[53] The mechanism behind osteopontin is that this protein has the ability to bind calcium, which will help to decrease the calcium concentration and possibility of nucleation, growth and agglomeration. Osteopontin also influences the binding of calcium oxalate crystals to the cells inside the kidney.[54]

Other studies show that magnesium is also a factor inhibiting stone formation by inhibition of nucleation and growth of crystals. The hypothesis is that urinary magnesium directly inhibits renal calcium absorption.[55-57]

1.6. Solubility of Calcium Oxalate

Small calcium oxalate crystals are commonly seen in the kidney. However, in some patients nucleation of crystals is followed by growth and macroscopic scale aggregation, eventually leading to stone formation.[58] The solubility of calcium oxalate (CaOx) in pure water and different solutions has been previously reported. The values vary significantly, depending on implemented method and used solution.[59-61] The studies show that background electrolytes like NaCl[62-64] cause an increased solubility, which has been attributed to the influence of the electrolyte solution on the activity coefficient of Ca^{2+} and $C_2O_4^{2-}$ ions.[63, 64] The pH of the solution also has a strong influence on the solubility of COM and the crystallization kinetics.[62-65]

The presence of organic and inorganic salt compounds alters the value of urine pH and consequently may cause the precipitation of calcium oxalate crystals.[66] Clinical studies indicated that pH values between 4.5 and 5.5 form the highest risk for forming kidney stones.[66, 67] Even though the average pH of urine is 6.0, it can range between 4.0 and 8.0.[68]

1.7. Lab on a chip technology

Nowadays, there are widespread applications in scientific and industrial contexts for microfluidic devices that are used for manipulating fluids using Lab on a chip technology.[69-73] Working with small volumes of solutions on a microliter scale while doing a large number of identical tests is achievable with this technology.[74-76]

Microfluidics comprises methods and devices used to regulate fluid flows with a length scale less than a millimeter. The design of these microfluidic devices involves different geometries and also depends on various physical effects such as capillarity, pressure gradients and electrokinetics since as dimensions decrease, the relative importance of surface to volume forces increase.

Lab on a chip technology can be used to understand and evaluate the condition of kidney stone formation such as hypercalciuria or hyperoxaluria have high calcium or oxalate content, respectively in the urine.[47, 77, 78] New technology to form uniform droplets using microfluidic devices has been investigated for years. These uniform-sized micro-droplets can act as micro-reactors in which chemical reactions occur. The formation of droplet-based chemical reactors is unique, useful and practical for chemical and biological applications.[70-72, 79] The nucleation rate can be determined from induction time measurements, where the emergence of the first crystal is recorded as the induction time at a fixed supersaturation.[80] Nucleation is a stochastic process, and it needs a large number of data points to evaluate a statistically accurate value of induction time for a particular value of supersaturation ratio.[81, 82] To work with microfluidic technology allows to execute a large number of experiments with relative ease with consuming less compound.

1.8. Objective of this thesis

To predict the likelihood of a patient developing kidney stones is difficult without looking at physicochemical interactions in our body. It is important to know the mechanism (why, when and how CaOx stones form) behind kidney stone formation to prevent it.

Thus, the objectives of the research are:

- To measure the solubility of COM, a nearly insoluble salt, which is the first step towards elucidating the physiochemical mechanism behind the formation of COM stones.

- To study the kinetics of COM as a function of supersaturation, pH and presence of inhibitors of stone formation, in particular magnesium ions (Mg^{2+}) and Osteopontin (OPN), in a droplet-based microfluidic device.

- To shed light on the role of hyaluronic acid (a nonprotein commonly found in urine) on the kinetics of CaOx nucleation in artificial urine in a microfluidic set up.

- To measure crystal growth rate of CaOx in a microfluidic device mimicking biological conditions which cause CaOx stones in the kidney in a continuous laminar flow of artificial urine.

1.9. Thesis outline

In Chapter 1, there is a brief introduction of kidney stone and lab on a chip technology.

In Chapter 2, a combined experimental study of COM solubility is studied by a model based on Debye-Hückel theory describing the solution chemistry and the complex formation. Inductively coupled plasma optical emission spectroscopy (ICP-OES) is identified as the most consistent detection method among the methods applied. In buffer solutions, the measured COM solubility varies dramatically across physiologically relevant pH values at body temperature. The suggested model explains the observed trends as a result of a combination of ionic strength, protonation processes, and the production of soluble complexes.

In Chapter 3, the rate of COM nucleation is evaluated using microfluidic induction time measurements in a droplet-based microfluidic platform as a function of supersaturation, pH, and in the presence of two inhibitors: Magnesium ions (Mg^{2+}), Osteopontin (OPN). This research presents a microfluidic device that allows us to quantify COM nucleation rates with statistical accuracy.

In Chapter 4, the effect of hyaluronic acid (HA) on CaOx nucleation is studied in artificial urine. Induction time measurements at varying oxalate and HA concentrations are quantified. The pseudo-polymorphic transitions of CaOx (COM and COD) are carefully investigated using polarized light. COM and COD nucleate in nearly the same time in artificial urine, although with distinct kinetics.

In Chapter 5, a coflowing microfluidic geometry is used to mimic crystal formation in the collecting duct in kidney. The crystal growth rates are recorded using an optical microscope platform, allowing observation of continuous growth during the experiment. All conditions: varying velocity, the molar ratio of calcium and oxalate, and adding different quantities of OPN in artificial urine are investigated by applying COMSOL simulation, JESS database and experiments.

In Chapter 6, our conclusions are summarized and discussed.

1.10. References

1. Hall, J. E., Hall, M.E., *Guyton and Hall textbook of medical physiology e-Book*. Elsevier Health Sciences: 2020.

2. Asmar, A.; Cramon, P. K.; Simonsen, L.; Asmar, M.; Sorensen, C. M.; Madsbad, S.; Moro, C.; Hartmann, B.; Jensen, B. L.; Holst, J. J.; Bulow, J., Extracellular Fluid Volume Expansion Uncovers a Natriuretic Action of GLP-1: A Functional GLP-1-Renal Axis in Man. *Journal of Clinical Endocrinology Metabolism* **2019,** *104* (7), 2509-2519.

3. Choi, H. Y.; Park, H. C.; Ha, S. K., High Water Intake and Progression of Chronic Kidney Diseases. *Electrolyte Blood Press* **2015,** *13* (2), 46-51.

4. Smith, H. W., *The kidney: structure and function in health and disease*. Oxford University Press, USA: 1951; Vol. 1.

5. Bruce, M. K., Bruce, A Stanton, *Renal physiology*. Philadelphia, PA : Elsevier Mosby: 2013; p 79.

6. Ogobuiro I, W. C., Tuma F, Anatomy, thorax, heart coronary arteries. *StatPearls* **2020**.

7. Hickling, D. R.; Sun, T. T.; Wu, X. R., Anatomy and Physiology of the Urinary Tract: Relation to Host Defense and Microbial Infection. *Microbiol Spectrum* **2015,** *3* (4).

8. Institute, N. Kidney and nephron. https://www.niddk.nih.gov/news/media-library/9555 (accessed 2021 January).

9. Romero, V.; Akpinar, H.; Assimos, D. G., Kidney stones: a global picture of prevalence, incidence, and associated risk factors. *Reviews in urology* **2010,** *12* (2-3), e86-96.

10. Alelign, T.; Petros, B., Kidney Stone Disease: An Update on Current Concepts. *Advences in Urology* **2018**, 3068365.

11. Wang, W.; Fan, J.; Huang, G.; Li, J.; Zhu, X.; Tian, Y.; Su, L., Prevalence of kidney stones in mainland China: A systematic review. *Scientific reports* **2017,** *7* (1), 41630.

12. Han, H.; Segal, A. M.; Seifter, J. L.; Dwyer, J. T., Nutritional Management of Kidney Stones (Nephrolithiasis). *Clinical nutrition research* **2015,** *4* (3), 137-152.

13. Asplin, J. R. In *Evaluation of the kidney stone patient*, Seminars in nephrology, Elsevier: 2008; pp 99-110.

14. Khan, S. R.; Pearle, M. S.; Robertson, W. G.; Gambaro, G.; Canales, B. K.; Doizi, S.; Traxer, O.; Tiselius, H. G., Kidney stones. *Nature Reviews. Disease Primers* **2016,** *2* (1), 16008.

15. Bihl, G.; Meyers, A., Recurrent renal stone disease—advances in pathogenesis and clinical management. *The Lancet* **2001,** *358* (9282), 651-656.

16. Coe, F. L., Favus, M.J., Pak, C.Y.C., Parks, J.H., Preminger, G.M.,; Tolley, D. A., Kidney stones: Medical and surgical management. *British Journal of Urology* **1996,** *78* (3), 482.

17. Reynolds, T. M., Best Practice No 181: Chemical pathology clinical investigation and management of nephrolithiasis. *Journal of clinical pathology* **2005,** *58* (2), 134-140.

18. Kramer, H. J. M., Jansens, P.J., *Tools for design and control of industrial crystallizers–state of art and future needs*. 2003; Vol. 26, p 247-255.

19. Radacsi, N. A., R.; Szunyogh, T.; Szabó-Révész, P.; Stankiewicz, A.; van der Heijden, A.; ter Horst, J.H., Electrospray crystallization for nanosized pharmaceuticals with improved properties. *Crystal growth & design* **2012,** *12* (7), 3514-3520.

20. Davey, R. J.; Schroeder, S. L.; ter Horst, J. H., Nucleation of organic crystals--a molecular perspective. *Angewandte Chemie International Edition* **2013,** *52* (8), 2166-2179.

21. Levi, A. C., Kotrla, M., Theory and simulation of crystal growth. *Journal of Physics: Condensed Matter* **1997,** *9* (2), 299.

22. Brunsteiner, M., Jones, A.G., Pratola, F., Price, S.L., Simons, S.J.R., Toward a molecular understanding of crystal agglomeration. *Crystal growth & design* **2005,** *5* (1), 3-16.

23. Bourque, A. J.; Locker, C. R.; Rutledge, G. C., Heterogeneous Nucleation of an n-Alkane on Tetrahedrally Coordinated Crystals. *The Journal of Physical Chemistry B* **2017,** *121* (4), 904-911.

24. Mullin, J. M., *Crystallization*. Elsevier: 2001.

25. El-Zhry El-Yafi, A. K. E.-Z., Hind., Technical crystallization for application in pharmaceutical material engineering. *asian journal of pharmaceutical sciences* **2015,** *10* (4), 283-291.

26. Kashchiev, D., Classical nucleation theory approach to two-step nucleation of crystals. *Journal of Crystal Growth* **2020,** *530*, 125300.

27. Jehannin, M.; Rao, A.; Colfen, H., New Horizons of Nonclassical Crystallization. *Journal of the American Chemical Society* **2019,** *141* (26), 10120-10136.

28. Kalikmanov, V. I., Classical nucleation theory. In *Nucleation theory*, Springer: 2013; pp 17-41.

29. Haas, C. D., J., Understanding protein crystallization on the basis of the phase diagram. *Journal of Crystal Growth* **1999,** *196* (2-4), 388-394.

30. Smeets, P. J. M.; Finney, A. R.; Habraken, W.; Nudelman, F.; Friedrich, H.; Laven, J.; De Yoreo, J. J.; Rodger, P. M.; Sommerdijk, N., A classical view on nonclassical nucleation. *Proceedings of the National Academy of Sciences* **2017,** *114* (38), E7882-E7890.

31. Banner, D. J. F., E.; Rehak, P.; Phakatkar, A.H.; Foroozan, T.; Osborn, J.K.; Sorokina, L.V.; Narayanan, S.; Tahseen, T.; Baggia, Y., In Situ Liquid-Cell TEM Observation of Multiphase

Classical and Nonclassical Nucleation of Calcium Oxalate. *Advanced Functional Materials* **2021,** *31* (18), 2007736.

32. Ruiz-Agudo, E.; Burgos-Cara, A.; Ruiz-Agudo, C.; Ibanez-Velasco, A.; Colfen, H.; Rodriguez-Navarro, C., A non-classical view on calcium oxalate precipitation and the role of citrate. *Nature communications* **2017,** *8* (1), 768.

33. Aggarwal, K. P.; Narula, S.; Kakkar, M.; Tandon, C., Nephrolithiasis: molecular mechanism of renal stone formation and the critical role played by modulators. *BioMed Research International* **2013,** *2013*, 292953.

34. Aggarwal, K. P.; Narula, S.; Kakkar, M.; Tandon, C., Nephrolithiasis: molecular mechanism of renal stone formation and the critical role played by modulators. *BioMed Research International* **2013,** *2013.*

35. Gill, W. B.; Jones, K. W.; Ruggiero, K. J., Protective effects of heparin and other sulfated glycosaminoglycans on crystal adhesion to injured urothelium. *The Journal of Urology* **1982,** *127* (1), 152-154.

36. Asselman, M. V., A.; De Broe, M. E.; Verkoelen, C. F.;, Calcium oxalate crystal adherence to hyaluronan-, osteopontin-, and CD44-expressing injured/regenerating tubular epithelial cells in rat kidneys. *Journal of American Society Nephrology* **2003,** *14* (12), 3155-3166.

37. Verkoelen, C. F.; Verhulst, A., Proposed mechanisms in renal tubular crystal retention. *Kidney international* **2007,** *72* (1), 13-8.

38. Fleisch, H., Inhibitors and promoters of stone formation. *Kidney international* **1978,** *13* (5), 361-371.

39. Brown, P., Ackerman, D., Finlayson, B., Calcium oxalate dihydrate (weddellite) precipitation. *Journal of Crystal Growth* **1989,** *98* (3), 285-292.

40. Chutipongtanate, S.; Thongboonkerd, V., Systematic comparisons of artificial urine formulas for in vitro cellular study. *Analytical biochemistry* **2010,** *402* (1), 110-112.

41. Lee, S. C.; Hutchinson, J. M.; Inn, K. G.; Thein, M., An intercomparison study of 237Np determination in artificial urine samples. *Health physics* **1995,** *68* (3), 350-8.

42. Ipe, D. S.; Horton, E.; Ulett, G. C., The Basics of Bacteriuria: Strategies of Microbes for Persistence in Urine. *Frontiers Cellular and Infection Microbiology* **2016,** *6*, 14.

43. Mitra, P.; Pal, D. K.; Das, M., Does quality of drinking water matter in kidney stone disease: A study in West Bengal, India. *Investigative and clinical urology* **2018,** *59* (3), 158-165.

44. Geng, X.; Sosa, R. D.; Reynolds, M. A.; Conrad, J. C.; Rimer, J. D., Alginate as a green inhibitor of barite nucleation and crystal growth. *Molecular Systems Design & Engineering* **2021,** (7), 508-519.

45. Chien, Y. C.; Masica, D. L.; Gray, J. J.; Nguyen, S.; Vali, H.; McKee, M. D., Modulation of calcium oxalate dihydrate growth by selective crystal-face binding of phosphorylated osteopontin and polyaspartate peptide showing occlusion by sectoral (compositional) zoning. *The Journal of Biological Chemistry* **2009,** *284* (35), 23491-23501.

46. Heijnen, W., Van Duijneveldt, F.B., The theoretical growth morphology of calcium oxalate dihydrate. *Journal of Crystal Growth* **1984,** *67* (2), 324-336.

47. Pleeging, R. M. B.; Ibis, F.; Fan, D.; Sasso, L.; Eral, H. B.; Staufer, U., Polymer nano manufacturing of a biomimicking surface for kidney stone crystallization studies. *Micro and Nano Engineering* **2021,** *13*, 100094.

48. Hartl, W. P.; Klapper, H.; Barbier, B.; Ensikat, H. J.; Dronskowski, R.; Müller, P.; Ostendorp, G.; Tye, A.; Bauer, R.; Barthlott, W., Diversity of calcium oxalate crystals in Cactaceae. *Botany* **2007,** *85* (5), 501-517.

49. Sheng, X.; Ward, M. D.; Wesson, J. A., Crystal surface adhesion explains the pathological activity of calcium oxalate hydrates in kidney stone formation. *Journal American Society of Nephrology* **2005,** *16* (7), 1904-1908.

50. Verhulst, A., Asselman, M., Persy, V.P, Schepers, M.S.J., Helbert, M.F., Verkoelen, C.F., De Broe, M.E., Crystal retention capacity of cells in the human nephron: involvement of CD44 and its ligands hyaluronic acid and osteopontin in the transition of a crystal binding-into a nonadherent epithelium. *Journal of the American Society of Nephrology* **2003,** *14* (1), 107-115.

51. Verkoelen, C. F.; Van Der Boom, B. G.; Romijn, J. C., Identification of hyaluronan as a crystal-binding molecule at the surface of migrating and proliferating MDCK cells. *Kidney international* **2000,** *58* (3), 1045-1054.

52. Asselman, M. V., A.; Van Ballegooijen, E.S.; Bangma, C.H.; Verkoelen, C.F.; De Broe, M.E., Hyaluronan is apically secreted and expressed by proliferating or regenerating renal tubular cells. *Kidney international* **2005,** *68* (1), 71-83.

53. Reinholt, F. P., Hultenby, K., Oldberg, A., Heinegård, D., Osteopontin--a possible anchor of osteoclasts to bone. *Proceedings of the National Academy of Sciences* **1990,** *87* (12), 4473-4475.

54. Tsuji, H.; Tohru, U.; Hirotsugu, U.; Masanori, I.; Yuji, H.; Takashi, K., Urinary concentration of osteopontin and association with urinary supersaturation and crystal formation. *International journal of urology* **2007,** *14* (7), 630-634.

55. Ratkalkar, V. N.; Kleinman, J. G., Mechanisms of Stone Formation. *Clinical reviews in bone and mineral metabolism* **2011,** *9* (3-4), 187-197.

56. Ebrahimpour, A. P., L.; Nancollas, G.H., Induced crystal growth of calcium oxalate monohydrate at hydroxyapatite surfaces. The influence of human serum albumin, citrate, and magnesium. *Langmuir* **1991,** *7* (3), 577-583.

57. Bonny, O.; Rubin, A.; Huang, C. L.; Frawley, W. H.; Pak, C. Y.; Moe, O. W., Mechanism of urinary calcium regulation by urinary magnesium and pH. *Journal of the American Society Nephrology* **2008,** *19* (8), 1530-1537.

58. Coe, F. L.; Evan, A. P.; Worcester, E. M.; Lingeman, J. E., Three pathways for human kidney stone formation. *Urological research* **2010,** *38* (3), 147-160.

59. Molzon, J. A. The solubility of calcium oxalate as a function of dielectric constant. 1976.

60. McComas, W. H.; Rieman, W., The Solubility of Calcium Oxalate Monohydrate in Pure Water and Various Neutral Salt Solutions at 25°. *Journal of the American Chemical Society* **1942,** *64* (12), 2946-2947.

61. Shehyn, H., Pall, D.B., The Solubility of Calcium Oxalate in Various Salt Solutions. *The Journal of Physical Chemistry* **1940,** *44* (2), 166-171.

62. Robertson, W. G., Diet and calcium stones. *Mineral and electrolyte metabolism* **1987,** *13* (4), 228-34.

63. Finlayson, B.; Roth, R., Appraisal of calcium oxalate solubility in sodium chloride and sodium-calcium chloride solutions. *Urology* **1973,** *1* (2), 142-144.

64. Streit, J., Tran-Ho, L., Königsberger, E., Solubility of the three calcium oxalate hydrates in sodium chloride solutionsand urine-like liquors. *Monatshefte für Chemie/Chemical Monthly* **1998,** *129* (12), 1225-1236.

65. Gardner, G. L., Nancollas, G. H., Crystal growth in aqueous solution at elevated temperatures. Barium sulfate growth kinetics. *The Journal of Physical Chemistry* **1983,** *87* (23), 4699-4703.

66. Ridley, J. W., *Fundamentals of the Study of Urine and Body Fluids*. Springer: 2018.

67. Childs-Sanford, S. E. The captive maned wolf: nutritional considerations with emphasis on management of cystinuria. University of Maryland, 2005.

68. Bono, M. J., Reygaert, W.C., Urinary tract infection. In *Urinary tract infection*, StatPearls Publishing: 2017.

69. Zheng, B.; Roach, L. S.; Ismagilov, R. F., Screening of protein crystallization conditions on a microfluidic chip using nanoliter-size droplets. *Journal of the American Chemical Society* **2003,** *125* (37), 11170-11171.

70. Envisiontec 3D Printer. https://envisiontec.com/3d-printers/desktop-3d-printers/micro-plus-hi-res/ (accessed January 2019).

71. Ai, Y.; Xie, R.; Xiong, J.; Liang, Q., Microfluidics for Biosynthesizing: from Droplets and Vesicles to Artificial Cells. *Small* **2020,** *16* (9), e1903940.

72. Tona, R. M.; McDonald, T. A. O.; Akhavein, N.; Larkin, J. D.; Lai, D., Microfluidic droplet liquid reactors for active pharmaceutical ingredient crystallization by diffusion controlled solvent extraction. *Lab Chip* **2019,** *19* (12), 2127-2137.

73. Li, S.; Ihli, J.; Marchant, W. J.; Zeng, M.; Chen, L.; Wehbe, K.; Cinque, G.; Cespedes, O.; Kapur, N.; Meldrum, F. C., Synchrotron FTIR mapping of mineralization in a microfluidic device. *Lab Chip* **2017,** *17* (9), 1616-1624.

74. Sia, S. K.; Whitesides, G. M., Microfluidic devices fabricated in poly(dimethylsiloxane) for biological studies. *Electrophoresis* **2003,** *24* (21), 3563-3576.

75. An, H. Z., Eral, H.B., Chen, L., Chen, M.B., Doyle, P.S.,, Synthesis of colloidal microgels using oxygen-controlled flow lithography. *Soft Matter* **2014,** *10* (38), 7595-7605.

76. Gupta, A.; Badruddoza, A. Z. M.; Doyle, P. S., A general route for nanoemulsion synthesis using low-energy methods at constant temperature. *Langmuir* **2017,** *33* (28), 7118-7123.

77. Worcester, E. M.; Coe, F. L., Nephrolithiasis. *Primary Care* **2008,** *35* (2), 369-391, vii.

78. Laffite, G., Leroy, C., Bonhomme, C., Bonhomme-Coury, L., Letavernier, E., Daudon, M., Frochot, V., Haymann, J.P., Rouzière, S.L., Ivan, T., Bazin, D., Babonneaub, F., Abou-Hassan, A., Calcium oxalate precipitation by diffusion using laminar microfluidics: toward a biomimetic model of pathological microcalcifications. *Lab on a Chip* **2016,** *16* (7), 1157-1160.

79. Nisisako, T.; Torii, T.; Higuchi, T., Droplet formation in a microchannel network. *Lab Chip* **2002,** *2* (1), 24-6.

80. Sear, R. P., Quantitative studies of crystal nucleation at constant supersaturation: experimental data and models. *CrystEngComm* **2014,** *16* (29), 6506-6522.

81. Kolbach-Mandel, A. M.; Kleinman, J. G.; Wesson, J. A., Exploring calcium oxalate crystallization: a constant composition approach. *Urolithiasis* **2015,** *43* (5), 397-409.

82. Kok, D. J.; Papapoulos, S. E.; Blomen, L. J.; Bijvoet, O. L., Modulation of calcium oxalate monohydrate crystallization kinetics in vitro. *Kidney international* **1988,** *34* (3), 346-50.

Chapter 2.

A combined experimental and modelling study on solubility of Calcium Oxalate Monohydrate at physiologically relevant pH and temperatures

This chapter is based on Fatma Ibis, Priya Dhand, Sanan Suleymanli, Antoine E. D. M. van der Heijden, Herman J. M. Kramer and Huseyin Burak Eral, Crystals 2020, 10(10), 924; https://doi.org/10.3390/cryst10100924.

Abstract

Accurate calcium oxalate monohydrate (COM) solubility measurements are essential for elucidating the physiochemical mechanism behind the formation of kidney stones, nephrolithiasis. Yet the reported solubility values of COM in ultrapure water, arguably the simplest solvent relevant for nephrolithiasis, vary significantly depending on implemented method. To address this variation, we present an experimental study of the solubility of COM validated by a model based on the Debye-Hückel theory describing the solution chemistry and the complex formation. We also carefully monitor potential pseudo-polymorphic/hydrate transitions during the solubility measurements with in-situ and ex-situ methods. Our results indicate that the solubility of COM in ultrapure water is a weak function of temperature. However, the measured solubility varies significantly in buffer solutions across physiologically relevant pH values at body temperature. The proposed model explains observed trends as a combined effect of ionic strength, protonation reactions and soluble complex formation. Moreover, it predicts solubility of COM in buffer solutions remarkably well using our measurements in ultrapure water as input, demonstrating the consistency of presented approach. The presented study parleying experiments and modelling provides a solid stepping stone to extend the physiochemical understanding of nephrolithiasis to more realistic solutions laden with biological complexity.

2.1. Introduction

Nephrolithiasis can be seen as the crystallization of inorganic salts and their consequent aggregation in the presence of biological complexity in the human kidney. This disease affects about 12% of the world population and its prevalence is increasing.[1, 2] The driving force behind nucleation, the first step in formation of kidney stones, is the supersaturation of urine concerning the stone constituents such as calcium, oxalate and phosphate ions.[3, 4] Patient specific information such as patient age, genetic effects, medical treatment history, fluid intake, diet habits, urine pH, and environmental conditions have also been reported as significant factors in formation of kidney stones.[5-7] To prevent kidney stone disease and its recurrence, first of all a better understanding of the underlying physiochemical mechanism of stone formation in the kidney is needed. Such an investigation should shed light on the questions such as why some people under normal physiological conditions form kidney stones in the urinary tract, while others do not.

There are three main types of stones: calcium oxalate, calcium phosphate and uric acid.[8-10] Calcium oxalate (CaOx) comprises 80% of the kidney stones which is found in the form of hydrates.[11-14] It occurs as dihydrate (weddellite) or monohydrate (whewellite).[5, 6] Calcium oxalate monohydrate (COM) is the most commonly seen and the most stable form with very low water solubility.[5, 9, 15, 16] It is attributed mostly to idiopathic hypercalciuria. Hypercalciuria stones are caused due to a high calcium level in urine.[5, 17]

Urine is a waste product of our body consisting of water, salts, and soluble nitrogen products in addition to various biomolecules. The presence of these compounds influences the pH of the urine solution and has a strong influence on the crystallization of calcium oxalate, the main component of kidney stones.[8] Clinical studies indicated that pH values between 4.5 and 5.5 form the highest risk for forming kidney stones.[8, 18] Even though the average pH of urine is 6.0, it can range between 4.0 and 8.0.[19] Prediction of the crystallization behavior of COM crystals in such an environment therefore required precise knowledge on the influences of the composition and pH of the urine solution in the kidney on the solubility as well as on the nucleation and growth kinetics of these crystals. In this study, we concentrate on the solubility of COM while carefully monitoring the potential polymorphic transitions. The solubility of COM is reported to be strongly influenced by solution properties--the pH and ionic strength--, emphasizing the presence of electrolytes, the speciation of the different ions as well as the formation of ionic pairs in the solution.[20-22]

The solubility of calcium oxalate (CaOx) in pure water has been previously reported in the literature.[23-27] However, the stated values vary significantly as shown in Table 2.1. This large variation among reported values might be related to either the accuracy of the detection techniques used to determine the calcium or the oxalate concentrations, or different preparation methods used to create a saturated COM solution i.e., dissolution or precipitation, potentially resulting different polymorphic forms of COM. More importantly, standard deviation was not reported in most of reported measurements making it difficult to pinpoint the origin of this variation.[23-29] This inconsistency calls for a systematic experimental study comparing different methods.

Table 2.1. The solubility of CaOx in Pure Water at 25 °C. In reports provided below hydrate form of dissolved CaOx has not been reported or characterized hence we can refer them as CaOx solubility unless hydrate form is explicitly mentioned.

Authors	**Year**	**Solubility [10^{-4}M]**	**Measurements Method**
Gutzow et al.[26]	1993	0.57	Atomic absorption spectrometry
Molzon[23]	1976	1.329	Dielectric constant measurements
McComas et al.[24]	1942	0.455	Titration
Shehyn and Pall[25]	1940	0.60	Titration
Hammarsten[28]	1929	0.466	Titration
Herz et al.[27]	1903	2.33	Titration
Singh et al.[20]	1989	0.564	Ion Chromatography

More recent studies have focused on solubilities in more physiologically relevant solutions for formation of kidney stones, such as urine-like or artificial urine solutions. Those studies revealed that background electrolytes like NaCl,[22, 30, 31] lead to an increased solubility, which has been attributed to the influence of the electrolyte solution on the activity coefficient of the Ca^{2+} and $C_2O_4^{2-}$ ions.[22, 31] In addition, it was shown that the pH of the solution, affects the speciation of the different components and thus the formation of ionic pair complexes of calcium and oxalate ions. As such the pH can have a strong influence on the solubility of COM and the crystallization kinetics.[22, 30-32] In more complex solutions, the ratio of Calcium and oxalate ions can vary considerably, stressing the need to express the solubility in terms of the thermodynamic solubility product.[21, 22, 33] Streit et al. compared own and literature values of the thermodynamic solubility product K_{sp} and reported a value of K_{sp} of $1.7 \cdot 10^{-9}$ mol^2L^{-2} for COM at 25 °C.[22] However, he also noted an inconsistency between solubility measurements using atomic absorption spectroscopy and those using the calcium electrode measurements.

The interpretation of solubility experiments in more complex solutions requires precise estimation of the composition effects on the activity of the relevant components. Besides, a detailed analysis of the possible reactions and complex formation is essential to understand the behavior of these solutions as a function of pH and composition. A number of attempts have been made to interpret solubility and crystallization results in different solutions with varying complexity ranging from the water with background electrolytes up to urine samples of stone-forming patients.[22, 24, 30, 31, 34-36] However, the previous studies did not consistently cover physiologically relevant pH and temperature ranges while considering composition effects on the activity of the relevant components. The aforementioned variation in reported the solubility measurements of COM in ultrapure water and the lack of a systematic study on pH dependency of this solubility hampers modeling efforts.

This work describes a coupled experimental and modeling study on the solubility of the calcium oxalate monohydrate as a function of temperature and pH, monitoring the polymorphic form of the crystalline phase to rule out possible transformations into other hydrates of CaOx. To select the most appropriate analytical method to measure the solubility of this sparsely soluble compound, we first conducted a comparative study of the solubility measurements using a number of analytical methods as a function of temperature. Once the most appropriate analytical method was identified, we proceeded to measure the solubility of COM as a function of pH in buffer solutions at body temperature. Moreover, we developed a solution chemistry model based on Davies extension of Debye-Hückel theory and compared the theoretical predictions to experimental results. The influence of the pH on the solubility of COM is quantified at body temperature in two different buffer solutions, i.e., citric acid-disodium phosphate and glycine-sodium hydroxide chosen to stabilize the pH between 3.2-7.55 and from 9.0 to 10.6 respectively. Finally we used the developed a solution chemistry model to elucidate the effects of the process conditions, ionic strength, and complex formation on the solubility of COM.[37] The proposed model coupled with the Van 't Hoff equation enabled the calculation of the solubility product of COM, K_{sp} from the solubility measurements as a function of temperature. These K_{sp} values implemented in the developed model provided excellent predictions for the soluble Ca^{2+} ion concentration measurements at different pH values in two different buffer solutions kept at body temperature. This excellent prediction without fudge factors highlights the consistency of the presented study parleying experiments with modeling. We believe our combined study provides a solid stepping stone to extend the developed physiochemical understanding to more realistic and complex solutions relevant for nephrolithiasis.

2.2. Materials and Methods

As mentioned previously, solubility measurements of sparsely separated compounds are challenging due to minute amounts of material involved. To identify the ideal measurement method for this task, we systematically tested the following methods: (i) gravimetric method to isolate non-volatile components saturated COM, (ii) the turbidity based solubility method using multiple reactor systems Crystal16 and Crystalline (Avantium Technologies, Amsterdam, The Netherlands), (iii) UV-VIS Spectrophotometry, (iv) Focused Beam Reflectance Measurement (FBRM D600L, Mettler Toledo, Columbus, OH, USA), (v) In situ Infrared spectroscopy (ReactIR iC10 Mettler Toledo, Columbus, OH, USA) coupled to temperature-controlled and well-mixed vessel, EasyMax[38-40], (vi) Titration, (vii) Inductively coupled plasma optical emission spectroscopy (ICP-OES, SPECTRO Analytical Instruments, Kleve, Germany), (viii) Inductively coupled plasma mass spectroscopy (ICP-MS, Analytik Jena AG, Jena, Germany). The tested methods are illustrated in Figure 2.1. For the sake of completeness, we provide here a list of all tested methods yet only titration, ICP-OES and ICP-MS produced consistent results presented in Figure 2.2 and Figure 2.3. The detailed procedures and discussion for other methods are provided in the Appendix A. The experimental section is organized as follows: First the method for preparing an equilibrated suspension is described in sections 2.2.1 and 2.2.2, followed by description of analytical detection methods in sections 2.2.3 to 2.2.5 and finally, pseudo-polymorphic/hydrate characterization of excess COM in-situ and ex-situ in section 2.2.6.

2.2.1. Preparation of equilibrated suspensions and sampling for ICP-OES and ICP-MS

In all of the experiments described above, an excess amount of calcium oxalate monohydrate ($CaC_2O_4{\cdot}H_2O$, Sigma-Aldrich, CAS563-72-4) crystals are brought in equilibrium with an aqueous solution (pure water (ELGA PURELAB, Resistivity:18.2 MΩ·cm at 23.6 °C) or a buffer solution at a given temperature in a well-mixed, temperature-controlled vessel (Figure 2.1). Once the equilibrium is established, an aliquot of the saturated solution carrying calcium and oxalate ions in equilibrium with COM in crystal phase is filtered, diluted with pure solvent (either ultrapure water or buffer solution) and analyzed. We used EasyMax 102 (Mettler Toledo) a jacketed vessel to control the temperature and stirring rate (400 rpm). 20 mg of COM crystals were suspended in 100 ml ultrapure water or 100 ml buffer solution and allowed to equilibrate at targeted temperature and pH for one hour. To ensure that thermodynamic equilibrium is reached, we conducted experiments at different equilibration times namely, 30 min, one hour, two hours and four hours. The measured solubility values did not change significantly (<1%) after one hour, hence we chose one hour as our canonical equilibration time. For temperature dependence of solubility measurements, COM crystal dispersed in ultrapure water were rigorously mixed, and the resulting suspension was allowed to equilibrate at 25 ^{o}C, 37 ^{o}C, 60 ^{o}C, 90 ^{o}C. For measuring the pH dependence of solubility of COM, the suspension was allowed to equilibrate in buffer solutions with set pH values 3.2, 5.36, 6.0, 7.55, 9.0, 10.6 respectively at 37 ^{o}C. After the solution was kept at the desired temperature and pH to reach solid-liquid equilibrium, the stirrer was stopped, and samples were taken from the top portion of the vessel.

Aliquoting of the saturated solution is performed in three steps: pipetting, filtration, and dilution. When the stirrer of Easymax is stopped, the crystals are allowed to sediment and 1 ml solution is taken with a 1ml pipette. The equilibrated solution is filtered with syringe and filter (Whatman, 0.22 µm pore diameter) kept at the same temperature as the suspension in a separate oven. The samples were 10X diluted into 10 ml volumes with pure ultrapure water or buffer solution kept at the same temperature as the suspension to avoid precipitation. 10 ml samples are needed for the analysis with ICP-OES and ICP-MS. For each experimental condition, the identical samples are divided into two groups for ICP-OES and ICP-MS analysis.

A buffer solution is chosen considering the possibilities of the binding capacity of calcium with other compounds present in the buffer solution. The most convenient options are citric acid- disodium phosphate for the lower pH range and glycine-sodium hydroxide for the higher pH range. The buffer solutions are prepared in 1000 ml Erlenmeyer and placed in the ultrasonic bath for 10 minutes. Afterward, the buffer solution is placed on the magnetic stirrer at 37 ^{o}C and 400 rpm. The buffer solutions used in pH dependent solubility measurements are given in Table 2.2.

Table 2.2. Used buffer solutions for different pH values.[41, 42]

pH	**Mixing of buffer solutions**
3.2	Citric Acid ($C_6H_8O_7$)
5.36	(Merck, CAS: 77-92-9)
6.0	Disodium phosphate (Na_2HPO_4)
7.55	(Sigma-Aldrich, CAS: 7558-79-4)
	Sodium hydroxide (NaOH)
9.0	(Sigma-Aldrich, CAS: 7558-79-4)
10.6	Glycine ($C_2H_5NO_2$)
	(Sigma-Aldrich, CAS: 1310-73-2)

2.2.2. Preparation of equilibrated suspensions for titration

This procedure is analogous to preparation of equilibrated suspensions for ICP-OES and ICP-MS yet certain details such as amount of suspension and method to maintain the solution constant temperature are adapted for the requirements of titration experiment. 10 mg COM is mixed with 50 ml of ultrapure water in a beaker. The suspension is equilibrated on a hot plate at the targeted temperature at a stirring rate of 400 rpm for three hours. A longer equilibration time, three hours instead of one hour used in ICP-OES and ICP-MS measurements, was chosen to account for the less stringent temperature control of the hot plate compared jacketed EasyMax 102 reactor.

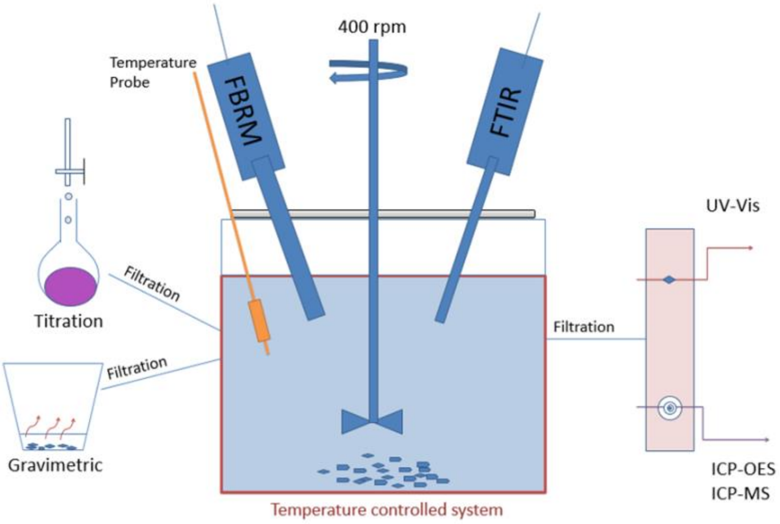

Figure 2.1. Schematic illustration of isothermal solubility experiments. A suspension of excess COM crystals in ultrapure water or a buffer solution was brought in equilibrium at designated temperature and pH values. The suspension is filtered to isolate the saturated solution from crystals at fixed temperature. The saturated solution is diluted at the same temperature to avoid crystallization. The calcium and oxalate ion concentrations in filtered saturated solution are analyzed with the following methods, commonly used for measuring solubility of highly insoluble compounds in literature (from the left to right); gravimetric, titration, FBRM, FTIR, UV-Vis, ICP-OES and ICP-MS. The pseudo-polymorphic/hydrate form of the excess solute is quantified prior to and at the end of experiments via in-situ and ex-situ methods.

2.2.3. Inductively coupled plasma-optical emission spectrometry (ICP-OES)

The filtrate of the COM suspensions equilibrated at different temperature and pH values were analyzed at three possible calcium emission lines at 317.9, 393.4 and 396.3 nm

(See Appendix A). The measurements conducted at all three wavelengths show quantitatively the same trend yet the emission line of 317.9 nm gave smallest standard deviation. This situation is also observed in literature and attributed to interference from other ions present[43-45]. The experiments were conducted with more than seven samples for each temperature, 25 ºC, 37 ºC, 60 ºC, 90 ºC. At body temperature condition, nine replicate samples were analyzed for each pH; namely, 3.2, 5.36, 7.55, 9.0, 10.6 and five replicate samples were analyzed for pH 6.0.[42, 46]

2.2.4. Inductively coupled plasma-mass-spectrometry (ICP-MS)

We prepared at least seven replicates for each temperature and nine samples for each pH. The filtrates of each sample are analyzed with ICP-MS. While ICP-OES can detect ppm level, ICP-MS can detect parts per billion (ppb level)[38] as ICP-MS measures a mass-to-charge ratio, an intrinsically more sensitive approach compared to optical emission used in ICP-OES.[40]

2.2.5. Titration

After filtration, the COM filtrate is mixed (1:10 volume-based) with a 9.5% sulfuric acid solution (Merck, CAS: 7664-93-9). Triplicate experiments are performed at 25, 37, 60 and 90 °C. In the titration reactions, filtrated samples are titrated with a $7 \cdot 10^{-4}$ M potassium permanganate (MnO_4^-) solution until the color change is observed. The concentration of oxalate is calculated via the amount of titrated permanganate.

2.2.6. Pseudo-polymorphic/Hydrate form characterization of excess COM crystals in equilibrated suspension

To check whether COM crystals in suspension transformed to other calcium oxalate hydrates during solubility measurements at experimental temperature and pHs, we quantified the polymorphic form of the crystals prior to and after equilibration via in-situ via Raman scattering, and ex-situ methods via powder X-ray diffraction, PXRD. Due to low solubility of COM, we repeated the procedure for preparation of equilibrated suspensions described in section a 10 times to get sufficient amount of COM crystals to employ Raman and X-ray diffraction detection (at different temperatures; 25 ^oC, 37 ^oC, 60 ^oC, 90 ^oC, at each pH values; 3.2, 5.36, 6.0, 7.55, 9.0, 10.6, and additionally COM suspension in ultrapure water referred to as no treatment--). The suspensions were left undisturbed for one hour to allow the crystals to sediment. For in-situ Raman measurements, the sediment is decanted and the concentrated suspension were analysed with a Raman probe (Kaiser Optical Systems) immersed in suspension. For X-ray diffraction analysis, the crystals were isolated by filtration with 0.45-µm pore size filter (Whatman® membrane filters nylon), then washed with ultrapure water three times and dried to avoid unwanted co-crystallization of buffer constituents, crystal attrition or agglomeration. The washed crystals were kept at room temperature to dried for two days prior to PXRD experiments. Approximately 150 milligrams of crystals were collected for each experimental condition. PXRD experiments were performed with these crystals placed on a silicon holder with a powder X-ray diffractometer (Bruker, Cu Ka1, k = 1.5406 A°). The acquired spectra were compared to reference spectra of COM, calcium oxalate dihydrate (COD), calcium oxalate trihydrate (COT) in Cambridge Crystallographic Data Centre (CCDC). The plotted PXRD patterns taken from the CCDC software tool are the following COM (CALOXM03), COD(CAOXAL) and COT(ZZZUOQ01).

A model was developed to describe the dissolution of COM in ultrapure water based on the solution chemistry which describes the protonation reactions of the oxalate ions in the solution and also the formation of the ion pairs between Ca^{2+} and $C_2O_4^{2-}$ ions to form soluble complexes of CaC_2O_4.[30, 47] Equation 2.1 and Equation 2.2 describe the equilibrium of the protonation reaction of $HC_2O_4^-$ and of $C_2O_4^{2-}$ respectively using their temperature dependent association constants.

$$K_{H_2C_2O_4} = \frac{a_{H_2C_2O_4}}{a_{H^+} a_{HC_2O_4^-}} \qquad \text{Equation 2.1}$$

$$K_{HC_2O_4^-} = \frac{a_{HC_2O_4^-}}{a_{H^+} a_{C_2O_4^{2-}}} \qquad \text{Equation 2.2}$$

In these equations, a_i represents the activity of the species i, which is according to its definition equal to the product of the concentration in solution multiplied with the activity coefficient. In electrolyte solutions part of the Ca^{2+} ions and $C_2O_4^{2-}$ ions will be bound in so-called soluble ion pair complexes and are as such not available for crystallization. At Equation 2.3, the amount of such a complex can be described using an association constant.

$$K_{CaC_2O_4} = \frac{a_{CaC_2O_4,aq}}{a_{Ca^+} a_{C_2O_4^{2-}}} \qquad \textit{Equation 2.3}$$

Table 2.3. Associations constants K_0, solubility products of COM, and enthalpy of reaction of the given reactions from literate and the estimated values of $K_{sp,0}$ and ΔH_R of COM in this study. Estimated values are calculated using the temperature dependent solubility data of COM in ultrapure water given in Figure 2.4 using the proposed model.

Parameters	**Reaction**	**Source**	**K**	**ΔH_R** [kJmol^{-1}]
$K_{H_2C_2O_4}$	$H^+ + HC_2O_4^- \rightleftharpoons H_2C_2O_4$	33	18.17 [L. mol^{-1}]	3.2
$K_{HC_2O_4^-}$	$H^+ + HC_2O_4^{2-} \rightleftharpoons HC_2O_4^-$	33	18450 [L. mol^{-1}]	8.32
$K_{CaC_2O_4}$	$Ca^{2+} + C_2O_4^{2-} \rightleftharpoons CaC_2O_4$	48	2746 [L. mol^{-1}]	0
K_{sp}	$Ca^{2+} + C_2O_4^{2-} \rightleftharpoons CaC_2O_4.H_2O$	22	$1.7 \cdot 10^{-9}$ [mol^2 L^{-2}]	17.9
Estimated K_{sp}	$Ca^{2+} + C_2O_4^{2-} \rightleftharpoons CaC_2O_4.H_2O$	This study	$6.7 \cdot 10^{-9}$ [mol^2 L^{-2}]	5.5

Where $CaC_2O_4.aq$ represents the ion pair or the aqueous form of CaC_2O_4. The presence of ion pair complexes can decrease the amount of free Ca^{2+} and $C_2O_4^{2-}$ ions in the solution and will thus affect the solubility of the COM.[22, 30, 31] The solubility product of COM has been reported by Nancollas and Gardner[47] is given in Equation 2.4.

$$K_{sp} = a_{Ca^{2+}} a_{C_2O_4^{2-}} \qquad \textit{Equation 2.4}$$

The solubility product of COM, K_{sp} is again assumed to be a temperature dependent constant. The temperature dependence of the equilibrium constants or solubility product, K(T) is related to the enthalpy of the reaction using the Van ‘t Hoff equation given below

$$\ln\left(\frac{K(T)}{K_0}\right) = -\frac{\Delta H_R}{R}\left(\frac{1}{T} - \frac{1}{T_0}\right) \qquad \textit{Equation 2.5}$$

Where $K_0=K(T_0)$ is the value of the reaction or stabilization constant at standard conditions at 25°C, ΔH_R [$Jmol^{-1}$] is the enthalpy of the reaction, R [$Jmol^{-1}K^{-1}$] the gas constant and T and T_0 [K] the actual and the standard temperature, respectively. The values used for the different equilibrium constants and those for the enthalpy change of reaction are given in Table 2.3.

In case ΔH_R was not given and temperature dependent K values were available, those values were fitted using the Van ‘t Hoff equation estimating the parameters K_0 and T. The ΔH_R was assumed to be zero otherwise. The presence of a dicalcium oxalate complex ($Ca_2C_2O_4^{2+}$) is also mentioned by some authors, but formation of this complex is generally assumed to be negligible in solubility experiments with low and stoichiometric calcium and oxalate concentrations.[32, 33] Unfortunately, the reported K_{sp} values are not very consistent, which leads to a large discrepancy between experimental measured and simulated solubility values, as will be discussed later in detail.

The activity coefficients, γ_i in the model are estimated using the Davis extension of the Debye-Hückel theory[3] in which the activity coefficients of the different ions are directly related to the ionic strength of the solution I, and the charge of the ions, z_i.

$$\log(\gamma_i) = -Az_i^2\left[\frac{\sqrt{I}}{1+\sqrt{I}} - 0.3I\right] \qquad \textit{Equation 2.6}$$

Here A is a temperature dependent constant around 0.5[33, 49], and I is the ionic strength of the solution defined as:

$$I = -0.5\sum_{i=1}^{N_{species}} c_i z_i^2 \qquad \textit{Equation 2.7}$$

Where c_i is the molar concentration of ion and z_i the charge of these ions. In order to simulate the solubility experiments in ultrapure water at different temperatures, the model calculates the concentrations of the possible species shown in Table 2.3 at the given conditions. For the COM water system, the concentration of the seven possible components, H^+, Ca^{2+} $C_2O_4^{2-}$, $HC_2O_4^-$, $H_2C_2O_4^{2-}$, $CaC_2O_{4.aq}$ and COM are calculated using the material balances for oxalate, and calcium, the charge balance and Equation 2.1-Equation 2.4, while the relation between concentration and activities of the different species is described by the activity coefficients given by Equation 2.6 and Equation 2.7. These equations are solved simultaneously using the Matlab function fsolve.

To simulate the experiments at different pH's in the buffer solutions, the approach is similar. However, the equilibrium between the protonation/de-protonation reactions of the acid species of the buffer solution, again described by an association constant, are considered as well.

As an example, for the citric acid (Cit), the four species Cit^{3-}, $HCit^{2-}$, H_2Cit^- and H_3Cit are, at equilibrium, related by the following three equations:

$$K_{H_3Cit} = \frac{a_{H_3Cit}}{a_{H^+} a_{H_2Cit^-}} \qquad \textit{Equation 2.8}$$

$$K_{H_2Cit^-} = \frac{a_{H_2Cit^-}}{a_{H^+} a_{HCit^{2-}}} \qquad \textit{Equation 2.9}$$

$$K_{HCit^{2-}} = \frac{a_{HCit^{2-}}}{a_{H^+} a_{Cit^{3-}}} \qquad \textit{Equation 2.10}$$

Where Cit^{3-} represents the fully deprotonated citric acid ion. The temperature dependence of the association constant is again described by the Van 't Hoff equation (Equation 2.5). Besides the protonation reactions, complexation reactions of the citric acid species with anions in the solution are considered. According to literature, the following complexes are relevant, $CaCit^-$, CaHCit, and $NaCit^{2-}$.[22, 34, 48] For the phosphate and glycine species, similar protonation reactions can be formulated. Relevant complexes for the phosphate and glycine ions that are considered in the program are $CaHPO_4$, $CaPO_4^-$, $NaPO_4^{2-}$ and $CaGly^+$. The values for the standard values of the association constants for the de-protonation and the complexation reactions and the ΔH_R values were taken from the literature[48, 50, 51] and are given in Appendix A.

2.3. Results and Discussion

The temperature dependent solubility of COM is determined in the simplest solution, ultrapure water. The solubility experiments were performed with the three methods described in the experimental section to find the most suitable method for this sparsely soluble salt (Figure 2.1). Titration, ICP-OES and ICP-MS gave the most consistent results hence discussed in the main text. The rest of the methods are detailed in the supporting information.

First of all, we have to realize that using the titration method, the total oxalate concentration, including the free $C_2O_4^{2-}$ ions, the protonated species of the oxalate and the oxalate in the CaOx complexes, is determined. In contrast, the total Calcium (free and complexed calcium) concentration is determined in ICP-OES and ICP-MS methods. However, the total dissolved calcium or oxalate ion concentrations are not simply equal to the solubility of COM. The solubility of COM is defined as the square root of the solubility product, K_{sp} which is equal to the product of the activities of free Ca^{2+} and $C_2O_4^{2-}$ ions as defined in Equation 2.4. The experimental results are thus expressed either as the total dissolved Ca concentration, the total dissolved oxalate concentration or the total dissolved COM which should be the same for these simple dissolution experiments in water due to stoichiometry. To determine the solubility product K_{sp}, however the activities of the ions should be estimated as well as the contribution of the protonated forms of the oxalate species and of the ion pair complexes, which is done using the model after validation.

In Table 2.4, the results of the solubility experiments are given for the three methods at four different temperatures. The results show a reasonable agreement in terms of the mean values for all methods. However, sizeable differences are found in the standard deviations of the different methods. Especially the titration method shows large standard deviations in Table 2.4. This is even better illustrated in Figure 2.2 and its inset, showing the temperature dependent solubilities measured with the three methods, including the standard deviations of the measurements. The error bars denoting the standard deviation of the ICP-OES measurements are distinctly smaller than those of the ICP-MS and the titration method, indicating that ICP-OES is the most suitable detection method for measuring the solubility of COM among the tested alternatives. Therefore, we use this technique in the remainder of this study as the standard measurement technique.

The large standard deviations observed with the titration method might be due to manual nature of titration method where the experimentalist measures the titrated volume by judging color change by eye. In addition, saturated solution preparation for titration experiments were conducted with a beaker placed on a hot-plate. We suspect that hot-plate used in titration is less accurate in controlling the temperature compared to automated EasyMax 102 (Mettler Toledo) used in saturated solution preparation for ICP-MS and ICP-OES. The larger variation observed with ICP-MS compared to those of the ICP-OES were more of a surprise as in general the ICP-MS can detect elements down to ppb levels.[38] However, in the detection of calcium ions in the mass spectrometer, there is an overlap between the calcium and argon, which have similar molar masses. Due to the overlap with argon, we could not use the normal calcium peak but were forced to measure the calcium isotope, Ca-44, which, however, is much weaker leading to much higher uncertainties.

The measured values of the total dissolved calcium concentration at room temperature in this study are generally high compared to the literature values (see Table 2.1 & Table 2.4) with the exception of the dielectric measurements of Molzon[23] and titration experiments by Herz et al.[27] Yet it is difficult to pinpoint the origin of this difference as most studies do not report a standard deviation.[23-27] Based on the hands-on experience from our measurements, we can only speculate on the origin of this variation. First of all, measurements of sparsely soluble salts are a challenge due to small amounts of material involved that are difficult to weigh accurately. Moreover, techniques requiring visual inspection such as manual titration are subject to human errors hence large standard deviations are expected. We observed standard deviation to vary between

$0.3 \cdot 10^{-4}$ M to $0.5 \cdot 10^{-4}$ M in our titration experiments, if we were to speculate similar standard deviations for four out of seven reported values in Table 2.1, the error bars between our measurements and these experiments will overlap for all but one report. In addition to detection method, the saturated solution preparation can also play a role in this variation between measured and reported values. For instance, saturated solution preparation methods such as rapid precipitation at high supersaturations are susceptible to impurity incorporation to crystals. This may result in impurity doped or coated crystals that dissolve slower than pure crystals. Such slow dissolution kinetics may lead to preparation of undersaturated solutions as opposed to saturated solutions. Also, high supersaturations created in rapid precipitation approach can lead to crystallization of other hydrates (calcium oxalate dihydrate (COD) or calcium oxalate trihydrate (COT)) that have different solubilities. Finally, we characterize the pseudo-polymorphic/hydrate form of the raw material prior and right after solubility measurements (Figure 2.3) this characterization step is essential in dissolution measurements of compounds showing multiple phases or hydrates.[52] If the starting material is not pure COM but contains other hydrates, the measured solubility values will be influenced.

Moreover, the discussion in literature on ideal titration procedure is far from settled. The reported titration experiments in Table 2.1 vary in terms of sample preparation and various authors criticized each other's procedure. Richards et al. have studied calcium oxalate solubility[53] and their method was to treat hot and slightly acid solution of calcium chloride with an excess of oxalic acid. After neutralization, the solution was made distinctly ammoniacal by adding a large excess of ammonium oxalate. They found the solubility of COM as $0.531 * 10^{-4}$ M. Hall has criticized that Richards` study due to presence of "large excess of ammonium oxalate"[54], which could make the calcium oxalate less soluble in accordance with the solubility product principle and the common ion effect. This common ion effect along with our speculations on impurity incorporation and potential phase transitions[52] may explain the difference between the reported titration experiments in Table 2.1 and our measurements. Shehyn and Pall have found solubility of COM in pure water as $0.646 \cdot 10^{-4}$ M at 30 °C and $1.132 \cdot 10^{-4}$ M at 95 °C[25]. Interestingly, their solubility value at 95 °C is quite similar to our results at 90 °C. More recently Streit et al. reported solubility of COM in NaCl solutions of low concentrations[22]. They reported averaged solubilities of $0.78 \cdot 10^{-4}$ M at 25 °C and $0.98 \cdot 10^{-4}$ M at 37 °C, which are lower than our values but larger that most titration experiments in literature. The authors reported however a discrepancy between two methods utilized, i.e. Atomic Absorption Spectroscopy and a Ca selective electrode, which could not be explained by the modelled amount of $CaC_2O_4^{2-}$ ion pair complex formed. With increasing temperatures, the solubility of calcium was found to increases only slightly in our experiments in agreement with earlier results.[30, 32, 51]

To ensure that pH of the solution did not change during solubility measurements at different temperatures, we measured the pH of COM solution in ultrapure water at each temperature shown in Figure 2.2 via IDS pH electrode (pH-meter 914 pH/Conductometer Metrohm). It was found that the dissolution of COM has no significant effect on the pH of the solution in all measurements.

Table 2.4. The results of solubility of COM measurements in ultrapure water as a function of the temperature. The reported results are shown as the mean total ion concentration along with the standard deviations, σ.

	Titration [10^{-4} M]		**ICP-OES [10^{-4} M]**		**ICP-MS [10^{-4} M]**	
Temperature (°C)	**$[C_2O_4^{2-}]_{tot}$**	**σ**	**$[Ca^{2+}]_{tot}$**	**σ**	**$[Ca^{2+}]_{tot}$**	**σ**
25	1.198	0.521	1.054	0.087	0.931	0.086
37	1.244	0.307	1.238	0.103	1.296	0.463
60	1.258	0.378	1.246	0.140	1.102	0.089
90	1.279	0.290	1.332	0.055	1.238	0.216

To quantify the pseudo-polymorphic/hydrate form of excess crystals, we performed Raman and PXRD measurements of our samples before and after the experiments. Figure 2.3.a shows Raman spectra of crystals suspended in ultrapure water during isothermal dissolution experiment at different temperatures. In addition, Figure 2.3.a contains Raman spectra of ultrapure water (without suspended crystals) and of suspended COM crystals as purchased from the manufacturer prior to dissolution experiment denoted as “COM suspended in water”.

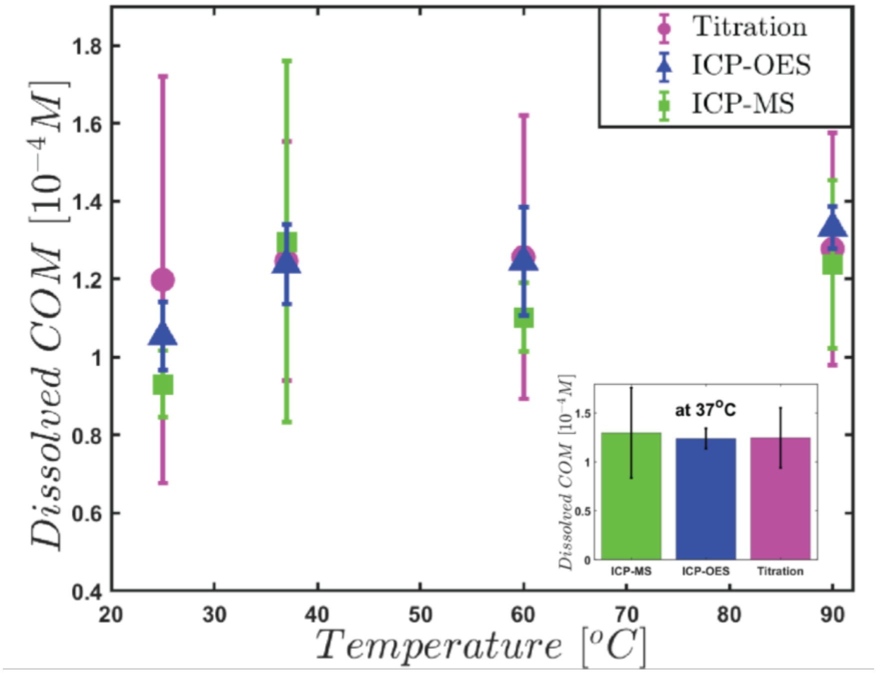

Figure 2.2. Measured dissolved COM in ultrapure water as a function of temperature for the three analysis methods. Average values and their standard deviations are given for titration; magenta circles, ICP-OES; blue triangles and ICP-MS; green squares. The error bars denote the standard deviation of independent repetitions. The inset shows the solubilities measured at body temperature.

The characteristic COM Raman bands were observed in Figure 2.3.a at 504, 508 (O-C-O), 897 (C-C), 1463, 1490 (C-O), and 1629 (C-O) cm^{-1}.[55-57] These shared peaks evident in four different temperatures and "The suspension of COM in water" spectra imply that the pseudo-polymorphic/hydrate form of excess COM crystals did not change throughout dissolution experiments, even at highest temperature 90 °C. In addition to in-situ Raman measurements, we performed ex-situ PXRD measurements where the excess crystals are filtered, washed and dried for diffraction measurements. Figure 2.3.b provides PXRD spectra of excess crystals after dissolution experiments at four different temperatures along with reference spectra of three calcium oxalate phases from CCDC data base, namely calcium oxalate monohydrate (COM), calcium oxalate dihydrate (COD) or calcium oxalate trihydrate (COT).[58] The PXRD peaks of COM reference match with the spectra from different temperatures as well as the PXRD spectra of COM crystals as purchased from supplier referred as "Powder". In line with Raman results in Figure 2.3.a, this result points out that the polymorphic form of COM did not change throughout the dissolution measurements. Moreover, we checked rather the drying procedure required to conduct PXRD measurements induced phase transformations.

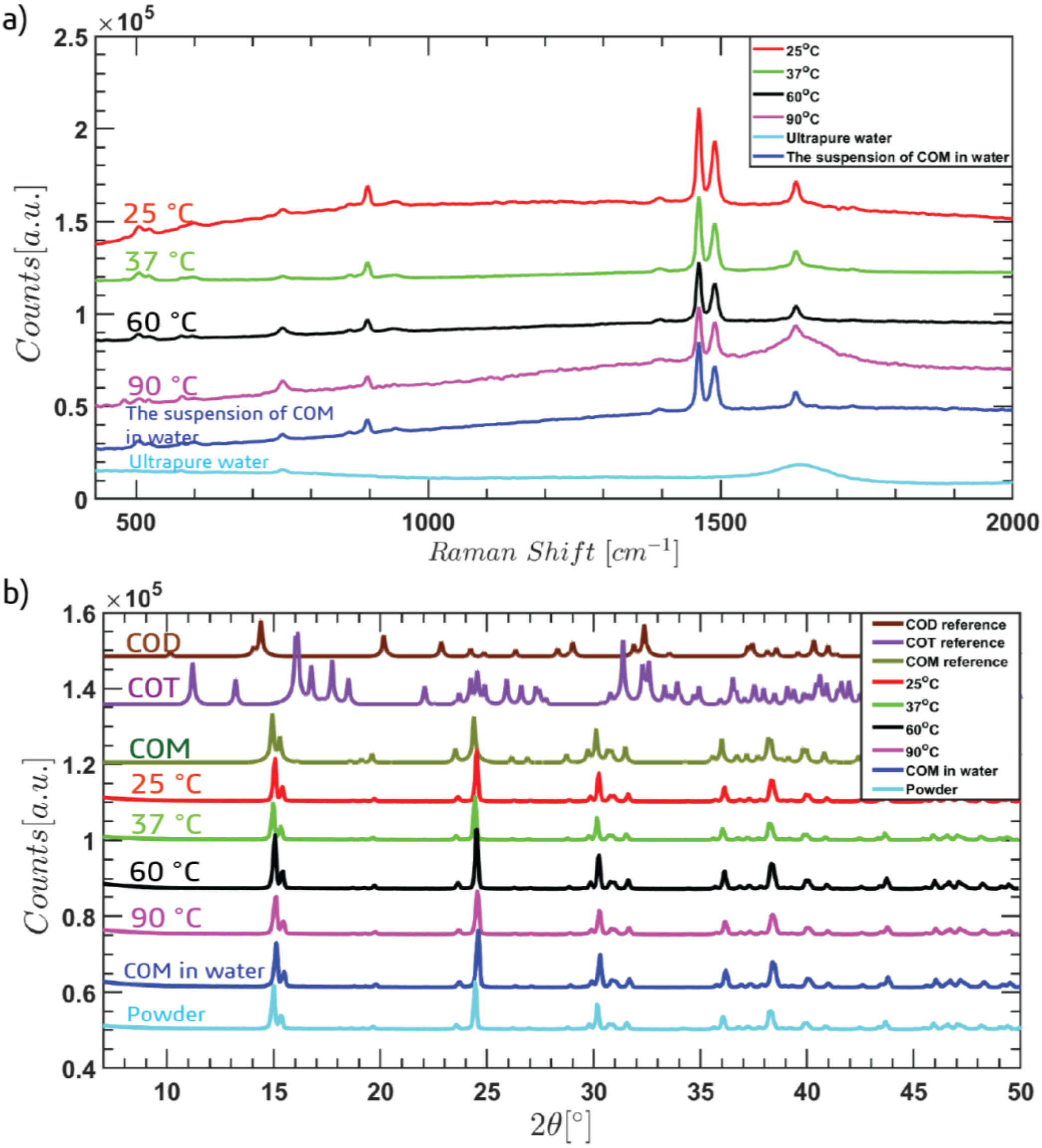

Figure 2.3. Characterization of suspended crystals in ultrapure water at different temperatures for ICP-OES experiments. a) The results of six Raman measurements, 25ºC; red, 37ºC; green, 60ºC; black; 90ºC; magenta; The suspension of COM in water prior to experiment; blue, ultrapure water; cyan. b) The results of nine XRD measurements. 25 ºC; red, 37 ºC; green, 60 ºC; black; 90 ºC; magenta, COM suspension filtered and dried at room temperature denoted as "COM in water"; blue, Powder (COM powder from supplier); cyan, COM reference; dark green, COD reference; brown and COT reference; purple.

To this end, COM crystals were suspended in ultrapure water, filtered and dried without being exposed to isothermal dissolution experiments. The spectra belonging to these crystals exposed only to drying process, denoted as “COM in Water”, share the identical peaks as the powder and COM reference. We can also conclude that drying process did not induce pseudo-polymorphic /hydrate.

In addition to polymorphic form characterization in dissolution in ultrapure water, we also characterized the excess COM crystals from dissolution experiments at experimental pH values with Raman and PXRD (see Appendix A). The PXRD and Raman spectra of excess crystals prior and after pH dependent solubility measurements were identical to COM patterns given in Figure 2.3.[59] For brevity, we provide these spectra in the supplementary information. We can conclude from our characterization, provided in Figure 2.3 and in supplementary information, that isothermal dissolution experiments performed did not induce a detectable transition from COM to other CaOx hydrate forms. Naturally, we can only conclude that phase transition did not happen during our measurements within the accuracy of Raman and PXRD techniques. These techniques cannot detect pseudo-polymorphic/hydrate below 5-10% by weight[60] hence we cannot entirely exclude possibility of phase transitions. We also explored techniques that offer single crystal level insights to potential transitions such as scanning electron microscopy, polarized light and bright field microscopy (Appendix A). Yet it was difficult to visually identify CaOx hydrate morphologies from micrographs as most crystals were found as aggregates. We speculate this aggregation originates from capillary forces emerging in drying process.[61] In the light of these results, we only confirm no phase transitions occurred during solubility measurements within the accuracy of experimental techniques utilized in this study.

In Figure 2.4, the measured solubility of COM with ICP-OES at the four temperatures is given together with the simulated solubility values based on the literature values of the K values given in Table 2.3. The total calculated calcium ion concentration in the saturated solution using literature K_{sp} values from Streit et al.[22] are also shown (black stars) in Figure 2.4. It can be concluded that the use of these K_{sp} values results in a much lower solubility of COM compared to our measured values shown in Figure 2.4. This is hardly surprising given the significant variations of the solubility data in literature from which these K_{sp} values are estimated (Table 2.3). To remove this discrepancy, we estimated new K_{sp} values for COM based on our measurements. We used the Van 't Hoff equation given in Equation 2.5 to describe the temperature dependency of the K_{sp}.

Note that we cannot fit Equation 2.5 directly to the data of Figure 2.4, as we measure the total dissolved Ca ion concentration and the K_{sp} is expressed in terms of the activities of the free Ca^{2+} and $C_2O_4^{2-}$ ions. Therefore, we applied a parameter estimation procedure using the proposed model instead. To estimate the parameters in Van't Hoff equation, $K_{sp,0}$ and ΔH_R where $K_{sp,0}$ is the solubility product of COM at standard conditions, simulations with the developed model were performed at the experimental temperatures. Then the sum of the errors between the experimental and simulated total Ca^{2+} concentrations were calculated for a given parameter set. Finally, this error was minimized by variation of the two parameters numerically with a custom written code in MATLAB.

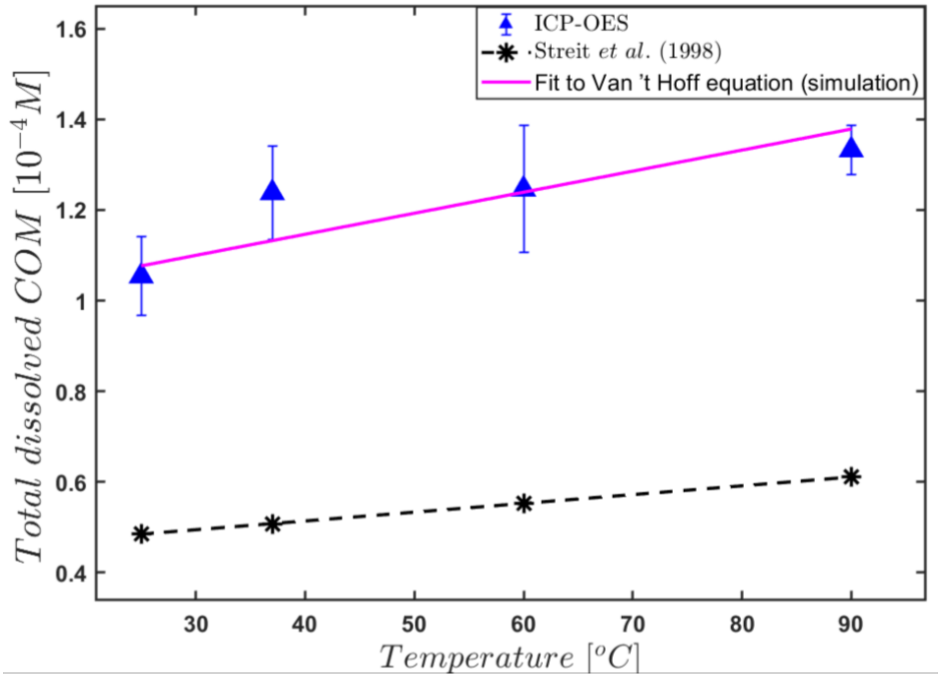

Figure 2.4. Total dissolved COM in ultrapure water measured by ICP-OES as a function of temperature (blue triangles). Simulated values using the K_{sp} values of Streit et al.[22] (black stars) and the fit of the ICP-OES results with the simulated total soluble Ca concentration after estimation of $K_{sp,0}$ and ΔH_R using the Van 't Hoff equation (solid magenta line).

Figure 2.4 shows the results of the parameter estimation comparing the experimental solubilities and the simulated values as a function of the temperature (magenta solid line). Only the K_{sp} values were fitted, while the temperature dependence of the other K values for the protonation and dissociation constants were taken from the literature sources.[34, 48, 50] The results show an adequate fit of the experimental data using the parameters of $6.7 \cdot 10^{-9}$ [mol^2/L^2] and 5.5 [kJ mol^{-1}] for the $K_{sp,0}$ and ΔH_R respectively (see Table 2.3).

The estimated K_{sp} values are somewhat higher than the ones reported in literature. Most literature values at 25 °C are at least a factor of two lower than our estimated K_{sp} value of $6.7 \cdot 10^{-9}$ [mol^2/L^2]. The reported values are in the range from $1.77 \cdot 10^{-9}$ to $2.85 \cdot 10^{-9}$ [mol^2/L^2].[22, 34, 62] This deviation stresses the need for a systematic comparison of the different methods to determine the solubility of such electrolyte crystallization systems with extreme low solubilities. We can only speculate that this variation might be due to experimental difficulties in measuring solubility of sparsely soluble salts such as COM or the presence of different pseudo-polymorphic/hydrate which we, to our best ability, monitor before and after dissolution experiments.

The total dissolved Ca^{2+} ion concentrations, measured using the ICP-OES method as a function of the pH at body temperature 37 °C in the presence two different buffer solutions are given in Figure 2.5. The experiments in the low pH range up to a pH of 7.55 were measured in the citric acid-disodium phosphate buffer (blue triangles), while the last two data points at the higher pH values, were measured in the glycine-sodium hydroxide buffer (blue circles).

The results show a large change in the total dissolved Ca^{2+} ion concentration as a function of the pH and a strong increase in the solubility compared to that in water, especially in the citric acid- disodium phosphate buffer.

The solution pH is observed to strongly influence the solubility of COM. A peak value of $(8.847 \pm 0.112) \cdot 10^{-4}$mol/L is found at a pH of 6.0 in a citric acid-disodium phosphate buffer. which is a factor of 8 higher than the one in ultrapure water at pH 7. In the glycine-sodium hydroxide buffer at pH 9.0 and 10.6, the solubility is much lower (between $1.43 \cdot 10^{-4}$ M and $2.11 \cdot 10^{-4}$ M at pH values of 9.0 and 10.6 respectively). Both towards lower and higher pH values the solubility drops to lower values. This is in accordance with results from medical studies showing a higher risk of formation of kidney stones pH values between 4.5 and 5.5.[8, 18]

The theoretical model we developed explains this behavior. Our model suggests that the pH and the added buffer solution influence the ionic strength of the solution and consequently the solution chemistry and the speciation of the solution. Due to the increased ionic strength, the activity coefficients especially of the ions with high valence will decrease drastically reducing the activity and thus increasing the actual concentration at equilibrium.

Secondly, ion pair formation of calcium and oxalate ions with ions from the buffer solution can lower the free concentration of these ions in the solution considerably. Both effects will lead to a higher solubility of the COM in buffers compared to water. In the glycine-sodium hydroxide buffer solution at higher pH (at 9.0 and 10.6), the ionic strength is also high but apparently the ionic pair formations of the calcium and oxalate ions are much weaker than citric acid-disodium phosphate buffer.

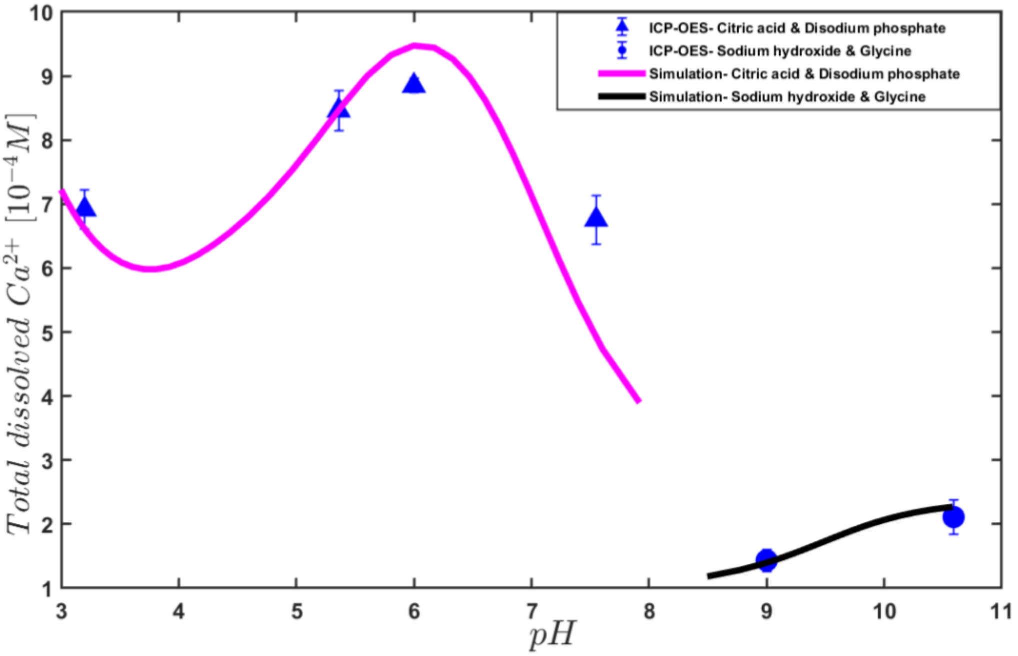

Figure 2.5. Total dissolved COM expressed as the total dissolved Calcium concentration in the solution citric acid-disodium phosphate buffer with a pH of 3.2, 5.36, 6.0, 7.55 (blue triangles) and glycine-sodium hydroxide buffer with a pH of 9.0, 10.6 (blue dots) at 37 °C. In addition, the simulated total dissolved Ca concentration as function of pH in a citric acid-disodium phosphate buffer (magenta line) and in a glycine-sodium hydroxide buffer (black line) is given.

In Figure 2.5, also the pH dependence of the experimental and simulated total Calcium concentrations are given (magenta and black solid lines denote simulations, circles and triangles denote experiments). As outlined before, the adapted values for the K_{sp} determined from the temperature dependent measurements in COM/water system were used in these simulations. The model predicts very well the observed measurements using the adapted K_{sp} value of $7.3 \cdot 10^{-9}$ [mol^2/L^2], at 37 °C. In fact, the simulations results give an excellent match with the experimental results without any fudge factors, with a peak value of the solubility at pH 6 in the citric acid- disodium phosphate buffer. The lower total calcium ion concentrations at pH 3.2 compared to that at pH 7.55 in the citric acid- disodium phosphate buffer is described adequately. The prediction of the lower solubility of COM in the glycine- sodium hydroxide buffer by the model is also remarkable. Such remarkable prediction of the solubility in two different buffers from the solubility measurements of COM in pure water emphasizes the self-consistency of the proposed model and experimental procedure.

To explain the increased solubility of COM in the buffer solutions and its variation as a function of the pH we must have a closer look at the speciation calculated using the developed model. The simulation results given in Figure 2.6 and Figure 2.7 explain the observed trends and shed light to the speciation in the system under study. In Figure 2.6.a, the distribution of the Ca^{2+} species is shown as a function of pH in the citric acid- disodium phosphate buffer while Figure 2.6.b shows the distribution of the $C_2O_4^{2-}$ in the same buffer. From Figure 2.6.a, it can be seen that the fraction of free Ca^{2+} in solution is very small compared to the amount of Ca^{2+} ions bound at the citric acid complexes. Figure 2.6 also shows the strong variation of the relative amount of $CaCit^-$ and CaHCit as a function of pH as a result of the protonation reactions of the citric acid species. Concerning the oxalate species shown in Figure 2.6.b, it is remarkable how high the free concentration becomes at pH values between 5 and 7. This is enabled by the deprotonation of the $HC_2O_4^-$ species and the low free Ca^{2+} concentration and the low activity of the Ca^{2+} and the $C_2O_4^{2-}$ ions in the high ionic strength of the buffer solutions. Comparison of panel a and b in Figure 2.6 also clearly shows that the stoichiometry of the free Ca^{2+} and $C_2O_4^{2-}$ varies strongly in the solution as a function of pH. A completely different ion speciation is observed in Figure 2.7 for calcium (panel a) and oxalate (panel b) ions in glycine-sodium hydroxide buffer at the same temperature. Figure 2.7 shows that in the glycine-sodium hydroxide buffer, a considerable portion of total calcium ions is free Ca^{2+} in solution. The relative amount of free Ca^{2+} decreases with increasing pH significantly by the formation of $CaGly^{+}$ complexes. In the glycine-sodium hydroxide buffer almost all the oxalate consists of free $C_2O_4^{2-}$ ions over the entire pH range as is shown in Figure 2.7.b. Apparently, the speciation of the oxalate is not much affected by complex formation in this solution, the increase in the solubility with respect to that in pure water is caused by the ionic strength of the solution.

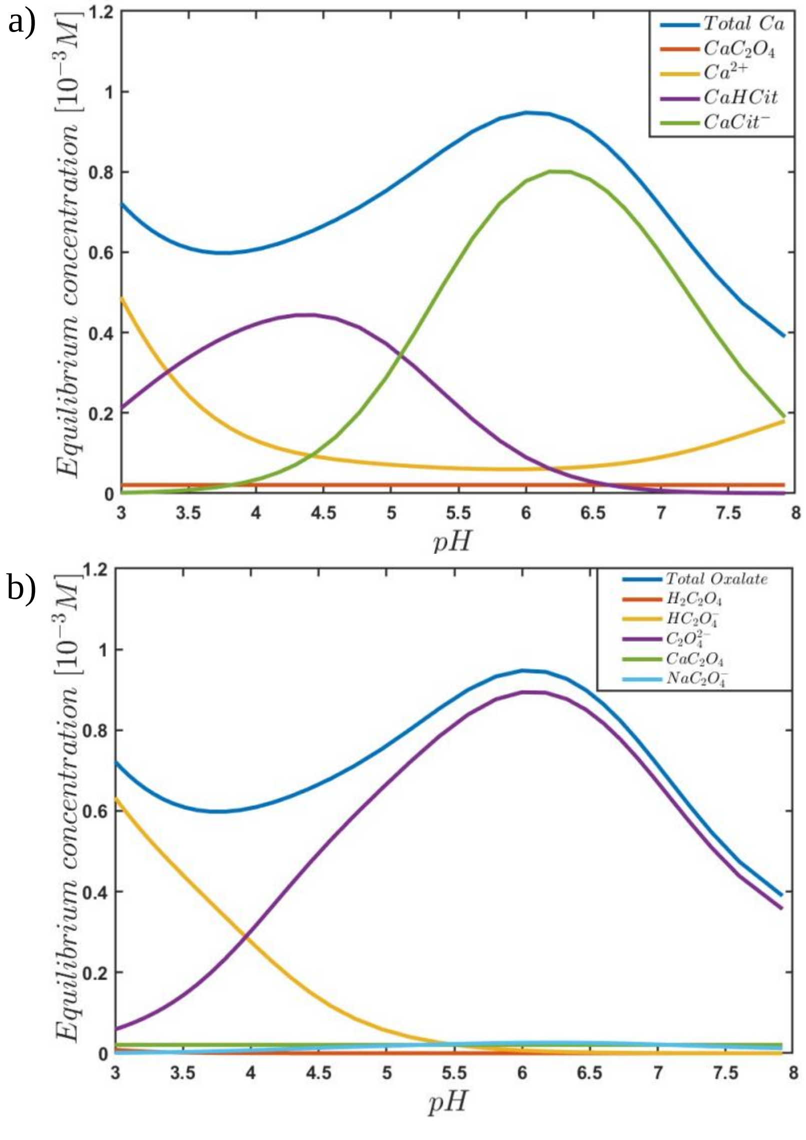

Figure 2.6. Simulated equilibrium concentrations of the Calcium (a) and the Oxalate (b) species at various pH in citric acid-disodium phosphate buffer at 37 °C.

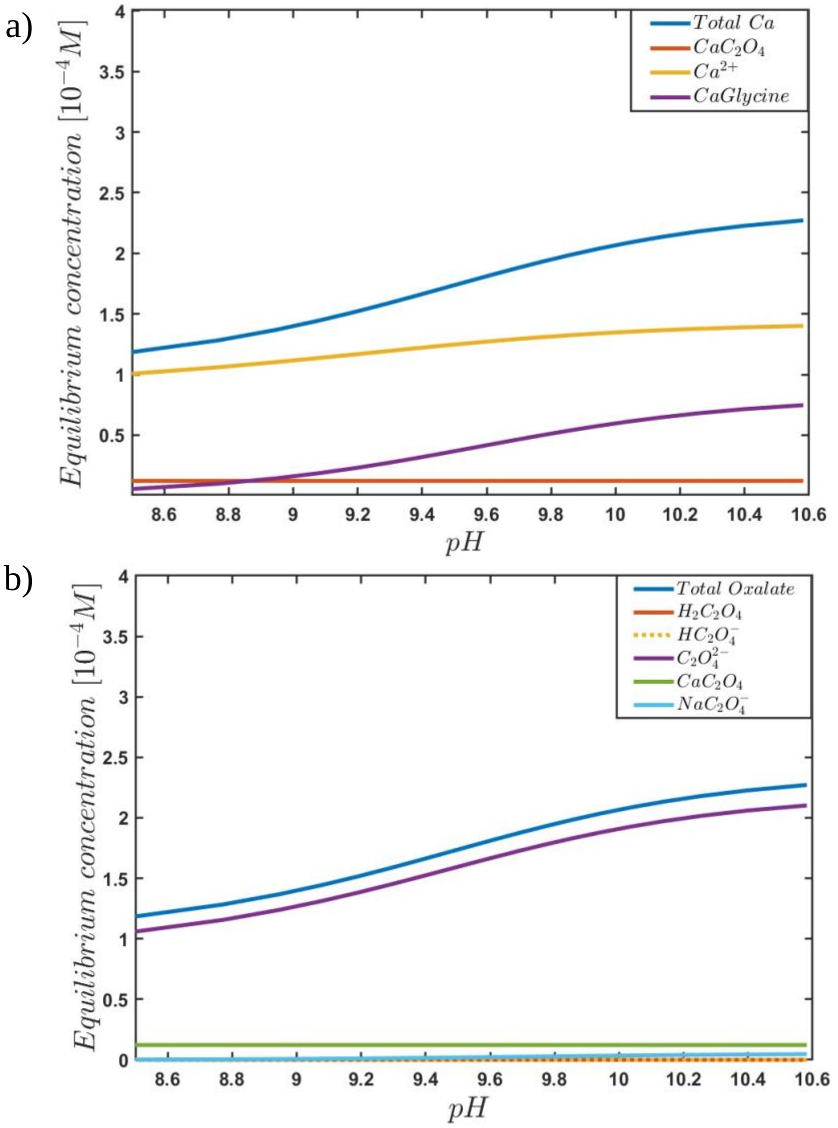

Figure 2.7. Simulated distribution of the Calcium (a) and the Oxalate (b) species at various pH in citric acid-disodium phosphate buffer at 37 °C.

2.4. Conclusion

The reported solubility values of COM in ultrapure water vary significantly depending on the source and technique evoked in literature. To shed light on the origin of this variability and to establish a self-consistent methodology, we present a cross-validated experimental and modelling study of solubility of COM as a function of temperature and pH while carefully monitoring potential phase transitions.

In this study, the measured solubility of COM in ultrapure water at room temperature is higher than majority of literature values[24-26, 28], yet some studies report even higher values than our measurements. We discuss the origin of this variation and speculate that it might arise from experimental challenges, particularly subjectivity in manual methods such as titration, impurity incorporation and potential pseudo-polymorphic/hydrate transitions. Our experimental results indicate that solubility of COM has only modest temperature dependence, in agreement with earlier measurements.[19, 26] We estimated K_{sp} values from measured solubilities as a function of temperature using the Van 't Hoff equation and the proposed model. Parameter estimation of the Van 't Hoff equation is performed minimizing the error between the simulated and the measured solubility of COM in ultrapure water at different temperatures to estimate K_{sp} values. The resulting parameters for Van 't Hoff equation are estimated to be $6.7 \cdot 10^{-9}$ [mol^2/L^2] and 5.5 [J mol^{-1}] for $K_{sp,0}$ and ΔH_R, respectively. Using these parameters, the developed model not only describes the temperature dependent solubilities in ultrapure water, but also permits the prediction of the pH dependent measurements in buffer solutions at body temperature.

The solubility of COM as a function of pH measured at body temperature in two different buffer solutions, showed a strong dependence of the solubility on the pH with an eightfold increased solubility around a pH of 6 in a citric acid-disodium phosphate buffer compared to that of COM in ultrapure water. The proposed model enabled the interpretation of this enhanced solubility of COM in buffer solutions as the combined effect of increased ionic strength, protonation reactions and soluble complex formation. Moreover, the developed model estimates the solubility in the two separate buffer solutions remarkably well using K_{sp} values extracted from the measurements in ultrapure water without any fudge factors, highlighting the self-consistency of our approach. The presented combined experimental and modelling study establishes a firm basis to extend the physiochemical understanding of nephrolithiasis to more complex biological solutions.

2.5. References

1. Alelign, T.; Petros, B., Kidney Stone Disease: An Update on Current Concepts. *Advences in Urology* **2018**, 3068365.

2. Bowers, G. M., Kirkpatrick, R.J., Natural abundance 43Ca NMR as a tool for exploring calcium biomineralization: renal stone formation and growth. *Crystal growth & design* **2011,** *11* (12), 5188-5191.

3. Goldfarb, D. S., A woman with recurrent calcium phosphate kidney stones. *Clinical Journal of the American Society of Nephrology* **2012,** *7* (7), 1172-1178.

4. Zhai, H.; Wang, L.; Putnis, C. V., Inhibition of Spiral Growth and Dissolution at the Brushite (010) Interface by Chondroitin 4-Sulfate. *The Journal of Physical Chemistry B* **2019,** *123* (4), 845-851.

5. Worcester, E. M.; Coe, F. L., Nephrolithiasis. *Primary Care* **2008,** *35* (2), 369-391, vii.

6. Skorecki, K., , Chertow, G.M.; Marsden, P.A.; Taal, M.W.; Alan, S.L.; Luyckx, V., *Brenner and Rector's The Kidney E-Book*. Elsevier Health Sciences: 2015.

7. Romero, V.; Akpinar, H.; Assimos, D. G., Kidney stones: a global picture of prevalence, incidence, and associated risk factors. *Reviews in urology* **2010,** *12* (2-3), e86-96.

8. Ridley, J. W., *Fundamentals of the Study of Urine and Body Fluids*. Springer: 2018.

9. Bird, V. Y., Khan, S.R., How do stones form? Is unification of theories on stone formation possible? *Archivos espanoles de urologia* **2017,** *70* (1), 12.

10. Hall, V. M.; Thornton, A.; Miehls, E. K.; Bertke, J. A.; Swift, J. A., Uric Acid Crystallization Interrupted with Competing Binding Agents. *Crystal growth & design* **2019,** *19* (12), 7363-7371.

11. Khan, S. R.; Pearle, M. S.; Robertson, W. G.; Gambaro, G.; Canales, B. K.; Doizi, S.; Traxer, O.; Tiselius, H. G., Kidney stones. *Nature Reviews Disease Primers* **2016,** *2*, 16008.

12. Miller, G. H.; Vermeullen, C. W.; Moore, J. D., Calcium oxalate solubility in urine; experimental urolithiasis. XIV. *The Journal of Urology* **1958,** *79* (3), 607-612.

13. Izatulina, A. R. G., V.V.; Krzhizhanovskaya, M.G.; Kuz'mina, M.A.; Leoni, M.; Frank-Kamenetskaya, O.V., Hydrated Calcium Oxalates: Crystal Structures, Thermal Stability, and Phase Evolution. *Crystal growth & design* **2018,** *18* (9), 5465-5478.

14. Kelland, M. A.; Mady, M. F.; Lima-Eriksen, R., Kidney Stone Prevention: Dynamic Testing of Edible Calcium Oxalate Scale Inhibitors. *Crystal growth & design* **2018,** *18* (12), 7441-7450.

15. Pahira, J. J., Pevzner, M., Nephrolithiasis. In *Penn Clinical Manual of Urology*, Elsevier: 2007; pp 235-257.

16. Sun, X. Y., Zhang, C.Y., Bhadja, P., Ouyang, J.M., Preparation, properties, formation mechanisms, and cytotoxicity of calcium oxalate monohydrate with various morphologies. *CrystEngComm* **2018,** *20* (1), 75-87.

17. Worcester, E. M.; Coe, F. L., Clinical practice. Calcium kidney stones. *The New England Journal of Medicine* **2010,** *363* (10), 954-63.

18. Childs-Sanford, S. E. The captive maned wolf: nutritional considerations with emphasis on management of cystinuria. University of Maryland, 2005.

19. Bono, M. J., Reygaert, W.C., Urinary tract infection. In *Urinary tract infection*, StatPearls Publishing: 2017.

20. Singh, R. P., On the existence of NaC2O4− ion pair complex. *Bulletin of the Chemical Society of Japan* **1989,** *62* (12), 4089-4091.

21. Pan, H. B.; Darvell, B. W., Calcium phosphate solubility: the need for re-evaluation. *Crystal growth & design* **2009,** *9* (2), 639-645.

22. Streit, J., Tran-Ho, L., Königsberger, E., Solubility of the three calcium oxalate hydrates in sodium chloride solutionsand urine-like liquors. *Monatshefte für Chemie/Chemical Monthly* **1998,** *129* (12), 1225-1236.

23. Molzon, J. A. The solubility of calcium oxalate as a function of dielectric constant. 1976.

24. McComas, W. H.; Rieman, W., The Solubility of Calcium Oxalate Monohydrate in Pure Water and Various Neutral Salt Solutions at 25°. *Journal of the American Chemical Society* **1942,** *64* (12), 2946-2947.

25. Shehyn, H., Pall, D.B., The Solubility of Calcium Oxalate in Various Salt Solutions. *The Journal of Physical Chemistry* **1940,** *44* (2), 166-171.

26. Gutzow, I.; Atanassova, S.; Budevsky, G.; Neykov, K., Solubility, inhibited growth and dissolution kinetics of calcium oxalate crystals in solutions, containing hippuric acid. *Urological research* **1993,** *21* (3), 181-185.

27. Herz, W., .; Muhs, G., Ueber die Lösliohkeit einiger Salze der Ekdalkalimetalle mit organisohen Sauren in Essigsiiure *Bcr., 36, 3717* **1903**.

28. Hammarsten, G., On calcium oxalate and its solubility in the presence of inorganic salts with special reference to the occurrence of oxaluria. *C.R. Trav. Lab. Carlsberg* **1929,** *17,1*.

29. Gardner, G. L., Nancollas, G. H., Kinetics of dissolution of calcium oxalate monohydrate. *The Journal of Physical Chemistry* **1975,** *79* (24), 2597-2600.

30. Robertson, W. G., Diet and calcium stones. *Mineral and electrolyte metabolism* **1987,** *13* (4), 228-34.

31. Finlayson, B.; Roth, R., Appraisal of calcium oxalate solubility in sodium chloride and sodium-calcium chloride solutions. *Urology* **1973,** *1* (2), 142-144.

32. Gardner, G. L., Nancollas, G. H., Crystal growth in aqueous solution at elevated temperatures. Barium sulfate growth kinetics. *The Journal of Physical Chemistry* **1983,** *87* (23), 4699-4703.

33. Garside, J.; Brečević, L.; Mullin, J. W., The effect of temperature on the precipitation of calcium oxalate. *Journal of Crystal Growth* **1982,** *57* (2), 233-240.

34. Garside, J. B., Lj.; Mullin, J.W., The effect of temperature on the precipitation of calcium oxalate. *Journal of Crystal Growth* **1982,** *57* (2), 233-240.

35. Baumann, J. M., Ackermann, D., Affolter, B., The influence of hydroxyapatite and pyrophosphate on the formation product of calcium oxalate at different pHs. *Urological research* **1989,** *17* (3), 153-155.

36. Tiselius, H. G., The effect of pH on the urinary inhibition of calcium oxalate crystal growth. *British Journal of Urology* **1981,** *53* (5), 470-4.

37. Hojgaard, I.; Fornander, A. M.; Nilsson, M. A.; Tiselius, H. G., The effect of pH changes on the crystallization of calcium salts in solutions with an ion composition corresponding to that in the distal tubule. *Urological research* **1999,** *27* (6), 409-416.

38. University, R. Elemantal analysis. https://www.ru.nl/science/gi/facilities-activities/elemental-analysis/ (accessed 2019).

39. University, R. Elemental analysis_ICP-OES. https://www.ru.nl/science/gi/facilities-activities/ (accessed 2019).

40. Elkadi, M.; Pillay, A.; Fok, S. C.; Feghali, F.; Bassioni, G.; Stephen, S., Depth profiling (ICP-MS) study of toxic metal buildup in concrete matrices: Potential environmental impact. *Sustainability* **2010,** *2* (10), 3258-3269.

41. Sigma Buffer Reference Center- Biological-buffers. https://www.sigmaaldrich.com/life-science/core-bioreagents/ (accessed May 2019).

42. Ruzin, S. E. Buffers. https://microscopy.berkeley.edu/Resources/instruction/buffers.html (accessed February 2019).

43. Vallapragada, V. V., Inti, G., Ramulu, J.S., A Validated inductively coupled plasma-optical emission spectrometry (ICP-OES) method to estimate free calcium and phosphorus in in vitro phosphate binding study of eliphos tablets. *American Journal of Analytical Chemistry* **2011,** *2* (06), 718.

44. Green, D. R. H.; Cooper, M. J.; German, C. R.; Wilson, P. A., Optimization of an inductively coupled plasma–optical emission spectrometry method for the rapid determination of high-precision Mg/Ca and Sr/Ca in foraminiferal calcite. *Geochemistry, Geophysics, Geosystems* **2003,** *4* (6).

45. de Souza, R. M., Leocádio, Luiz Gustavo, da Silveira, Carmem Lúcia P., ICP OES simultaneous determination of Ca, Cu, Fe, Mg, Mn, Na, and P in biodiesel by axial and radial inductively coupled plasma-optical emission spectrometry. *Analytical Letters* **2008,** *41* (9), 1615-1622.

46. Sigma Biological buffer - Citric. https://www.sigmaaldrich.com/life-science/core-bioreagents/biological-buffers/learning-center/buffer-reference-center.html#citric2 (accessed 2019).

47. Nancollas, G. H., Gardner, G.L., Kinetics of crystal growth of calcium oxalate monohydrate. *Journal of Crystal Growth* **1974,** *21* (2), 267-276.

48. Singh, R. P., Yeboah, Y.D., Pambid, E.R., Debayle, P., Stability constant of the calcium-citrate (3-) ion pair complex. *Journal of chemical and engineering data* **1991,** *36* (1), 52-54.

49. May, P., The use of glass electrodes for the determination of formation constants—II: Simulation of titration data. *Talanta* **1985,** *32* (6), 483-489.

50. Davies, C. W., Hoyle, B.E., 842. The interaction of calcium ions with some phosphate and citrate buffers. *Journal of the Chemical Society (Resumed)* **1953**, 4134-4136.

51. Robertson, W. G., Measurement of ionized calcium in biological fluids. *Clinica Chimica Acta* **1969,** *24* (1), 149-57.

52. Vazquez Marrero, V. R.; Berrios, C. P.; Dios Rodriguez, L.; Stelzer, T.; Lopez-Mejias, V., In the Context of Polymorphism: Accurate Measurement, and Validation of Solubility Data. *Crystal growth & design* **2019,** *19* (7), 4101-4108.

53. Richards, T. W. M., C.T.; Bisbee, H., *Zeitschrift für anorganische und allgemeine Chemie* **1901,** *28*.

54. Hall, W. T., The oxalate method for separating calcium and magnesium. *Journal of the American Chemical Society* **1928,** *50* (10), 2704-2707.

55. Kodati, V. R.; Tomasi, G. E.; Turumin, J. L.; Tu, A. T., Raman spectroscopic identification of calcium-oxalate-type kidney stone. *Applied spectroscopy* **1990,** *44* (8), 1408-1411.

56. Frausto-Reyes, C.; Loza-Cornejo, S.; Terrazas, T.; Miranda-Beltran Mde, L.; Aparicio-Fernandez, X.; Lopez-Macias, B. M.; Morales-Martinez, S. E.; Ortiz-Morales, M., Raman spectroscopy study of calcium oxalate extracted from cacti stems. *Applied spectroscopy* **2014,** *68* (11), 1260-1265.

57. Castiglione, V.; Sacre, P. Y.; Cavalier, E.; Hubert, P.; Gadisseur, R.; Ziemons, E., Raman chemical imaging, a new tool in kidney stone structure analysis: Case-study and comparison to Fourier Transform Infrared spectroscopy. *PloS one* **2018,** *13* (8), 1-18.

58. Orlando, M. T. D.; Kuplich, L.; de Souza, D. O.; Belich, H.; Depianti, J. B.; Orlando, C. G. P.; Medeiros, E. F.; da Cruz, P. C. M.; Martinez, L. G.; Corrêa, H. P. S.; Ortiz, R., Study of calcium oxalate monohydrate of kidney stones by X-ray diffraction. *Powder diffraction* **2008,** *23* (S1), S59-S64.

59. Manzoor, M. A. P.; Agrawal, A. K.; Singh, B.; Mujeeburahiman, M.; Rekha, P. D., Morphological characteristics and microstructure of kidney stones using synchrotron radiation μCT reveal the mechanism of crystal growth and aggregation in mixed stones. *PloS one* **2019,** *14* (3), e0214003.

60. Hammond, R. B.; Pencheva, K.; Roberts, K. J., Molecular modeling of crystal− crystal interactions between the α-and β-polymorphic forms of l-glutamic acid using grid-based methods. *Crystal growth & design* **2007,** *7* (5), 875-884.

61. Eral, H. B., O'Mahony, M., Shaw, R.; Trout, B.L., Myerson, A.S., Doyle, P.S., Composite hydrogels laden with crystalline active pharmaceutical ingredients of controlled size and loading. *Chemistry of materials* **2014,** *26* (21), 6213-6220.

62. Blomen, L. J. M. J.; Will, E. J.; Bijvoet, O. L. M.; van der Linden, H., Growth kinetics of calcium oxalate monohydrate: II. The variation of seed concentration. *Journal of Crystal Growth* **1983,** *64* (2), 306-315.

Chapter 3.

Nucleation kinetics of calcium oxalate monohydrate as a function of pH, magnesium and osteopontin concentration quantified with droplet microfluidics

This chapter is based on Fatma Ibis, Tsun Wang Yu, Frederico Marques Penha, Debadrita Ganguly, Manzoor Alhaji Nuhu, Antoine E.D.M. van der Heijden, Herman J. M. Kramer, Huseyin Burak Eral, Biomicrofluidic 2021, DOI: 10.1063/5.0063714

Abstract

A droplet-based microfluidic platform is presented to study the nucleation kinetics of calcium oxalate monohydrate (COM), the most common constituent of kidney stones, while carefully monitoring the pseudo-polymorphic transitions. The precipitation kinetics of COM is studied as a function of supersaturation and pH as well as in the presence of inhibitors of stone formation, magnesium ions (Mg^{2+}) and osteopontin (OPN). We rationalize the trends observed in the measured nucleation rates leveraging a solution chemistry model validated using isothermal solubility measurements. In equimolar calcium and oxalate ion concentrations with different buffer solutions, dramatically slower kinetics is observed at pH 6.0 compared to pH's 3.6 and 8.6. The addition of both Mg^{2+} and OPN to the solution slows down kinetics appreciably. Interestingly, complete nucleation inhibition is observed at significantly lower OPN, namely $3.2 \cdot 10^{-8}$ M, than Mg^{2+} concentrations, $0.875 \cdot 10^{-4}$ M. The observed inhibition effect of OPN emphasizes the often-overlooked role of macromolecules on COM nucleation due to their low concentration presence in urine. Moreover, analysis of growth rates calculated from observed lag-times suggests that inhibition in the presence of Mg^{2+} cannot be explained solely on altered supersaturation. The presented study highlights the potential of microfluidics in overcoming a major challenge in nephrolithiasis research, the overwhelming physiochemical complexity of urine.

3.1. Introduction

Kidney stone (renal lithiasis or nephrolithiasis) is a serious health problem worldwide with increasing incidence.[1, 2] Stone formation is a physiochemical process, where crystallization of inorganic salts in the presence of biological constituents is followed by growth, aggregation and retention within the urinary tract. Although urine consists mainly of water (95%), it also contains organic solutes such as urea, creatinine, uric acid, trace amounts of peptides, enzymes, carbohydrates, hormones, fatty acids and pigments, and inorganic ions such as sodium, potassium chloride, magnesium, calcium, ammonium, sulfates, and phosphates.[3, 4] In other words, kidney stone formation occurs in a complex solution matrix. This matrix-complexity is a major challenge in constructing a physical understanding of kidney stone formation. Remarkably, the relative amounts of these components can be affected by patient-specific conditions such as age, genetic effects, medical history, fluid intake, diet habits, fluctuation in urine pH, or environmental conditions such as temperature and climate.[5-8] The average pH of urine is 6.0, yet it can range between 4 and 8.0; clinical studies have shown that lower pH values cause the highest risk for forming kidney stones.[3, 9] Despite a broad body of literature, a physiochemical mechanism explaining the causal relationship between kidney stone formation and patient-specific urine composition is not yet established. The overwhelming complexity of the urine matrix is a major roadblock in developing preventive treatments informed by a mechanistic understanding, particularly in the pesky case of re-emerging stones.

The analyses of kidney stones from patients reveal that they contain inorganic crystals merged with organic constituents such as proteins and dead cells.[10, 11] There are three main types of crystals in kidney stones: calcium oxalate (CaOx), calcium phosphate, and uric acid. Almost 80% of stones consist predominantly of hydrate crystals of calcium oxalate.[10-15] Calcium oxalate crystals can be present as dihydrate (weddellite) or calcium oxalate monohydrate (COM, whewellite), which is the most common and the most stable form at body temperature (37 °C).[3, 5, 16, 17] People who exhibit a high risk for kidney stones formation tend to excrete urine with higher supersaturation with respect to COM compared to non-stone formers. This condition is referred to as hypercalciuria, high calcium levels in the urine, and the amount of calcium can reach values greater than 300 mg/24 h for men and 250 mg/24 h for women.[2, 5, 18, 19]

In the human body, there are numerous organic and inorganic compounds that might either facilitate (promoters) or prevent (inhibitors) stone formation. Low urine volume and high calcium, sodium, oxalate and urate concentrations in the urine are known to promote the formation of kidney stones.[20] On the other hand, stone formation is considered to be inhibited by various inorganic substances such as citrate, and magnesium and organic substances such as nephrocalcin, urinary prothrombin fragment-1 and osteopontin (OPN).[21] OPN is a single-chain protein with a molecular weight of approximately 33 kDa, present in urine in amounts higher than 100 nM.[22] Reports in the literature mention that OPN inhibits crystal growth and changes the morphology of CaOx crystals.[22-24] Studies on the effect of magnesium mention that Mg^{2+} ions suppress COM formation by increasing its solubility.[25, 26] Various methods have been used to study nucleation and growth kinetics of COM[25, 27] and the effect of additives on the kinetics.[28, 29]

In studies focusing on nucleation kinetics, effective nucleation rates have been determined from induction time measurements where the emergence of the first crystal is recorded as the induction time at a fixed supersaturation.[30] Since nucleation is a stochastic process, a large number of identical experiments (in the order of hundred) are needed to get a statistically accurate value of the induction time distribution for a particular value of supersaturation ratio.[25, 27] Using the induction time distribution, cumulative induction time probability, p(t) curves can be constructed. Fitting models such as single exponential, Weibull function (discussed in 3.2.2.3) allow the determination of effective nucleation rates. Once effective nucleation rates at different supersaturations are experimentally extracted, analysis and interpretation in terms of the “often criticized” classical nucleation theory (CNT) allows a deeper look into the nucleation mechanics. There is a broader discussion in the literature on the possible nucleation pathways describing the evolution of structure. There are two schools of thought describing the nucleation pathway: classical and non-classical, also referred to as two-step nucleation. CNT describes the formation of an ordered nucleus as the association of monomeric units that overcome a free-energy barrier at a critical nucleus size. On the other hand, the non-classical pathway considers the formation of an intermediate amorphous dense state prior to the formation of an ordered nucleus. A broader review of the evidence for non-classical nucleation can be found in studies by Vekilov with a focus on protein crystallization[31] as well as Gebauer and Cölfen focusing on prenucleation clusters as seen in inorganic systems.[32] For CaOx nucleation, Hajir et al.[33] and others discuss the nucleation pathway and provide evidence for pre-nucleation clusters hence non-classical path.[34] Smeets et al. demonstrated that CNT concepts can be used to describe complex nucleation mechanisms.[35] Most recently, Kashchiev published an extension of the CNT to include two-step nucleation of crystals reconfirming the idea that CNT concepts can be used to study non-classical pathways.[36] In this study, we use CNT without making assumptions on the nucleation pathway to rationalize observed trends.

As shown by Ruiz-Agudo et al.[34] for nucleation of CaOx and by Gebauer et al.[37] and Smeets et al.[35] for $CaCO_3$ precipitation, the activities of both the free and bound anions and cations in the solution are essential in the investigation of nucleation kinetics. However, in electrolyte solutions such as the solutions used in this study and the urine solutions in the kidney, the supersaturation of the solution with respect to the aforementioned stone forming crystals is strongly dependent on the properties of the solution[38, 39] such as the presence of background electrolytes, often characterized by the ionic strength[40, 41], and the pH, which influences the composition of the ions in the solution due to protonation and deprotonation reactions.[40, 42] Moreover, the supersaturation can also be strongly affected by the formation of soluble ion pair complexes.[42] Therefore a solution chemistry model must be used to describe the speciation of the electrolyte solutions used for the nucleation experiments.[43] Recently such a model has been described extensively, which gave an excellent prediction of the solubility of calcium ions in different buffered and nonbuffered calcium oxalate solutions.[43] This model considers the (de)-protonation reactions and the ion pair formation, often referred to as complexation reactions, in solution and the solid formation of the different species in the electrolyte solution. The model is based on the Davies equation of the Debye-Hückel theory to describe the activities of the species in the solution. In this way, the effects of the various process conditions on both the supersaturation and the nucleation kinetics can be separated.[38, 43, 44]

To generate a statistically significant number of data points via batch lab-scale approaches is a labor and time-intensive process.[45, 46] To this end, microfluidic approaches have been proposed and successfully implemented.[47-53] With microfluidic techniques, one can work with minute amounts of solutions at microliter scale while conducting a significant number of identical experiments.[49, 54-56] Particularly, the use of uniformly sized micro-droplets as isolated crystallization micro-reactors has been investigated in multiphase droplet microfluidics.[57-59] In a droplet microfluidic system, a dispersed phase flow is emulsified in continuous phase in the presence of surfactants.[49, 52] Despite the recent surge in applications of lab-on-a chip technology in studies focusing on CaOx stone formation, a droplet based microfluidic platform enabling nucleation/precipitation kinetics studies of CaOx compounds with focus on nephrolithiasis[5] has not been reported, to the best of our knowledge.

In this work, we describe a droplet based microfluidic platform designed and optimized for measuring the nucleation/precipitation kinetics of the calcium oxalate monohydrate. To this end, the following functions are realized in the 3D printed microfluidic platform: (i) bringing together two aqueous flows carrying prescribed concentrations of calcium chloride ($CaCl_2$) and sodium oxalate (NaOx) along with other additives for the induction time experiments, (ii) creation of uniform size water droplets carrying calcium and oxalate ions dispersed in a carrier oil phase, (iii) rigorously mixing droplet contents to ensure constant supersaturation immediately after the two streams are brought in contact and (iv) trapping and stabilization of droplets within observation contraptions allowing monitoring throughout induction time measurements (up to 12 h). The advantage of the proposed microfluidic system is that the operations of bringing two reactive solutions and mixing them are rapidly conducted to avoid any biasing coming from manual handling of fluids. Using this microfluidic platform, we study COM nucleation kinetics at varying calcium and oxalate ion concentrations in ultrapure water and in buffer solutions dictating the solution pH. Moreover, we quantify the effect of magnesium (Mg^{2+}) and osteopontin (OPN) on the nucleation kinetics of COM. The pseudo-polymorphic form of CaOx is monitored during induction time measurements with *in situ* and *ex situ* techniques. We interpret the measured nucleation rates in the context of classical nucleation theory (CNT) without making assumptions whether the nucleation pathway is non-classical or classical.[60] To this end, we leverage a solution chemistry model describing the solution chemistry and the complex formation, based on the Davies extension of the Debye–Hückel theory where the details of the model can be found in the study by Ibis et al.[43] The previously developed solution chemistry model is validated by comparing the measured and modeled solubility of COM for all of the samples used in the nucleation induction experiments. We observe that the presence of OPN and Mg^{2+} ions inhibit apparent nucleation. The observed inhibition effect of OPN at significantly lower concentrations than Mg^{2+} ions emphasizes the often-overlooked role of macromolecules on COM nucleation due to their low concentration presence in urine.[61] Moreover, analysis of growth rates calculated from observed lag-times in induction time measurements suggests that the presence of Mg^{2+} ions alter the growth process and their effect cannot be explained solely on supersaturation.

3.2. Materials and Methods

The overarching design objective is to create a statistically significant number (order hundred to thousand) of well-mixed micro batch reactors with controlled supersaturation to acquire statistically significant nucleation induction time measurements. To this end, we describe the developed microfluidic platform designed for the following purposes: (a) to generate stable, well-mixed droplets from two reacting streams dispersed in an inert oil medium and (b) to minimize the droplet coalescence during the observation phase.

3.2.1. Microfluidic design

The microfluidic device can be divided into three different zones; droplet formation, mixing and storage, Figure 3.1.b. Aqueous droplets are formed in this K junction zone in the presence of a surfactant in the droplet formation zone. The mixing zone, ensures complete mixing with serpentine-shaped bends that act as passive mixers.[62] These bends ensure complete internal mixing of the droplets before they reach the storage section (Figure 3.1.b). The storage zone is the last section where the droplets are trapped for observation throughout an induction time experiment (up to 6 h).

3.2.1.1. Droplet formation and mixing

Three inlets two for the aqueous solutions, one for the continuous phase (oil phase) are brought together in a K shaped junction shown in Figure 3.1.b for droplet generation. To ensure the mixing of two aqueous streams carrying calcium and oxalate ions, serpentine-shaped passive mixers are utilized after the K-junction.[63] As the droplets move through serpentine-shaped passive mixers, an asymmetric drag force acts on droplets and creates asymmetric flow patterns, consequently mixing the droplet contents in each bend.[64] Previously developed experimental correlations based on droplet mixing experiment channels of various geometries predict that a droplet subject to the flow rate and channel geometry used in this study is completely mixed after five bends.[64] In the design of the proposed microfluidic platform, we included 13 bends ensuring complete mixing of the contents of the droplet. Hence, we ensure that the contents of the droplets have been mixed rigorously when they enter the storage section shown in Figure 3.1.b. Complete mixing is an important design requirement for the microfluidic platform as the interpretation of nucleation rates requires constant supersaturation assumption, i.e., ion concentrations inside droplets need to be uniform. Tightly regulated air pressure is utilized to avoid pressure fluctuations commonly observed in syringe pumps (pressure pump, Fluigent, MFCS–EZ). A mixture of hydrofluoroether oil (HFE3-Ethoxy-1,1,1,2,3,4,4,5,5,6,6,6-dodecafluoro-2-trifluoromethylhexane, 3M, CAS297730-93-9) and fluorinated surfactant (Sphere Fluidics, CAS240119-1) is used as continuous phase. The surfactant is added to prevent the Polydimethylsiloxane (PDMS, $(C_2H_6OSi)_n$, The DOW Chemical Company) matrix from absorbing the oil and to help droplet formation/stabilization. The continuous phase contains 0.5% V/V surfactant in hydrofluoroether. The effect of the surfactant on COM nucleation was not investigated, as producing stable droplets without surfactant was not possible.

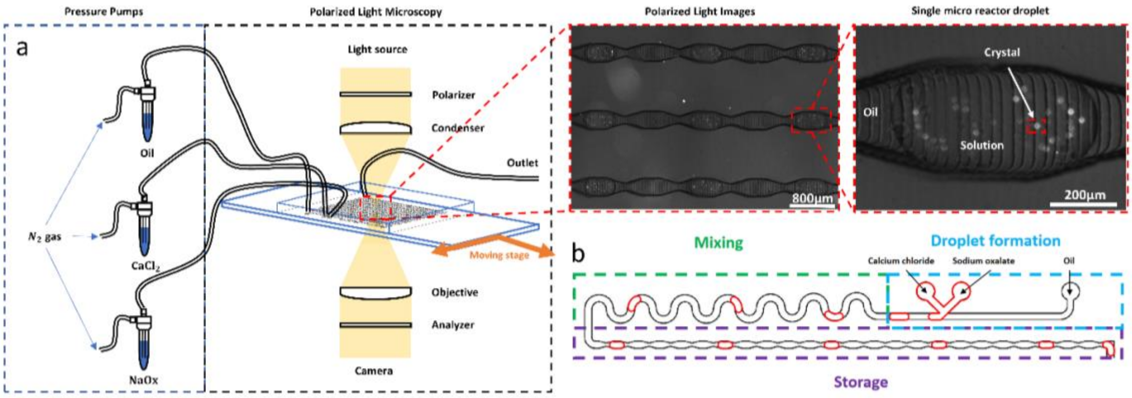

Figure 3.1.Experimental setup and microfluidic platform: (a) Schematic of the experimental set up with insets showing polarized light microscopy images of droplets during induction time measurements. (b) Illustration of the droplet formation, the mixing and the storage zones in the microfluidic platform.

3.2.1.2. Storage

Once the droplets are produced, they are stored in hydrodynamic traps whose sizes are 200 µm depth, 400 µm width and 1200 µm length, as shown in Figure 3.1.a. The hydrodynamic traps ensure that droplets stay in the designated positions throughout the induction time measurements. The elevated hydrodynamic resistance due to the narrow necks (180 µm) at the entrance and exit of hydrodynamic traps ensures that the droplets do not drift or coalesce due to the evaporation of continuous and dispersed phases through the PDMS or through the inlet/exit ports. Such drift and coalescence are undesired as these effects promote coalescence decreasing the number of droplets contributing to nucleation induction time measurements and alters supersaturation. Ensuring that the droplets do not drift and merge is essential to acquire statistically sound measurements.

3.2.1.3. Microfluidic mold preparation

The microfluidic chip is designed in SolidWorks and 3D printed (EnvisionTEC Micro Plus Hi-Res - 43x27mm). The printer has a resolution of 30 µm for the x and y direction and a resolution of 25 µm for the z-direction.[49, 50] A UV curing chamber (Photopol light-curing furnace, Dentalfarm) is used to make a fully cured mold. To peal chips off easily from the mold, the printed mold is hydrophobized with Trichloro (1H,1H,2H,2Hperfluorooctyl) silane (Sigma-Aldrich, CAS 78560-45-9). Further details on the chip can be found in the Appendix B.

3.2.1.4. Chip fabrication

To fabricate a chip, PDMS and curing agent at a 7:1 (w/w) ratio are prepared. The mixture is stirred until it appears to be cloudy. Upon mixing, the mixture is centrifuged (Universal 320 R, Hettich Zentrifugen) at 7400 rpm and 20ºC for 15 min to remove bubbles. The resulting transparent PDMS mixture is poured on the 3D printed mold and the mold is placed inside a desiccator. A vacuum pump is connected to the desiccator to remove the air bubbles introduced during the pouring process. Then, the mold is placed in the oven at 65ºC overnight to ensure complete curing of the PDMS. Once the chip is completely cured, holes are punched at the inlets. Subsequently, PDMS and curing agent at a 10:1 (w/w) ratio are prepared to coat the microscope slide (Thickness 1mm) with PDMS. 0.5 ml of this new PDMS solution is spincoated at 4500 rpm and semi-cured for 1 min. The pealed and cured PDMS (with 7:1 ratio) channel top is placed on the microscope slide with semi-cured PDMS layer (10:1) for 20 min at 65 °C. Once they stick with each other, the device is kept in the oven overnight at 65 °C to complete curing. The experiments are performed in a thermostated room at 20 °C.

3.2.1.5. Monitoring crystal induction with polarized light microscopy

To enhance the contrast between the crystals and the surroundings, polarized light microscopy is used with two polarizing filters, as shown in Figure 3.1.a Polarized microscopy ensures that a dark background is created while the crystals shine bright and can be easily detected. Moreover, polarized microscopy enables the identification of the pseudo-polymorphic form of the crystals.

3.2.2. Microfluidic induction time measurements

3.2.2.1. Solution preparation for microfluidic experiments

$CaCl_2$ and NaOx are dissolved separately into two beakers containing 50 ml ultrapure water or buffer. The solutions are connected to separate microfluidic device inlets. Once two droplets merge, the concentration of $CaCl_2$ and NaOx solutions fed to inlets are diluted by a factor of two and final ion concentrations inside droplets are determined. The final concentrations of $CaCl_2$ and NaOx in droplets for different supersaturated solutions are given in Table 3.2. The equimolar concentrations, namely $4.1\cdot10^{-4}$ M of $CaCl_2$ and $4.1\cdot10^{-4}$ M of NaOx are used as a final concentration in the droplets for three different buffer solutions (see Table 3.3).

For the inhibitor experiments, the droplets contain the equimolar concentrations, namely, $4.1\cdot10^{-4}$ *M* $CaCl_2$ *and* $4.1\cdot10^{-4}$ *M NaOx with varying amounts of* $MgCl_2$ *(*

Table 3.4) and osteopontin (Osteopontin human recombinant, Sigma-Aldrich, expressed in HEK 293 cells, ≥97%). In microfluidic induction time experiments, $MgCl_2$ is dissolved in an aqueous stream containing $CaCl_2$ and organic inhibitor; osteopontin is dissolved in an aqueous stream containing NaOx. The osteopontin stock solution (8 μg/ml) is prepared. Other OPN concentrations, $1.6\cdot10^{-8}$, $3.2\cdot10^{-8}$ and $4.8\cdot10^{-8}$ M are obtained by dilution. The solutions for microfluidic induction time experiments are prepared fresh for every experiment to avoid contamination.

3.2.2.2. Procedure for induction time measurements

Once the droplets are produced, mixed and stored, they are imaged with polarized light microscopy automatically with Nikon Eclipse Ti Series Inverted Microscope. The automated microscope stage, shown in Figure 3.1.a, takes a micrograph of droplets within a given field of view and moves to an adjacent field of view till the whole chip is imaged. Once the whole chip is imaged, the individual micrographs are stitched together and stored constructing a time stamp image for induction time measurements. One such image is shown in Figure 3.2.a. The imaging process including the acquisition and stitching takes 2 min. Once the first image is acquired, the imaging process for the second one immediately begins. A time-lapse movie is recorded and the time frame in which the first crystal emerges in each droplet is manually analyzed to construct cumulative induction time probability functions, p(t) shown in Figure 3.4-Figure 3.7. The spatial resolution for detecting a crystal in a droplet is dictated by the optical resolution of the microscope lens and camera used (one pixel is ~1.67 μm). It is noteworthy to mention that a reference image was taken at $t=t_0$ for each droplet in the storage section. To distinguish the crystals from artifacts such as random white pixels or dirt, the analysis was made by comparing every droplet image at t_n with the immediate previous one at t_{n-1} and at t_0, thus detecting white crystals accurately. Owing to the stochastic nature of nucleation events, over 100 droplets are tested simultaneously for one measurement to obtain the cumulative induction time probability function for the nucleation induction time.

3.2.2.3. *Analysis of induction time measurements*

Using a statistically significant collection of induction time experiments, a cumulative induction time probability function, p(t), can be constructed as described in the section above. The experimentally acquired p(t) are fitted by different models to calculate effective nucleation rate, J, using models such as single exponential with delay time in Equation 3.1 or Weibull function shown in Equation 3.2.

$$p(t) = 1 - e^{(-JV(t-t_G))} = 1 - e^{\left(-((t-t_G)/\tau)\right)} \qquad \textit{Equation 3.1}$$

Where V is the volume of the liquid phase, J the nucleation rate, t the time and t_G the time it takes for a formed nucleus to grow to a crystal of a detectable size, which is dependent on the detection system; the parameter τ is defined as 1/JV.

The Weibull function is commonly used to describe the probability distribution to account for measured deviations from the exponential behavior of the p(t) plot,

$$p(t) = 1 - e^{\left(-(t/\tau)^k\right)} \qquad \textit{Equation 3.2}$$

The shape parameter k, is well suited to fit the sometimes-encountered s-shaped p(t) plots and informs us of the functional form of the nucleation rate. When $k = 1$, the Weibull model reduces to an exponential model. For $k < 1$, the nucleation rate is decreasing and for $k > 1$, the nucleation rate is increasing with time. The physical interpretation of increasing or decreasing nucleation rates under conditions with constant concentrations and temperature indicated by the Weibull function is however not straightforward.[30] Once the p(t) functions are fitted with these models, the estimated nucleation rates, J are calculated as shown in Table 3.5. The combined J values along with the corresponding the supersaturation values extracted from solution chemistry modeling facilitates classical nucleation theory (CNT)[30, 65] analysis of nucleation induction time experiments. Using the CNT expression given in Equation 3.3, the nucleation induction time measurements with different solutions can be compared as shown in Figure 3.8. The CNT expression is given as:

$$J(S) = AS\exp\left(-B/(\ln^2 S)\right) \qquad \textit{Equation 3.3}$$

where A and B are called the kinetic and thermodynamic nucleation rate parameter, respectively, and S is the supersaturation ratio.

3.2.3. COM solubility, modeling, pseudo-polymorph characterization, and error propagation

3.2.3.1. Procedure for COM solubility measurements

We quantify COM solubility under the same conditions used in this study for the nucleation induction time experiments. In fact, the isothermal solubility experiments[43] represent the end points in the induction time measurements assuming that equilibrium is reached. To measure the COM solubility in ultrapure water, two aqueous solutions of $4.1\cdot10^{-4}$ M calcium chloride ($CaCl_2$, Sigma-Aldrich, CAS10043-52-4, ≥93.0%) and $4.1\cdot10^{-4}$ M sodium oxalate ($Na_2C_2O_4$, Sigma-Aldrich, CAS62-76-0,≥99.5%) are mixed rigorously and allowed to crystallize. After approximately 24 h, the supernatant is isolated by filtration and analyzed with inductively coupled plasma optical emission spectroscopy (ICP-OES). To check whether 24 h equilibration time is sufficient to reach the thermodynamic equilibrium between the crystals and the dissolved calcium and oxalate ions in the solution, we measured the Ca^{2+} concentration as a function of time. The Ca^{2+} concentration remained stable after a couple of hours later[43]. To quantify the effect of magnesium on COM solubility, five different amounts of magnesium chloride ($MgCI_2$, Sigma-Aldrich, CAS7786-30-3, ≥98.0%) are mixed with equimolar ion concentration $4.1 \cdot 10^{-4}$ M of $CaCl_2$ and NaC_2O_4 in ultrapure water. Finally, isothermal solubility experiments with three different pH buffers are conducted using the equimolar concentration of $CaCl_2$ and NaOx in buffer solutions (See Table 3.1) for the composition of the buffer solutions. The results of the solubility measurements, which represent the equilibrium end point of the experiments described in section 3.2.2.2. are given in Figure 3.2 and will be discussed in section 3.2.3.2.

The procedure for isothermal solubility measurement is as follows: $CaCl_2$ and NaOx are dissolved separately in two beakers containing 50 ml ultrapure water (ELGA PURELAB, resistivity:18.2 MΩ·cm at 23.6 °C). Both solutions are rigorously stirred with the ultrasonicator (Branson 2510, Ultrasonic Cleaner) for 10 min at room temperature to ensure that all compounds dissolve. The solutions are mixed and allowed to crystallize in a 100 ml Easymax reactor (Mettler Toledo, Columbus, OH, USA). For experiments with magnesium, $0.05 \cdot 10^{-4}$, $0.5 \cdot 10^{-4}$, $0.875 \cdot 10^{-4}$, $1.0 \cdot 10^{-4}$, and $1.25 \cdot 10^{-4}$ M of $MgCI_2$ are dissolved in aqueous $CaCl_2$ solution then mixed with NaOx in the Easymax 102 reactor. For pH experiments, $CaCl_2$ and NaOx are dissolved in buffer solutions and then brought together and mixed in Easymax reactor. The stirring rate is set at 400 rpm through 24 h to ensure proper mixing. Then the stirrer of Easymax was stopped, the crystals were allowed to sediment and 1 ml equilibrated solution was taken with a 1 ml pipet. The equilibrated solution was filtered with a syringe and filter (Whatman, 0.22 μm pore diameter). The samples were 10x diluted into 10 ml volumes with ultrapure water or buffer solution (for the pH experiments) and kept at room temperature. 10 ml samples were needed for the analysis with ICP-OES (SPECTRO Analytical Instruments, Kleve, Germany). Each experimental condition was repeated three times. The filtrate solutions were analyzed at three calcium emission lines at 317.9, 393.4 and 396.3 nm. The measurements conducted at all three wavelengths show quantitatively the same results yet the emission line of 317.9 nm gave the smallest standard deviation. This situation was also observed in the literature and attributed to interference from other ions present.[66, 67]

The chemicals used to prepare the buffer solutions and their final concentrations are listed in Table 3.1. For the lower pH of 3.5, glycine ($C_2H_5NO_2$, Sigma-Aldrich, CAS-

1310-73-2, ≥95%) and hydrogen chloride (HCl, Sigma-Aldrich, CAS-7647-01-0, 1 M) were used, for the intermediate pH = 6, sodium acetate (CH_3COONa, Sigma-Aldrich, CAS-127-09-3, ≥99%) and acetic acid (CH_3COOH, Sigma-Aldrich, CAS-64-19-7, 99.8%) were used; and glycine and sodium hydroxide (NaOH, Sigma-Aldrich, CAS-1310-73-2, ≥95%) were used for the higher pH, 8.6.[68, 69]

Table 3.1. List of reagents and their concentrations used in the preparation of buffer solutions for microfluidic induction time and isothermal solubility experiments.

pH values	Chemical Name	Final Concentration [M]
3.6	Glycine	$5.0\cdot10^{-2}$
	Hydrogen Chloride	$5.0\cdot10^{-3}$
6.0	Sodium Acetate	$1.8\cdot10^{-3}$
	Acetic Acid	$1.6\cdot10^{-3}$
8.6	Glycine	$5.0\cdot10^{-2}$
	Sodium Hydroxide	$4.0\cdot10^{-3}$

3.2.3.2. Solution chemistry model

To interpret microfluidic induction time measurements in the context of the classic nucleation theory, we evoke a previously developed solution chemistry model[43] taking into account the effects of the process conditions, ionic strength, and complex formation on the COM solubility. This model also considers the protonation reactions of the oxalate and the ions of the buffer solution as well as the formation of soluble complexes, i.e. stable ion pairs between positive and negative ions in the solution.[42, 70] This model, which is extensively described by Ibis et al.[43], uses the Davies approximation of the Debye–Hückel equation for the estimation of the activities in the solution, providing excellent predictions for the COM solubility measurements at different concentrations of calcium and different pH values.[43] The supersaturation ratio with respect to the COM is calculated according to Equation 3.4,

$$S = \sqrt{\frac{[\mathrm{Ca}^{2+}][\mathrm{C_2O_4^{2-}}]\gamma^2}{K_{SP,COM}}} \qquad \text{Equation 3.4}$$

in which $K_{SP,COM}$ is the solubility product of COM, which was estimated in a previous study to be $6.7 \cdot 10^{-9}$ at 25 °C[43] on the basis of the solubility measurements of COM in pure water. $[Ca^{2+}]$ and $[C_2O_4^{2-}]$ are the free ion concentrations in the solutions at equilibrium in the absence or prior to precipitation of COM. To calculate the S values of the different solutions, the model calculates the free ion concentrations and their activity coefficients (γ) taking into account the protonation, de-protonation and ion pair reactions of all present species, including the buffer species. The added initial concentration of Ca^{2+} and $C_2O_4^{2-}$ are given in Table 3.2- Table 3.4 for different amounts of $CaCl_2$ and NaOx, in different buffer solutions and different amounts of magnesium additives.

To validate the model, the isothermal solubility measurements described in detail in section 3.2.3.1, were compared with the simulated values of the model. The total dissolved calcium concentration at equilibrium is measured with ICP-OES. The total dissolved calcium concentrations from ICP-OES measurements and modeling results are given for varying pH values in Figure 3.2.a and for different magnesium ion concentrations in Figure 3.2.b. The measurements indicate the strong effect of the pH and the used buffer solution on the solubility of COM, represented here as the total dissolved Ca^{2+} ion concentration which is determined by ICP-OES method. The total dissolved $[Ca^{2+}]$ is the highest at pH 6.0 in the sodium acetate buffer and somewhat lower in the glycine buffers at pH values of 8.6 and 3.6, which are however still higher than $1.14 \cdot 10^{-4}$ M found for COM in ultrapure water. It is worth nothing that the ICP-OES results for pH = 3.6 deviate from the simulation. This might be explained by the fact that around this pH, the CaOx solubility curve is steep. During the storage period (max 24 h) of the samples prior to ICP-OES measurement a slight variation in the pH value could occur by CO_2 absorption or evaporation. The results of the model and the experiments closely agree and confirm the much higher solubility of COM at pH 6.0. Further analysis of the model results learns that the high ionic strength of the sodium acetate buffer, resulting in low values of the activity coefficients, and the formation of calcium acetate ion pairs have a strong influence on the increased solubility of COM under these conditions.

The effect of the increasing Mg^{2+} ion concentration on the total dissolved $[Ca^{2+}]$ is only small as shown in Figure 3.2.b and hardly exceeds the standard deviation of the experiments. However, the model calculates values for the total dissolved $[Ca^{2+}]$ very close to the experimental values and also shows a small but distinct increase in the solubility of COM as a function of the Mg^{2+} ion concentration mainly due to the formation of $MgC_2O_4^+$ ion pairs.

As the solution chemistry model gives very good predictions of the solubility for the different conditions, we are confident that the model will provide us with a trustworthy estimation of the supersaturation of the various solutions used for the nucleation induction time experiments in Figure 3.2.a&b. The differences in the total dissolved $[Ca^{2+}]$ values found at different pH values and Mg^{2+} concentrations mean that the equal concentration of calcium and oxalate ions added in the different samples will not lead to equal supersaturation levels and thus to different nucleation rates in the nucleation induction time experiments performed at the different conditions.

Table 3.2. Added equimolar concentrations of $CaCl_2$ and NaOx in ultrapure water. The free $[Ca^{2+}]$ & $[C_2O_4^{2-}]$, the activity coefficients, γ and the S values in the droplets were determined using the solution chemistry model and represent equilibrium values prior possible precipitation of COM. The latter these values are only accurate until the point of nucleation.

Added total $[Ca^{2+}]=[C_2O_4^{2-}]$ $\cdot 10^{-4}$ M	**Free $[Ca^{2+}]$ $\cdot 10^{-4}$ M**	**Free $[C_2O_4^{2-}]$ $\cdot 10^{-4}$ M**	**Activity coefficient (γ)**	**Estimated S (in droplets)**
1.35	1.09	1.09	0.89	1.18
2.05	1.55	1.55	0.87	1.64
2.75	1.97	1.97	0.85	2.05
4.10	2.72	2.71	0.83	2.74
5.50	3.42	3.41	0.81	3.36

Table 3.3. pH values and the added equimolar $CaCl_2$ and NaOx concentrations of the different buffer solutions for the nucleation induction experiments. Buffer solutions used to obtain the different pH values are specified in Table 3.1. The free $[Ca^{2+}]$ and $[C_2O_4^{2-}]$ concentrations, the activity coefficients, γ and the S values in the droplets were found using the solution chemistry model. These values are equilibrium values prior to possible precipitation of COM and are only accurate until the point of the first nucleation.

pH	**Added total $[Ca^{2+}]=[C_2O_4^{2-}]$ $\cdot 10^{-4}$ M**	**Free $[Ca^{2+}]$ $\cdot 10^{-4}$ M**	**Free $[C_2O_4^{2-}]$ $\cdot 10^{-4}$ M**	**Activity coefficient (γ)**	**Estimated S (in droplets)**
3.6	4.1	3.61	0.75	0.81	1.64
6.0	4.1	2.06	3.64	0.32	1.09
8.6	4.1	2.75	2.91	0.73	2.53

Table 3.4. Added $MgCl_2$, $CaCl_2$ and $Na_2C_2O_4$ concentrations in the samples, used to study the effect of Mg^{2+} ions on the nucleation induction time. The free $[Ca^{2+}]$ and $[C_2O_4^{2-}]$ concentrations, the activity coefficients γ and the S values in the droplets were found using the solution chemistry model. These values are equilibrium values prior possible precipitation of COM and are only accurate up to the point of the first nucleation.

Added total $[Ca^{2+}]=$ $[C_2O_4^{2-}]$ $\cdot 10^{-4}$ M	**$[Mg^{2+}]$ $\cdot 10^{-4}$ M**	**Free $[Ca^{2+}]$ $\cdot 10^{-4}$ M**	**Free $[C_2O_4^{2-}]$ $\cdot 10^{-4}$ M**	**Activity coefficient (γ)**	**Estimated S (in droplets)**
4.1	0.0	2.72	2.71	0.827	2.74
4.1	0.05	2.72	2.70	0.827	2.74
4.1	0.5	2.78	2.56	0.823	2.68
4.1	0.875	2.82	2.46	0.821	2.64
4.1	1.0	2.83	2.42	0.820	2.62
4.1	1.25	2.86	2.36	0.818	2.60

The S values of the different samples estimated by the solution chemistry model are given in Table 3.2-Table 3.4. The estimated S values are also important for the analysis of the cumulative induction time probability function in terms of the CNT.

For the magnesium inhibitor experiments, part of the ultrapure water is substituted with magnesium chloride solution, according to Table 3.4.

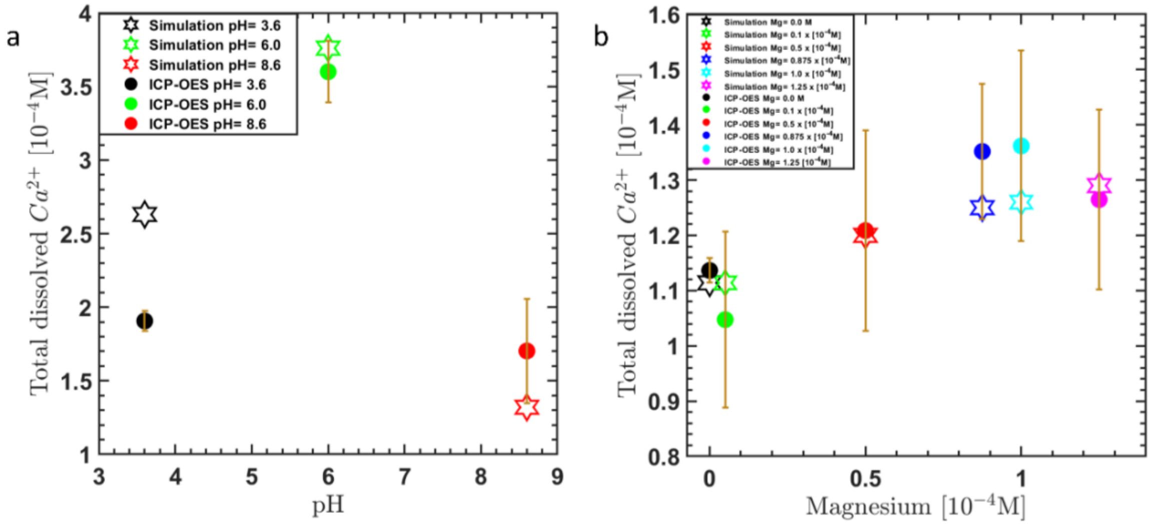

Figure 3.2. The total dissolved calcium concentration in equilibrium for different pH values (panel a) and for different Magnesium concentrations (panel b). The solid symbols are measured values with ICP-OES and open symbols are the predicted values via our solution chemistry model[43] *respectively. Calcium values represent the average of nine data points for each pH value and Magnesium concentration. The regression statistics give a p-value of 0.08 for Figure 3.2.b.*

3.2.3.3. *Polymorphic characterization of crystals in droplets and the excess COM crystals in ultrapure water*

To check whether the nucleated crystals are COM or other calcium oxalate hydrates, the polymorphic form of the crystals in the microfluidic induction time experiments are characterized *in situ*, using polarized light microscopy and Raman scattering, and *ex situ* with powder x-ray diffraction (PXRD). Due to the low calcium and oxalate concentrations in the experiments, we repeated the preparation of equilibrated suspensions described in the Materials and Methods section, ten times to get a sufficient amount of crystals to employ Raman and x-ray diffraction detection for the control group experiment. To characterize crystals in droplets, the microfluidic system is operated continuously to collect a sufficient volume of droplets (40 ml) in a Falcon tube. Consequently, the sample is centrifuged at 7400 rpm during 15 min to remove the oil phase around the collected droplets. The suspensions were left for 1 h to allow the crystals to sediment. Additionally, COM ($CaC_2O_4{\cdot}H_2O$, Sigma-Aldrich, CAS563-72-4) is mixed with ultrapure water (ELGA PURELAB, resistivity:18.2 MΩ·cm at 23.6

°C) – referred to COM suspended in water in Figure 3.9.a. For *in situ* Raman measurements in Figure 3.9.a, the sedimented suspension is decanted, and the concentrated suspension is analysed with a Raman probe (Kaiser Optical Systems) immersed in the suspension. For x-ray diffraction analysis, the crystals are isolated by filtration with a 0.45 µm pore size filter (Whatman® membrane filters nylon), then washed with ultrapure water three times and dried to avoid unwanted contaminant crystallization. The washed crystals are kept at room temperature for drying for two days prior to PXRD experiments. PXRD experiments are performed with these crystals placed on a silicon holder with a powder x-ray diffractometer (Bruker, Cu Ka1, k = 1.5406 A°) as shown in Figure 3.9.b. The acquired spectra are compared to reference spectra of COM, calcium oxalate dihydrate (COD), and calcium oxalate trihydrate (COT) in the CCDC database. The plotted PXRD patterns are taken from the Mercury tool of the Cambridge Structural Database corresponding to COM (CALOXM03), COD(CAOXAL) and COT(ZZZUOQ01).

3.2.3.4. Error propagation

Droplets are stored in chambers in the storage part of the chip. They take an ellipsoidal shape. Droplet volumes are estimated using the images from the microfluidic chip. The average surface area of droplets is found using three droplets via publicly available software, Image J. The projected surface area $0.257\ (\pm 0.013)\cdot 10^{-6}\ m^2$ is multiplied with the channel depth ($2.0\cdot 10^{-4}$ m) to calculate the volume of the droplets. The droplet volume is found as $5.15\cdot 10^{-11}\ m^3$. The droplets stayed at the same positions throughout the induction time measurement. Their sizes did not change significantly throughout experiments, as shown in Figure B. 2 in the Appendix B.

Induction times are obtained considering the 95% confidence interval of the fitted equation. Errors are then calculated following the standard procedure for error propagation, i.e., by calculating the root of the added quadratic errors for each variable.

$$\delta f = \sqrt{((\partial f/\, \partial x \delta x)^2 + (\partial f/\, \partial y \delta y)^2)}$$ *Equation 3.5*

where f is the calculated function, in this case, $f = \ln\left({}^{J}/_{S}\right)$, where $J = {}^{1}/_{\tau V}$ and δ is the uncertainty of every variable.

3.3. Result and Discussion

In a typical experiment, the microfluidic chip is loaded with over 100 droplets at identical concentrations and temperature hence supersaturation as shown in Figure 3.3. Individual droplets are monitored as a function of time as presented in Figure 3.3.b, c and d. The emergence of the first crystal in each droplet is detected and recorded to generate a list of induction times for each droplet under constant supersaturation assumption. From the measured induction times, the cumulative induction time probability function, p(t), is constructed. The p(t) is defined as the cumulative number of droplets containing at least one detected crystal divided by the total number of droplets at a given time, t.

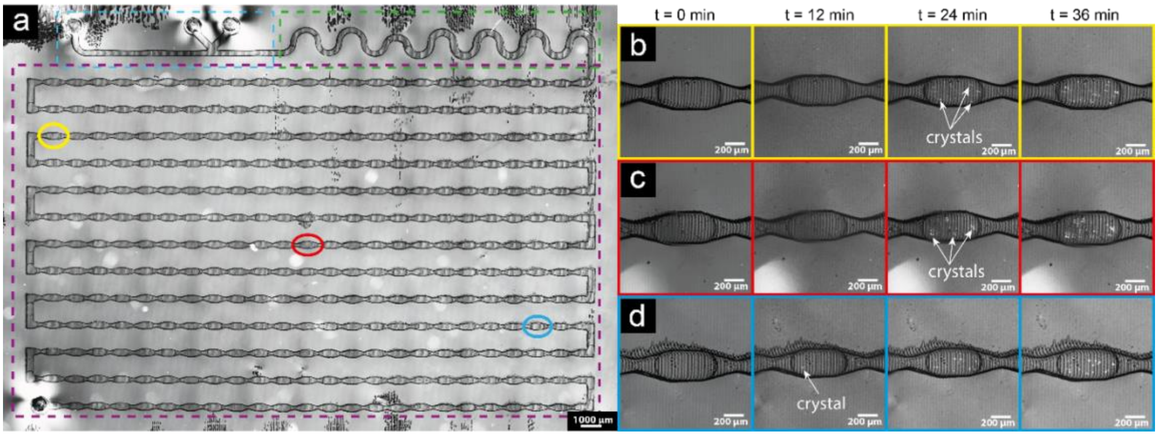

Figure 3.3. Microscopy image of the microfluidic chip (panel a) showing droplet generation, mixing and storage zones. Time-lapse images of individual droplets captured under polarized light microscopy (panels b,c&d). The calcium and oxalate ion concentrations in ultrapure water are equal $[Ca^{2+}]=[C_2O_4^{2-}]=4.10\cdot10^{-4}$ *M which corresponds to S=2.74 predicted by the solution chemistry model.*

The effect of different values of added equimolar calcium and oxalate concentrations on the kinetics of nucleation from the solution is quantified by microfluidic nucleation induction time measurements described in detail in section 3.2.2.2. The cumulative induction time probability distributions, p(t) for a set of initial calcium and oxalate concentrations are plotted against the detection time in Figure 3.4. Table 3.2 provides the added concentrations of Ca^{2+} and $C_2O_4^{2-}$ ions and corresponding initial free concentrations of Ca^{2+} and $C_2O_4^{2-}$ ions, their activity coefficients and the resulting initial supersaturation of COM in the droplets calculated using the aforementioned solution chemistry model. To calculate the initial values, it is assumed that equilibrium is obtained for the protonation, de-protonation and ion pair reactions, but COM has not yet precipitated. Fitting a single exponential with delay time given in Equation 3.1 to p(t) curves in Figure 3.4 allows determining the initial lag time, t_G, and the average nucleation induction time, τ. The initial lag time can be considered as the time required for crystals to grow to an observable size, determined by the resolution of microscope optics. The nucleation rate is predominantly related to the slope of p(t) curves, hence τ.[36] Increasing supersaturations result in smaller average induction times, corresponding to faster nucleation rates evident from steeper slopes of the p(t) curves in Figure 3.4. At the lowest calcium concentration of $1.35 \cdot 10^{-4}$ M (corresponding to supersaturation, S=1.18 in Table 3.2), no crystals were formed over 6 h.

Interestingly, decreasing lag times are observed for the samples with $[Ca^{2+}]$ of $2.05 \cdot 10^{-4}$ M, $2.75 \cdot 10^{-4}$ M, and $4.1 \cdot 10^{-4}$ M, while at $[Ca^{2+}]$ of $5.50 \cdot 10^{-4}$ (S=3.36), no lag time can be identified anymore. At the higher $[Ca^{2+}]$ concentrations, crystals are already present in all droplets 2 min after the start of the experiment, the minimal detection time step in our system. Considering the observed p(t) curves in Figure 3.4, equimolar calcium and oxalate concentration of $4.1 \cdot 10^{-4}$ M was chosen as the reference concentration to be tested at different pH values and in the presence of additives as higher concentrations cannot be studied with our experimental approach.

Figure 3.4 also shows the fits to Equation 3.1 along with 95% confidence intervals. The numerical values of the determined τ, J and t_G values are given in Table 3.5 together with the confidence intervals and the statistical errors of the estimated values. In the calculation, a constant volume is assumed for all droplets and the uncertainty in droplet size is considered as described in section 3.2.3.4.

Table 3.5. The fitted parameters with 95% confidence intervals and the corresponding statistics from the single exponential model with delay time for the different experimental conditions. MSE stands for mean squared error.

	Delay time (t_G) [min]		**τ [min]**		**J [$m^{-3}s^{-1}$]**	**Statistics**	
	Value	**Std Error**	**Value**	**Std Error**	**Value**	**Reduced Chi-Squared**	**MSE**
[Ca] = $2.05\cdot10^{-4}$	240.49	4.16	31.82	4.05	$6.18\cdot10^{11}$	$7.23\cdot10^{-3}$	0.085
[Ca] = $2.75\cdot10^{-4}$	20.74	0.22	11.62	0.37	$2.26\cdot10^{11}$	$4.34\cdot10^{-4}$	0.021
[Ca] = $4.1\cdot10^{-4}$	11.34	0.16	4.30	0.24	$8.34\cdot10^{10}$	$8.90\cdot10^{-4}$	0.030
pH = 3.6	35.41	0.84	30.61	1.65	$6.61\cdot10^{9}$	$1.56\cdot10^{-3}$	0.039
pH = 8.6	23.41	0.08	6.06	0.15	$3.34\cdot10^{10}$	$1.72\cdot10^{-4}$	0.013
[Mg] = $0.05\cdot10^{-5}$	13.52	0.46	6.05	0.72	$1.18\cdot10^{11}$	$5.59\cdot10^{-3}$	0.075
[Mg] = $0.5\cdot10^{-5}$	11.65	0.20	6.68	0.31	$1.30\cdot10^{11}$	$1.03\cdot10^{-3}$	0.032
[Mg] = $0.875\cdot10^{-5}$	19.06	0.22	4.94	0.39	$9.59\cdot10^{10}$	$1.00\cdot10^{-3}$	0.032
[Mg] = $1\cdot10^{-5}$	37.73	0.35	9.25	0.56	$1.80\cdot10^{11}$	$2.25\cdot10^{-3}$	0.047
[OPN] = $1.6\cdot10^{-8}$	48.73	5.02	60.28	7.86	$1.17\cdot10^{12}$	$1.27\cdot10^{-2}$	0.112

The results of this quantitative analysis will be discussed together with the experiments in Figure 3.5 and Figure 3.6 in the following. Figure 3.5 shows how COM nucleation kinetic is altered in a set of buffer solutions producing solutions of different pH values. Nucleation kinetics of COM is studied at fixed added equimolar calcium and oxalate concentrations of $4.1\cdot10^{-4}$ M in Figure 3.5.

Table 3.1 gives the composition of the used buffer solutions and Table 3.3 shows the calculated supersaturations in the droplets. At pH 6.0 in the sodium acetate/acetic acid buffer, no nucleation was observed. Even after 700 minutes, no crystals were detected, which can be explained by the low supersaturation of the droplets in this experiment (S= 1.09). Also, in the experiments in ultrapure water with a comparable S value (S= 1.18), no crystals were detected within the experimental time scale. At pH 8.6, the nucleation rate is comparable and at pH 3.6 somewhat lower than that in the reference concentration in ultrapure water (Figure 3.4).

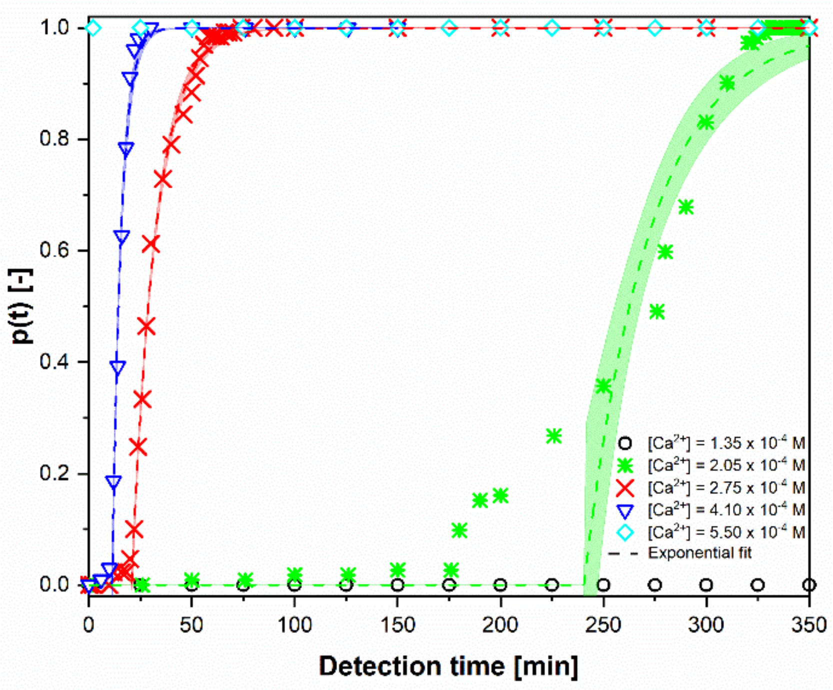

Figure 3.4. The cumulative induction time probability, p(t) as a function of the detection time, t, for different added Ca^{2+} *concentrations in ultrapure water fitted with the exponential function with delay time (Equation 3.1). The numbers of used droplets are 107, 112, 129, 102 and 103 for concentrations of* $1.35\cdot10^{-4}$ *M,* $2.05\cdot10^{-4}$ *M,* $2.75\cdot10^{-4}$ *M,* $4.10\cdot10^{-4}$ *M and* $5.50\cdot10^{-4}$ *M, respectively. The ratio of added molar concentration of* Ca^{2+} *and* $C_2O_4^{2-}$ *ions is the same for all experiments* $[Ca^{2+}]/[C_2O_4^{2-}]=1$ *for all solutions. The calculated initial free* Ca^{2+} *and* $C_2O_4^{2-}$ *ion concentrations, their activity coefficient and the initial supersaturation of COM in the droplets are given in Table 3.2.*

However, if we compare the experiments at pH 3.6 with that in ultrapure water at the same supersaturation ($[Ca^{2+}]=[C_2O_4^{2-}]=2.05\cdot10^{-4}$ M, S=1.64), the nucleation rate is much faster and the lag time is much smaller at the low pH. It should be noted that in addition to S value, the ratio of the free Ca^{2+} and $C_2O_4^{2-}$ ion concentrations are different at different pH values, whereas this ion ratio is still about one at pH of 8.6. At the low pH value, the free Ca^{2+} ions concentration is almost five times higher than that of the $C_2O_4^{2-}$ ions, due to ion pair formation and protonation of the oxalate ion (See Table 3.3). Also, the shape of the p(t) is slightly different at the low pH, bending off at p(t) values around 0.9, which could give an indication of (pseudo) polymorphism.[71] The possible formation of COD crystals instead of COM has been examined using XRD and Raman (see Figure 3.9), but no indication of polymorphism was found within the sensitivity of aforementioned methods. Yet one should not completely rule out this (pseudo) polymorphism explanation as XRD and Raman cannot detect (pseudo) polymorphs if they are present below 5-10% by weight.

To summarize the experiments at different pH values, we did not observe crystal formation within the experimental time scale at pH 6.0, but observed fast nucleation rates at acidic (pH=3.6) and basic conditions (pH=8.6). This result is qualitatively in line with the medical literature[72, 73], where low and high urine pH are considered to play a significant role in stone formation.[74, 75]

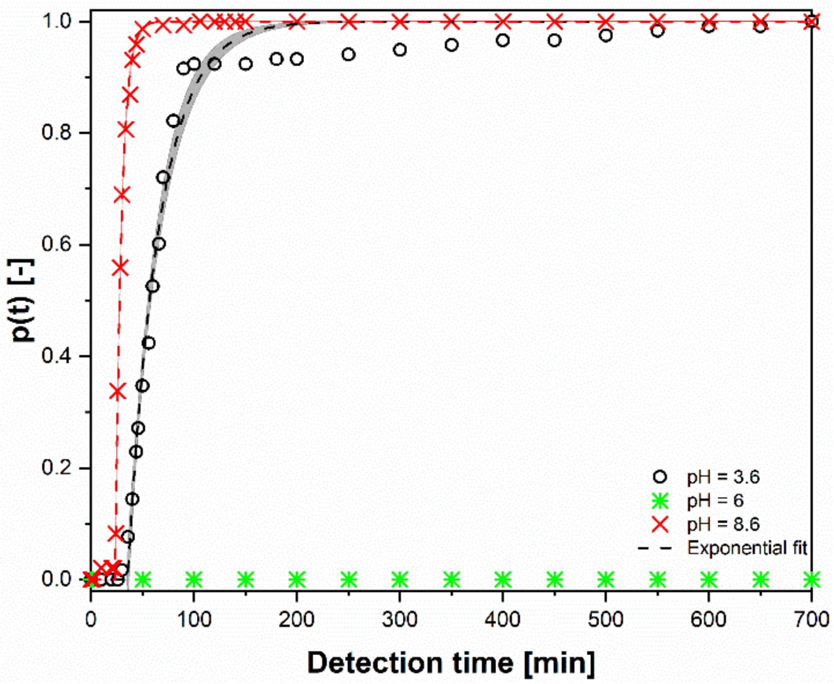

Figure 3.5. The cumulative induction time probability, p(t) curves for different pH values fitted with the single exponential with delay time (Equation 3.1). The numbers of used droplets are 118, 105 and 124 for pH values of 3.6, 6.0 and 8.6 respectively. The composition of the buffer solutions for pH values of 3.6, 6.0, and 8.6 are shown in Table 3.1. The added equimolar Ca^{2+} *and* $C_2O_4^{2-}$ *concentration of* $4.1 \cdot 10^{-4}$ *M is used in all experiments. The calculated initial free* Ca^{2+} *and* $C_2O_4^{2-}$ *ion concentrations, their activity coefficient and the initial supersaturation of COM in the droplets are given in Table 3.3.*

Figure 3.6 focuses on the influence of magnesium ions on the nucleation kinetics of COM in ultrapure water. In all the experiments given in Figure 3.6, the reference equimolar calcium and oxalate concentrations of $4.1 \cdot 10^{-4}$ M are used. The initial S values in the experiments shown in Figure 3.5 depends on the added Mg concentrations and are calculated using the solution chemistry model described in 3.2.3.2. (see Table 3.4) The supersaturation in the droplets decreases only slightly with increasing Mg^{2+} concentrations (from 2.74 to 2.60). Figure 3.6 shows that also the slopes of p(t) curves decreased only slightly with the Mg^{2+} concentration, in line with the small changes in supersaturation values given in Table 3.4 On the other hand, we see a strong influence of the Mg^{2+} concentrations on the lag times of the p(t) curves. This will be further analyzed in the following through a quantitative analysis of the probability curves.

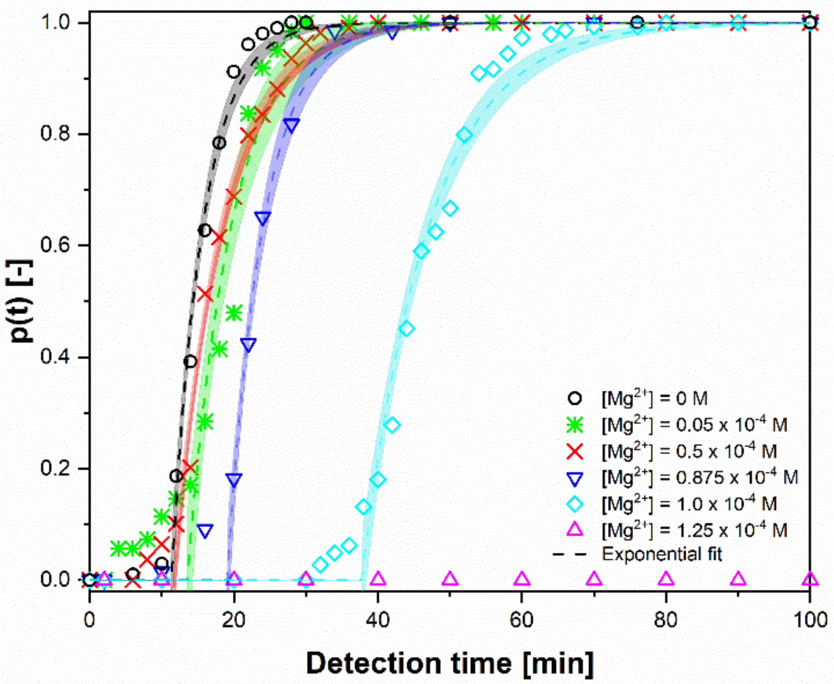

Figure 3.6. The cumulative induction time probability curves, p(t) at specific Mg^{2+} concentrations fitted with the single exponential with delay time (Equation 3.1). The numbers of used droplets are 107, 106, 109, 113, 108 and 102 for concentrations of Magnesium 0 M, $0.05\cdot10^{-4}$ M, $0.5\cdot10^{-4}$ M, $0.875\cdot10^{-4}$ M, $1\cdot10^{-4}$ M and $1.25\cdot10^{-4}$ M respectively. The varying concentrations of Mg^{2+} ions are added to equimolar calcium and oxalate concentration of $[Ca^{2+}]=[C_2O_4^{2-}]=4.1x10^{-4}$ M. The calculated initial free Ca^{2+} and $C_2O_4^{2-}$ ion concentrations, their activity coefficient and the initial supersaturation of COM in the droplets are given in

Table 3.4.

Finally, the inhibitory effect of OPN on COM nucleation kinetics is reported in Figure 3.7. Three different OPN concentrations, $1.6\cdot10^{-8}$ M, $3.2\cdot10^{-8}$ M, and $4.8\cdot10^{-8}$ M, were added to the droplets carrying equimolar calcium and oxalate concentrations

$[Ca^{2+}]=[C_2O_4^{2-}]=4.1\cdot10^{-4}$ M. The experiments conducted with OPN concentrations of $3.2\cdot10^{-8}$ M and $4.8\cdot10^{-8}$ M, did not show any crystals after running the experiments for more than 3 h. A striking observation is the distinct shape p(t) curve with $1.6\cdot10^{-8}$ M OPN. At this OPN concentration p(t) have a sigmoidal shape different from curves observed in Figure 3.4-Figure 3.6.

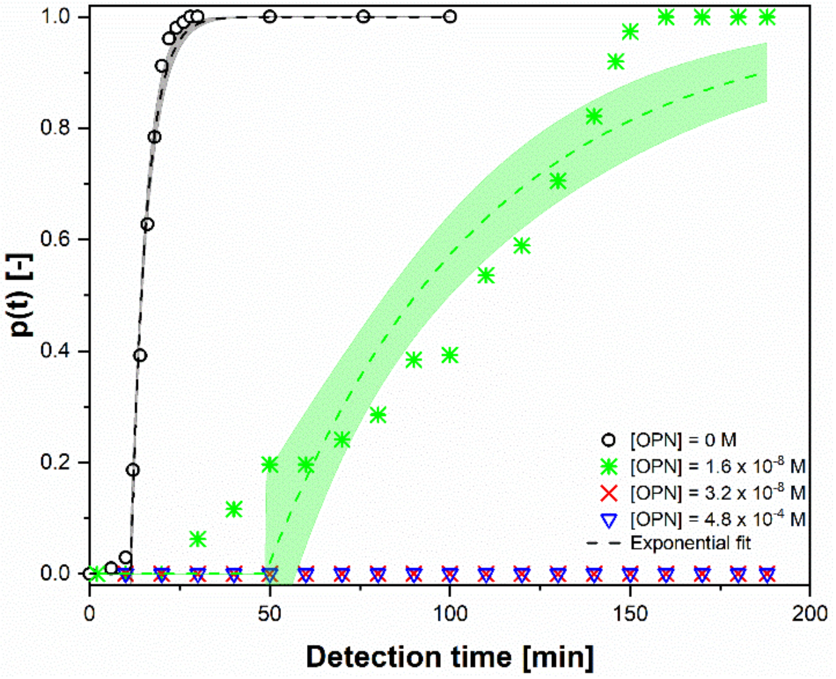

Figure 3.7. The cumulative induction time probability, p(t) curves at specific osteopontin concentrations fitted with the single exponential with delay time (Equation 3.1). The numbers of used droplets are 107, 102, 111 and 105 for concentrations of Osteopontin 0 M, 1.6 $\cdot10^{-8}$ M, $3.2\cdot10^{-8}$ M and $4.8\cdot10^{-8}$ M, respectively. The Ca^{2+} and $C_2O_4^{2-}$ concentrations are kept constant at $4.1\cdot10^{-4}$ M.

The sigmoidal shape and effective inhibition at significantly lower concentrations than magnesium ions might be connected to the molecular structure complexity of OPN relative to simple magnesium ions. Due to the fact that OPN is rich in dicarboxylic acids, stronger interaction of OPN with crystal faces is expected.[76] The chemical structure of OPN might promote binding to a mineral surface[22] or Ca^{2+} ions might induce fixed conformation of OPN.[77, 78] All these possibilities may result in slower kinetics with an increasing amount of OPN. Moreover, medical literature suggests that OPN is present in urine at concentrations higher than 100 nM and it might play a critical role in kidney stone formation. Previously published reports point out that patients with urolithiasis have lower concentrations of OPN in their excretion.[79] Despite the simplicity of the solution matrix in our experiments, we find that OPN suppresses COM formation completely at the same order of magnitude concentrations as it is found in urine. Even at this level, this finding calls for more investigation on the role OPN and other macromolecules play in kidney stone formation when present in patient urine despite their minute concentration.

To summarize the results of microfluidic induction time measurements, given in Figure 3.4-Figure 3.7 the numerical values of the fitted parameters for τ, t_G and J and the statistical fit parameters, given in Table 3.5 will be discussed. In general, reasonably good fits of the single exponential curve were obtained for most of the experiments. Only in a few cases [$CaCl_2$]= 0.205 mM in ultrapure water, at the lowest magnesium concentration and at pH 3.6. (see Table 3.3), the p(t) curve showed non-typical shapes sometimes with a large delay which was difficult to fit with Equation 3.1 and gave rise to a large uncertainty. (see Table 3.5). Therefore, p(t) fits were also made using the Weibull function (Equation 3.2) comparing the results in terms of their goodness of fit statistics. We did not find a clear improvement in the goodness of fit using the Weibull function except in the aforementioned two cases and concluded that Equation 3.1 described the cumulative probability curves adequately for our purpose. The fits to p(t) curves with the Weibull function are given and discussed in the Figure B. 3- Figure B. 6 and Table B. 1- Table B. 4 in the Appendix B.

Hammadi et al.[59] showed longer induction times in smaller volumes with a series of solute/solvent systems where the solubility depends strongly on temperature. Despite the fact that solubility of our system does not strongly depend on temperature, we should as well expect longer induction times in smaller droplet volumes. At this stage, we can only hypothesize about the origin of the deviations from Equation 3.1 observed in some of the experiments. Our first hypothesis is that the observed variations from single exponential behavior may originate from two separate nucleation events occurring at different time scales, a fast and a slow process. As nucleation occurs at a higher rate on surfaces in contact with the solution compared to homogeneous nucleation[80], one may suspect that droplets in contact with impurities, solid microfluidic walls and liquid-liquid interfaces[81] may trigger nucleation at different rates giving raise to observed deviation. However, this hypothesis is at odds with the finding of Duft and Leisner[82], who deduced that surface nucleation does not lead to deviation of the shape of the p(t) curve but only to its steepness. Second, due to the density difference between the droplets and the surrounding oil phase, the thin oil film[83] between the droplets and channel walls can be squeezed out bringing the droplets in contact with PDMS walls.[55] Both these solid-liquid and liquid-liquid interfaces might trigger time dependent heterogeneous nucleation rates which could affect the shape of the p(t) curve. Finally, earlier nucleation events can be triggered at the liquid-liquid mixing front when the two reactive streams make contact before the droplet reaches the mixing zone shown in Figure 3.1.a. Another potential explanation can be the non-classical nucleation pathway supported by reports focusing on the nucleation pathway of CaOx.[34] One may imagine the distribution of pre-nucleation clusters triggering nucleation at different time scales resulting in p(t) deviating from a single exponential. The last potential explanation is the formation of pseudo-polymorphs below the detection limit of PXRD and Raman. It should be noted that all of these rationalizations are mere hypotheses that need further deductions.

As discussed in the introduction and in section 3.2.2.3. , the CNT predicts an exponential shape of the p(t) curve and the t_G delay can be interpreted as the time for the nuclei to grow from the nanoscale into a detectable crystal size. The clear advantage of such quantitative analysis of the experimental data is that it provides a statistics-based analysis of the nucleation and growth kinetics from the presented experiments; it also gives us insight in the underlying nucleation mechanisms. Yet using CNT analysis should not be blindly interpreted as assuming that the nucleation pathway is classic. As demonstrated by Smeets et al.[35] experimentally and later in a CNT extension by Kashchiev, CNT concepts can be used to gain insights into nucleation even for systems following non-classical pathways.[36]

To rationalize the influence of the supersaturation on the nucleation rate, we turn to Equation 3.3 where ln(J/S) values are plotted against $1/(\ln^2(S))$ in Figure 3.8 (complete analysis can be found in the Appendix B). The plotted experimental J values are extracted from fitting the p(t) functions in Figure 3.4-Figure 3.6 and the estimated S values are calculated using the solution chemistry model. The dashed line in Figure 3.8

represents the fit of Equation 3.3 to experiments conducted in ultrapure water (presented in Figure 3.4) and the shaded area corresponds to the confidence interval of the fit. The fitted A and B values and their confidence intervals are A= $4.05 \cdot 10^8$ $m^{-3}s^{-1}$ ($1.83 \cdot 10^7$; $8.96 \cdot 10^9$) and B = 0.47 (-0.80; 1.73), respectively.

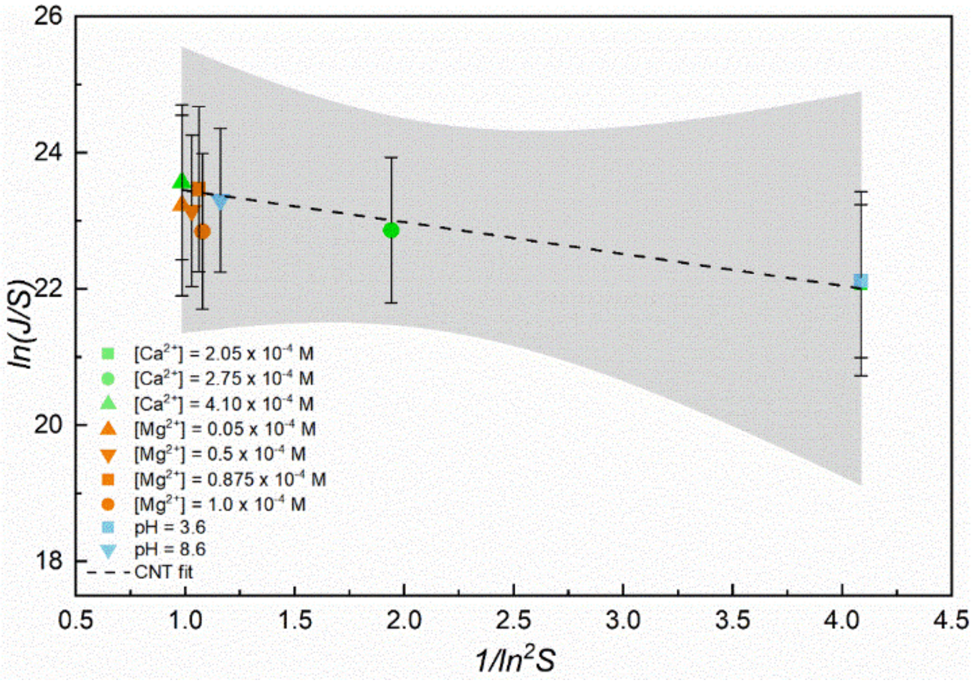

Figure 3.8. Apparent nucleation rate, J and the corresponding S value for all of the measured induction times of COM at different conditions plotted in the context of classic nucleation time, i.e., different calcium and oxalate ion concentrations in ultrapure water given in Figure 3.4, different pH values given in Figure 3.5, and magnesium ion concentrations given in Figure 3.6. Only the induction time data for different calcium and oxalate ion concentrations (green data points) in ultrapure water is fitted to Equation 3.3. The dotted line is the fit with the parameters A= $4.05 \cdot 10^8$ $m^{-3}s^{-1}$ *(*$1.83 \cdot 10^7$; $8.96 \cdot 10^9$*) and B = 0.47 (-0.80; 1.73) and grey shaded area is the 95% confidence interval.*

Note that only the experiments with varying initial concentrations of Ca^{2+} and $C_2O_4^{2-}$ ions in ultrapure water are used in this fit. It is highly likely that a varying composition in the different samples resulting from the additions of the buffer solutions and/or the $MgCl_2$ solutions will affect the kinetic parameter A of the solution and thus making the fit of Equation 3.3 to all experiments illegitimate.

According to Roelands et al.[84], the nucleation process can be categorized through the kinetic parameter into homogeneous ($A_{HON} \sim 10^{35}$ [m^{-3} s^{-1}]) or heterogeneous ($A_{HEN} \sim$

10^{15}-10^{25}). Thus, for the conditions tested in this work, we can conclude that COM nucleation is heterogeneous under the experimental conditions covered in Figure 3.4. This is expected as the nucleation happens inside droplets dispersed in a continuous oil phase, so that the liquid-liquid interface or microfluidic device walls can provide heterogeneous surfaces promoting COM nucleation. It is noteworthy to mention that the confidence interval of CNT fit in Figure 3.8 is very large indicating a bad fit. This is due to the low number of data points available in Figure 3.4 as two of the chosen S values provided J values outside measuring capabilities of the microfluidic setup. The broad confidence intervals can also be attributed to a non-classical pathway providing a broad distribution of time scales, hence a bad fit to a single exponential. Moreover, the nucleation kinetic parameter for COM crystals was estimated by Hsu et al.[85] as $2.57 \cdot 10^{11}$ $m^{-3}s^{-1}$. Yet, these values are not comparable since in their work COM crystallization was performed in 250 ml stirred crystallizers using synthetic urine medium resulting in S = 13.65; while the present work studied the crystallization of COM on droplets in ultrapure water solutions and at significantly lower supersaturations. In summary, Figure 3.8 provides limited insight, yet we think attempting such analysis is relevant provided that one does not make assumptions on the classical or non-classical nature of nucleation. Despite previous reports providing evidence on the non-classic nature of COM nucleation, the CNT framework can still provide insights as demonstrated experimentally by Smeets et al.[35] and more recently by Kashchiev.[36]

In the next step, we turn our attention to the analysis of observed delay time, t_G in p(t) curves. From the fitted values of t_G given in Table 3.5, the experimental growth rate, $G_{exp,}$ can be calculated assuming that t_G is the time required for a crystal to grow to the detection limit. The detection limit is estimated as 4 pixels± 1 pixel corresponding to 6.4± 1.7 μm based on the resolution of the microscope images used to detect the crystals in the microfluidic induction time measurements. G_{exp} is then calculated for each experiment presented in Figure 3.4 and Figure 3.5 by dividing the detection limit to t_G. The obtained G_{exp} values calculated from this procedure and the corresponding S values are plotted in Figure 3.9. The data presented in Figure 3.9 can be further analyzed to gain insight into the growth mode of COM crystals. The G_{exp} and S values then can be used to estimate the parameters of a simple growth rate equation; $G_{exp}= k_G\ (S\text{-}1)^p$, where p is the power of the supersaturation term and S is the calculated supersaturation value in the droplets of these experiments. A p value of 1 is attributed to diffusion limited or rough growth and a p value of 2 or higher is expected for birth and spread or spiral growth model.[86]

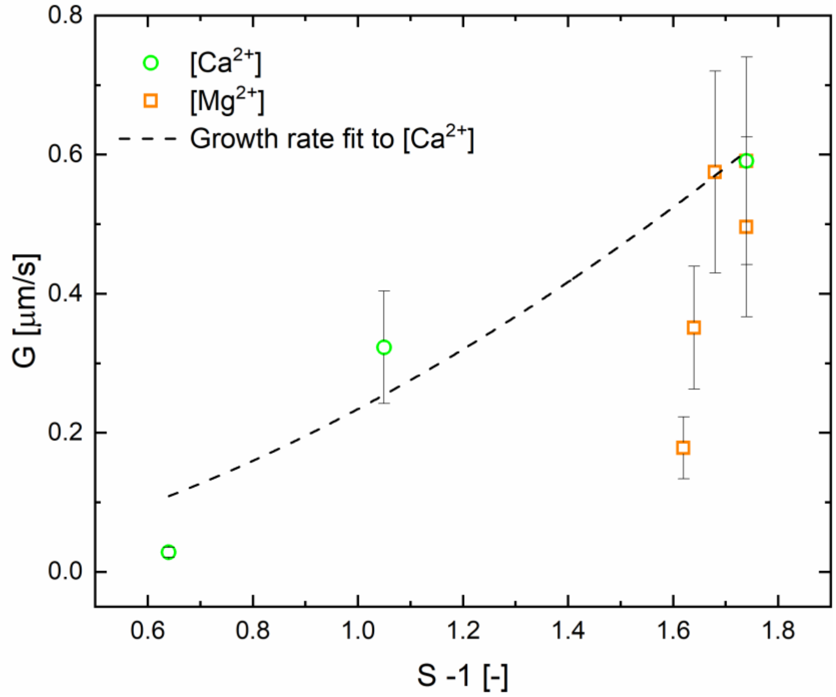

Figure 3.9. Analysis of measured growth rates of COM calculated from delay times in p(t) curves for different calcium and oxalate ion concentrations given in Figure 3.4 (green dots), and magnesium ion concentrations given in Figure 3.6 (red squares).

The most striking observation from Figure 3.9 is the distinct S dependence of G_{exp} of experiments conducted in with (red squares) and without Mg^{2+} ions (green circles) presented in Figure 3.4 and Figure 3.5, respectively. These growth rates show distinct S dependences. The growth rates with different added total Ca^{2+} concentrations in ultrapure water show a milder S dependence whereas increasing the Mg^{2+} ion concentration shows a steeper dependence. Next, we turn our attention to the analysis of growth mode by fitting the growth rate model, $G_{exp}= k_G\ (S\text{-}1)^p$ to experiments conducted with and without Mg^{2+} ions. The estimated parameters k_G and p for green circles (experiments without Mg^{2+} ions presented in Figure 3.4) are estimated by fitting the growth rate model as 0.23 ± 1.05 and 1.7 ± 8.8, respectively. The quality of the fit is not so high, due to the low number of data points used and due to the uncertainties related to the estimation of the t_G parameter. The aforementioned atypical shape of the p(t) curves gave rise to considerable uncertainty in the estimation of the t_G. This large uncertainty prevents us from reaching any conclusion on the exact nature of the growth model. The second striking deduction emerges from fitting G_{exp} values increasing Mg^{2+} ion concentrations to the growth rate model. Fitting of the growth rate function on the basis of these experiments would require a p value in the order of 10, which is unrealistic. This suggests that inhibition of the growth rate by Mg^{2+} ions is not caused directly by the change in the supersaturation but that another mechanism is involved. The observed non typical shape of the experimental p(t) curves mostly in combination with large lag times could be an indication of a different nucleation mechanism, the occurrence of the surface nucleation at the oil-water interface, preferential binding of Mg^{2+} ions to kink sites or be caused by polymorphism.[71]

As has been shown by Duft and Leisner[82], the occurrence of surface nucleation at the liquid-air interface is not likely to give rise to a completely different shape of the p(t) curve[82] and still an exponential behavior is expected. For the nucleation in sparingly soluble systems such as $CaCO_3$ and CaC_2O_4 a non-classical nucleation mechanisms have been proposed[35, 37], due to the formation of amorphous intermediates or precursors, which would lead to other characteristics of the probability curve. Finally, the possible formation of COD crystals instead of COM has been examined using XRD and Raman in Figure 3.10, but no indication of polymorphism was found. Yet as previously mentioned in the discussion about the deviation of exponential behavior of p(t) curves, the formation of pseudo-polymorphs below the detection limit of PXRD and Raman should not be ruled out.

Finally, we explore the possibility of pseudo-polymorphs forming in microfluidic experiments by Raman (Figure 3.10.a) and PXRD (Figure 3.10.b) characterization described in detail in the Materials and Methods section.

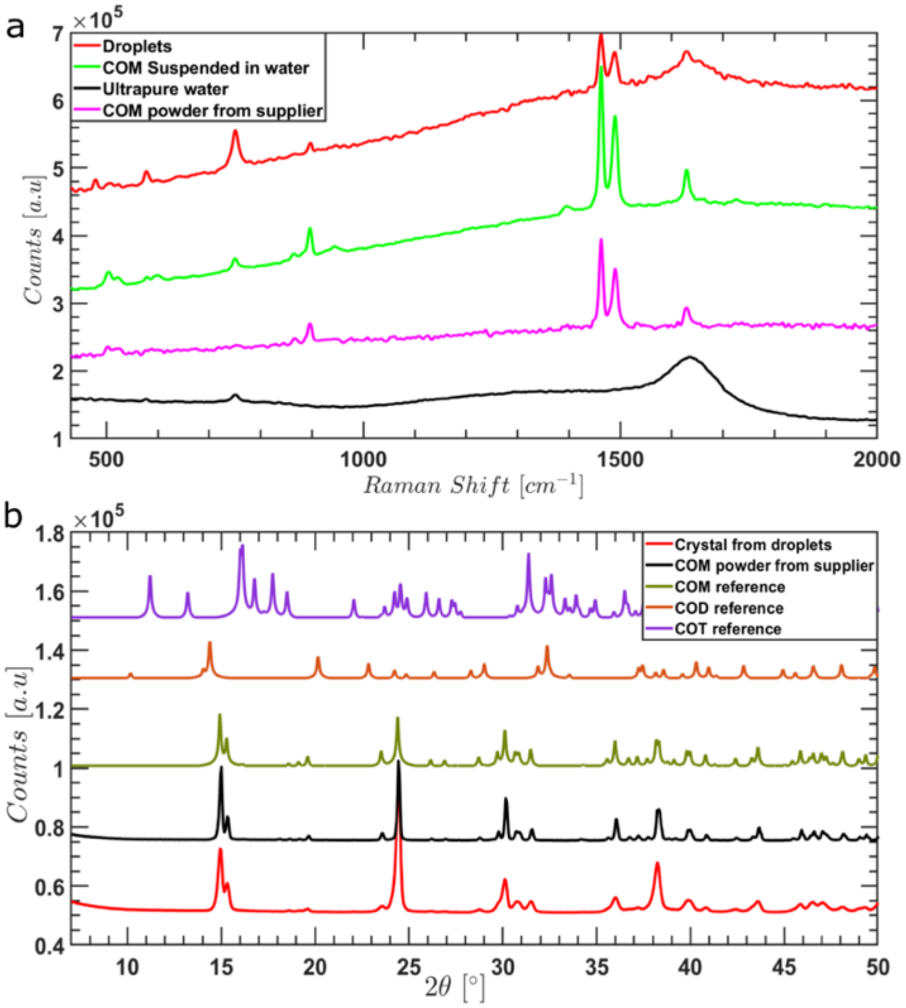

Figure 3.10. Characterization of the crystal structure of the formed crystals under various conditions. a) Raman spectra of collected droplets removed from the oil phase (red); COM crystals suspended in ultrapure water (green), COM Powder from supplier (magenta), and Ultrapure water (black), b) XRD spectra of dried crystals from droplets (red), COM powder from supplier (black), COM reference (dark green), COD reference (orange) and COT reference (purple).

The characteristic COM Raman bands are observed in Figure 3.10.a at 504, 508 (O-C-O), 897 (C-C), 1463, 1490 (C-O), and 1629 (C-O) cm^{-1}.[87-89] These shared peaks, evident in spectra corresponding to crystals formed inside microfluidic droplets denoted "Droplets" and in the reference case of COM crystals from supplier suspended in ultrapure water denoted as "COM suspended in water", imply that the pseudo-polymorphic form crystallized with microfluidic experiments is COM. In addition to *in situ* Raman measurements conducted in the solution, *ex situ* PXRD measurements where the excess crystals are filtered, washed and dried before diffraction measurements are conducted. Figure 3.10.b provides PXRD spectra of the precipitated crystals from canonical microfluidic experiments denoted as “Crystal from droplets” and the reference case of COM crystals denoted as “COM powder from supplier” along with reference spectra of three calcium oxalate (pseudo)polymorph/hydrate from CCDC database, namely calcium oxalate monohydrate (COM), calcium oxalate dihydrate (COD) or calcium oxalate trihydrate (COT).[90] The PXRD peaks of COM reference share the identical peaks with the PXRD spectra of “Crystals from droplets”, and the PXRD spectra of COM crystals as purchased from supplier referred as “COM powder from supplier”. After precipitation, no transition from COM to other CaOx hydrate forms was observed during the induction time measurements within the accuracy of Raman and PXRD techniques.

3.4. Conclusions

We present a coupled experimental and modeling study focusing on COM nucleation rate, quantified using microfluidic induction time measurements in a droplet-based microfluidics platform. Leveraging the multiplexing capability of droplet microfluidics, ours minimizes the use of materials while ensuring statistically significant number of identical experiments. We interpret the presented nucleation induction time experiments using a previously published solution chemistry model based on the Davies extension of Debye-Hückel theory, which was validated using isothermal solubility measurements.[43] The model enables the interpretation of the pronounced effects of pH, ionic strength, solution chemistry on the solubility of the COM crystals and on the prevailing supersaturation under the studied conditions. The presented induction time measurements and p(t) curves coupled with modeling point out that the presence of Mg^{2+} ions appear to slightly alter supersaturation from 2.74 to 2.60 for, while its effect on the lag time is considerable. Further analysis on the growth rate in the presence of Mg^{2+} ions reveals that the inhibition mechanism cannot be explained solely by supersaturation. Furthermore, we observed that OPN suppresses COM nucleation at significantly lower concentrations compared to Mg^{2+} ions. The pronounced inhibition effect of OPN at much lower concentrations compared to Mg^{2+} ions emphasize the often-overlooked role of macromolecules on COM nucleation due to their low concentration presence in urine. We hope that the presented study highlights the potential of microfluidics in unraveling the underlying the physicochemical mechanisms behind kidney stone formation, particularly in addressing the overwhelming complexity of the urine composition phase space. With our following work, we will use this study as a stepping stone to focus on more complex artificial urine solutions essential for our overarching goal of quantitatively predicting CaOx formation in kidney from patient urine composition.

3.5. References

1. Evan, A.; Lingeman, J.; Coe, F. L.; Worcester, E., Randall's plaque: pathogenesis and role in calcium oxalate nephrolithiasis. *Kidney international* **2006,** *69* (8), 1313-1318.

2. Bushinsky, D. A.; Asplin, J. R.; Grynpas, M. D.; Evan, A. P.; Parker, W. R.; Alexander, K. M.; Coe, F. L., Calcium oxalate stone formation in genetic hypercalciuric stone-forming rats. *Kidney international* **2002,** *61* (3), 975-987.

3. Ridley, J. W., *Fundamentals of the Study of Urine and Body Fluids*. Springer: 2018.

4. Rose, C.; Parker, A.; Jefferson, B.; Cartmell, E., The Characterization of Feces and Urine: A Review of the Literature to Inform Advanced Treatment Technology. *Critical reviews in environmental science and technology* **2015,** *45* (17), 1827-1879.

5. Worcester, E. M.; Coe, F. L., Nephrolithiasis. *Primary Care* **2008,** *35* (2), 369-391, vii.

6. Skorecki, K., , Chertow, G.M.; Marsden, P.A.; Taal, M.W.; Alan, S.L.; Luyckx, V., *Brenner and Rector's The Kidney E-Book*. Elsevier Health Sciences: 2015.

7. Romero, V.; Akpinar, H.; Assimos, D. G., Kidney stones: a global picture of prevalence, incidence, and associated risk factors. *Reviews in urology* **2010,** *12* (2-3), e86-96.

8. Kalaitzidis, R. G.; Damigos, D.; Siamopoulos, K. C., Environmental and stressful factors affecting the occurrence of kidney stones and the kidney colic. *International urology and nephrology* **2014,** *46* (9), 1779-1784.

9. Bono, M. J., Reygaert, W.C., Urinary tract infection. In *Urinary tract infection*, StatPearls Publishing: 2017.

10. Moe, O. W., Kidney stones: pathophysiology and medical management. *Lancet* **2006,** *367* (9507), 333-344.

11. Khan, S. R.; Pearle, M. S.; Robertson, W. G.; Gambaro, G.; Canales, B. K.; Doizi, S.; Traxer, O.; Tiselius, H. G., Kidney stones. *Nature Reviews Disease Primers* **2016,** *2*, 16008.

12. Miller, G. H.; Vermeullen, C. W.; Moore, J. D., Calcium oxalate solubility in urine; experimental urolithiasis. XIV. *The Journal of Urology* **1958,** *79* (3), 607-612.

13. Izatulina, A. R. G., V.V.; Krzhizhanovskaya, M.G.; Kuz'mina, M.A.; Leoni, M.; Frank-Kamenetskaya, O.V., Hydrated Calcium Oxalates: Crystal Structures, Thermal Stability, and Phase Evolution. *Crystal growth & design* **2018,** *18* (9), 5465-5478.

14. Kelland, M. A.; Mady, M. F.; Lima-Eriksen, R., Kidney Stone Prevention: Dynamic Testing of Edible Calcium Oxalate Scale Inhibitors. *Crystal growth & design* **2018,** *18* (12), 7441-7450.

15. Laffite, G., Leroy, C., Bonhomme, C., Bonhomme-Coury, L., Letavernier, E., Daudon, M., Frochot, V., Haymann, J.P., Rouzière, S.L., Ivan, T., Bazin, D., Babonneaub, F., Abou-Hassan, A., Calcium oxalate precipitation by diffusion using laminar microfluidics: toward a biomimetic model of pathological microcalcifications. *Lab on a Chip* **2016,** *16* (7), 1157-1160.

16. Pahira, J. J., Pevzner, M., Nephrolithiasis. In *Penn Clinical Manual of Urology*, Elsevier: 2007; pp 235-257.

17. Bird, V. Y., Khan, S.R., How do stones form? Is unification of theories on stone formation possible? *Archivos espanoles de urologia* **2017,** *70* (1), 12.

18. Kok, D. J.; Papapoulos, S. E., Physicochemical considerations in the development and prevention of calcium oxalate urolithiasis. *Bone and mineral* **1993,** *20* (1), 1-15.

19. Favus, M. J., Zeytinoglu, M., Coe, F.L., Idiopathic hypercalciuria and nephrolithiasis. In *Vitamin D*, Elsevier: 2018; pp 485-505.

20. Ratkalkar, V. N.; Kleinman, J. G., Mechanisms of stone formation. *Clinical reviews in bone mineral metabolism* **2011,** *9* (3-4), 187-197.

21. Aggarwal, K. P.; Narula, S.; Kakkar, M.; Tandon, C., Nephrolithiasis: molecular mechanism of renal stone formation and the critical role played by modulators. *BioMed Research International* **2013,** *2013*.

22. Qiu, S. R.; Wierzbicki, A.; Orme, C. A.; Cody, A. M.; Hoyer, J. R.; Nancollas, G. H.; Zepeda, S.; De Yoreo, J. J., Molecular modulation of calcium oxalate crystallization by osteopontin and citrate. *Proceedings of the National Academy of Sciences of the United States of America* **2004,** *101* (7), 1811-5.

23. Denhardt, D. T., *Osteopontin: Role in Cell Signalling and Adhesion.* New York Academy of Sciences: 1995.

24. Wesson, J. A.; Johnson, R. J.; Mazzali, M.; Beshensky, A. M.; Stietz, S.; Giachelli, C.; Liaw, L.; Alpers, C. E.; Couser, W. G.; Kleinman, J. G.; Hughes, J., Osteopontin is a critical inhibitor of calcium oxalate crystal formation and retention in renal tubules. *Journal of the American Society of Nephrology* **2003,** *14* (1), 139-147.

25. Kok, D. J.; Papapoulos, S. E.; Blomen, L. J.; Bijvoet, O. L., Modulation of calcium oxalate monohydrate crystallization kinetics in vitro. *Kidney international* **1988,** *34* (3), 346-50.

26. Molzon, J. A. The solubility of calcium oxalate as a function of dielectric constant. 1976.

27. Kolbach-Mandel, A. M.; Kleinman, J. G.; Wesson, J. A., Exploring calcium oxalate crystallization: a constant composition approach. *Urolithiasis* **2015,** *43* (5), 397-409.

28. Taranets, Y. V., Crystallization kinetics of calcium oxalate monohydrate in the presence of amino acids. *Functional materials* **2018**.

29. Xie, B.; Halter, T. J.; Borah, B. M.; Nancollas, G. H., Aggregation of Calcium Phosphate and Oxalate Phases in the Formation of Renal Stones. *Crystal growth & design* **2015,** *15* (1), 204-211.

30. Sear, R. P., Quantitative studies of crystal nucleation at constant supersaturation: experimental data and models. *CrystEngComm* **2014,** *16* (29), 6506-6522.

31. Vekilov, P. G., Nucleation. *Crystal growth & design* **2010,** *10* (12), 5007-5019.

32. Gebauer, D. C., Helmut, Prenucleation clusters and non-classical nucleation. *Nanotoday* **2011,** *6* (6), 564-584.

33. Hajir, M.; Graf, R.; Tremel, W., Stable amorphous calcium oxalate: synthesis and potential intermediate in biomineralization. *Chemical Communications* **2014,** *50* (49), 6534-6536.

34. Ruiz-Agudo, E.; Burgos-Cara, A.; Ruiz-Agudo, C.; Ibanez-Velasco, A.; Colfen, H.; Rodriguez-Navarro, C., A non-classical view on calcium oxalate precipitation and the role of citrate. *Nature communications* **2017,** *8* (1), 1-10.

35. Smeets, P. J. M.; Finney, A. R.; Habraken, W.; Nudelman, F.; Friedrich, H.; Laven, J.; De Yoreo, J. J.; Rodger, P. M.; Sommerdijk, N., A classical view on nonclassical nucleation. *Proceedings of the National Academy of Sciences* **2017,** *114* (38), E7882-E7890.

36. Kashchiev, D., Classical nucleation theory approach to two-step nucleation of crystals. *Journal of Crystal Growth* **2020,** *530*, 125300.

37. Gebauer, D.; Volkel, A.; Colfen, H., Stable prenucleation calcium carbonate clusters. *Science* **2008,** *322* (5909), 1819-1822.

38. Zhai, H.; Wang, L.; Putnis, C. V., Inhibition of spiral growth and dissolution at the brushite (010) interface by chondroitin 4-sulfate. *The Journal of Physical Chemistry B* **2019** *123* (4), 845-851.

39. Robertson, W. G.; Peacock, M.; Nordin, B. E., Activity products in stone-forming and non-stone-forming urine. *Clinical Science* **1968,** *34* (3), 579-94.

40. Streit, J., Tran-Ho, L., Königsberger, E., Solubility of the three calcium oxalate hydrates in sodium chloride solutionsand urine-like liquors. *Monatshefte für Chemie/Chemical Monthly* **1998,** *129* (12), 1225-1236.

41. Singh, R. P., On the existence of NaC2O4− ion pair complex. *Bulletin of the Chemical Society of Japan* **1989,** *62* (12), 4089-4091.

42. Nancollas, G. H., Gardner, G.L., Kinetics of crystal growth of calcium oxalate monohydrate. *Journal of Crystal Growth* **1974,** *21* (2), 267-276.

43. Ibis, F.; Dhand, P.; Suleymanli, S.; van der Heijden, A. E. D. M.; Kramer, H. J. M.; Eral, H. B., A Combined Experimental and Modelling Study on Solubility of Calcium Oxalate Monohydrate at Physiologically Relevant pH and Temperatures. *Crystals* **2020,** *10* (10), 924.

44. Hojgaard, I.; Fornander, A. M.; Nilsson, M. A.; Tiselius, H. G., The effect of pH changes on the crystallization of calcium salts in solutions with an ion composition corresponding to that in the distal tubule. *Urological research* **1999,** *27* (6), 409-416.

45. Irimia, D.; Jose Shirley, J.; Garg, A. S.; Nijland, D. P. A.; van der Heijden, A. E. D. M.; Kramer, H. J. M.; Eral, H. B., Influence of Laser Parameters and Experimental Conditions on Nonphotochemical Laser-Induced Nucleation of Glycine Polymorphs. *Crystal growth & design* **2020**.

46. Penha, F. M. G., A.; Meijlink, J.C.; Ibis, F.; Eral, H.B., Selective Crystallization of d-Mannitol Polymorphs Using Surfactant Self-Assembly. *Crystal growth & design* **2021**.

47. Laval, P.; Salmon, J.-B.; Joanicot, M., A microfluidic device for investigating crystal nucleation kinetics. *Journal of Crystal Growth* **2007,** *303* (2), 622-628.

48. Zheng, B.; Roach, L. S.; Ismagilov, R. F., Screening of protein crystallization conditions on a microfluidic chip using nanoliter-size droplets. *Journal of the American Chemical Society* **2003,** *125* (37), 11170-11171.

49. Nisisako, T.; Torii, T.; Higuchi, T., Droplet formation in a microchannel network. *Lab Chip* **2002,** *2* (1), 24-6.

50. Envisiontec 3D Printer. https://envisiontec.com/3d-printers/desktop-3d-printers/micro-plus-hi-res/ (accessed January 2019).

51. Ai, Y.; Xie, R.; Xiong, J.; Liang, Q., Microfluidics for Biosynthesizing: from Droplets and Vesicles to Artificial Cells. *Small* **2020,** *16* (9), e1903940.

52. Tona, R. M.; McDonald, T. A. O.; Akhavein, N.; Larkin, J. D.; Lai, D., Microfluidic droplet liquid reactors for active pharmaceutical ingredient crystallization by diffusion controlled solvent extraction. *Lab Chip* **2019,** *19* (12), 2127-2137.

53. Li, S.; Ihli, J.; Marchant, W. J.; Zeng, M.; Chen, L.; Wehbe, K.; Cinque, G.; Cespedes, O.; Kapur, N.; Meldrum, F. C., Synchrotron FTIR mapping of mineralization in a microfluidic device. *Lab Chip* **2017,** *17* (9), 1616-1624.

54. Sia, S. K.; Whitesides, G. M., Microfluidic devices fabricated in poly(dimethylsiloxane) for biological studies. *Electrophoresis* **2003,** *24* (21), 3563-3576.

55. An, H. Z., Eral, H.B., Chen, L., Chen, M.B., Doyle, P.S.,, Synthesis of colloidal microgels using oxygen-controlled flow lithography. *Soft Matter* **2014,** *10* (38), 7595-7605.

56. Gupta, A.; Badruddoza, A. Z. M.; Doyle, P. S., A general route for nanoemulsion synthesis using low-energy methods at constant temperature. *Langmuir* **2017,** *33* (28), 7118-7123.

57. Dos Santos, E. C.; Maggioni, G. M.; Mazzotti, M., Statistical Analysis and Nucleation Parameter Estimation from Nucleation Experiments in Flowing Microdroplets. *Cryst Growth and Design* **2019,** *19* (11), 6159-6174.

58. Lange, T.; Charton, S.; Bizien, T.; Testard, F.; Malloggi, F., OSTE+ for in situ SAXS analysis with droplet microfluidic devices. *Lab on a Chip* **2020,** *20* (16), 2990-3000.

59. Hammadi, Z. C., N.; Grossier, R.; Ildefonso, M.; Morin, R.; Veesler, S., Small-volume nucleation. *Comptes Rendus Physique* **2013,** *14* (2-3), 192-198.

60. Kashchiev, D., *Nucleation*. Elsevier: 2000.

61. Li, X.; Liu, K.; Pan, Y.; Zhang, J.; Lv, Q.; Hua, L.; Wang, Z.; Li, J.; Yin, C., Roles of osteopontin gene polymorphism (rs1126616), osteopontin levels in urine and serum, and the risk of urolithiasis: a meta-analysis. *BioMed Research International* **2015,** *2015*, 315043.

62. Qian, J. L., X.; Gao, Z.; Jin, Z., Mixing efficiency and pressure drop analysis of liquid-liquid two phases flow in serpentine microchannels. *Journal of Flow Chemistry* **2019,** *9* (3), 187-197.

63. Ottino, J. M., *The kinematics of mixing: stretching, chaos, and transport*. Cambridge university press: 1989; Vol. 3.

64. Harshe, Y. M. v. E., M.J.; Kleijn, C.R.; Kreutzer, M.T.; Boukany, P.E., Scaling of mixing time for droplets of different sizes traveling through a serpentine microchannel. *Rsc Advances* **2016** *6*(101), 98812-98815.

65. Jiang, S. t. H., J.H. , Crystal nucleation rates from probability distributions of induction times. **2011,** *11* (1), 256-261.

66. Vallapragada, V. V., Inti, G., Ramulu, J.S., A Validated inductively coupled plasma-optical emission spectrometry (ICP-OES) method to estimate free calcium and phosphorus in in vitro phosphate binding study of eliphos tablets. *American Journal of Analytical Chemistry* **2011,** *2* (06), 718.

67. Green, D. R. H.; Cooper, M. J.; German, C. R.; Wilson, P. A., Optimization of an inductively coupled plasma–optical emission spectrometry method for the rapid determination of high-precision Mg/Ca and Sr/Ca in foraminiferal calcite. *Geochemistry, Geophysics, Geosystems* **2003,** *4* (6).

68. Sigma Buffer Reference Center- Biological-buffers. https://www.sigmaaldrich.com/life-science/core-bioreagents/ (accessed May 2019).

69. Ruzin, S. E. Buffers. https://microscopy.berkeley.edu/Resources/instruction/buffers.html (accessed February 2019).

70. Robertson, W. G., Diet and calcium stones. *Mineral and electrolyte metabolism* **1987,** *13* (4), 228-34.

71. Dela Cruz, I. J. C. P., Jem Valerie.;; Alamani, B. G. C., Gerard.;; Myerson, A. S., Influence of Volume on the Nucleation of Model Organic Molecular Crystals through an Induction Time Approach. *Crystal growth and design* **2021,** *21* (5), 2932-2941.

72. Manissorn, J.; Fong-Ngern, K.; Peerapen, P.; Thongboonkerd, V., Systematic evaluation for effects of urine pH on calcium oxalate crystallization, crystal-cell adhesion and internalization into renal tubular cells. *Scientific reports* **2017,** *7* (1), 1-11.

73. Tiselius, H. G., The effect of pH on the urinary inhibition of calcium oxalate crystal growth. *British Journal of Urology* **1981,** *53* (5), 470-4.

74. Wagner, C. A.; Mohebbi, N., Urinary pH and stone formation. *Journal of Nephrology* **2010,** *23 Suppl 16* (16), S165-S169.

75. Carvalho, M., Urinary pH in calcium oxalate stone formers: does it matter? **2018**, 6-7.

76. Addadi, L. W., S., Interactions between acidic proteins and crystals: stereochemical requirements in biomineralization. *Proceedings of the National Academy of Sciences* **1985,** *82* (12), 4110-4114.

77. Hoyer, J. R.; Otvos, L., Jr.; Urge, L., Osteopontin in urinary stone formation. *Annals of the New York Academy of Sciences* **1995,** *760* (1), 257-265.

78. Fisher, L. W.; Torchia, D. A.; Fohr, B.; Young, M. F.; Fedarko, N. S., Flexible structures of SIBLING proteins, bone sialoprotein, and osteopontin. *Biochemical and Biophysical Resrach Communication* **2001,** *280* (2), 460-465.

79. Tsuji, H.; Tohru, U.; Hirotsugu, U.; Masanori, I.; Yuji, H.; Takashi, K., Urinary concentration of osteopontin and association with urinary supersaturation and crystal formation. *International journal of urology* **2007,** *14* (7), 630-634.

80. Keshavarz, L.; Steendam, R. R. E.; Blijlevens, M. A. R.; Pishnamazi, M.; Frawley, P. J., Influence of Impurities on the Solubility, Nucleation, Crystallization, and Compressibility of Paracetamol. *Crystal growth & design* **2019,** *19* (7), 4193-4201.

81. Kacker, R. D., S.; Irimia, D.; Ghatkesar, M.K.; Stankiewicz, A.; Kramer, H.J.M.; Eral, H.B. , Multiparameter Investigation of Laser-Induced Nucleation of Supersaturated Aqueous KCl Solutions. *Crystal growth & design* **2018,** *18* (1), 312-317.

82. Duft, D., Leisner, T., Laboratory evidence for volume-dominated nucleation of ice in supercooled water microdroplets. *Atmospheric Chemistry and Physics* **2004,** *4* (7), 1997-2000.

83. Bretherton, F. P., The motion of long bubbles in tubes. *Journal of Fluid Mechanics* **2006,** *10* (2), 166-188.

84. Roelands, C. P. M.; ter Horst, J. H.; Kramer, H. J. M.; Jansens, P. J., Analysis of nucleation rate measurements in precipitation processes. *Crystal growth & design* **2006,** *6* (6), 1380-1392.

85. Hsu, Y.-C.; Lin, Y.-H.; Shiau, L.-D., Effects of Various Inhibitors on the Nucleation of Calcium Oxalate in Synthetic Urine. *Crystals* **2020,** *10* (4), 333.

86. Lewis, A. S., M.; Kramer, H.J.M.; Van Rosmalen, G., *Industrial crystallization: Fundamentals and applications*. Cambridge University Press: 2015.

87. Kodati, V. R.; Tomasi, G. E.; Turumin, J. L.; Tu, A. T., Raman spectroscopic identification of calcium-oxalate-type kidney stone. *Applied spectroscopy* **1990,** *44* (8), 1408-1411.

88. Frausto-Reyes, C.; Loza-Cornejo, S.; Terrazas, T.; Miranda-Beltran Mde, L.; Aparicio-Fernandez, X.; Lopez-Macias, B. M.; Morales-Martinez, S. E.; Ortiz-Morales, M., Raman spectroscopy study of calcium oxalate extracted from cacti stems. *Applied spectroscopy* **2014,** *68* (11), 1260-1265.

89. Castiglione, V.; Sacre, P. Y.; Cavalier, E.; Hubert, P.; Gadisseur, R.; Ziemons, E., Raman chemical imaging, a new tool in kidney stone structure analysis: Case-study and comparison to Fourier Transform Infrared spectroscopy. *PloS one* **2018,** *13* (8), 1-18.

90. Orlando, M. T. D.; Kuplich, L.; de Souza, D. O.; Belich, H.; Depianti, J. B.; Orlando, C. G. P.; Medeiros, E. F.; da Cruz, P. C. M.; Martinez, L. G.; Corrêa, H. P. S.; Ortiz, R., Study of calcium oxalate monohydrate of kidney stones by X-ray diffraction. *Powder diffraction* **2008,** *23* (S1), S59-S64.

Chapter 4.

Role of hyaluronic acid on the nucleation kinetics of calcium oxalate hydrates in artificial urine quantified with droplet microfluidics

The cover image of thesis was captured under polarized light microscopy in this work

This chapter is based on the work on Role of hyaluronic acid on the nucleation kinetics of calcium oxalate hydrates in artificial urine quantified with droplet microfluidics, Fatma Ibis, Manzoor Alhaji Nuhu, Frederico Marques Penha, Tsun Wang Yu, Antoine E.D.M. van der Heijden, Herman J. M. Kramer, Huseyin Burak Eral. Crystal Growth & Design 2022, DOI: 10.1021/acs.cgd.2c00198.

Abstract

The increasing prevalence of urolithiasis in industrialized societies triggered considerable interest in how various species found in urine regulate the nucleation and growth of common kidney stone constituents such as calcium oxalate (CaOx). Yet, the role macromolecules play in kidney stone formation is often overlooked due to their low concentration in urine. In this study, we investigate the nucleation kinetics of CaOx in artificial urine with droplet-based microfluidic induction time measurements at varying concentrations of oxalate and hyaluronic acid (HA), a polysaccharide commonly found in urine. The formation of two pseudo-polymorphic forms of calcium oxalate crystals, calcium oxalate monohydrate (COM) and calcium oxalate dihydrate (COD), are carefully monitored using polarized light microscopy in induction time experiments. COM and COD nucleated concomitantly in artificial urine yet with distinct kinetics. Our results indicate that higher oxalate concentrations favor the formation of COD, the metastable form, over COM, the most stable form. Moreover, COD is also the fastest nucleating form in droplets under studied conditions. Furthermore, increasing the concentration of HA at fixed calcium and oxalate concentrations favored the nucleation of COM. We observed that in droplets where COM nucleated first, COD was not formed within the experimental time scale. However, in the droplets where COD appeared first, also COM crystals were observed later. We hope our findings shed light on the role macromolecules such as HA plays in dictating the pseudo-polymorphic form of CaOx and guide next generation treatments.

4.1. Introduction

Kidney stones contain inorganic crystals merged with organic constituents.[1-3] Formation of kidney stones, also known as urolithiasis, is attributed to a plethora of underlying patient conditions. The frequency of urolithiasis cases varies based on age, sex, genetics, medical history, fluid intake, diet, physical activity, urine pH and climate.[4-6] It is reported that 7% and 13% of all women and men, respectively, will develop kidney stones in their lifetime.[4, 7-10] Kidney stones can be flushed from the urinary system easily, in case their diameter is less than five millimeters.[11] Stones with sizes above seven millimeters are problematic and generally need a urological intervention.[11, 12] The obvious question that of interest to both medical scientists and engineers is how kidney stones nucleate in urine in nanoscale then grow to millimeter scale. A complete mechanistic understanding of urolithiasis will inform development of more effective treatments.

Analyses of kidney stones from patients showed three main types of crystals, calcium oxalate, calcium phosphate, and uric acid. Regular human urine is supersaturated with respect to calcium oxalate and calcium phosphate.[13, 14] A low urine volume often goes along with high calcium, sodium, oxalate and urate concentrations and can result in a state of supersaturation of the urine solution with respect to the calcium oxalate and calcium phosphate crystals. Such a supersaturated condition is the driving force behind the nucleation of these inorganic crystals and is the first step in the formation of kidney stones.[15] Nearly 80% of stones consist mainly of hydrates of calcium oxalate. Calcium oxalate (CaOx) crystals can be present as calcium oxalate dihydrate (COD, weddellite) or calcium oxalate monohydrate (COM, whewellite), which is the most common and the most stable form at body temperature (37 °C).[1, 16-20] People with a high risk of kidney stones produce urine with a higher supersaturation of CaOx as compared to non-stone formers.[21, 22] Hypercalciuria and hyperoxaluria, high levels of calcium and oxalate in the urine, respectively, are two conditions connected to the high frequency of kidney stones. A patient is considered to exhibit hypercalciuria when the amount of calcium in urine reaches values greater than 300 mg/24 h for men and 250 mg/24 h for women.[2, 7, 23, 24] The daily oxalate excretion can vary between 10-40 mg per 24 h. The amount of oxalate exceeding 40-45 mg per 24 h is considered as hyperoxaluria.[25-27]

Urine also comprises different types of organic and inorganic substances capable of influencing the formation of CaOx crystals (or stones).[28] These compounds might either facilitate – promoters – or prevent – inhibitors – the stone formation. Stone formation is considered inhibited by various inorganic substances such as magnesium, and organic substances like nephrocalcin and other organic macromolecules such as Hyaluronic acid (HA).[29, 30] HA is a negatively charged, high molecular weight polysaccharide found in practically all biological tissues. It is a copolymer of N-acetyl-D-glucosamine and D-glucuronic acid.[31] HA is thought to play an important role in binding cations, especially Ca^{2+}, and retaining water.[32] Moreover, overexpressed HA induced by long-term hydrodynamic stress or the impact of stone fragments is long suspected to play a role in kidney stone formation.

The studies of HA expression and CaOx retention in cells have been reported in the literature. Borges et al. report that kidney cells synthesize HA as a protection mechanism from the presence of CaOx crystals and oxalate ions, which was seen to partially affect crystallization kinetics.[33] Gan et al. found that the expression of HA was increased during wound healing because of cell injury and also this injury contributes to CaOx adhesion to cell surface.[34] Asselman et al. reported that the expression of HA by injured cells seems to play a role in the retention of CaOx crystals.[35] The effect of HA on CaOx stone formation was evaluated in the presence of additives, such as citrate as well as various amino acids, dipeptides and enzymes in solutions with varying pH values.[36, 37] However, an in-vitro study focusing on how HA influences the kinetics of CaOx crystallization, and its pseudo-polymorphic transitions has not been reported in the literature, to the best of our knowledge.

Laboratory experiments in well-mixed vessels are commonly used to investigate CaOx formation in the presence of different additives in water or artificial urine. Xie et al. found that the aggregation of amorphous CaOx complexes induced COM stone formation in water.[38] Gardner et al. observed that sodium pyrophosphate exhibited a strong inhibiting effect on COM growth in water.[39] In other studies that used artificial urine as a solvent, Hsu et al. investigated the nucleation kinetics of CaOx using a batch crystallizer in the presence of various additives in synthetic urine.[40] Cerini et al. worked on nucleation of CaOx in urine with the additive of albumin, leading to COD formation particularly.[41] Polat and Eral characterized CaOx crystals forming in a well-mixed litre size crystallizer in water and artificial urine media. This study reported emergence of a small fraction of COD crystals in the presence of HA only for aqueous medium, where the control samples with no HA nucleated as COM exclusively.[42] To sum up, a large body of in-vitro CaOx crystallization experiments aiming to shed light on the underlying mechanism behind kidney stone formation appeared in literature. These laboratory studies used broad range of techniques ranging from thermodynamic studies focusing on the properties of the resulting crystal form[43-45] to atomic force microscopy studies monitoring growth and nucleation kinetics[46] have been reported.

Recently Lab on a chip technology has been applied to investigate CaOx crystallization. The driver to implement this technology is the ability to explore a broad range of experimental condition with minute amounts of solute, a feature most attractive for difficult to synthesize or isolate macromolecules such as proteins. Lattife et al. used a microfluidic device to understand CaOx formation by mimicking the conditions for CaOx precipitation in collecting duct kidneys.[47] Gombedza et al. investigated effect of melamine on CaOx growth, and they found that melamine induced CaOx formation.[48] In addition to aforementioned advantages, Lab on a chip technology, particularly droplet microfluidics enables researchers to strictly control length scales for momentum, mass transfer, heat transport.[49-55] Furthermore, microfluidics enables rapidly scanning a large phase space with a significant number of identical experiments[51, 56-59]—a feat deemed laborious and time-intensive batch lab-scale approaches.[60, 61] In a microfluidic system, uniformly sized micro-droplets can act as isolated microreactors enabling the realization of a large number of experiments under excellently controlled and identical circumstances. A number of in-vitro studies focusing on promoters and inhibitors have been reported[62-65] yet a with a wide range of artificial urine formulations.[66-69] The multiplexing ability of microfluidics can facilitate a precise parametric search of the broad range of urine formulations reported and test the validity of observations across different formulations. These advantages may benefit researchers looking to quantify nucleation and growth rates[59, 70-72] and compare them to in-vivo kidney stone formation rates. Yet, microfluidics come with its challenges. To mention a few, (i) the micro to nanoliter droplets offer long induction times due to their small volume, (ii) rapidly mixing droplets at aforementioned volumes is dominated by viscous forces and requires dedicated micromixers.

Each human kidney has around 1.2 million nephrons, which are the smallest structural and functional units of this organ. The nephrons comprise a renal corpuscle, proximal tubule, loop of Henle, distal tubule, and collecting duct system[73-75]. About 10 nephrons give birth to one single collecting duct with a diameter of ca. 100 µm.[47, 76] Most kidney stone formation is seen in these collecting ducts. Moreover, the flow rate in these ducts is roughly 10.0 nl/min, showing laminar flow inside the collecting duct.[47, 77] The dimensions of our droplets and the microfluidic device are inspired by the dimensions of the collecting duct in a kidney.

Nucleation kinetics can be quantified with broad list of approaches implemented both in macroscopic vessels[78, 79] as well as microfluidic devices.[80] In a nutshell, the nucleation kinetics in droplet based microfluidic induction time measurements is measured by identifying the emergence of the first crystal in a droplet, also known as induction time, for a large number of droplet (>60) in this study. The cumulative fraction of droplets nucleated at a given time after mixing of reactive species, p(t) is fitted with models discussed in detail in 4.2.2. to extract characteristic induction time and effective nucleation rate. Microfluidic induction time measurement conducted with polarized light microscopy offers unique advantages. Polarized light microscopy leverages an optical property called birefringence in which the refractive index varies depending on the polarization and the propagation direction of light[81, 82]. COM predominantly shows strong birefringence[83], whereas COD is only slightly birefringent[66]. Polarized light microscopy has previously been used to differentiate calcium oxalate pseudo-polymorphic forms.[84, 85] Consequently, implementing polarized light microscopy in microfluidic nucleation kinetics measurement enables us to identify concomitantly nucleating pseudo-polymorphs and transformation kinetics of these pseudo-polymorphs.

In this study, the nucleation kinetics of CaOx at varying concentrations of oxalate and hyaluronic acid (HA) in artificial urine[86] is quantified with a tailor-made microfluidic device providing advective chaotic mixing along with monitoring the polymorphic form of the nucleating crystal as a function of time in each droplet. In a typical microfluidic induction time experiment, prescribed concentrations of aqueous $CaCl_2$ and NaOx solutions are brought in contact, as shown in Figure 4.1.a. The two reacting solutions are dispersed in mineral oil, and the droplets of controlled size are formed in a K-junction in “droplet formation” zone shown in Figure 4.1.b. The content of aqueous droplets is mixed rigorously with serpentine shaped micromixers; complete advective chaotic mixing is achieved in the “mixing zone” of the device[87] (Figure 4.1.b). The well-mixed droplets are stored and monitored in “storage & observation zone”. The nucleation and growth kinetics of two CaOx hydrates, COM and COD under hypercalciuria and hyperoxaluria conditions using a fixed Ca and varying Ox concentration is quantified. In addition, the effect of HA on nucleation behavior has been investigated.

4.2. Materials and Methods

In this section the microfluidic device design and production, the experimental procedure for preparing solution and monitoring crystal induction will be described.

4.2.1. Microfluidic design and device preparation

The microfluidic device is designed to disperse a statistically significant number of well-mixed droplets acting as isolated crystallization vessels and to monitor these droplets as a function of time for nucleation kinetics measurements. The microfluidic device contains tailored micromixers and hydrodynamic traps. Three sections of the microfluidic device, namely, droplet formation, mixing, and storage & observation zones are depicted in (Figure 4.1.b). A more detailed description of the microfluidic chip design and the optimization of the chip geometry is given in Ibis et al.[88] and in C.1 section in Appendix C.

To acquire statistically significant nucleation kinetics measurements of COM and COD under studied conditions, both the induction time – the first moment a crystal is observed – and the pseudo-polymorphic form of the crystal are identified. The experiments are done at thermostated room at 20 °C.

4.2.1.1. Droplet formation and mixing

Two aqueous artificial urine solutions and a continuous phase (oil phase) are brought together in a K shaped junction as shown in Figure 4.1.b for droplet generation. The droplets are stabilized by a fluorinated surfactant (Sphere Fluidics, CAS240119-1) and dispersed in the mixture of hydrofluoroether oil phase (HFE3-Ethoxy-1,1,1,2,3,4,4,5,5,6,6,6-dodecafluoro-2-trifluoromethylhexane, 3M, CAS297730-93-9). In the mixing region, serpentine-shaped bends serve as passive mixers. The serpentine passive mixers ensure complete advective chaotic mixing of droplet contents within seconds, a time scale significantly smaller than measured induction times (Figure 4.1.b). Just after the K-junction, the serpentine shaped passive mixers are used to ensure the mixing of two aqueous streams carrying calcium and oxalate ions. While the droplets move along the serpentine passive mixers, an asymmetric drag force forms asymmetric flow patterns on droplets; consequently, the contents of droplets are mixed in each bend.[89-91]

4.2.1.2. Storage of droplets

The droplets carrying designated concentrations of calcium, oxalate and HA are placed in hydrodynamic traps with dimensions of 200 µm depth, 400 µm width, and 1200 µm length (in Figure 4.1.b). The positional stability of droplets in hydrodynamic traps during the induction time measurements is critical as we want to keep track of every single droplet while capturing images. The hydrodynamic resistance of the narrow necks (180 µm) at the entrance and exit of hydrodynamic traps ensures that the trapped droplets are kept inside the traps throughout the measurement. A small change in the pressure between the reservoir and the microfluidic device will either cause the droplets to recede into the inlet tubes or proceed out of the chambers through the outlet tube. To nullify the pressure head, we keep the reservoir and device at the same height. Furthermore, the droplets should not drift or coalesce due to the evaporation of continuous and dispersed phases through the PDMS or through ports. The proposed microfluidic chip design with built in hydrodynamic traps ensured that the trapped droplets did not drift or merge ensuring statistically significant measurements. The trapped droplets were monitored up to five hours.

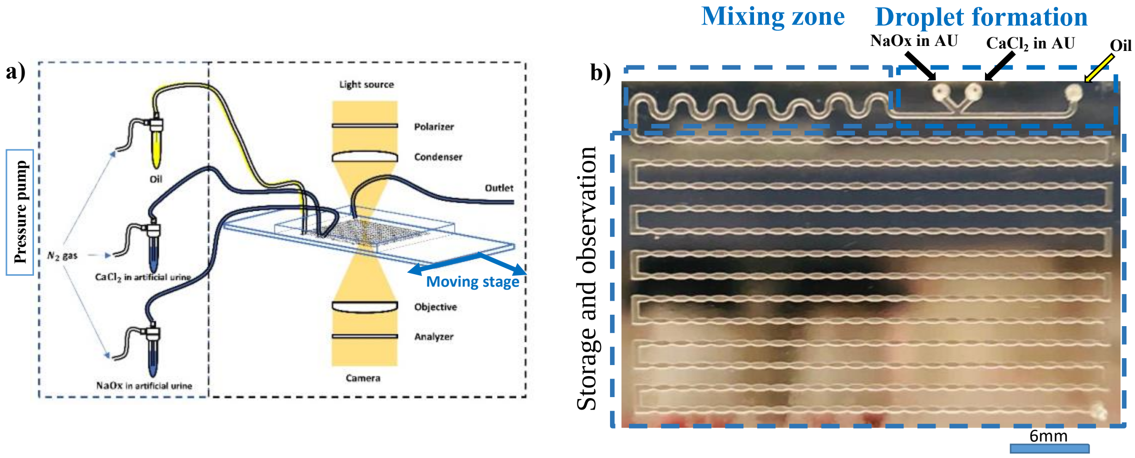

Figure 4.1. Experimental setup with the microfluidic platform: a) Schematic of the experimental set showing the microfluidic system, the motorized stage and the polarized light microscopy optics used during induction time measurements. b) A photo of the complete microfluidic chip showing the "droplet formation", "mixing" along with "storage and observation" zones on the PDMS microfluidic platform, scale bar 6mm.

4.2.1.3. Monitoring crystal induction with polarized light microscopy

Both the induction time and the polymorphic form of the crystals are detected with polarized light microscopy. The basic concept of crossed polarization is as follows: when a polarizer and an analyzer are oriented perpendicularly to each other, the analyzer inhibits the transmission of plane polarized light. This results in a black field of view visible via the microscope eyepiece or camera. A COD crystal is uniaxial, has only one optical axis[92, 93]. Various angles were systematically tested to determine the optimal angle allowing the identification of both COM & COD crystals. The polarized microscopy at 20° degree enabled identification of the COM as bright spots while the COD appears as black spots, as shown in Figure 4.2. In addition to the identification of pseudo-polymorphs with birefringence behavior, the crystal morphology was confirmed by high magnification imaging for a limited number of cases post-experiment. Due to the larger area of the chip and difficulties to focus on crystals inside the microfluidic chip with high magnification objectives, we could not use high magnification during the microfluidic induction time experiments. Consequently, high magnification images could only be acquired after the experiments.

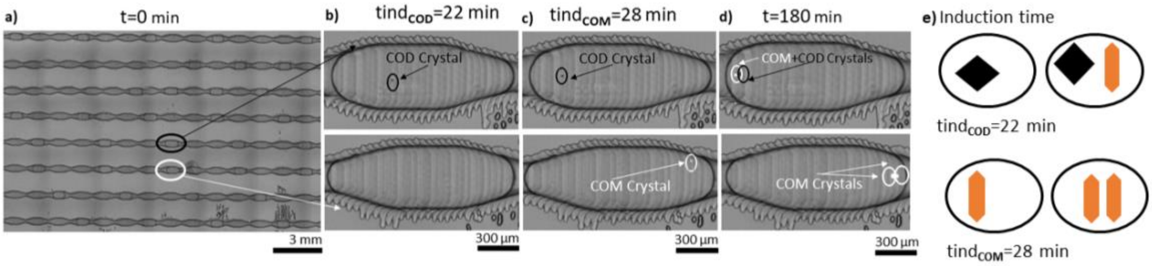

Figure 4.2. Polarized light microscopy images during induction time measurements with 20° angle a) Observed microfluidic chip area showing droplets stored in hydrodynamic traps with 10x objective with 20° angle, scale bar: 3mm, Panels b,c,d show time-lapse images focusing on two droplets. In the droplet on the top panel, COD nucleates first (highlighted with a black circle) followed by nucleation of COM (highlighted with a white circle). In the second droplet, only COM crystals (highlighted with a white circle) nucleate. The images are taken with 10x objective with 20° angle, white crystals: COM, black crystals: COD, scale bar: 300µm. Panel e illustrates two populations of droplets encountered in microfluidic induction time experiments.

4.2.1.4. Microfluidic chip production

The microfluidic chip is produced by a soft lithography.[43, 94-96] The mold used in soft lithography was designed in SolidWorks and then it is printed with a 3D printed (EnvisionTEC Micro Plus Hi-Res - 43x27mm). The mold was then hydrophobized to minimize the PDMS adhesion. Uncured PDMS is poured into the mold and the PDMS is cured for 24 hours as described previously by Ibis et al.[94] The cured PDMS is peeled from the mold to release the top section PDMS section of the chip. The inlet and exit holes are prepared with a biopsy punch. The final transparent PDMS chip shown in Figure 4.1.b is then placed on a glass slide coated with a semi-cured PDMS to ensure that the top PDMS section forms a leakage-free chip.[97]

4.2.2. Microfluidic Induction time measurements

In this section, we describe the microfluidic induction time measurements. Particularly, the procedures for image processing, induction time measurements, analysis of cumulative probability functions and solution preparation are detailed.

4.2.2.1. Image acquisition procedure

When all droplets are stored in the hydrodynamic traps, the pressure pump is stopped. Immediately, an automated macro controlling the microscope stage and image acquisition is triggered. This macro ensures that the whole chip area is imaged and the acquired images are stored in a time-lapse movie. The process for acquisition of images from the whole chip and bringing frames together takes two minutes. Once the first image is acquired, the microscope stage automatically moves to the next position and the imaging process for the second one immediately begins. Figure 4.2.a shows a stitched image. Each image from the five hours recorded video is manually scanned to identify the first crystal emerging in each droplet.

The optical resolution of the microscope lens and camera utilized (one pixel ~ 0.67 µm) determines the spatial resolution for detecting a crystal in a droplet. The time point at which the first crystal is detected is regarded as the induction time of the droplet regardless whether the crystal is a COD or a COM crystal (Figure 4.2.b&c).

4.2.2.2. Procedure for induction time measurements

The droplets are imaged automatically with polarized light microscopy in this case a Nikon Eclipse Ti Series Inverted Microscope fitted with cross polarizers. To observe both morphologies (COM and COD) with an optimal polarized angle chosen. 10x objective is chosen for image acquisition to ensure the resolution required to detect crystals while imaging the. With this lens, half the area of the microfluidic device (middle part of the chip) could be observed. Once the middle of the chip is placed in focus, the capturing of the individual micrographs via the movement of an XY stage is started. After completing capturing of the desired area of the chip, the images are stitched together and stored constructing a time stamp image for induction time measurements. Our experimental and analytical methods allow for a clear distinction between the induction time of COD and COM. Two experiments are done for each concentration and at least 60 droplets are collected totally (Section C.4, Table C.3 in Appendix C).

4.2.2.3. Analysis of induction time measurements to extract effective nucleation rates CaOx pseudo-polymorphs

The composite microscopy images of stored droplets at different time stamps are analyzed manually to identify the fraction of droplets with COM and COD crystals emerging as a function of time. At least 60 droplets are analyzed per experimental condition. The ratio of COM and COD crystals nucleating as a function of time is called the cumulative induction time probability function, p(t). The effective nucleation rate, J, for each polymorph is calculated with a single exponential with delay time, an empirical function shown in Equation 4.1.

$$p(t) = \alpha\left(1 - e^{-JV(t-t_g)}\right) = \alpha\left(1 - e^{-\left(\frac{t-t_g}{\tau}\right)}\right) \qquad \textit{Equation 4.1}$$

Where V is the volume of the liquid phase, J the nucleation rate, t the time and t_g the delay time corresponding to time a nucleus requires to grow to a detectable size dictated by the resolution of the microscope; the parameter τ, the average induction time, is defined as 1/JV. While the p(t) value of CaOx reaches a value of 1 when all droplets have nucleated, the p(t) for COM and COD separately is the fraction of droplets in which either one of these pseudo-polymorphs nucleated first and thus forms a proportion of the p(t) value of CaOx. Consequently, the p(t) value of the separate hydrates does not necessarily reach the maximum value of 1. The parameter Alpha (α) is a factor that accounts for the fact that two populations are observed in microfluidic induction time measurements, where p(t) of COM and p(t) of COD are based on the fraction of droplets in which a COM or a COD is nucleated first respectively and represents the value of p(t) at infinite time. The values for the COM and COD populations add up to a value of 1.

In microfluidic induction time measurements, the growth rate (G_{exp}) for a given experimental condition can be extracted by dividing the lower detection limit (D_{det}) of the crystals in the microscope by the t_g value; $G_{exp} = D_{det}/t_g$. However, it should be noted that these growth rates are averaged over all crystals contributing. To calculate G_{exp}, D_{det} is estimated as 4 pixels (1 pixel ≈ 0.67 microns) corresponding to 2.7 microns based on the resolution of the microscope images used to detect the crystals. It should be noted that these growth rates are averaged over all crystals contributing.

4.2.2.4. Preparation of artificial urine

In our work, the composition of artificial urine selected is based on Streit et al.[86], shown in Table 4.1, with adjustments to calcium and oxalate levels and HA additive when necessary. To prepare artificial urine, each chemical (see Table 4.1) is weighed and dissolved in ultrapure water (ELGA PURELAB, Resistivity:18.2 MΩ·cm at 23.6 °C). The glassware used and microfluidic chip are rigorously rinsed with ultrapure water to minimize contamination. To accurately control the concentration of calcium and oxalate in the droplets, designated calcium and oxalate concentrations are reached by dissolving known amounts of either $CaCl_2$ or NaOx in separate artificial urine solutions. The prepared solutions are rigorously mixed using an ultrasonicator (Branson 2510, Ultrasonic Cleaner) for 20 min at 20°C. After dissolution, both solutions carrying calcium and oxalate ions are filtered (Whatman, 0.45 µm pore diameter filters). Mixing calcium and oxalate solutions, droplet formation and filling the entire channel with droplets is completed in ten seconds. The moment image acquisition starts right after the channel is filled is registered as t=0. As the time required for droplet formation, mixing and filling operations take significantly less time than the image acquisition of two minutes, the major experimental uncertainty comes from image acquisition. Any induction time below two minutes cannot be accurately measured with the proposed setup.

Table 4.1. The ingredients of artificial urine.[86] *The measured pH value of artificial urine is 5.57.*

Compounds	**Molarity [mM]**	**Source**
Sodium chloride (NaCl)	90	Fluka
Potassium Chloride (KCl)	42	Emsure
Ammonium chloride (NH_4Cl)	20	Sigma-Aldrich
Creatinine ($C_4H_7N_3O$)	7	Sigma-Aldrich
Urea (CH_4N_2O)	300	Emprove
Tri sodium citrate ($Na_3C_6H_5O_7$)	2	Emprove
Magnesium sulphate heptahydrate ($MgSO_4.7H_2O$)	2	Sigma-Aldrich
Sodium sulphate ($NaSO_4$)	13	Sigma-Aldrich
Sodium phosphate monobasic (NaH_2PO_4)	16	Sigma-Aldrich

4.2.2.5. Solution preparation for microfluidic experiments

Calcium chloride ($CaCl_2$) and sodium oxalate (NaOx) are dissolved in 50 ml of basis artificial urine (AU) separately into two beakers. These two solutions are connected to two different microfluidic device inlets. When the pressure pump is started, solutions move from the inlet and merge into a droplet. Once the streams merge, the concentration of $CaCl_2$ and NaOx solutions fed to inlets are diluted by a factor of two, reaching the desired concentrations inside the droplets. The final concentration of $CaCl_2$ is 6.0 mM and NaOx are 0.5, 0.85 and 1.2 mM in the droplets.

For inhibition experiments with HA, the droplets contain the concentrations as 6 mM of $CaCl_2$ and 0.85 mM of NaOx with three different HA solutions: 0.035, 0.25, 0.50 mg/ml in artificial urine. HA is dissolved in an aqueous stream containing NaOx and sent to the device just from one inlet to protect the reaction with the calcium ion. To avoid contamination, all solutions for microfluidic induction time experiments are made fresh for each experiment.

4.3. Result and discussion

Microfluidic nucleation induction time measurements were used to quantify the effect of varying levels of added oxalate or HA on the kinetics of CaOx nucleation from solution.

The ability to determine both the time and the type of pseudo-polymorphic form of the nucleating crystals resulted in interesting observations. In all experiments, two distinct droplet populations, as illustrated in Figure 4.2.d&e, were found that were representative for all our observations. In the upper droplet population in Figure 4.2.d&e, COD crystals nucleated first, followed by COM crystal nucleation at later times. In a second population given in the second row of Figure 4.2.d&e, a COM crystal nucleated first, and only COM crystals nucleated at later time points.

Initially, we focus on the effect of increasing oxalate concentration at fixed calcium concentration in the artificial urine in Figure 4.3. Figure 4.3.a gives the nucleation probability distribution function of all CaOx crystals irrespective of the crystal hydrate form (either COD or COM). As expected, the p(t) curves observed in Figure 4.3.a reach unity faster at higher oxalate concentrations. This behavior can be attributed to increased supersaturation in the samples with the higher oxalate concentrations. Using polarized light microscopy, we were able to quantify the nucleation kinetics of COM and COD independently. Figure 4.3.b reports the ratio of droplets in which COD nucleated first, while Figure 4.3.c shows the ratio of droplets in which a COM crystal was first observed as a function of time.

The fraction of the droplets in which COD nucleated first seems to be proportional to the added oxalate concentration (or the supersaturation), as shown in Figure 4.3.b. On the other hand, in the second population where a COM crystal nucleated first, no COD but only COM crystals were observed at later time points. Moreover, the ratio of the droplets in which COM nucleated first was inversely proportional to the added oxalate concentration (and thus the supersaturation) as shown in Figure 4.3.c. In addition, the p(t) curves of COM display lower slopes and larger delay times compared to the p(t) curves of COD nucleation.

The nucleation probability curves for CaOx, irrespective of the type of hydrate, as well as for the probability distribution of droplets in which COD or COM nucleation occurred first respectively, were fitted with an exponential function with delay time (Equation 4.1), as shown in Figure 4.3. The fitting procedure provided estimates of delay time (t_g), induction time (τ) and nucleation rate (J), as well as the proportion of each pseudo-polymorph formed (α), given in Table 4.2. The fits are also shown in Figure 4.3 as dashed curves, with the confidence intervals of the fits shown as the shaded area around the fits.

Comparison of the fit parameters for COD and COM for all the oxalate concentrations studied, reveals that the induction times for COD are always shorter than those for COM nucleation, which means that the nucleation rate of COD is higher than that of COM under identical conditions. Looking at the α values in Table 4.2, i.e., the values at which the fraction of droplets saturate in Figure 4.3.b&c, we can also conclude that at high oxalate concentrations, the formation of the metastable form COD is favored over the stable form COM. At lower oxalate concentrations COM nucleation appears to be dominant (the alpha value for COM increases from 0.46 to 0.70 with decreasing oxalate concentrations), see Figure 4.3.c and Table 4.2.

Daudon et al.[98], year observed that once the Ca:Ox molar ratio is between 5 and 14, a mixture of COM and COD crystals is present in urine. It is noteworthy to mention that the frequency of finding COM is much higher than that of COD in patient's kidney stones.[4] Interpretation of this medical observation in the context of our results might indicate that nucleation of CaOx in patient urine may be occurring at a lower Ca:Ox ratio. Yet this interpretation operates under the assumption that the artificial urine used in this study is a very good representative of patient urine. In reality, the patient urine contains more complex macromolecules, dead cells, and its composition varies constantly in response to environmental changes.

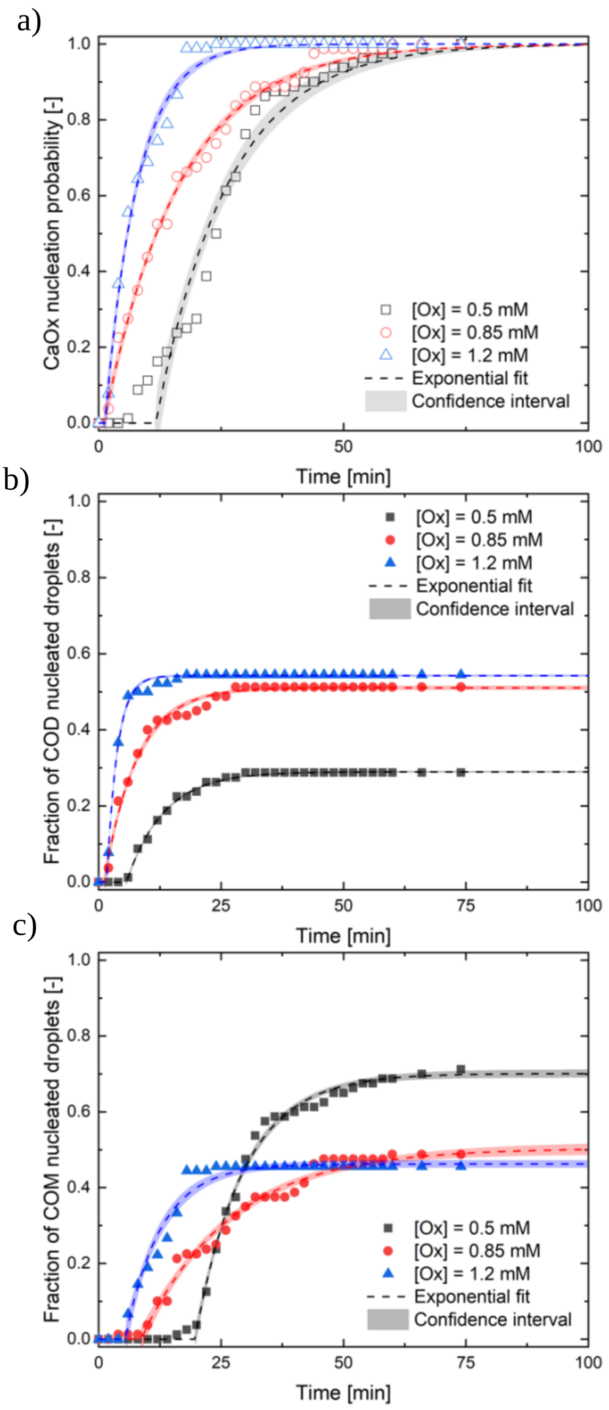

Figure 4.3. Cumulative induction time probability curves, p(t) for (a) COD and COM, (b) only COD crystals and (c) only COM crystals where the $C_2O_4^{2-}$ *concentrations, [Ox] is varied at fixed* Ca^{2+} *concentration of 6.0 mM in artificial urine. The p(t) curves are fitted with the exponential function with delay time (Equation 4.1).*

It is noteworthy that a solution mediated transformation from COD to COM could also explain the dominant COM content in Kidney stones. In our experiments, a transformation from COD into COM was not detected in the droplets, possibly due to limitations on experiments duration, the inability to observe the crystal structure at the nanoscale, or the molar ratios of Ca:Ox used.[99]

Table 4.2 also shows that the values for the tg decrease with the increase in the oxalate concentration for both of COD and COM crystals indicating an increase in the growth rate. For all oxalate concentrations, the delay time, t_g, for COD is shorter than for COM indicating that the COD grows faster to a detectable size (see section 4.2.1.3). Interestingly, increasing the oxalate concentration has a stronger effect on the growth rate of COM than of COD crystals. An increasing oxalate concentration from $0.5\cdot10^{-3}$ M to $1.2\cdot10^{-3}$ M caused a decrease in the molar ratio of Ca:Ox and increased the COD nucleation rate. Remarkably the COD nucleation rate increases more than a factor of three from $2.66\cdot10^{10}$ m^{-3} min^{-1} to $9.57\cdot10^{10}$ $m^{-3}min^{-1}$, whereas for COM the nucleation rates only slightly increase from $2.05\cdot10^{10}$ $m^{-3}min^{-1}$ to $2.77\cdot10^{10}$ $m^{-3}min^{-1}$ (see Table 4.2).

Figure 4.4.a shows the effect of the addition of different concentrations of HA on the p(t) curves of CaOx irrespective of the crystal hydrate form. The fraction of the droplets of where COD and COM nucleated first are given in Figure 4.4.b&c, respectively. The dashed lines are fits to Equation 4.1 with 95% confidence intervals shown as shaded regions. The numerical values of the determined α, τ, J, and t_g values are given in Table 4.3 together with the confidence intervals and the statistical errors of the estimated values. At first glance, the p(t) curves in Figure 4.4.a do not reveal a pronounced trend. Both the p(t) curves for HA concentration of 0.035 mg/ml and the control as well as the curves for HA concentrations of 0.25 and 0.50 mg/ml appear to overlap. Increasing the concentration of HA at fixed calcium and oxalate concentrations appears to slightly increase CaOx nucleation kinetics, yet the effect of HA on nucleation kinetics appears to be small.

Table 4.2. The fitted parameters, standard errors and the error statistics of the fits from a single exponential model with a delay time of COD and COM for the different added oxalate concentrations. MSE stands for mean squared error.

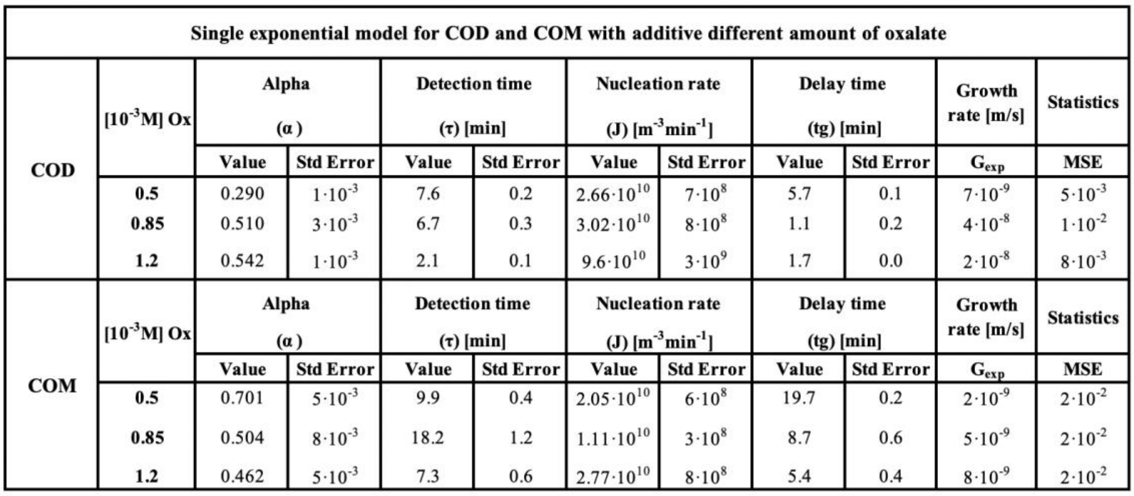

Single exponential model for COD and COM with additive different amount of oxalate											
COD	**[10^{-3}M] Ox**	**Alpha (α)**		**Detection time (τ) [min]**		**Nucleation rate (J) [$m^{-3}min^{-1}$]**		**Delay time (tg) [min]**		**Growth rate [m/s]**	**Statistics**
		Value	**Std Error**	**Value**	**Std Error**	**Value**	**Std Error**	**Value**	**Std Error**	**G_{exp}**	**MSE**
	0.5	0.290	$1\cdot10^{-3}$	7.6	0.2	$2.66\cdot10^{10}$	$7\cdot10^{8}$	5.7	0.1	$7\cdot10^{-9}$	$5\cdot10^{-3}$
	0.85	0.510	$3\cdot10^{-3}$	6.7	0.3	$3.02\cdot10^{10}$	$8\cdot10^{8}$	1.1	0.2	$4\cdot10^{-8}$	$1\cdot10^{-2}$
	1.2	0.542	$1\cdot10^{-3}$	2.1	0.1	$9.6\cdot10^{10}$	$3\cdot10^{9}$	1.7	0.0	$2\cdot10^{-8}$	$8\cdot10^{-3}$
COM	**[10^{-3}M] Ox**	**Alpha (α)**		**Detection time (τ) [min]**		**Nucleation rate (J) [$m^{-3}min^{-1}$]**		**Delay time (tg) [min]**		**Growth rate [m/s]**	**Statistics**
		Value	**Std Error**	**Value**	**Std Error**	**Value**	**Std Error**	**Value**	**Std Error**	**G_{exp}**	**MSE**
	0.5	0.701	$5\cdot10^{-3}$	9.9	0.4	$2.05\cdot10^{10}$	$6\cdot10^{8}$	19.7	0.2	$2\cdot10^{-9}$	$2\cdot10^{-2}$
	0.85	0.504	$8\cdot10^{-3}$	18.2	1.2	$1.11\cdot10^{10}$	$3\cdot10^{8}$	8.7	0.6	$5\cdot10^{-9}$	$2\cdot10^{-2}$
	1.2	0.462	$5\cdot10^{-3}$	7.3	0.6	$2.77\cdot10^{10}$	$8\cdot10^{8}$	5.4	0.4	$8\cdot10^{-9}$	$2\cdot10^{-2}$

A different picture emerges when the fraction of droplets where COD and COM nucleated first are plotted. The fraction of the droplets in which COD nucleated first decreases with increasing HA concentrations evident from the values for COD in Table 4.3 and the plateaus observed at later times (>50 minutes) in Figure 4.4.b. Furthermore, Figure 4.4.c shows the opposite trend for the droplets in which a COM crystal nucleated first. The fraction of the droplets nucleated as COM increased (alpha increased from 0.50 to 0.78) with increasing HA concentrations. This followed the trend also observed for the nucleation rate for COM, which increased under the same conditions (see Table 4.3). In contrast with the droplets where COD nucleated first, which showed only a marginally increase in the nucleation rate. Looking at the results of the control experiment (without HA) and those of 0.035 mg/ml HA, the delay times for COD decrease from 1.09 to 0.22 and for COM from 8.65 to 3.88. The lowest HA concentration, 0.035 mg/ml HA, does not show any effect on nucleation rates and alpha values for any of the pseudo-polymorphs, whilst growth rate visibly increases in both cases.

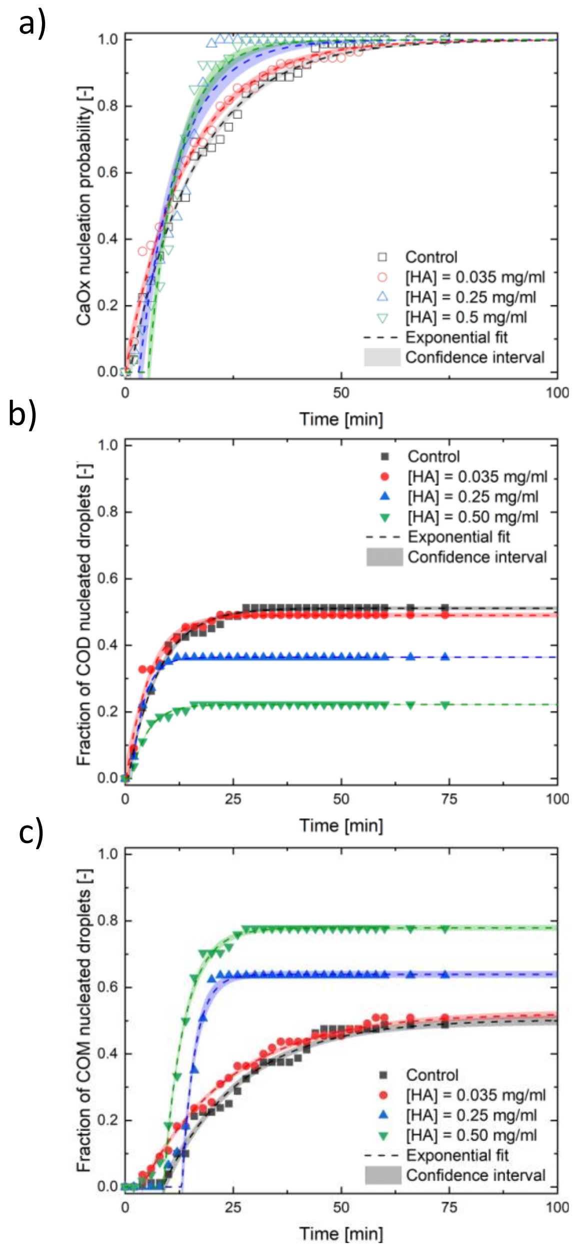

Figure 4.4. Cumulative induction time probability curves, p(t) for (a) COD and COM, (b) only COD crystals and (c) only COM crystals where HA concentrations at fixed Ca^{2+} and $C_2O_4^{2-}$ concentrations in artificial urine fitted with the exponential function with delay time (Equation 4.1). Added molar concentrations of HA are 0.035, 0.25, 0.50 mg/ml at fixed Ca^{2+}; 6.0 mM and $C_2O_4^{2-}$; 0.85 mM in artificial urine.

The highest nucleation rate of COD, $7.10 \cdot 10^{10}$ $m^{-3}min^{-1}$ and the highest nucleation rate of COM, $6.85 \cdot 10^{10}$ $m^{-3}min^{-1}$ are observed at 0.25 mg/ml HA. Delay times increase for COD from 0.22 to 1.44 and for COM from 3.88 to 13.12 (compared to 0.035 mg/ml HA). Surprisingly the increment from 0.25 mg/ml HA to 0.5 mg/ml HA decreases the nucleation rate for both COD and COM, i.e., from $3.0\cdot10^{10}$ to $5.14\cdot10^{10}$ $m^{-3}min^{-1}$ and from $1.1\cdot10^{10}$ to $4.22\cdot10^{10}$ $m^{-3}min^{-1}$ respectively, while the delay time decreases implying an increase in growth rate when increasing the HA concentration from 0.25 mg/ml to 0.5 mg/ml (See Table 4.3).

Table 4.3. The fitted parameters, standard errors and the error statistics of the fits from a single exponential model with a delay time of COD and COM for the different amount of added HA. MSE stands for mean squared error.

Single exponential model of COD and COM for the different amount HA conditions											
	mg/ml HA	**Alpha (α)**		**Detection time (τ) [min]**		**Nucleation rate (J) [$m^{-3}min^{-1}$]**		**Delay time (tg) [min]**		**Growth rate [m/s]**	**Statistics**
		Value	**Std Error**	**Value**	**Std Error**	**Value**	**Std Error**	**Value**	**Std Error**	**G_{exp}**	**MSE**
COD	**Control**	0.510	$2\cdot10^{-3}$	6.7	0.3	$3.02\cdot10^{10}$	$8\cdot10^{8}$	1.1	0.2	$4\cdot10^{-8}$	$1\cdot10^{-2}$
	0.035	0.490	$3\cdot10^{-3}$	5.5	0.5	$3.7\cdot10^{10}$	$1\cdot10^{9}$	0.2	0.4	$2\cdot10^{-7}$	$2\cdot10^{-2}$
	0.25	0.3643	$7\cdot10^{-4}$	2.9	0.1	$7.1\cdot10^{10}$	$2\cdot10^{9}$	1.44	0.05	$3\cdot10^{-8}$	$4\cdot10^{-3}$
	0.50	0.2221	$6\cdot10^{-4}$	3.9	0.1	$5.1\cdot10^{10}$	$1\cdot10^{9}$	1.2	0.1	$3\cdot10^{-8}$	$4\cdot10^{-3}$
	mg/ml HA	**Alpha (α)**		**Detection time (τ) [min]**		**Nucleation rate J [$m^{-3}min^{-1}$]**		**Delay time (tg) [min]**		**Growth rate [m/s]**	**Statistics**
		Value	**Std Error**	**Value**	**Std Error**	**Value**	**Std Error**	**Value**	**Std Error**	**G_{exp}**	**MSE**
COM	**Control**	0.504	$8\cdot10^{-3}$	18.1	1.2	$1.11\cdot10^{10}$	$3\cdot10^{8}$	8.7	0.6	$8\cdot10^{-8}$	$2\cdot10^{-2}$
	0.035	0.523	$5\cdot10^{-3}$	20.4	0.8	$9.91\cdot10^{9}$	$3\cdot10^{8}$	3.9	0.4	$1\cdot10^{-7}$	$1\cdot10^{-2}$
	0.25	0.639	$5\cdot10^{-3}$	3.0	0.3	$6.85\cdot10^{10}$	$2\cdot10^{9}$	13.1	0.2	$2\cdot10^{-7}$	$2\cdot10^{-2}$
	0.50	0.779	$4\cdot10^{-3}$	4.8	0.3	$4.22\cdot10^{10}$	$1\cdot10^{9}$	8.9	0.2	$2\cdot10^{-7}$	$2\cdot10^{-2}$

At this point, it is informative to compare our results with liter scale experiments presented by Polat and Eral despite significantly different scales and protocols involved.[42] Polat and Eral characterized CaOx crystals forming post-reaction with methods such as scanning electron microscopy, atomic force microscopy, thermogravimetric analysis.[42] In this bulk crystallization study conducted in a well-stirred, liter size vessel at Ca:Ox ratio of 20, COD crystals were sparsely observed with increasing HA concentration in water where the control experiments conducted without HA produced only COM. Identical experiments conducted in artificial urine produced only COD with and without HA. In other words, all crystals nucleated as COD both in control and in the presence of HA in artificial urine. At a first sight, one may think that results of Polat and Eral[42] contradict reported results in this study. A closer inspection reveals that the bulk experiments of Polat and Eral were conducted at significantly higher Ca:Ox ratio with rigorous mixing at 37 °C using slightly different procedures.

We suspect that the combined effect of high Ca:Ox ratio in experiments of Polat and Eral[42] and mixing might collectively induce higher rate of COD nucleation in liter size vessel overshadowing the potential emerge of COM in all artificial urine samples due to presence of HA. Mixing triggered secondary nucleation influencing resulting polymorphic form has been previously reported in l-Glutamic Acid.[100] Moreover, our control experiments conducted at Ca:Ox ratio of 7 produced almost 50/50 mixture COM and COD hence the change in COM & COD nucleation rates upon addition of HA can be easily detected unlike experiments of Polat and Eral[42] where the control experiment produced 100% COD. In addition, our experimental procedure focusses on the first crystal nucleating in the droplet while Polat and Eral report collected crystals after precipitation. Another significant difference is the larger surface area to volume ratio in microfluidic droplets compared to bulk experiments. The larger surface per volume ration might enhance the heterogeneous nucleation rate of COM in the presence of HA in our study. Surfactants at air-liquid interfaces have been previously reported to influence phase transitions.[61] This comparison points out that the rate of COM and COD nucleation as well as their transition may be influenced by stirring and the presence of interfaces hence opening new alleys of investigation while emphasizing the relevance of our study at a length scale comparable to collecting duct.

Lamontagne et al. worked on the interaction of HA and CaOx stone by focusing on the adhesion of the HA.[36] These authors report that HA binds at the [100] face of COM crystals. They found that saturated calcium oxalate condition leads to interactions between the HA and COM.[36] Daudon et al. observed that COM crystals were predominant in urine once the molar ratio of Ca:Ox was less than 5.[98, 99] These reports in literature may help rationalizing the trend shown in Figure 4.4 where increasing HA concentration results in a higher fraction of the COM droplets. As HA binds to COM crystals[36] and COM crystals are predominantly observed for a molar ratio of Ca:Ox less than 5[98], it can be expected that increasing HA concentration may result in a smaller molar ratio of Ca:Ox. Because COM crystals are closely connected with kidney stone illness, the discovery of additive-mediated suppression of COM but preferred COD production is noteworthy.[101-103] Since COD is less frequently linked to epithelial cells at the tip of the renal papilla than COM, it is, consequently, easier to remove from the organ with the urine.[101] Therefore, by controlling the pseudo-polymorph of CaOx stone with an additive like HA, favoring COM upon COD, might be helpful for the medical treatment in preventing the adhesion to cells and further growth of renal calculi.

4.4. Conclusion

We present the nucleation kinetics of CaOx at varying concentrations of oxalate and HA in artificial urine using droplet microfluidics technology. The unique contribution of this work is the ability to extract the kinetics of individual CaOx hydrates as COD and COM instead of considering them as a CaOx crystal. An increase in the oxalate concentration raises the fraction of COD nucleation and slows down the growth of COD crystals in artificial urine. We observed that in droplets where COD nucleated COM emerged at later times. However, when COM nucleated first, COD was not formed within the experimental time scale. An antagonistic effect of HA on the fraction of COD and COM was observed. HA promoted COM formation while inhibiting COD. Moreover, it is observed that COD nucleation rate is always higher than COM nucleation rate for each experimental condition studied. This study highlights the underlying mechanism of the effect of HA on CaOx stone formation. The results can be helpful for the medical treatment by bringing understanding of COD over COM using HA as an additive.

4.5. References

1. Khan, S. R.; Pearle, M. S.; Robertson, W. G.; Gambaro, G.; Canales, B. K.; Doizi, S.; Traxer, O.; Tiselius, H.-G., Kidney stones. *Nature Reviews Disease Primers* **2016,** *2* (1), 1-23.

2. Bushinsky, D. A.; Asplin, J. R.; Grynpas, M. D.; Evan, A. P.; Parker, W. R.; Alexander, K. M.; Coe, F. L., Calcium oxalate stone formation in genetic hypercalciuric stone-forming rats. *Kidney international* **2002,** *61* (3), 975-987.

3. Uribarri, J.; Oh, M. S.; Carroll, H. J., The first kidney stone. *Annals of internal medicine* **1989,** *111* (12), 1006-1009.

4. Alelign, T.; Petros, B., Kidney stone disease: an update on current concepts. *Advances in urology* **2018,** *2018*.

5. Ridley, J. W., *Fundamentals of the Study of Urine and Body Fluids*. Springer: 2018.

6. Bono, M. J.; Reygaert, W. C., Urinary tract infection. In *StatPearls [Internet]*, StatPearls Publishing: 2018.

7. Worcester, E. M.; Coe, F. L., Nephrolithiasis. *Primary Care: Clinics in Office Practice* **2008,** *35* (2), 369-391.

8. Scales Jr, C. D.; Smith, A. C.; Hanley, J. M.; Saigal, C. S.; Project, U. D. i. A., Prevalence of kidney stones in the United States. *European urology* **2012,** *62* (1), 160-165.

9. Long, L.; Park, S., Update on nephrolithiasis management. *Minerva urologica e nefrologica= The Italian journal of urology and nephrology* **2007,** *59* (3), 317-325.

10. Rule, A. D.; Lieske, J. C.; Li, X.; Melton, L. J.; Krambeck, A. E.; Bergstralh, E. J., The ROKS nomogram for predicting a second symptomatic stone episode. *Journal of the American Society of Nephrology* **2014,** *25* (12), 2878-2886.

11. Evan, A. P., Physiopathology and etiology of stone formation in the kidney and the urinary tract. *Pediatric Nephrology* **2010,** *25* (5), 831-841.

12. Takazawa, R.; Kitayama, S.; Tsujii, T., Appropriate kidney stone size for ureteroscopic lithotripsy: When to switch to a percutaneous approach. *World journal of nephrology* **2015,** *4* (1), 111.

13. Finlayson, B., Physicochemical aspects of urolithiasis. *Kidney international* **1978,** *13* (5), 344-360.

14. Grases, F.; Villacampa, A.; Söhnel, O.; Königsberger, E.; May, P., Phosphate Composition of Precipitates from Urine-like Liquors. *Crystal Research and Technology* **1997,** *32* (5), 707-715.

15. Ratkalkar, V. N.; Kleinman, J. G., Mechanisms of stone formation. *Clinical reviews in bone and mineral metabolism* **2011,** *9* (3-4), 187-197.

16. Moe, O. W., Kidney stones: pathophysiology and medical management. *The lancet* **2006,** *367* (9507), 333-344.

17. Hanno, P. M.; Guzzo, T. J.; Malkowicz, S. B.; Wein, A. J., *Penn clinical manual of urology*. Elsevier Health Sciences: 2007.

18. Ogawa, Y.; Miyazato, T.; Hatano, T., Oxalate and urinary stones. *World journal of surgery* **2000,** *24* (10), 1154-1159.

19. Robertson, W.; Peacock, M., The cause of idiopathic calcium stone disease: hypercalciuria or hyperoxaluria? *Nephron* **1980,** *26* (3), 105-110.

20. Bhasin, B.; Ürekli, H. M.; Atta, M. G., Primary and secondary hyperoxaluria: Understanding the enigma. *World journal of nephrology* **2015,** *4* (2), 235.

21. Parks, J. H.; Coward, M.; Coe, F. L., Correspondence between stone composition and urine supersaturation in nephrolithiasis. *Kidney international* **1997,** *51* (3), 894-900.

22. WEBER, D. V.; COE, F. L.; PARKS, J. H.; DUNN, M. S. L.; TEMBE, V., Urinary saturation measurements in calcium nephrolithiasis. *Annals of internal medicine* **1979,** *90* (2), 180-184.

23. Kok, D. J.; Papapoulos, S. E., Physicochemical considerations in the development and prevention of calcium oxalate urolithiasis. *Bone and mineral* **1993,** *20* (1), 1-15.

24. Favus, M. J.; Zeytinoglu, M.; Coe, F. L., Idiopathic hypercalciuria and nephrolithiasis. In *Vitamin D*, Elsevier: 2018; pp 485-505.

25. Asplin, J. R., Hyperoxaluric calcium nephrolithiasis. *Endocrinology and Metabolism Clinics* **2002,** *31* (4), 927-949.

26. Milliner, D. S., The primary hyperoxalurias: an algorithm for diagnosis. *American journal of nephrology* **2005,** *25* (2), 154-160.

27. Robijn, S.; Hoppe, B.; Vervaet, B. A.; D'haese, P. C.; Verhulst, A., Hyperoxaluria: a gut–kidney axis? *Kidney international* **2011,** *80* (11), 1146-1158.

28. Basavaraj, D. R.; Biyani, C. S.; Browning, A. J.; Cartledge, J. J., The role of urinary kidney stone inhibitors and promoters in the pathogenesis of calcium containing renal stones. *EAU-EBU update series* **2007,** *5* (3), 126-136.

29. Aggarwal, K. P.; Narula, S.; Kakkar, M.; Tandon, C., Nephrolithiasis: molecular mechanism of renal stone formation and the critical role played by modulators. *BioMed research international* **2013,** *2013*.

30. Verhulst, A.; Asselman, M.; Persy, V. P.; Schepers, M. S.; Helbert, M. F.; Verkoelen, C. F.; De Broe, M. E., Crystal retention capacity of cells in the human nephron: involvement of CD44 and its ligands hyaluronic acid and osteopontin in the transition of a crystal binding-into a nonadherent epithelium. *Journal of the American Society of Nephrology* **2003,** *14* (1), 107-115.

31. Horkay, F.; Basser, P. J.; Londono, D. J.; Hecht, A.-M.; Geissler, E., Ions in hyaluronic acid solutions. *The Journal of chemical physics* **2009,** *131* (18), 184902.

32. Verkoelen, C. F., Crystal retention in renal stone disease: a crucial role for the glycosaminoglycan hyaluronan? *Journal of the American Society of Nephrology* **2006,** *17* (6), 1673-1687.

33. Borges, F. T.; Michelacci, Y. M.; Aguiar, J. A.; Dalboni, M. A.; Garófalo, A. S.; Schor, N., Characterization of glycosaminoglycans in tubular epithelial cells: calcium oxalate and oxalate ions effects. *Kidney international* **2005,** *68* (4), 1630-1642.

34. Gan, Q.-Z.; Sun, X.-Y.; Bhadja, P.; Yao, X.-Q.; Ouyang, J.-M., Reinjury risk of nano-calcium oxalate monohydrate and calcium oxalate dihydrate crystals on injured renal epithelial cells: aggravation of crystal adhesion and aggregation. *International journal of nanomedicine* **2016,** *11*, 2839.

35. Asselman, M.; Verhulst, A.; De Broe, M. E.; Verkoelen, C. F., Calcium oxalate crystal adherence to hyaluronan-, osteopontin-, and CD44-expressing injured/regenerating tubular epithelial cells in rat kidneys. *Journal of the American Society of Nephrology* **2003,** *14* (12), 3155-3166.

36. Lamontagne, C. A.; Plante, G. E.; Grandbois, M., Characterization of hyaluronic acid interaction with calcium oxalate crystals: implication of crystals faces, pH and citrate. *Journal of Molecular Recognition* **2011,** *24* (4), 733-740.

37. Verkoelen, C. F.; van Der Boom, B. G.; Romijn, J. C., Identification of hyaluronan as a crystal-binding molecule at the surface of migrating and proliferating MDCK cells. *Kidney international* **2000,** *58* (3), 1045-1054.

38. Xie, B.; Halter, T. J.; Borah, B. M.; Nancollas, G. H., Aggregation of calcium phosphate and oxalate phases in the formation of renal stones. *Crystal Growth & Design* **2015,** *15* (1), 204-211.

39. Gardner, G. L.; Nancollas, G. H., Kinetics of dissolution of calcium oxalate monohydrate. *The Journal of Physical Chemistry* **1975,** *79* (24), 2597-2600.

40. Hsu, Y.-C.; Lin, Y.-H.; Shiau, L.-D., Effects of various inhibitors on the nucleation of calcium oxalate in synthetic urine. *Crystals* **2020,** *10* (4), 333.

41. Cerini, C.; Geider, S.; Dussol, B.; Hennequin, C.; Daudon, M.; Veesler, S.; Nitsche, S.; Boistelle, R.; Berthézène, P.; Dupuy, P., Nucleation of calcium oxalate crystals by albumin: involvement in the prevention of stone formation. *Kidney international* **1999,** *55* (5), 1776-1786.

42. Polat, S.; Eral, H. B., Elucidating the role of hyaluronic acid in the structure and morphology of calcium oxalate crystals. *Advanced Powder Technology* **2021,** *32* (10), 3650-3659.

43. Pleeging, R.; Ibis, F.; Fan, D.; Sasso, L.; Eral, H.; Staufer, U., Polymer nano manufacturing of a biomimicking surface for kidney stone crystallization studies. *Micro and Nano Engineering* **2021,** *13*, 100094.

44. Schuurmans, C. C.; Abbadessa, A.; Bengtson, M. A.; Pletikapic, G.; Eral, H. B.; Koenderink, G.; Masereeuw, R.; Hennink, W. E.; Vermonden, T., Complex coacervation-based loading and tunable release of a cationic protein from monodisperse glycosaminoglycan microgels. *Soft Matter* **2018,** *14* (30), 6327-6341.

45. Akbarieh, M.; Tawashi, R., Calcium oxalate crystal growth in the presence of mucin. *Scanning microscopy* **1991,** *5* (4), 12.

46. Farmanesh, S.; Ramamoorthy, S.; Chung, J.; Asplin, J. R.; Karande, P.; Rimer, J. D., Specificity of growth inhibitors and their cooperative effects in calcium oxalate monohydrate crystallization. *Journal of the American Chemical Society* **2014,** *136* (1), 367-376.

47. Laffite, G.; Leroy, C.; Bonhomme, C.; Bonhomme-Coury, L.; Letavernier, E.; Daudon, M.; Frochot, V.; Haymann, J.-P.; Rouzière, S.; Lucas, I. T., Calcium oxalate precipitation by diffusion using laminar microfluidics: toward a biomimetic model of pathological microcalcifications. *Lab on a Chip* **2016,** *16* (7), 1157-1160.

48. Gombedza, F.; Evans, S.; Shin, S.; Boadi, E. A.; Zhang, Q.; Nie, Z.; Bandyopadhyay, B. C., Melamine promotes calcium crystal formation in three-dimensional microfluidic device. *Scientific reports* **2019,** *9* (1), 1-14.

49. Laval, P.; Salmon, J.-B.; Joanicot, M. J. J. o. C. G., A microfluidic device for investigating crystal nucleation kinetics. **2007,** *303* (2), 622-628.

50. Zheng, B.; Roach, L. S.; Ismagilov, R. F. J. J. o. t. A. c. s., Screening of protein crystallization conditions on a microfluidic chip using nanoliter-size droplets. **2003,** *125* (37), 11170-11171.

51. Nisisako, T.; Torii, T.; Higuchi, T., Droplet formation in a microchannel network. *Lab on a Chip* **2002,** *2* (1), 24-26.

52. 3D Printer. https://envisiontec.com/3d-printers/desktop-3d-printers/micro-plus-hi-res/.

53. Ai, Y.; Xie, R.; Xiong, J.; Liang, Q., Microfluidics for Biosynthesizing: from Droplets and Vesicles to Artificial Cells. *Small* **2019**, 1903940.

54. Tona, R.; McDonald, T. A.; Akhavein, N.; Larkin, J. D.; Lai, D., Microfluidic Droplet Liquid Reactors for Active Pharmaceutical Ingredient Crystallization by Diffusion Controlled Solvent Extraction. *Lab on a Chip* **2019**.

55. Li, S.; Ihli, J.; Marchant, W. J.; Zeng, M.; Chen, L.; Wehbe, K.; Cinque, G.; Cespedes, O.; Kapur, N.; Meldrum, F. C. J. L. o. a. C., Synchrotron FTIR mapping of mineralization in a microfluidic device. **2017,** *17* (9), 1616-1624.

56. Sia, S. K.; Whitesides, G. M., Microfluidic devices fabricated in poly (dimethylsiloxane) for biological studies. *Electrophoresis* **2003,** *24* (21), 3563-3576.

57. An, H. Z.; Eral, H. B.; Chen, L.; Chen, M. B.; Doyle, P. S. J. S. M., Synthesis of colloidal microgels using oxygen-controlled flow lithography. **2014,** *10* (38), 7595-7605.

58. Gupta, A.; Badruddoza, A. Z. M.; Doyle, P. S. J. L., A general route for nanoemulsion synthesis using low-energy methods at constant temperature. **2017,** *33* (28), 7118-7123.

59. Baroud, C. N.; Gallaire, F.; Dangla, R., Dynamics of microfluidic droplets. *Lab on a Chip* **2010,** *10* (16), 2032-2045.

60. Irimia, D.; Jose Shirley, J.; Garg, A. S.; Nijland, D. P.; van der Heijden, A. E.; Kramer, H. J.; Eral, H. B., Influence of Laser Parameters and Experimental Conditions on Nonphotochemical Laser-Induced Nucleation of Glycine Polymorphs. *Crystal Growth & Design* **2020**.

61. Penha, F. M.; Gopalan, A.; Meijlink, J. C.; Ibis, F.; Eral, H. B., Selective Crystallization of d-Mannitol Polymorphs Using Surfactant Self-Assembly. *Crystal growth & design* **2021**.

62. Fleisch, H., Inhibitors and promoters of stone formation. *Kidney international* **1978,** *13* (5), 361-371.

63. Downey, J.; Nickel, J.; Clapham, L.; McLean, R., In vitro inhibition of struvite crystal growth by acetohydroxamic acid. *British journal of urology* **1992,** *70* (4), 355-359.

64. Jones, D. S.; Djokic, J.; Gorman, S. P., Characterization and optimization of experimental variables within a reproducible bladder encrustation model and in vitro evaluation of the efficacy of urease inhibitors for the prevention of medical device-related encrustation. *Journal of Biomedical Materials Research Part B: Applied Biomaterials: An Official Journal of The Society for Biomaterials, The Japanese Society for Biomaterials, and The Australian Society for Biomaterials and the Korean Society for Biomaterials* **2006,** *76* (1), 1-7.

65. Chow, K.; Dixon, J.; Gilpin, S.; Kavanagh, J. P.; Rao, P. N., Citrate inhibits growth of residual fragments in an in vitro model of calcium oxalate renal stones. *Kidney international* **2004,** *65* (5), 1724-1730.

66. Brown, P.; Ackermann, D.; Finlayson, B., Calcium oxalate dihydrate (weddellite) precipitation. *Journal of Crystal Growth* **1989,** *98* (3), 285-292.

67. Chutipongtanate, S.; Thongboonkerd, V., Systematic comparisons of artificial urine formulas for in vitro cellular study. *Analytical biochemistry* **2010,** *402* (1), 110-112.

68. Lee, S. C.; Hutchinson, J.; Inn, K.; Thein, M., An intercomparison study of 237Np determination in artificial urine samples. *Health physics* **1995,** *68* (3), 350-358.

69. Ipe, D. S.; Horton, E.; Ulett, G. C., The basics of bacteriuria: strategies of microbes for persistence in urine. *Frontiers in cellular and infection microbiology* **2016,** *6*, 14.

70. dos Santos, E. C. n.; Maggioni, G. M.; Mazzotti, M. J. C. G.; Design, Statistical Analysis and Nucleation Parameter Estimation from Nucleation Experiments in Flowing Microdroplets. **2019,** *19* (11), 6159-6174.

71. Lange, T.; Charton, S.; Bizien, T.; Testard, F.; Malloggi, F. J. L. o. a. C., OSTE+ for in situ SAXS analysis with droplet microfluidic devices. **2020,** *20* (16), 2990-3000.

72. Ferreira, J.; Castro, F.; Rocha, F.; Kuhn, S., Protein crystallization in a droplet-based microfluidic device: Hydrodynamic analysis and study of the phase behaviour. *Chemical Engineering Science* **2018,** *191*, 232-244.

73. Ogobuiro, I.; Tuma, F., Physiology, renal. **2019**.

74. Smith, H. W., *The kidney: structure and function in health and disease*. Oxford University Press, USA: 1951; Vol. 1.

75. Koeppen, B.; Stanton, B., Regulation of body fluid osmolality: Regulation of water balance. *Renal Physiology. Philadelphia: Elsevier* **2013**, 79.

76. Vize, P. D.; Woolf, A. S.; Bard, J. B., *The kidney: from normal development to congenital disease*. Elsevier: 2003.

77. Tabeling, P., *Introduction to microfluidics*. OUP Oxford: 2005.

78. Jiang, S.; ter Horst, J. H., Crystal nucleation rates from probability distributions of induction times. *Crystal growth & design* **2011,** *11* (1), 256-261.

79. Kacker, R.; Dhingra, S.; Irimia, D.; Ghatkesar, M. K.; Stankiewicz, A.; Kramer, H. J.; Eral, H. B., Multiparameter Investigation of laser-induced nucleation of supersaturated aqueous KCl solutions. *Crystal growth & design* **2018,** *18* (1), 312-317.

80. Devos, C.; Van Gerven, T.; Kuhn, S., A Review of Experimental Methods for Nucleation Rate Determination in Large-Volume Batch and Microfluidic Crystallization. *Crystal growth & design* **2021,** *21* (4), 2541-2565.

81. Hood, K., Comprehensive Polymer Science and Supplements. Elsevier London: 1996.

82. Tudose, A. E.; Dumitrascu, I.; Dumitrascu, L.; Dimitriu, D. G.; Dorohoi, D. O. In *Methods for determining the linear birefringence of some inorganic uniax crystals*, AIP Conference Proceedings, AIP Publishing LLC: 2017; p 030007.

83. Luqman, A.; Stanifer, J.; Siddiqui, O. M. A.; Naseer, A.; Wall, B. M., Calcium oxalate monohydrate crystals: a clue to ethylene glycol poisoning. *The American journal of the medical sciences* **2011,** *341* (4), 338.

84. Isotalo, P. A.; Lloyd, R. V., Presence of birefringent crystals is useful in distinguishing thyroid from parathyroid gland tissues. *The American journal of surgical pathology* **2002,** *26* (6), 813-814.

85. Tornos, C.; Silva, E.; El-Naggar, A.; Pritzker, K., Calcium oxalate crystals in breast biopsies. *Am J Surg Pathol* **1990,** *14* (10), 961-968.

86. Streit, J.; Tran-Ho, L.-C.; Königsberger, E., Solubility of the three calcium oxalate hydrates in sodium chloride solutionsand urine-like liquors. *Monatshefte für Chemie/Chemical Monthly* **1998,** *129* (12), 1225-1236.

87. Harshe, Y. M.; van Eijk, M. J.; Kleijn, C. R.; Kreutzer, M. T.; Boukany, P. E. J. R. A., Scaling of mixing time for droplets of different sizes traveling through a serpentine microchannel. **2016,** *6* (101), 98812-98815.

88. Ibis, F.; Yu, T. W.; Penha, F. M.; Ganguly, D.; Nuhu, M. A.; van der Heijden, A. E. D. M.; Kramer, H. J. M.; Eral, H. B., Nucleation kinetics of calcium oxalate monohydrate as a function of pH, magnesium, and osteopontin concentration quantified with droplet microfluidics. *Biomicrofluidics* **2021,** *15* (064103 (2021)), 1-17.

89. Qian, J.-y., Chen, Min-rui, Wu, Zan, Jin, Zhi-jiang, Sunden, Bengt, Effects of a Dynamic Injection Flow Rate on Slug Generation in a Cross-Junction Square Microchannel. *Processes* **2019,** *7* (10), 765.

90. Ottino, J. M., *The kinematics of mixing: stretching, chaos, and transport*. Cambridge university press: 1989; Vol. 3.

91. Harshe, Y. M., van Eijk, M.J., Kleijn, C.R., Kreutzer, M.T., Boukany, P.E., Scaling of mixing time for droplets of different sizes traveling through a serpentine microchannel. *Rsc Advances* **2016,** *6* (101), 98812-98815.

92. Frey-Wyssling, A., Crystallography of the two hydrates of crystalline calcium oxalate in plants. *American Journal of Botany* **1981,** *68* (1), 130-141.

93. Stoiber, R. E., Morse, S.A., Uniaxial Crystal Optics. In *Crystal Identification with the Polarizing Microscope*, Springer: 1994; pp 116-122.

94. Fatma Ibis, T. W. Y., Frederico Marques Penha, Debadrita Ganguly, Manzoor Alhaji Nuhu, Antoine E.D.M. van der Heijden, Herman J. M. Kramer, Huseyin Burak Eral, Nucleation kinetic…. **2021**.

95. An, H. Z.; Eral, H. B.; Chen, L.; Chen, M. B.; Doyle, P. S., Synthesis of colloidal microgels using oxygen-controlled flow lithography. *Soft Matter* **2014,** *10* (38), 7595-7605.

96. Georgiev, R. N.; Toscano, S. O.; Uspal, W. E.; Bet, B.; Samin, S.; van Roij, R.; Eral, H. B., Universal motion of mirror-symmetric microparticles in confined Stokes flow. *Proceedings of the National Academy of Sciences* **2020,** *117* (36), 21865-21872.

97. Rehor, I.; van Vreeswijk, S.; Vermonden, T.; Hennink, W. E.; Kegel, W. K.; Eral, H. B., Biodegradable microparticles for simultaneous detection of counterfeit and deteriorated edible products. *Small* **2017,** *13* (39), 1701804.

98. Daudon, M.; Letavernier, E.; Frochot, V.; Haymann, J.-P.; Bazin, D.; Jungers, P., Respective influence of calcium and oxalate urine concentration on the formation of calcium oxalate monohydrate or dihydrate crystals. *Comptes Rendus Chimie* **2016,** *19* (11-12), 1504-1513.

99. Zhang, J.; Wang, L.; Zhang, W.; Putnis, C. V., Role of Hyperoxaluria/Hypercalciuria in Controlling the Hydrate Phase Selection of Pathological Calcium Oxalate Mineralization. *Crystal Growth & Design* **2020,** *21* (1), 683-691.

100. Ferrari, E. S.; Davey, R. J., Solution-mediated transformation of α to β L-glutamic acid: Rate enhancement due to secondary nucleation. *Crystal growth & design* **2004,** *4* (5), 1061-1068.

101. Wesson, J. A.; Worcester, E. M.; Wiessner, J. H.; Mandel, N. S.; Kleinman, J. G., Control of calcium oxalate crystal structure and cell adherence by urinary macromolecules. *Kidney international* **1998,** *53* (4), 952-957.

102. Chen, Z.-H.; Ren, X.-L.; Zhou, H.-H.; Li, X.-D., The role of hyaluronic acid in biomineralization. *Frontiers of Materials Science* **2012,** *6* (4), 283-296.

103. WESSON, J. A.; WORCESTER, E. M.; KLEINMAN, J. G., Role of anionic proteins in kidney stone formation: interaction between model anionic polypeptides and calcium oxalate crystals. *The Journal of Urology* **2000,** *163* (4), 1343-1348.

Chapter 5.

Crystal growth of calcium oxalate monohydrate and calcium oxalate dihydrate under laminar flow

This chapter is based on Crystal Growth of Calcium Oxalate Monohydrate and Calcium Oxalate Dihydrate under laminar flow, Fatma Ibis, René Smeets, Jiali Wang, Priya Dhand, Majid Mohamedhoesein, Frederico Marques Penha, Johan Grievink, Antoine E.D.M. van der Heijden, Herman J. M. Kramer and Huseyin Burak Eral. To be submitted to Crystal Growth & Design.

Abstract

Calcium oxalate (CaOx) crystallization was studied in a microfluidic device, simulating flow conditions the geometry of kidney collecting ducts under laminar relevant for kidney stone formation. In a typical microfluidic experiment, two reactive solutions with designated concentrations of calcium (Ca) and oxalate (Ox) ions were brought in contact in a microfluidic channel to create laminar co-flow of streams. During the translation in the channel diffusion takes place between the two streams across the channel width, resulting in CaOx crystals along the mixing front. We studied the growth of these crystals as a function of three main parameters; fluid flow rate, the molar ratio of Ca:Ox and additive of Osteopontin (OPN) as an organic inhibitor in artificial urine. Three different flow velocities (U), 0.015, 0.035, 0.075 m/s were used at a molar ratio of Ca:Ox=7.5. Following, four molar ratios of Ca:Ox between 5 to 10 were tested at fixed velocity (U=0.035 m/s). Lastly, three additive OPN concentrations $1.6 \cdot 10^{-8}$ mol/m^3 , $6 \cdot 10^{-8}$ mol/m^3 and $8.4 \cdot 10^{-8}$ mol/m^3 were evaluated. The velocity did not affect growth rate of CaOx. The altering molar ratio of Ca:Ox has high impact on growth rate and it caused to see two pseudo-polymorphic forms of CaOx crystals; calcium oxalate monohydrate (COM) and calcium oxalate dihydrate (COD) together. Additive of lowest OPN decreased growth rate of COD, while higher concentrations of OPN successfully inhibited crystal forms in artificial urine. COD was seen in all main conditions, COM was seen in experiments whose has only molar ratio value of five and six. We rationalized our results using finite element simulations supported with solution chemistry modelling.

5.1. Introduction

Kidney stone is a serious health problem affecting around 12% of the world's population.[1-3] Each human kidney has around 1.2 million nephrons comprised of hollow tubes assembled of a single cell layer. It is the smallest structural and functional unit of this organ. The nephrons comprise a renal corpuscle, proximal tubule, loop of Henle, distal tubule, and collecting duct system.[4-6] Around 10 nephrons give birth to one single collecting duct whose diameter is about 100 μm.[7, 8] Urine flow rate is roughly 10.0 nl/min, showing laminar flow inside the collecting duct.[7, 9] Overall, the urinary system filters around 150-180 L/day fluid from renal blood flow to keep essential compounds in the blood while removing toxins, ions, and metabolic waste products. 1.5 liters of urine are extracted after absorbing water through diffusion and active transport per day.[10, 11] If excess solute reaches supersaturated condition in the kidney, mineralization, i.e., crystallization of a so-called kidney stone, happens. A plethora of physicochemical phenomena such as nucleation, crystal growth, and aggregation, adhesion play a role the formation of kidney stones, making the kidney stone formation a multiscale challenging process to understand.[1-3, 10, 11]

The main compound of kidney stones is calcium oxalate (CaOx), which comprises approximately 80% of kidney stones.[12-14] CaOx occurs in nature as monohydrate (whewellite, $CaC_2O_4.H_2O$, COM), dihydrate (weddellite, $CaC_2O_4.2H_2O$, COD) and trihydrate (caoxite, $CaC_2O_4.3H_2O$, COT), each specified by the amount of H_2O in their crystalline structure.[15-17] Calcium oxalate monohydrate (COM) is the most commonly seen and the most stable form with very low water solubility; $1.24 \cdot 10^{-4}$ M in ultrapure water at 37 °C.[15, 18-20]

Kidney stones are known to occur when urine volume is low and calcium, salt, oxalate, and urate concentrations are high.[21] When compared to non-stone formers, people who have a high risk of kidney stones produce urine with a higher supersaturation in terms of CaOx. The exceeded concentrations of oxalate and calcium in urine causes hypercalciuria and hyperoxaluria. In the condition referred to as hypercalciuria, high levels of Ca can be found in the urine, reaching values greater than 300 mg/24 h for men and 250 mg/24 h for women.[15, 22-24] When the oxalate concentrations are abnormally high – the normal daily oxalate excretion can vary between 10-40 mg per 24 h –and exceed 40-45 mg per 24 h, the condition is considered as hyperoxaluria.[25-27]

Numerous compounds may either increase (promote) or hinder (inhibit) the production of stones in the human body. Various inorganic and organic compounds such as citrate, magnesium, and nephrocalcin, urine prothrombin fragment-1, and osteopontin (OPN) are thought to inhibit stone formation.[28] OPN is a single-chain protein with a molecular weight of roughly 33 kDa, existent in urine in amounts greater than 100 nM.[29] Studies in the literature show that OPN hinders crystal formation and alters the shape of CaOx crystals.[29-31]

In vitro studies focusing on CaOx stone formation in water or artificial urine with different additives have been extensively reported.[32-36] Researchers have examined the effect of the molar ratio[33], potential inhibitors[32, 36], and quality of water on kidney stone formation.[35] To control momentum, heat and mass transfer in micro-scale, the microfluidic approaches have been proposed and successfully implemented for various subjects, including kidney stone formation.[37-43]

We report on growth of calcium oxalate (CaOx) crystals in a microchannel, mimicking the geometry of kidney collecting ducts, under flow conditions relevant for kidney stone formation. In this device two solutions carrying Ca^{2+} and Ox^{2-} ions respectively are brought in contact with each other in the microchannel and time lapse images of the emerging crystals are analyzed to extract the type of pseudo-polymorph that nucleated and growth rates of the crystals. The growth of the nucleated COM or COD crystals were studied as a function of the fluid flow rate, the molar ratio of Ca:Ox and the inhibitor concentration in artificial urine.

To rationalize qualitatively the crystals growing in microfluidic, the velocity and the concentration of a diffusing species under laminar flow in the microchannel were calculated via COMSOL Multiphysics. The values from COMSOL were used in solution chemistry modeling, Joint Expert Speciation System (JESS) software to find supersaturation values (see details in Appendix D).

5.2. Materials and Methods

5.2.1. Microfluidic device

A microfluidic device is used to mimic the collecting duct in the nephron, a polydimethylsiloxane (PDMS, (C2H6OSi)n, The DOW Chemical Company). The microchannel has a length of 1500 µm, a depth of 45 µm and a width of 295 µm.

A mixture of PDMS and curing agents at a 7:1 (w/w) ratio is arranged to prepare the chips. The mixture is stirred with a spatula until it is filled with air bubbles and becomes cloudy. Upon mixing, the mixture is centrifuged (Universal 320 R, Hettich Zentrifugen) at 7400 rpm and 20^{o}C for 15 minutes to remove air bubbles. Then, the transparent PDMS mixture is put onto the silicon wafer produced by lithography in a cleanroom. To prepare the microfluidic devices with PDMS using the silicon wafer, the wafer (Figure D.1 in Appendix D) needs to be coated with a thin hydrophobic layer of trichloro (1H,1H,2H,2H-perfluorooctyl) silane (Sigma-Aldrich, CAS 78560-45-9) to make the peeling process easier. The silicon wafer is put upside down in a desiccator with 10µl of trichlorosilane and connected to a vacuum pump. The pressure is lowered to 100 mbar and kept it for two hours. After this process, the trichlorosilane-coated silicon wafer can be used four times, then the hydrophobization protocol needs to be repeated to use wafer again. The wafer filled with the PDMS mixture is later placed in a desiccator connected to a vacuum pump for 1 hour to eliminate the air bubbles created during the pouring step. The wafer is placed in a 65^{o}C oven overnight to ensure that the PDMS is completely cured.

Spin coating (Polos 300, Netherlands) is used to make a closed microfluidic system. A 0.5 ml aliquot of a mixture of 10:1 ratio of PDMS and curing agent is poured onto the glass slide (VWR international), and the glass slide is fully covered with a thin layer of PDMS at 4500 rpm for one minute. The spin-coated glass slide is placed in a 90°C oven for 20 minutes. The solid PDMS bonds to a glass slide to make a closed microfluidic device. This device is left in the oven at 65°C overnight to cure thoroughly. Three holes are punched in the PDMS chip after the curing step is completed: two for inlets and one for an outlet. The resulting microfluidic device is displayed in Figure D.1 in Appendix D.

5.2.2. Experimental set-up

In the microfluidic device, the growth of CaOx crystals, either COM or COD, was induced by sending in two inlets containing $CaCl_2$ and NaOx aqueous solutions in artificial urine (see subsection 5.2.5.). The reservoirs with filtered (0.45 µm filter) $CaCl_2$ and NaOx aqueous solutions were connected to a pressure pump (Fluigent, MFCS- EZ) and to the microfluidic device with capillary tubing (Warner Instruments, 0.28 mm inner diameter)(in

Figure 5.1.a). The applied pressure difference 25-85 dPa resulted in flow velocities of 0.015-0.075m/s, respectively. Crystal growth was monitored using an automated optical microscope (Nikon Ti Series Inverted Microscope). Each image was saved every 4 seconds during 30 minutes. The crystal growth was shown at t=0, t=7.3 and t=30 minutes for sample AU4 in Figure 5.1.b.

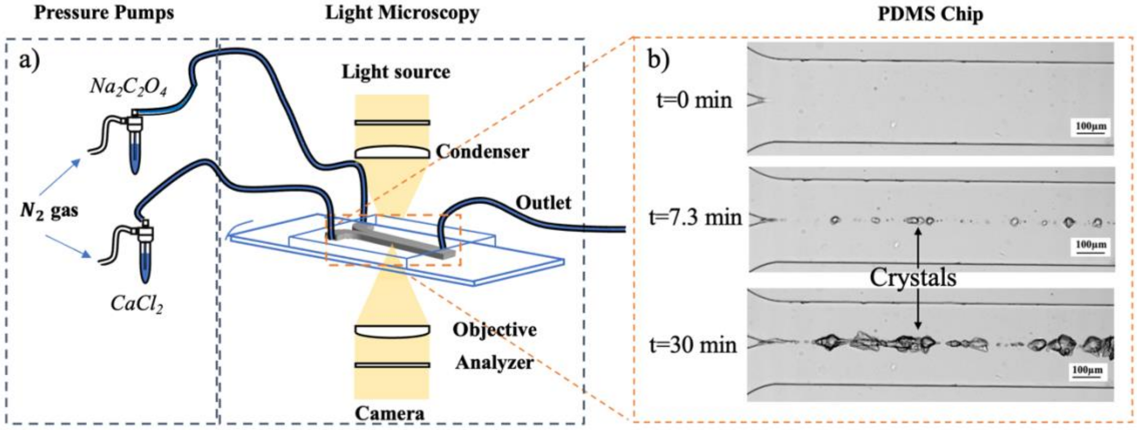

Figure 5.1. The experiment setup with microfluidic platform including the computer, pressure pump, and microscope with the chip. The $CaCl_2$ and $Na_2C_2O_4$ were dissolved in artificial urine. The images were taken from the same experiment condition (sample AU4) at three time lapses as 0, 7.3 and 30 minutes after first crystal emerged.

5.2.3. COMSOL model and JESS software

To rationalize crystal growth of calcium oxalate qualitatively, the concentration gradients established due to diffusion under laminar flow in the microchannel were calculated using COMSOL Multiphysics (see Appendix D). Following, these precursors concentrations values in artificial urine were used to find supersaturation values using Joint Expert Speciation System (JESS) software (see Appendix D) The calculated concentrations (1.2, 1.6, 2.0 and 2.4 mol/m^3 NaOx at fixed 12 mol/m^3 $CaCl_2$), profiles in the channel were then used to calculate the relative supersaturation (σ) (Table 5.2) profiles in artificial urine values using Joint Expert Speciation System (JESS) software (see Appendix D). Since OPN and creatinine were not included in JESS' database, these compounds were not considered in the supersaturation profiles estimation.

5.2.4. Calculation method for Crystal Growth Rate

The image analysis tool Cellprofiler was used to analyze crystal areas using crystal images from the experiments. This detection was repeated for consecutive images with a 40 seconds time step during 7.3 minutes from the first crystal emerged. This period for the growth rate calculation was chosen to avoid contamination of growth rate calculations by agglomeration in the channels which was observed later in the experiments. An equivalent spherical shape was considered to calculate the radial growth of CaOx crystals. The measured 2D surface area (A) of about five crystals was converted to average radial size ($\mathrm{r_{avg}}$) using Equation 5.1.

$$\mathrm{r_{avg}} = \sqrt{(\mathrm{A}/\pi)} \qquad \textit{Equation 5.1}$$

To calculate the average growth rate ($\dot{r}_{\mathrm{avg}}$) a linear fit was used regarding average radial size ($\mathrm{r_{avg}}$) and time step. In total, 11 data points are considered for each experiment condition during 7.3 minutes observation time.

5.2.5. Solution preparation with artificial urine

Three main conditions, varying velocity, the molar ratio of Ca:Ox, in other words, supersaturation (σ) (in Table 5.2), and addition of OPN (Table 5.3) were tested with nine different experiment conditions in artificial urine (AU) at room temperature. The recipe for the ingredients of AU was based on the work of Streit et al.[44] (see Table 5.1).

Table 5.1. Ingredients of artificial urine[44]

Compounds	Molarity [mM]	Source
Sodium chloride (NaCl)	90	Fluka
Potassium Chloride (KCl)	42	Emsure
Ammonium chloride (NH_4Cl)	20	Sigma-Aldrich
Creatinine ($C_4H_7N_3O$)	7	Sigma-Aldrich
Urea (CH_4N_2O)	300	Emprove
Tri sodium citrate ($Na_3C_6H_5O_7$)	2	Emprove
Magnesium sulphate heptahydrate ($MgSO_4.7H_2O$)	2	Sigma-Aldrich
Sodium sulphate ($NaSO_4$)	13	Sigma-Aldrich
Sodium phosphate monobasic (NaH_2PO_4)	16	Sigma-Aldrich

The compounds (from Table 5.1) were dissolved in ultrapure water by an ultrasonic sonicator to prepare artificial urine. $CaCl_2$ and NaOx were added and dissolved in separate beakers just before the experiments and sent via two different inlets. $CaCl_2$ and NaOx concentrations in fresh artificial urine as seen in Table 5.2.

Table 5.2. Overview of added concentrations of $CaCl_2$ and NaOx in artificial urine. Supersaturation (σ) values are determined using the JESS model. The latter these values are only accurate until the point of nucleation.

Sample Name	Molar ratio Ca:Ox	Added $CaCl_2$ [mol/m^3]	Added NaOx [mol/m^3]	U [m/s]	σ values for COM from JESS	σ values for COD from JESS
AU1	7.5	12	1.6	0.015	46.8	17.8
AU2				0.035		
AU3				0.075		
AU4	5		2.4	0.035	67.6	26.3
AU5	6		2		57.5	21.9
AU6	10		1.2		34.7	13.5

Table 5.3. Overview of added concentrations of OPN in artificial urine at 12 mol/m^3 $CaCl_2$ and 1.6 mol/m^3 NaOx with U=0.015 m/s. OPN is dissolved in NaOx inlet and meet $CaCl_2$ in the channel.

Sample Name	Molar ratio Ca:Ox	Added $CaCl_2$ [mol/m^3]	Added NaOx [mol/m^3]	Added OPN [10^{-8} mol/m^3]
AU7	7.5	12	1.6	2.4
AU8				6
AU9				8.4

5.3. Result and discussion

The growth rates ($\dot{r}_{avg}$) of both COM & COD crystals in artificial urine were determined under nine different conditions (Figure 5.4-Figure 5.6). The concentrations of calcium and oxalate were estimated as a function of the position in the channel using COMSOL. The supersaturation profiles (σ) of COM and COD were calculated using these concentration profiles in JESS. As the crystals settled in the channel, the growth rates of individual crystals could be determined.

The values of the crystal growth obtained from the images in the different experiments are summarized in Table 5.4. The table also includes the values for the flow velocity, the concentration of OPN, and the estimated relative supersaturation (σ) using JESS in the different experiments, along with the determined values of the average growth rates at t=7.3 min.

5.3.1. Verification of the COMSOL Model and JESS software with Microscopic Experiments

Calcium and oxalate concentration profiles through the channel were simulated using COMSOL (see Figure 5.2.a & b). Because fixed crystals were observed on the bottom channel wall, c- and σ-profiles are shown at the channel bottom ($z = 0\mu m$) at various length positions. The profiles at different positions change and become smoother further down the length of the channel due to diffusion of the Ca and Ox ions (see Appendix D). Figure 5.2.c shows the concentration profile at x=800 μm for the ratio of Ca:Ox=7.5 (sample AU3). Figure 5.2.d as the logarithmic supersaturation σ-profiles for COM and COD vs channel width at x = 800 μm (length) and z = 0 μm (depth) (The detailed COMSOL method is in Section D.2 and D.3 in Appendix D). The maximum supersaturation values for COM and COD are seen at y =∼ 2 μm (width) as $log(\sigma_{\mathrm{COM}})$ = 1.67 (σ = 46.8) and $log(\sigma_{\mathrm{COD}})$ = 1.25 (σ = 17.8).

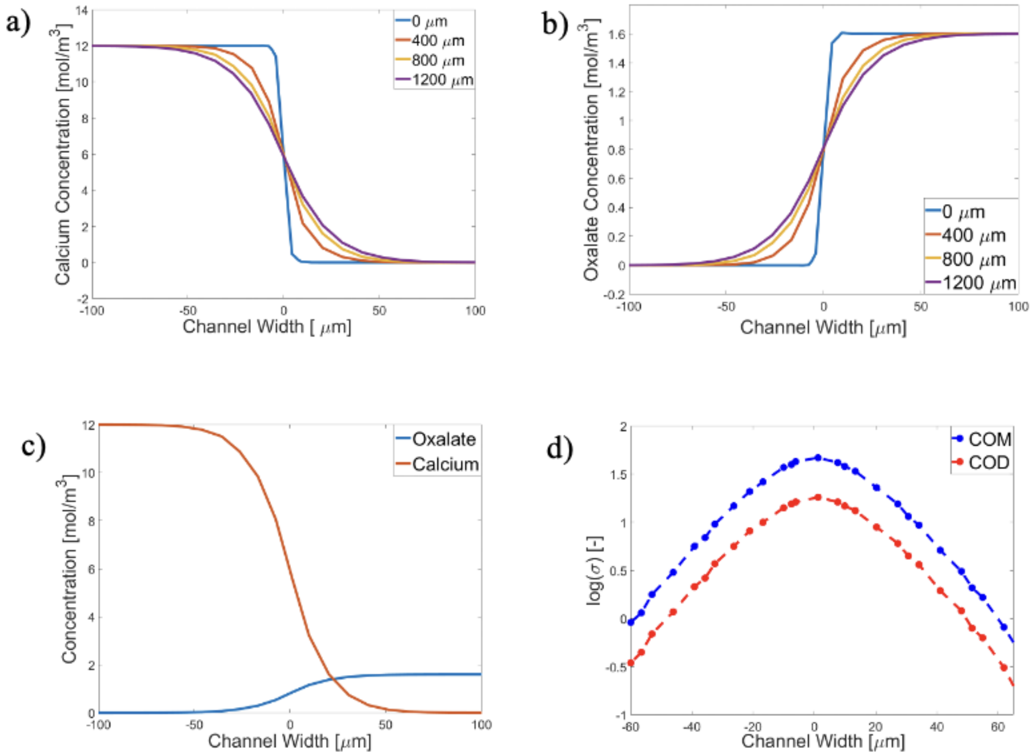

Figure 5.2. The calcium and oxalate concentration profiles and σ- profile in artificial urine at the bottom of the channel with concentrations of $[Ca^{2+}]=12\ mol/m^3$ and $[Ox^{2-}]=1.6\ mol/m^3$ at U=0.075 m/s. (a) concentration profiles of Ca^{2+} at different length positions. (b) concentration profiles of Ox^{2-} at different length positions (c) concentration profiles of Ca^{2+} (red) and Ox^{2-} (blue) at x=800 µm (See Figure D.3 in Appendix D). Ca^{2+} at the lower inlet (negative width region) and Ox^{2-} at the upper inlet (positive width region) are fed (sample AU3). (d) Logarithmic σ -profiles along the channel width for both COM and COD at x=8000 µm for sample AU3.

The analysis of σ-profiles is done for all length positions and plotted in Figure 5.3 after σ calculation with JESS using COMSOL concentration profiles (for details see Appendix D). The supersaturated region for COM is between the red lines, and for COD between the blue lines. Figure 5.3 shows the results of sample AU2 at 7.3 min after the first crystal was observed. The σ-profile is superimposed on the microscope image of AU2. The trend of the σ-profile from COMSOL overlaps with the measured result. AU2 has 12 mol/m^3 calcium and 1.6 mol/m^3 oxalate with molar ratio of 7.5 at velocity value of 0.035 m/s. This difference in ion concentrations play a role in ion diffusions. Figure 5.3 shows that small difference of ion concentrations allows that oxalate ions diffuses into calcium-rich side effectively and $\sigma_{\max}$ is at $\approx 2\ \mu m$ in the oxalate-rich side. The crystals (Sample AU2) emerged and grew at the interface, near the center of the channel, which overlaps with the COMSOL result.

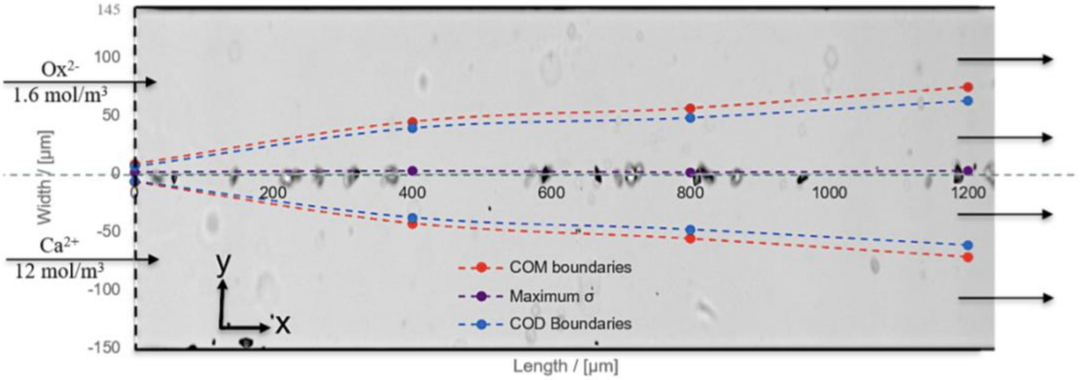

Figure 5.3. COMSOL model combined with image from artificial urine experiments at t = 7.3 min after the first observed crystal. Display of the situation for artificial urine sample; AU2 (see Figure 5.4) with its experimental image.

5.3.2. Effect of Average Velocity on CaOx Crystallization

To investigate the effect of flow velocity on the growth of the CaOx crystals, artificial urine samples of AU1, AU2 and AU3 for different velocities of 0.015, 0.035, 0,075 m/s were used at fixed supersaturation value of COD as 17.8. Figure 5.4 shows micrographs of the microfluidic channels at different times during the experiment. On the left side, the two inlet channels and their junction, where the $CaCl_2$ and NaOx solutions meet, can be visualized, as detailed previously (Figure 5.1). The spectrum for a tetragonal crystal, COD has Raman shifts 910 and 1474-1478 cm^{-1} [45-48] and oval crystal was identified as COM[49] (See Appendix D). Only crystals identified as COD were observed in the middle of the channel, which coincides with the interface between two flows. COD crystals are shown in the channels at t=3 and t=7.3 min after the first crystal emerged for each channel. The average growth rates ($\dot{r}_{avg}$) of COD were estimated as $0.95 \pm 0.27 \cdot 10^{-8}$ m/s, $0.93 \pm 0.45 \cdot 10^{-8}$ m/s, and $0.92 \pm 0.22 \cdot 10^{-8}$ m/s with flow velocities of 0.015, 0.035, 0,075 m/s, respectively (Table 5.4).

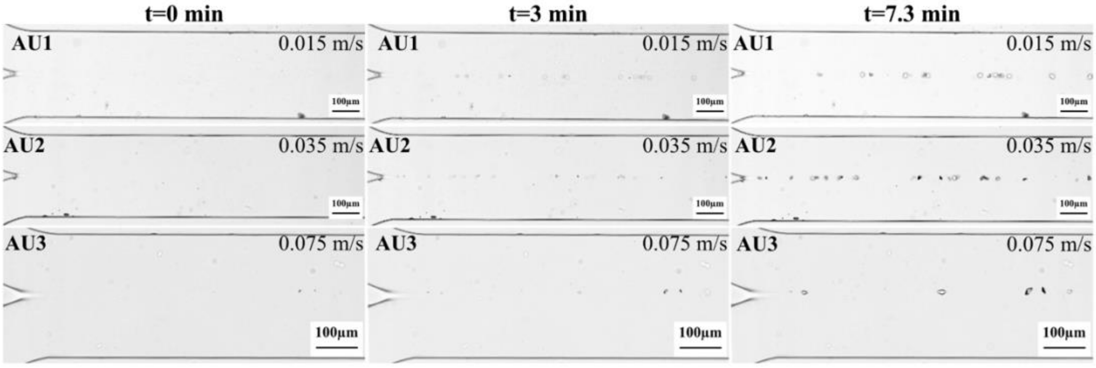

Figure 5.4. Microscopic images of the microfluidic channel for three experiments AU1, AU2 and AU3 (different rows) for varying flow velocity at 0.015, 0.035 and 0.075 m/s respectively at a fixed Ca:Ox molar ratio of 7.5. Three time lapses after the first appearance of crystals (in columns) with 10x objective, except AU3 (it is with 20x objective) with 100µm scale bar.

The results show that varying the flow velocity does not significantly affect the average growth rate ($\dot{r}_{avg}$) (Table 5.4) possibly due to the low Reynold number (Re=6.7 at the maximum velocity of 0.075 m/s). Only COD crystals were seen at the interface at the high supersaturation values. The composition of artificial urine containing magnesium and other trace metals may be responsible for the stabilization the COD formation at these supersaturation values, favoring the formation of COD over COM.[50-52]

5.3.3. The molar ratio of Ca:Ox effect on CaOx Crystallization

Figure 5.5 shows the experiments performed with different oxalate concentrations at a fixed calcium (12 mol/m^3) concentration. The molar proportions of Ca:Ox were 5, 6, 7.5, and 10 in the experiments. AU2 and AU6, resulting in minimum values of supersaturation and growth rate for COD. In experiments AU4 and AU5, both COD and COM crystals can be seen together. COM and COD crystals were observed in channels with Ca:Ox molar ratio values 5 and 6. Daudon et al. worked on 6869 urine samples with COM and COD crystals together.[53] They reported that patients with higher Ca:Ox ratios (>14) excreted predominantly COD crystals, while patients with low Ca:Ox ratios (<5) excreted mostly COM. For the Ca:Ox ratios between these values, COM and COD were more equally distributed. Our artificial urine results were in line with Daudon et al.`s results of patients’ urine samples within the experiment time.

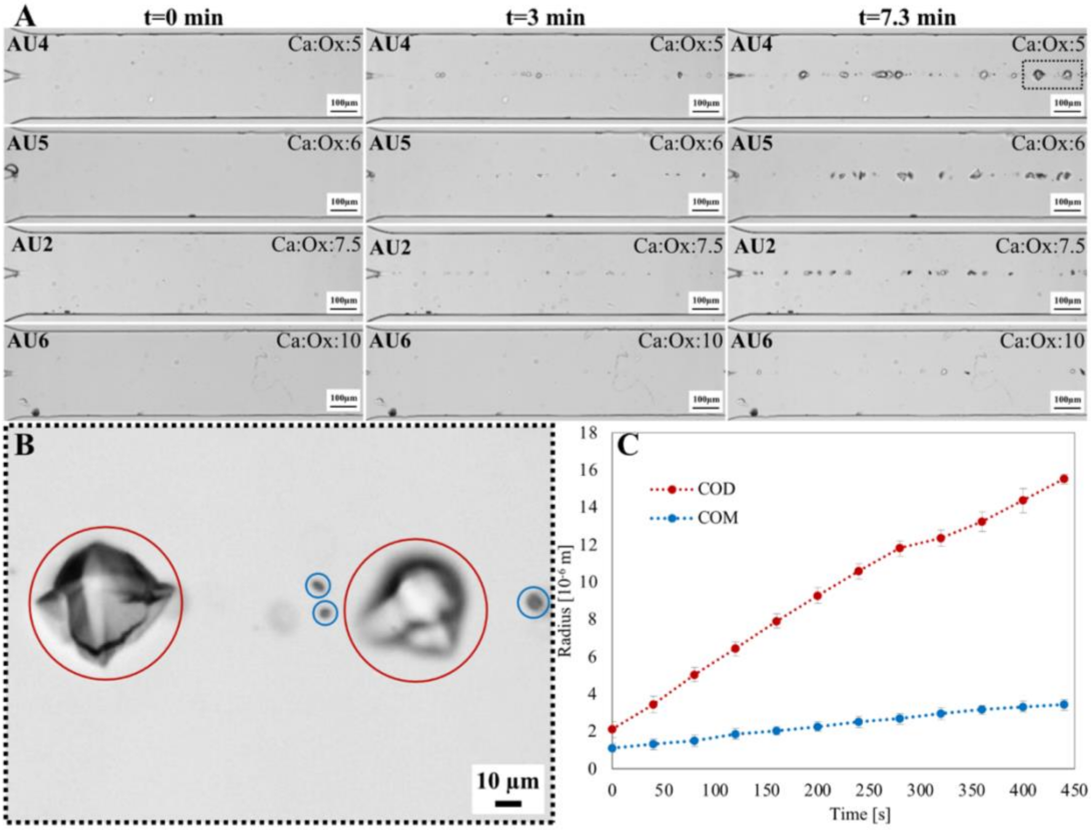

Figure 5.5. A) Microscopic images of the microfluidic channel for four experiments AU4, AU5, AU2 and AU6 (different rows) for molar ratios of Ca:Ox as 5, 6, 7.5 and 10 at a fixed flow velocity of 0.035 m/s. Three time-lapses are shown after the first appearance of crystals (in columns) monitored with a 10x objective. B) Zoomed-in image of sample AU4 at t=7.3 min visible in figure A in black rectangle emphasizes the difference in growth rates between COM and COD crystals, circled blue and red, respectively. C) shows the average radius of three COM and two COD crystals as a function of time from experiment AU4. The equation for COM is $\dot{r}_{avg}=0.0048t+1.124$ *with its standard deviation, 0.0027 µm/s. The equation for COD is* $\dot{r}_{avg}=0.0305t+2.109$ *with its standard deviation, 0.0043 µm/s.*

The growth rate of the COD crystals depends strongly on the supersaturation (see Table 5.4) and is the lowest at the highest Ca:Ox molar ratio of 10 in sample AU6. The calculation of the average crystal growth rate of COM and COD is shown in Figure 5.5.C, in which the average size of five crystals (two COD and three COM crystals) was plotted as a function of time, which allowed the estimation of the growth rate. Surprisingly the growth rates of the COM crystals did not vary significantly as a function of the Ca:Ox ratio of 5 and 6 and thus of the supersaturation.

5.3.4. Effect of Osteopontin on CaOx Crystallization

Figure 5.6. shows the formation and growth of CaOx crystals as a function of three different OPN concentrations of $2.4 \cdot 10^{-8}$ mol/m^3, $6.0 \cdot 10^{-8}$ mol/m^3 and $8.4 \cdot 10^{-8}$ mol/m^3 at a fixed Ca:Ox molar ratio of 7.5 and flow velocity of 0.015 m/s. The growth rate calculation was done using the image taken at t=7.3 after the first crystal emerged. To show small COD crystals clearly, the images at t=30 min were added in Figure 5.6.

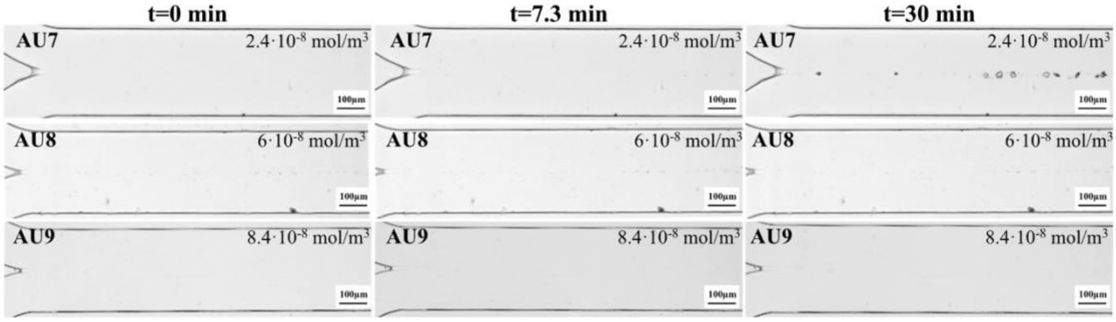

Figure 5.6. Microscopic images of the microfluidic channel for three experiments AU7, AU8 and AU9 (different rows) three different amount of OPN; $1.6 \cdot 10^{-8}$ mol/m^3 , $6 \cdot 10^{-8}$ mol/m^3 and $8.4 \cdot 10^{-8}$ mol/m^3, respectively at a fixed Ca:Ox molar ratio of 7.5 and at flow velocity of 0.015 m/s. Three time lapses after the first appearance of crystals (in columns) with 10x objective with 100µm scale bar.

Only formation of COD was observed with the lowest OPN concentration of $2.4 \cdot 10^{-8}$ mol/m^3 for sample AU7 (Figure 5.6). The higher OPN concentrations of $6.0 \cdot 10^{-8}$ mol/m^3 and $8.4 \cdot 10^{-8}$ mol/m^3 in AU8 and AU9 showed complete inhibition of CaOx crystal formation in artificial urine (Figure 5.6). To see the effect of the lowest OPN concentration, experiment AU7 should be compared with AU1 (see Figure 5.4 and Table 5.4). The growth rate of COD decreased from 0.95±0.27·10^{-8} m/s (AU1) to 0.34±0.15·10^{-8} m/s (AU7). Studies in the literature claim that OPN inhibits crystal growth and changes the morphology of CaOx crystals.[54-56] Also, since OPN is rich in dicarboxylic acids, a stronger interaction of OPN with CaOx crystal faces is probable.[57] The chemical structure of OPN might encourage binding to a mineral surface.[54]

Table 5.4. Flow conditions supersaturation and growth rates, $\dot{r}_{avg}$ of COM and COD crystal in artificial urine at fixed calcium concentration of 12 mol/m^3. The Ca:Ox ratio, flow velocity (U), added amount of OPN, supersaturation ratio values (σ) from JESS and growth rate ($\dot{r}_{avg}$) are shown. The effect of OPN was not taken into account in the calculation of supersaturation.

Experiment conditions				**COM**			**COD**		
Sample Name	**Ca:Ox**	**U [m/s]**	**OPN [10^{-8} mol/m^3]**	**σ [-]**	**$\dot{r}_{avg}$ [10^{-8} m/s]**	**std dev. [10^{-8} m/s]**	**σ [-]**	**$\dot{r}_{avg}$ [10^{-8} m/s]**	**std dev. [10^{-8} m/s]**
AU1	7.5	0.015	-	46.8	-	-	17.8	0.95	0.27
AU2	7.5	0.035	-	46.8	-	-	17.8	0.93	0.45
AU3	7.5	0.075	-	46.8	-	-	17.8	0.92	0.22
AU4	5	0.035	-	67.6	0.48	0.27	26.3	3.05	0.43
AU5	6	0.035	-	57.5	0.50	0.28	21.9	2.33	0.12
AU6	10	0.035	-	34.7	-	-	13.5	0.78	0.31
AU7	7.5	0.015	2.4	46.8	-	-	17.8	0.34	0.15
AU8	7.5	0.015	6.0	46.8	-	-	17.8		
AU9	7.5	0.015	8.4	46.8	-	-	17.8		

5.4. Conclusion

We reported growth rates of CaOx crystals in a geometry mimicking the collecting duct of the kidney under flow conditions relevant for kidney stone formation. The effect of varying flow velocities, molar ratio of Ca:Ox referring to distinct supersaturations and OPN concentrations on growth of CaOx crystal were investigated. Mainly COD crystals were observed in channels. Altering the flow velocity in the channel did not affect crystal growth at fixed supersaturation ratio. However, an increase of the oxalate concentration at a fixed value of the calcium concentration, decreasing the Ca:Ox molar ratio and increasing the supersaturation at a fixed flow velocity, resulted in a clear increase in the average growth rate of COD crystals. In addition, for the lower molar ratios of calcium and oxalate (5 and 6) COM nucleation was also observed competing with the COD nucleation which seemed to be reduced at these higher S values. The growth rate of the COM crystals did not show a clear dependence on the estimated supersaturation and was much lower than the COD growth rates.

The presence of the lowest amount (i.e. $2.4 \cdot 10^{-8}$ mol/m^3) of OPN in artificial urine caused a lower growth rate of the COD crystals. With increasing OPN concentration, it was found that OPN inhibits crystal formation for both pseudo-polymorphs of CaOx in artificial urine.

5.5. References

1. Romero, V.; Akpinar, H.; Assimos, D. G., Kidney stones: a global picture of prevalence, incidence, and associated risk factors. *Reviews in urology* **2010,** *12* (2-3), e86-96.

2. Alelign, T.; Petros, B., Kidney Stone Disease: An Update on Current Concepts. *Advences in Urology* **2018**, 3068365.

3. Wang, W.; Fan, J.; Huang, G.; Li, J.; Zhu, X.; Tian, Y.; Su, L., Prevalence of kidney stones in mainland China: A systematic review. *Scientific reports* **2017,** *7* (1), 41630.

4. Ogobuiro, I., Tuma, F., *Physiology renal*. StatPearls - NCBI Bookshelf, 2020.

5. Smith, H. W., *The kidney: structure and function in health and disease*. Oxford University Press, USA: 1951; Vol. 1.

6. Bruce, M. K., Bruce, A Stanton, *Renal physiology*. Philadelphia, PA : Elsevier Mosby: 2013; p 79.

7. Laffite, G., Leroy, C., Bonhomme, C., Bonhomme-Coury, L., Letavernier, E., Daudon, M., Frochot, V., Haymann, J.P., Rouzière, S.L., Ivan, T., Bazin, D., Babonneaub, F., Abou-Hassan, A., Calcium oxalate precipitation by diffusion using laminar microfluidics: toward a biomimetic model of pathological microcalcifications. *Lab on a Chip* **2016,** *16* (7), 1157-1160.

8. Vize, P. D., Woolf, A,S., Bard, J.B.L., *The kidney: from normal development to congenital disease*. 2003; Vol. 42.

9. Tabeling, P., *Introduction to microfluidics*. OUP Oxford: 2005.

10. Hall, J. E., Hall, M.E., *Guyton and Hall textbook of medical physiology e-Book*. Elsevier Health Sciences: 2020.

11. Asmar, A.; Cramon, P. K.; Simonsen, L.; Asmar, M.; Sorensen, C. M.; Madsbad, S.; Moro, C.; Hartmann, B.; Jensen, B. L.; Holst, J. J.; Bulow, J., Extracellular Fluid Volume Expansion Uncovers a Natriuretic Action of GLP-1: A Functional GLP-1-Renal Axis in Man. *Journal of Clinical Endocrinology Metabolism* **2019,** *104* (7), 2509-2519.

12. Bihl, G.; Meyers, A., Recurrent renal stone disease—advances in pathogenesis and clinical management. *The Lancet* **2001,** *358* (9282), 651-656.

13. Coe, F. L., Favus, M.J., Pak, C.Y.C., Parks, J.H., Preminger, G.M.,; Tolley, D. A., Kidney stones: Medical and surgical management. *British Journal of Urology* **1996,** *78* (3), 482.

14. Reynolds, T. M., Best Practice No 181: Chemical pathology clinical investigation and management of nephrolithiasis. *Journal of clinical pathology* **2005,** *58* (2), 134-140.

15. Worcester, E. M.; Coe, F. L., Nephrolithiasis. *Primary Care* **2008,** *35* (2), 369-391, vii.

16. Skorecki, K., , Chertow, G.M.; Marsden, P.A.; Taal, M.W.; Alan, S.L.; Luyckx, V., *Brenner and Rector's The Kidney E-Book*. Elsevier Health Sciences: 2015.

17. Conti, C.; Casati, M.; Colombo, C.; Possenti, E.; Realini, M.; Gatta, G. D.; Merlini, M.; Brambilla, L.; Zerbi, G., Synthesis of calcium oxalate trihydrate: New data by vibrational spectroscopy and synchrotron X-ray diffraction. *Spectrochim Acta Part A: Molecular and Biomolecular Spectroscopy* **2015,** *150*, 721-730.

18. Pahira, J. J., Pevzner, M., Nephrolithiasis. In *Penn Clinical Manual of Urology*, Elsevier: 2007; pp 235-257.

19. Bird, V. Y., Khan, S.R., How do stones form? Is unification of theories on stone formation possible? *Archivos espanoles de urologia* **2017,** *70* (1), 12.

20. Sun, X. Y., Zhang, C.Y., Bhadja, P., Ouyang, J.M., Preparation, properties, formation mechanisms, and cytotoxicity of calcium oxalate monohydrate with various morphologies. *CrystEngComm* **2018,** *20* (1), 75-87.

21. Ratkalkar, V. N.; Kleinman, J. G., Mechanisms of stone formation. *Clinical reviews in bone mineral metabolism* **2011,** *9* (3-4), 187-197.

22. Bushinsky, D. A.; Asplin, J. R.; Grynpas, M. D.; Evan, A. P.; Parker, W. R.; Alexander, K. M.; Coe, F. L., Calcium oxalate stone formation in genetic hypercalciuric stone-forming rats. *Kidney international* **2002,** *61* (3), 975-987.

23. Kok, D. J.; Papapoulos, S. E., Physicochemical considerations in the development and prevention of calcium oxalate urolithiasis. *Bone and mineral* **1993,** *20* (1), 1-15.

24. Favus, M. J., Zeytinoglu, M., Coe, F.L., Idiopathic hypercalciuria and nephrolithiasis. In *Vitamin D*, Elsevier: 2018; pp 485-505.

25. Asplin, J. R., Hyperoxaluric calcium nephrolithiasis. *Journal of Clinical Endocrinology Metabolism* **2002,** *31* (4), 927-949.

26. Milliner, D. S., The primary hyperoxalurias: an algorithm for diagnosis. *American journal of nephrology* **2005,** *25* (2), 154-160.

27. Robijn, S.; Hoppe, B.; Vervaet, B. A.; D'Haese, P. C.; Verhulst, A., Hyperoxaluria: a gut-kidney axis? *Kidney international* **2011,** *80* (11), 1146-58.

28. Aggarwal, K. P.; Narula, S.; Kakkar, M.; Tandon, C., Nephrolithiasis: molecular mechanism of renal stone formation and the critical role played by modulators. *BioMed Research International* **2013,** *2013*.

29. Qiu, S. R.; Wierzbicki, A.; Orme, C. A.; Cody, A. M.; Hoyer, J. R.; Nancollas, G. H.; Zepeda, S.; De Yoreo, J. J., Molecular modulation of calcium oxalate crystallization by osteopontin and citrate. *Proceedings of the National Academy of Sciences of the United States of America* **2004,** *101* (7), 1811-5.

30. Denhardt, D. T., *Osteopontin: Role in Cell Signalling and Adhesion.* New York Academy of Sciences: 1995.

31. Wesson, J. A.; Johnson, R. J.; Mazzali, M.; Beshensky, A. M.; Stietz, S.; Giachelli, C.; Liaw, L.; Alpers, C. E.; Couser, W. G.; Kleinman, J. G.; Hughes, J., Osteopontin is a critical inhibitor of calcium oxalate crystal formation and retention in renal tubules. *Journal of the American Society of Nephrology* **2003,** *14* (1), 139-147.

32. Fleisch, H., Inhibitors and promoters of stone formation. *Kidney international* **1978,** *13* (5), 361-371.

33. Brown, P., Ackerman, D., Finlayson, B., Calcium oxalate dihydrate (weddellite) precipitation. *Journal of Crystal Growth* **1989,** *98* (3), 285-292.

34. Ipe, D. S.; Horton, E.; Ulett, G. C., The Basics of Bacteriuria: Strategies of Microbes for Persistence in Urine. *Frontiers Cellular and Infection Microbiology* **2016,** *6*, 14.

35. Mitra, P.; Pal, D. K.; Das, M., Does quality of drinking water matter in kidney stone disease: A study in West Bengal, India. *Investigative and clinical urology* **2018,** *59* (3), 158-165.

36. Geng, X.; Sosa, R. D.; Reynolds, M. A.; Conrad, J. C.; Rimer, J. D., Alginate as a green inhibitor of barite nucleation and crystal growth. *Molecular Systems Design & Engineering* **2021,** (7), 508-519.

37. Laval, P.; Salmon, J.-B.; Joanicot, M., A microfluidic device for investigating crystal nucleation kinetics. *Journal of Crystal Growth* **2007,** *303* (2), 622-628.

38. Zheng, B.; Roach, L. S.; Ismagilov, R. F., Screening of protein crystallization conditions on a microfluidic chip using nanoliter-size droplets. *Journal of the American Chemical Society* **2003,** *125* (37), 11170-11171.

39. Nisisako, T.; Torii, T.; Higuchi, T., Droplet formation in a microchannel network. *Lab Chip* **2002,** *2* (1), 24-6.

40. Envisiontec 3D Printer. https://envisiontec.com/3d-printers/desktop-3d-printers/micro-plus-hi-res/ (accessed January 2019).

41. Ai, Y.; Xie, R.; Xiong, J.; Liang, Q., Microfluidics for Biosynthesizing: from Droplets and Vesicles to Artificial Cells. *Small* **2020,** *16* (9), e1903940.

42. Tona, R. M.; McDonald, T. A. O.; Akhavein, N.; Larkin, J. D.; Lai, D., Microfluidic droplet liquid reactors for active pharmaceutical ingredient crystallization by diffusion controlled solvent extraction. *Lab Chip* **2019,** *19* (12), 2127-2137.

43. Li, S.; Ihli, J.; Marchant, W. J.; Zeng, M.; Chen, L.; Wehbe, K.; Cinque, G.; Cespedes, O.; Kapur, N.; Meldrum, F. C., Synchrotron FTIR mapping of mineralization in a microfluidic device. *Lab Chip* **2017,** *17* (9), 1616-1624.

44. Streit, J., Tran-Ho, L., Königsberger, E., Solubility of the three calcium oxalate hydrates in sodium chloride solutionsand urine-like liquors. *Monatshefte für Chemie/Chemical Monthly* **1998,** *129* (12), 1225-1236.

45. Rakotozandriny, K.; Bourg, S.; Papp, P.; Tóth, Á.; Horváth, D.; Lucas, I. T.; Babonneau, F.; Bonhomme, C.; Abou-Hassan, A., Investigating CaOx Crystal Formation in the Absence and Presence of Polyphenols under Microfluidic Conditions in Relation with Nephrolithiasis. *Crystal growth & design* **2020,** *20* (12), 7683-7693.

46. Kuliasha, C. A., Rodriguez, D., Lovett, A., Gower, L.B., In situ flow cell platform for examining calcium oxalate and calcium phosphate crystallization on films of basement membrane extract in the presence of urinary 'inhibitors'. *CrystEngComm* **2020,** *22* (8), 1448-1458.

47. Castiglione, V.; Sacre, P. Y.; Cavalier, E.; Hubert, P.; Gadisseur, R.; Ziemons, E., Raman chemical imaging, a new tool in kidney stone structure analysis: Case-study and comparison to Fourier Transform Infrared spectroscopy. *PloS one* **2018,** *13* (8), 1-18.

48. Edwards, H. G.; Seaward, M. R.; Attwood, S. J.; Little, S. J.; de Oliveira, L. F.; Tretiach, M., FT-Raman spectroscopy of lichens on dolomitic rocks: an assessment of metal oxalate formation. *The Analyst* **2003,** *128* (10), 1218-1221.

49. Fatma Ibis, M. A. N., Frederico Marques Penha, Tsun Wang Yu,; Antoine E. D. M. van der Heijden, H. J. M. K., and Huseyin Burak Eral, Role of Hyaluronic Acid on the Nucleation Kinetics of Calcium
Oxalate Hydrates in Artificial Urine Quantified with Droplet Microfluidics. **2022**, 11.

50. Martin, X.; Smith, L. H.; Werness, P. G., Calcium oxalate dihydrate formation in urine. *Kidney international* **1984,** *25* (6), 948-952.

51. Walton, R.; Kavanagh, J.; Heywood, B.; Rao, P., The association of different urinary proteins with calcium oxalate hydromorphs. Evidence for non-specific interactions. *Biochimica et Biophysica Acta (BBA)-General Subjects* **2005,** *1723* (1-3), 175-183.

52. Tomazic, B.; Nancollas, G., The kinetics of dissolution of calcium oxalate hydrates. *Journal of Crystal Growth* **1979,** *46* (3), 355-361.

53. Daudon, M.; Letavernier, E.; Frochot, V.; Haymann, J.-P.; Bazin, D.; Jungers, P., Respective influence of calcium and oxalate urine concentration on the formation of calcium oxalate monohydrate or dihydrate crystals. *Comptes Rendus Chimie* **2016,** *19* (11-12), 1504-1513.

54. Qiu, S.; Wierzbicki, A.; Orme, C.; Cody, A.; Hoyer, J.; Nancollas, G.; Zepeda, S.; De Yoreo, J., Molecular modulation of calcium oxalate crystallization by osteopontin and citrate. *Proceedings of the National Academy of Sciences* **2004,** *101* (7), 1811-1815.

55. Denhardt, D. T., *Osteopontin: role in cell signalling and adhesion*. New York Academy of Sciences: 1995.

56. Wesson, J. A.; Johnson, R. J.; Mazzali, M.; Beshensky, A. M.; Stietz, S.; Giachelli, C.; Liaw, L.; Alpers, C. E.; Couser, W. G.; Kleinman, J. G. J. J. o. t. A. S. o. N., Osteopontin is a critical inhibitor of calcium oxalate crystal formation and retention in renal tubules. **2003,** *14* (1), 139-147.

57. Addadi, L.; Weiner, S., Interactions between acidic proteins and crystals: stereochemical requirements in biomineralization. *Proceedings of the National Academy of Sciences* **1985,** *82* (12), 4110-4114.

Chapter 6.

Conclusions

In this thesis, various physicochemical aspects of calcium oxalate (CaOx) kidney stone formation were studied to understand CaOx crystallization mechanism including solubility, nucleation kinetics, inhibition and growth. Tailored microfluidic devices were developed to execute statistically significant number of experiments under identical conditions, a unattainable feat using labor intensive manual experimentation, for in-depth analysis of formation and growth of kidney stones. In Chapter 2, the solubility of calcium oxalate monohydrate (COM) at different temperatures and pH was studied. The experiments revealed that COM is sparingly soluble in water even at elevated temperatures. Furthermore, COM solubility is observed to have a strong dependence on pH. These experimental findings are supported using a model based on the Debye-Hückel theory describing the solution chemistry.

In Chapter 3, a microfluidic approach was developed to quantifying the nucleation kinetics of CaOx in aqueous solution inside droplets acting as independent micro reactors while monitoring the pseudo-polymorphic transitions. The approach allows minimum material consumption while facilitating at least hundred identical experiments in a few hours. The precipitation kinetics of CaOx was studied using this approach as a function of supersaturation, pH and in the presence of inhibitors: magnesium ions (Mg^{2+}) and osteopontin (OPN). Only COM nucleated under studied conditions. The COM nucleation rate was quantified via microfluidic induction time measurements in a droplet-based microfluidics device. The solution chemistry model developed in Chapter 2 was extended to rationalize the trends observed in experiments. The microfluidic induction time measurements showed that the presence of magnesium (Mg^{2+}) in the solution slightly alters supersaturation yet the observed lag time intimately connected to growth is varied considerably. The other inhibitor, osteopontin, suppressed COM nucleation significantly. The study emphasizes that the multiplexing ability of microfluidics may hold the key to understanding the physicochemical mechanisms behind kidney stone obscured by the overwhelming number of experimental parameters.

Chapter 4 focused on how the presence of hyaluronic acid (HA) and the molar ratio of calcium to oxalate alter nucleation kinetics of CaOx in artificial urine. As the developed microfluidic approach enables discriminating which pseudo-polymorphic form nucleates from solution, nucleation kinetics of two CaOx pseudo-polymorphic forms were distinctly identified. The microfluidic induction time measurements showed that higher oxalate concentrations favor the formation of COD, the metastable form, over COM. Increasing the concentration of HA at fixed calcium and oxalate concentrations favored crystallization of COM, the most stable form, over COD. In droplets where COM nucleated first, COD was not formed. If COD crystals formed first, COM crystals were also observed at later times in the same droplet. The unique contribution of this work is the extraction of nucleation kinetics of COD and COM separately through microscopic characterization of crystals nucleated in a microfluidic chip.

In Chapter 5, growth rates of CaOx crystals in artificial urine were studied in a co-flow microfluidic device which mimicks the geometry of the collecting duct. The influence of flow velocity, calcium to oxalate molar ratio, and inhibitor osteopontin (OPN) concentration on growth of CaOx crystal were investigated. Mainly COD crystals were observed in channels under laminar flow. Varying the flow velocity did not affect crystal growth at fixed supersaturation ratio (S) value. Increasing the supersaturation of CaOx at a fixed flow velocity resulted in higher average growth rate of COD crystals. Furthermore, when the molar ratio of calcium to oxalate was set at five and six, both COM and COD crystals formed together in the channel, and the growth rate of the COM were lower than the growth rate of COD. At OPN concentrations of $6.0 \cdot 10^{-8}$ mol/m^{3}and $8.4 \cdot 10^{-8}$ mol/m^3, crystallization of both pseudo-polymorphs of CaOx were completely inhibited in artificial urine.

Briefly, various aspects of CaOx crystallization, from the solubility to the growth was studied under a broad range of techniques to shed light at kidney stones formation in this work. The cross-validated experimental and modelling study of the solubility of COM provided an framework to predict COM solubility at physiologically relevant pH and temperature values. The designed droplet-based microfluidic chip quantified the nucleation kinetics of CaOx in statistically significant identical experiments, a requirement for nucleation studies, within hours. Multiplexing ability of the developed microfluidic chip enables exploring experimental parameters such as different temperature, pH and solution compositions. Moreover, the ability to distinguish COM and COD crystals with polarized microscopy facilitated quantification of COM and

COD nucleation kinetics independently in microfluidic induction time measurements, a task not viable in liter scale manual experimentation. As the kidney stone formation occurs under flow , a part of the nephron was mimicked using a microfluidic co-flow geometry. The proposed co-flow geometry offered insight to how different supersaturation, flow velocities, and inhibitor concentrations can alter growth of CaOx crystals under physiologically relevant flow conditions at single nephron scale.

Based on the aforementioned findings, it can be said that several reasons for the formation of CaOx kidney stones were understood such as pH, temperature, supersaturation ratios, flow rate, the molar ratio of Ca:Ox, and the presence of inhibitors and macromolecules. Formations of different types of kidney stones could be studied taking advantage of these findings, as well. Furthermore, this physicochemical knowledge could be useful for experiments with cell culture to understand the interaction of kidney stones and cells. Besides, the designed microfluidic chips with integrated human cells can be used for different studies such as understanding protein crystallization.

Appendix A for Chapter 2

A.1. Other Methods Explored for solubility of COM

Accurate solubility of calcium oxalate monohydrate (COM) is needed to extend the current knowledge of nephrolithiasis. The solubility of COM is determined as a function of temperature and pH. The temperature dependent solubility is done by a mixture of COM and ultrapure water. To identify the most suitable method to measure solubility, explored different methods.

Firstly, we discuss the gravimetric method. In this method, 200 mg COM is suspended in 1000 ml solution volume to minimize the weighing error. Once the volatiles are evaporated, the amount of dry material; CaC_2O_4 was determined. The weighted amounts show large variations hence error bars. We suspect these large error bars originate from material sticking in vessels where evaporation occurs. Hence, we conclude that gravimetric method is not the most suitable approach for measuring solubility of this a sparely soluble compound.

Then we explore polythermal method based on turbidity with multiple reactor systems Crystal16 and Crystalline (Avantium Technologies). Volumes of one and eight milliliters respectively are tested. The vials with concentrations ranging between 0.1mg/ml and 1.6 mg/ml are placed in the setup at a stirring speed of 400 rpm. The heating and cooling rates are chosen as 0.1 ^{o}C/min and 1.0 ^{o}C/min respectively. The temperature profile is chosen from 5 ^{o}C to 90 ^{o}C. This temperature cycle is repeated three times for each sample. Following, we use different concentrations, temperatures profiles and heating cooling rate to find solubility curve of COM. In such turbidity-based measurements, we expect to see significant changes in transmittivity across the scanned temperature range. However, observed 100% transmittivity at all times indicating that the turbidity does not change throughout the measurements. We hypothesize that, due to low solubility of COM, the number of crystals forming is not sufficient to alter transmittivity. We also explore UV-Vis (Hach DR 6000) spectroscopy with measurements to quantify the solubility of COM. Samples with a concentration ranging between 0.1mg/ml and 1.6 mg/ml at 25, 37, 60 and 90 °C are tested at 620nm.[1]

However, there are not significant peaks regarding at 620 nm. We have also explored Focused Beam Reflectance Measurement (FBRM, Mettler Toledo D600L). The probe was inserted in Easymax reactor at experimental temperature and concentration ranges. We could not get any reproducible results with this method as well. We hypothesize that the small change in COM crystal size was beyond the detection limit FBRM. ReactIR iC10 (Mettler Toledo) is used to measure different oxalate concentrations. There are sharp drops in the absorbance. Yet repeated measurements under identical experimental conditions produced irreproducible results.

A.2. Supporting information on reported measurements

In this section, we provide raw data for each ICP-OES and ICP-MS measurement in Tables A.8 to A.11. In addition to the all raw data provided, information relevant to buffer solutions (Table A. 1-5), material list (Table A.6) and equipment list (Table A.7) are seen below. We hope these details listed below will make it easier for other experimentalist to reproduce our results.

Table A. 1. The amounts of materials used in buffer solution preparation[2, 3]

Compound	Volume of ultrapure water [ml]	Weight of the compound [g]
Citric acid ($C_6H_8O_7$)	658.32	12.65
Disodium phosphate (Na_2HPO_4)	781.92	22.20
Glycine ($C_2H_5NO_2$)	240	3.60
Sodium hydroxide (NaOH)	138	1.10

Table A. 2. pH values for two different buffer solutions[2, 3]

pH	**Buffer Solution**
3.2, 5.36, 6.0, 7.55	Citric Acid – Disodium phosphate
9.0, 10.6	Sodium hydroxide – Glycine

Table A. 3. Desired Buffer solution calculation for pH 3.0, 5.0, 6.0 and 7.4[2, 4]

pH	**0.1 M Citric acid ($C_6H_8O_7$) [ml]**	**0.2 M Disodium phosphate (Na_2HPO_4) [ml]**
3.0	381.36	98.64
5.0	233.04	247.20
6.0	184.25	315.75
7.4	43.92	436.08

We could not reach the same pH values for 3.0, 5.0, 7.4. We obtained 3.2, 5.36, 6.0, 7.55 values which are in Table A. 3

Table A. 4. Desired Buffer solution calculation for pH 9.0 and 10.6[2-4]

pH	**0.2 M - Glycine ($C_2H_5NO_2$) [ml]**	**0.2 M- Sodium hydroxide (NaOH) [ml]**	**Ultrapure water [ml]**
9.0	120.0	28.8	331.20
10.6	120.0	109.2	250.80

Table A. 5. Weight of the needed compounds for the buffer solution[2, 4]

Compound	**Ultrapure water [ml]**	**Weight of the compound [g]**
Citric acid ($C_6H_8O_7$)	658.32	12.66
Disodium phosphate (Na_2HPO_4)	781.92	22.20
Glycine ($C_2H_5NO_2$)	240.00	3.60
Sodium hydroxide (NaOH)	138.00	1.10

Table A. 6. Material list for Solubility Experiment

Materials	**Chemical Formula**	**CAS Number**	**Vendor**
Citric Acid	$C_6H_8O_7$	77-92-9	MERCK
Disodium phosphate	Na_2HPO_4	7558-79-4	Sigma-Aldrich
Sodium hydroxide	NaOH	7558-79-4	Sigma-Aldrich
Ultrapure water	H_2O	-	ELGA PURELAB Resistivity:18.2 MΩ·cm at 23.6 °C)
Glycine	$C_2H_5NO_2$	1310-73-2	Sigma-Aldrich
Calcium oxalate monohydrate	$CaC_2O_4 \cdot H_2O$	563-72-4	Sigma-Aldrich

Table A. 7. Equipment list for Solubility Experiment

Equipment	**Equipment Name**	**Brand**
Scale	Mettler PM2000	Mettler Toledo
Scale	Precision Balance MS4002TSDR/00	Mettler Toledo
Ultrasonic bath	Branson 2510 Ultrasonic Cleaner	Branson
Oven	-	Binder
Reactor	EasyMax 102 Advanced Synthesis Workstation	Mettler Toledo
pH-meter	914 pH/Conductomer	Metrohm

At least seven repetitions are done for each temperature point for ICP-OES and ICP-MS measurements. Measurements at three different wavelengths for ICP-OES is given in Chapter 2. Used wavelength is 317.9 nm in Chapter 2.

Table A.8 values are converted to molarity considering dilution factor and presented in Figure 2.2 and Figure 2.4 in the Chapter 2.

Table A. 8. The raw results of ICP-OES measurements (in ultrapure water) for different temperatures at 317.9, 393.4 and 396.8 nm.

T (^oC)	Ca [ppm] 317.9	Ca [ppm] 393.4	Ca [ppm] 396.8
25	0.4056	0.4016	0.4055
	0.4968	0.501	0.4913
	0.4219	0.4269	0.4244
	0.4255	0.4266	0.4261
	0.456	0.4587	0.4598
	0.5306	0.53	0.5195
	0.4234	0.4287	0.4211
	0.4112	0.4167	0.4126
	0.5088	0.5206	0.5039
	0.3898	0.4069	0.3941
	0.42	0.4305	0.4234
	0.4404	0.4646	0.4458
	0.4348	0.4488	0.4411
	0.4447	0.461	0.4509
	0.4174	0.4276	0.4199
	0.3572	0.359	0.3559
	0.4316	0.428	0.4239
	0.3718	0.367	0.3666
	0.3925	0.402	0.3904
	0.3852	0.4021	0.3866
	0.52	0.5324	0.514
37	0.5085	0.5032	0.4967
	0.5112	0.5138	0.5027
	0.5267	0.539	0.5288
	0.5363	0.5386	0.5291
	0.5165	0.5251	0.5142
	0.522	0.5187	0.508
	0.4398	0.4457	0.4384
	0.4516	0.4529	0.4538
	0.4963	0.4955	0.4934
60	0.482	0.4722	0.4737
	0.4567	0.4628	0.4665
	0.5139	0.5308	0.5145
	0.4683	0.4792	0.4728
	0.5687	0.5683	0.5506
	0.5353	0.5408	0.5297
	0.5386	0.5337	0.5229
	0.562	0.562	0.5506
	0.5019	0.5264	0.5098
	0.4994	0.5155	0.4999
	0.4307	0.4581	0.4368
	0.481	0.4846	0.4935
90	0.5581	0.5352	0.5426
	0.5419	0.5348	0.5444
	0.5129	0.5122	0.5222
	0.5627	0.5525	0.5638
	0.4995	0.5122	0.4983
	0.4701	0.4745	0.4746
	0.4389	0.4465	0.4382
	0.5154	0.5156	0.5038
	0.5253	0.5191	0.5072
	0.5529	0.5582	0.5451
	0.4986	0.5085	0.5002
	0.5085	0.5215	0.5128
	0.5769	0.5801	0.5709
	0.5203	0.53	0.5207
	0.5699	0.5688	0.5595
	0.5325	0.5363	0.5244
	0.5459	0.5506	0.5378
	0.5318	0.5346	0.5228
	0.5551	0.5597	0.5483
	0.5439	0.5376	0.5261

Table A. 9. The raw results of ICP-MS measurements (in ultrapure water) for different temperatures.

T (^{o}C)	**Ca44 ppm**
25	0.3607
	0.3573
	0.4426
	0.438
	0.4007
	0.3547
	0.403
	0.4613
	0.4311
	0.4031
	0.4256
	0.3954
	0.4307
	0.4464
	0.439
	0.3939
	0.3886
	0.4228
37	0.4781
	0.4685
	0.473
	0.5202
	0.5176
	0.5365
	0.6372
	0.5201
	0.4915
	0.4853
	0.5214
	1.2615

T (^{o}C)	**Ca44 ppm**
60	0.5364
	0.5263
	0.5092
	0.4737
	0.4376
	0.4126
	0.4977
	0.462
	0.4604
	0.462
	0.5038
	0.4911
90	0.4795
	0.603
	0.4645
	0.4443
	0.4595
	0.6168
	0.7694
	0.621
	0.7528
	2.483
	0.5325
	0.5192
	0.4841
	0.4691
	0.5304
	0.5013
	0.4711
	0.5009
	0.5631
	0.4781
	0.5267

Table A. 10. ICP-OES measurements for calcium in two different buffer solutions at different pH values at 317.9 nm.

pH	[10^{-4}M] Ca
3.2	6.9643
	6.6891
	7.5778
	7.1229
	6.8283
	6.9428
	6.5506
	6.5964
	6.9645
5.36	8.8569
	8.7473
	8.7014
	8.0327
	7.9405
	8.3122
	8.5062
	8.501
	8.5546

pH	[10^{-4}M] Ca
6	9.0308
	8.7389
	8.8617
	8.8143
	8.7908
7.55	6.6807
	6.8234
	6.5193
	6.6901
	6.3096
	6.274
	6.889
	7.3478
	7.2781

pH	[10^{-4}M] Ca
9	1.5217
	1.2382
	1.1448
	1.3272
	1.4097
	1.5232
	1.6705
	1.581
	1.4909
10.6	1.836
	1.7147
	2.1585
	2.0182
	2.1788
	2.1189
	2.32
	2.5504

At body temperature condition, nine replicate samples are analyzed for each pH; namely, 3.2, 5.36, 7.55, 9.0, 10.6 and five replicate samples are analyzed for pH 6.0.

Table A. 11. The average calcium values at different pH values using ICP-OES.

ICP-OES [10^{-4} M]		
pH	**[Calcium total]**	**std dev.**
3.2	6.929	0.277
5.36	8.478	0.101
6.0	8.847	0.112
7.55	6.770	0.210
9.0	1.437	0.128
10.6	2.152	0.158

The average values of Calcium molarity in two different buffer solutions at different pH values using ICP-OES are used in Figure 2.5 in Chapter 2.

A.3. Procedure for checking effect of pH change on solubility measurements

To ensure that the pH of ultrapure water did not change during solubility measurements due to added COM or carbon dioxide dissolving in water at elevated temperatures, we measured pH in only ultrapure water and in a suspension of COM. For both cases, we reproduced identical conditions as ICP-OES and ICP-MS measurements detailed in main text. The measurements are conducted in triplicates and given in Table A. 12.

Table A. 12. Measuring pH before and after adding of COM in ultrapure water (UPW) at measured temperatures.

T (°C)	**pH for UPW**	**Average**	**std dev.**	**pH for the COM in UPW**	**Average**	**std dev.**
25	7.12			7.09		
	7.15	7.07	0.109	7.17	7.08	0.101
	6.95			6.97		
37	6.88			6.91		
	6.8	6.82	0.049	6.85	6.83	0.086
	6.79			6.74		
60	6.2			6.1		
	6.55	6.47	0.248	6.68	6.493	0.341
	6.68			6.7		
90	6.2			6.33		
	6.4	6.26	0.118	6.3	6.26	0.096
	6.19			6.15		

A.4. Modelling: Detailed list of association constants

In this section, we provide detailed list of association constants used in modelling.

Table A. 13. Association reactions and their equilibrium constants at 37 ºC from literature.

Parameters	Reaction	Source	K value
K_{H_3Cit}	$H_3Cit \rightleftarrows H^+ + H_2Cit^-$	5	1348
$K_{H_2Cit^-}$	$H_2Cit^- \rightleftarrows H^+ + HCit^{2-}$	5	57544
$K_{HCit^{2-}}$	$HCit^{2-} \rightleftarrows H^+ + Cit^{3-}$	5	$2.51 \cdot 10^6$
$K_{H_3PO_4}$	$H_3PO_4 \rightleftarrows H^+ + H_2PO_4^-$	6	141.3
$K_{H_2PO_4^-}$	$H_2PO_4^- \rightleftarrows H^+ + HPO_4^{2-}$	6	$1.58 \cdot 10^7$
$K_{HPO_4^{2-}}$	$HPO_4^{2-} \rightleftarrows H^+ + PO_4^{3-}$	6	$2.4 \cdot 10^{12}$
K_{Gly}	$Gly \rightleftarrows H^+ + Gly^-$	7	$6.03 \cdot 10^9$
$K_{\mathrm{NaCit}^{2-}}$	$NaCit^{2-} \rightleftarrows Na^+ + Cit3^-$	5	8.5
K_{CaCit^-}	$CaCit^- \rightleftarrows Ca^{2+} + Cit3^-$	6	$4.76 \cdot 10^4$
K_{CaHCit}	$CaHCit \rightleftarrows Ca^{2+} + HCit^{2-}$	6	2860
$K_{\mathrm{NaC_2O_4^-}}$	$NaC_2O_4^- \rightleftarrows Na^+ + C_2O_4^{2-}$	8	1.035
K_{CaGly^+}	$CaGly^+ \rightleftarrows Ca^{2+} + Gly$	9	25.1

Table A. 14. Solubility of Calcium from Streit et al. study[10], dissolved COM in ultrapure water is measured by ICP-OES and simulation values are seen below;

T (°C)	Streit et al.[10]	ICP-OES	Simulation
	[Ca]M	[Ca]M	[Ca]M
25	$4.85\cdot10^{-5}$	$1.05\cdot10^{-4}$	$1.08\cdot10^{-4}$
37	$5.09\cdot10^{-5}$	$1.24\cdot10^{-4}$	$1.13\cdot10^{-4}$
60	$5.54\cdot10^{-5}$	$1.25\cdot10^{-4}$	$1.24\cdot10^{-4}$
90	$6.11\cdot10^{-5}$	$1.33\cdot10^{-4}$	$1.38\cdot10^{-4}$

Dissolved COM concentrations in ultrapure water are measured by ICP-OES as a function of temperature. Simulated values using the K_{sp} values of Streit et al.[10] and the fit of the ICP-OES results with the simulated total soluble Calcium concentration after estimation of $K_{sp,0}$ and ΔH_r using the Van 't Hoff equation. These values are used in Equation 2.4 in the Chapter 2.

A.5. Characterization of suspended crystals via Raman and XRD

To check the polymorph purity, Raman and PXRD measurements are done using samples before and after the solubility measurements.

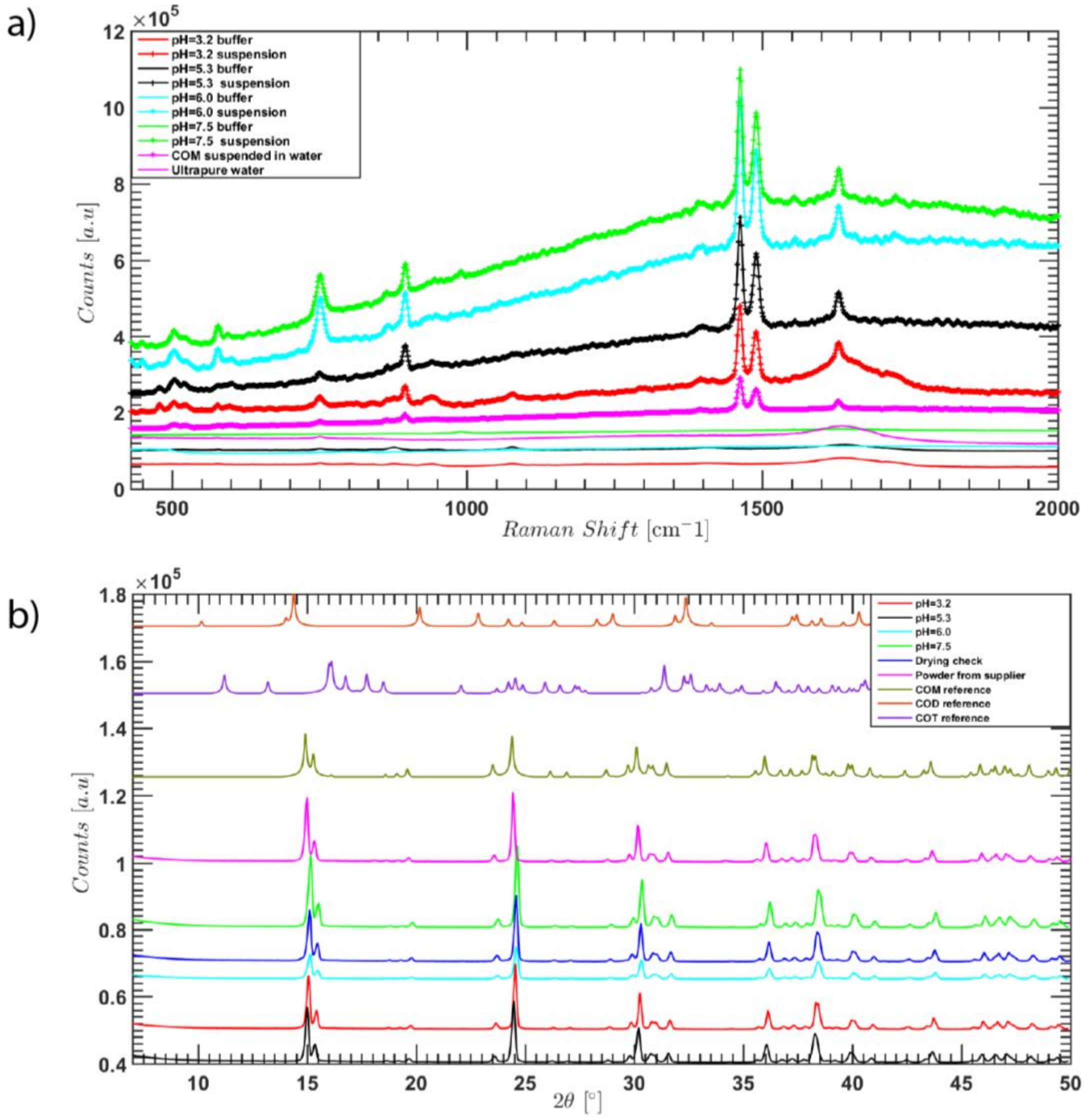

Figure A. 1. Characterization of suspended crystals in a citric acid-disodium phosphate buffer for pH values of 3.2, 5.36, 6.0, and 7.55. a) The results of Raman measurements include just buffer (-), just water (-) or the suspension (+) of COM in buffer. pH=3.2; red, pH=5.3; black, pH=6.0; cyan pH=7.55; green, ultrapure water; magenta (-), the suspension of COM in water; magenta (+). b) The results of XRD measurements. pH=3.2; red, pH=5.3; black, pH=6.0; cyan, pH=7.55; green, mixture of COM in water; blue, COM reference; dark green, COD; orange and COT; purple.

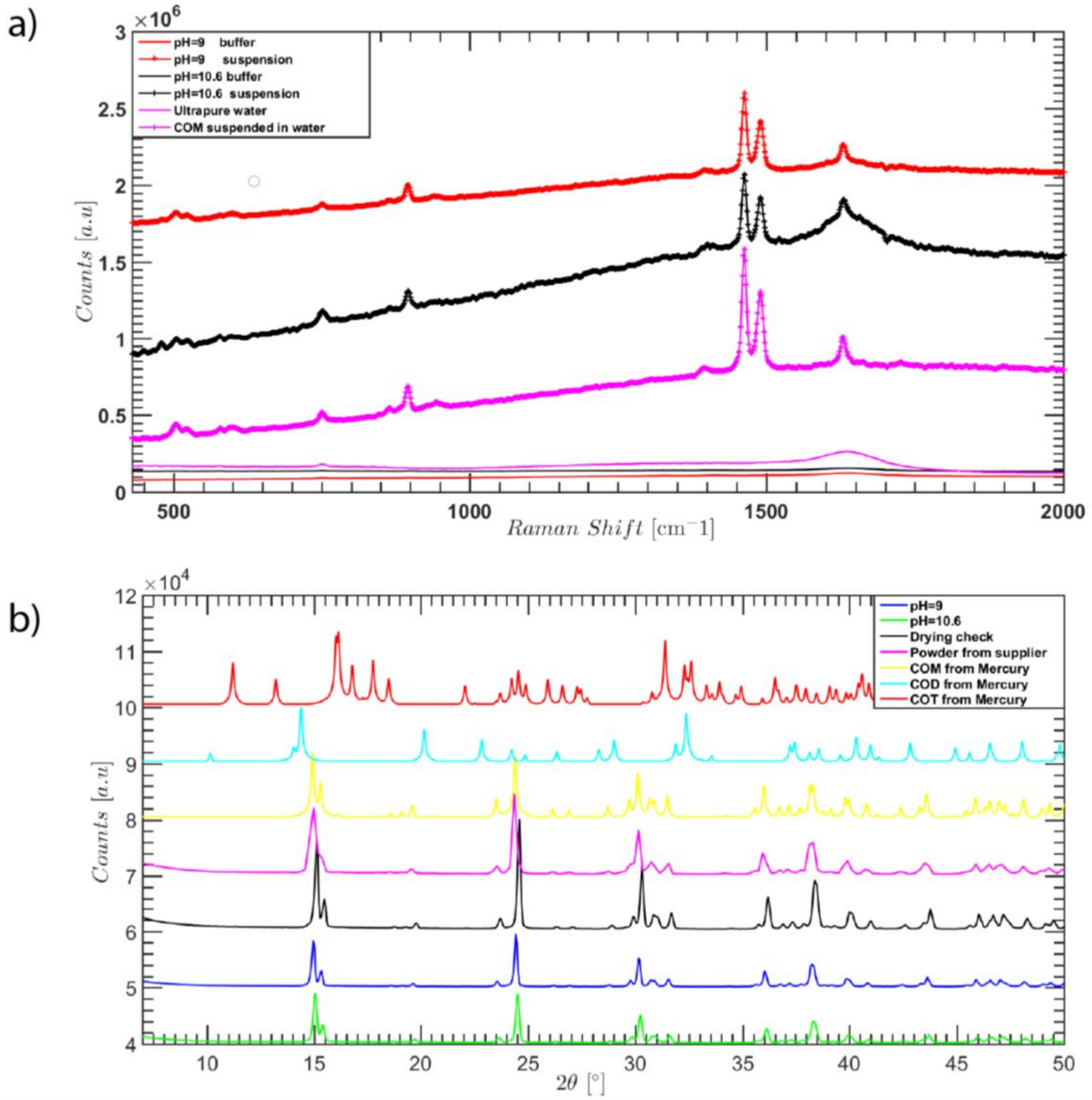

Figure A. 2. Characterization of suspended crystals in a Sodium hydroxide (NaOH) and for pH values of 9.0 and 10.6 a) The results of Raman measurements include just buffer (-), just water (-) or the suspension (+) of COM in buffer. pH=9.0; red, pH=10,6; black, ultrapure water; magenta (-), the suspension of COM in water; magenta (+). b) The results of XRD measurements. pH=9.0; blue, pH=10.6; green, mixture of COM in water; black, COM from supplier; magenta, COM reference; yellow, COD; cyan and COT; red.

Figure A. 1.a and Figure A. 2.a show that the characteristic COM Raman bands are obtained at 504, 508 (O-C-O), 897 (C-C), 1463, 1490 (C-O), and 1629 (C-O) cm^{-1}.[11-13] The peak values show that crystals stayed always as COM in different conditions. pH experimental conditions do not lead transition from COM to another CaOx hydrate form. Figure A. 1.b and Figure A. 2.b verify that tuning pH values do not cause phase transformation from COM to Calcium Oxalate Dihydrate (COD) or Calcium Oxalate Trihydrate (COT). Crystal structure of COM (CALOXM03), COD (CAOXAL) and COT (ZZZUOQ01) data are taken from the Mercury database. COM crystals from Mercury are showing as high peak intensity as at the same plane positions at different pH values.

A.6. Characterization of suspended crystals via Microscope and Scanning Electron Microscopy

The crystals are placed on the glass cover slip to visualize with an optical microscope (Nikon TE) and a scanning electron microscope (SEM) for different temperatures and pH values. 50 µl COM suspension are taken from Easymax reactor and put in two thin microscope slides for characterization. We could not identify different hydrate forms with optical and scanning electron microscopy measurements.

A.6.1. Microscope images at different temperatures

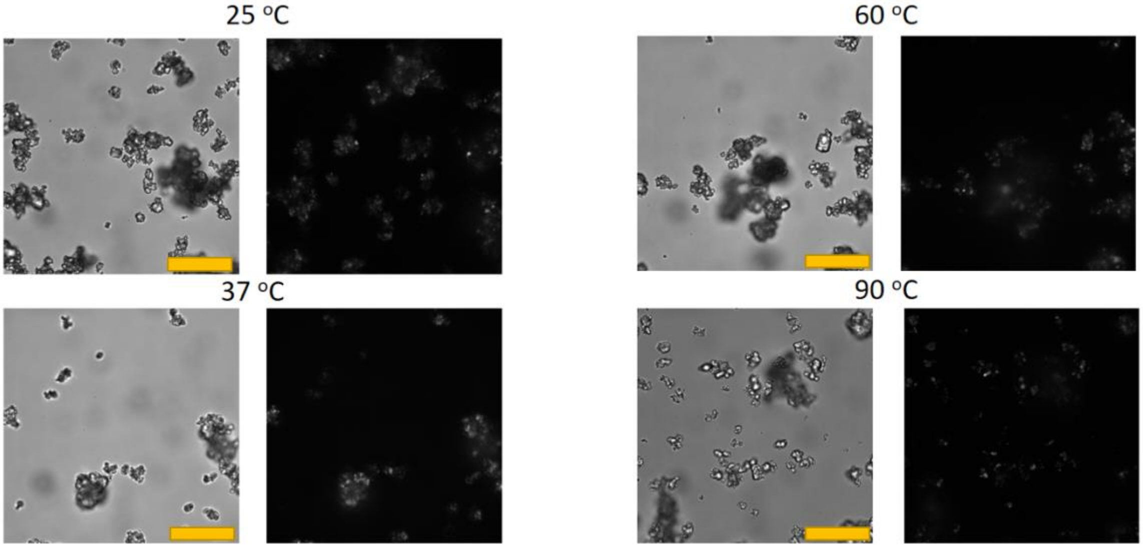

Figure A. 3. Characterization of CaOx forms via optical microscope at different temperatures. Left hand side images are taken in bright field mode (all the scale bars are 30µm), samples which are placed right are taken with crossed-polarized light at the same positions.

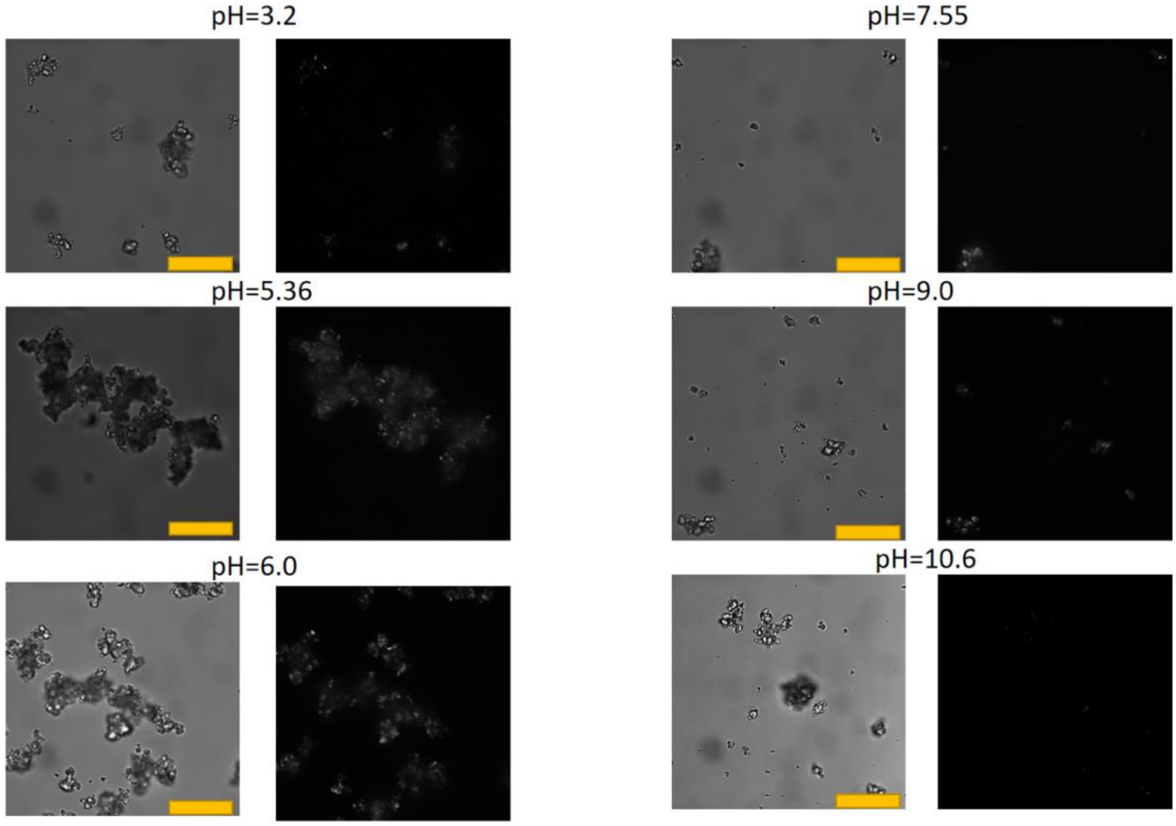

Figure A. 4. Characterization of CaOx forms via optical microscopy at different pH values. Left images were taken via at brightfield mode (all the scalebars are 30µm), samples which are placed right were taken with crossed-polarized light at the same positions.

A.6.2. Scanning Electron Microscopy (SEM)

SEM Images are taken for different temperatures, pH and without treatments of COM crystals.

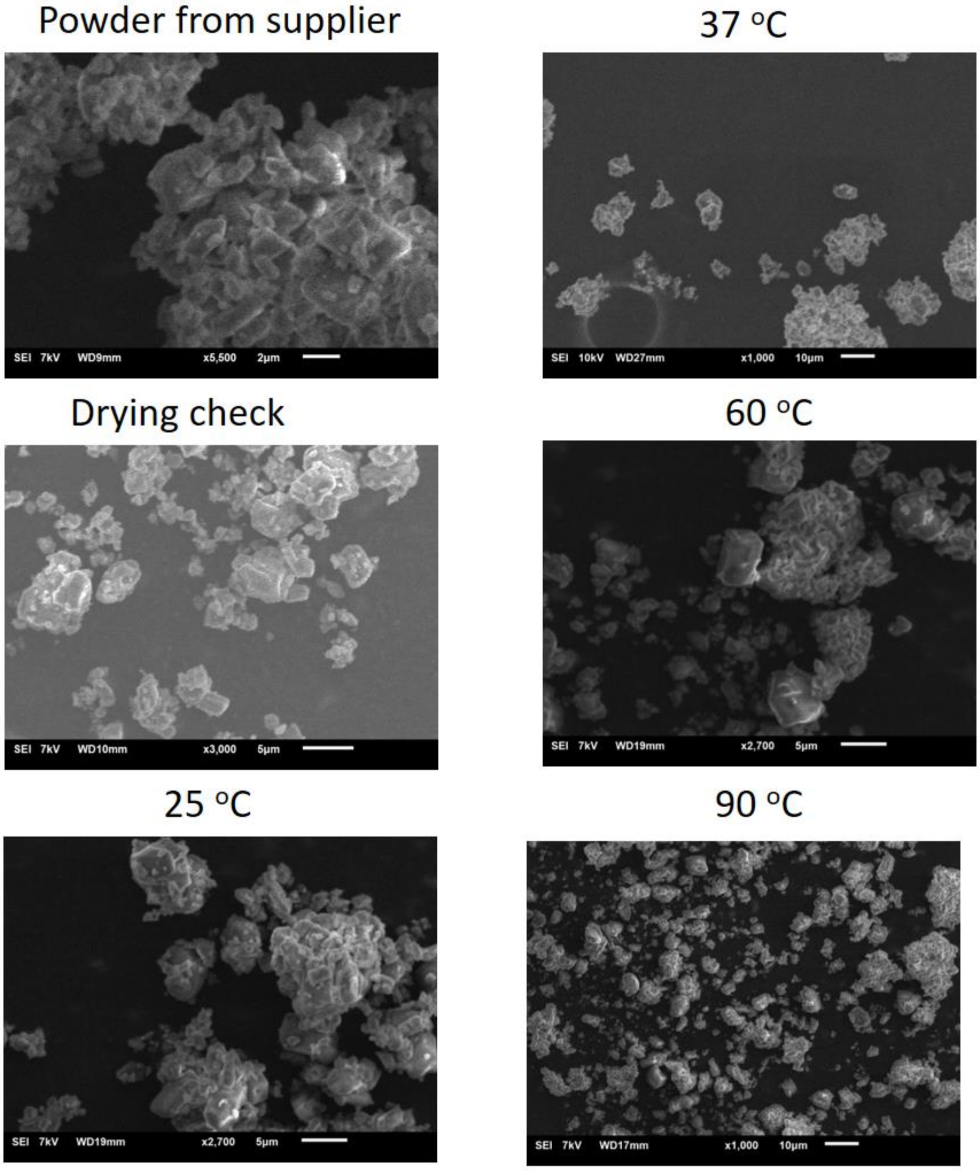
Powder from supplier

37 °C

Drying check

60 °C

25 °C

90 °C

Figure A. 5. Characterization of CaOx forms via SEM at different temperatures.

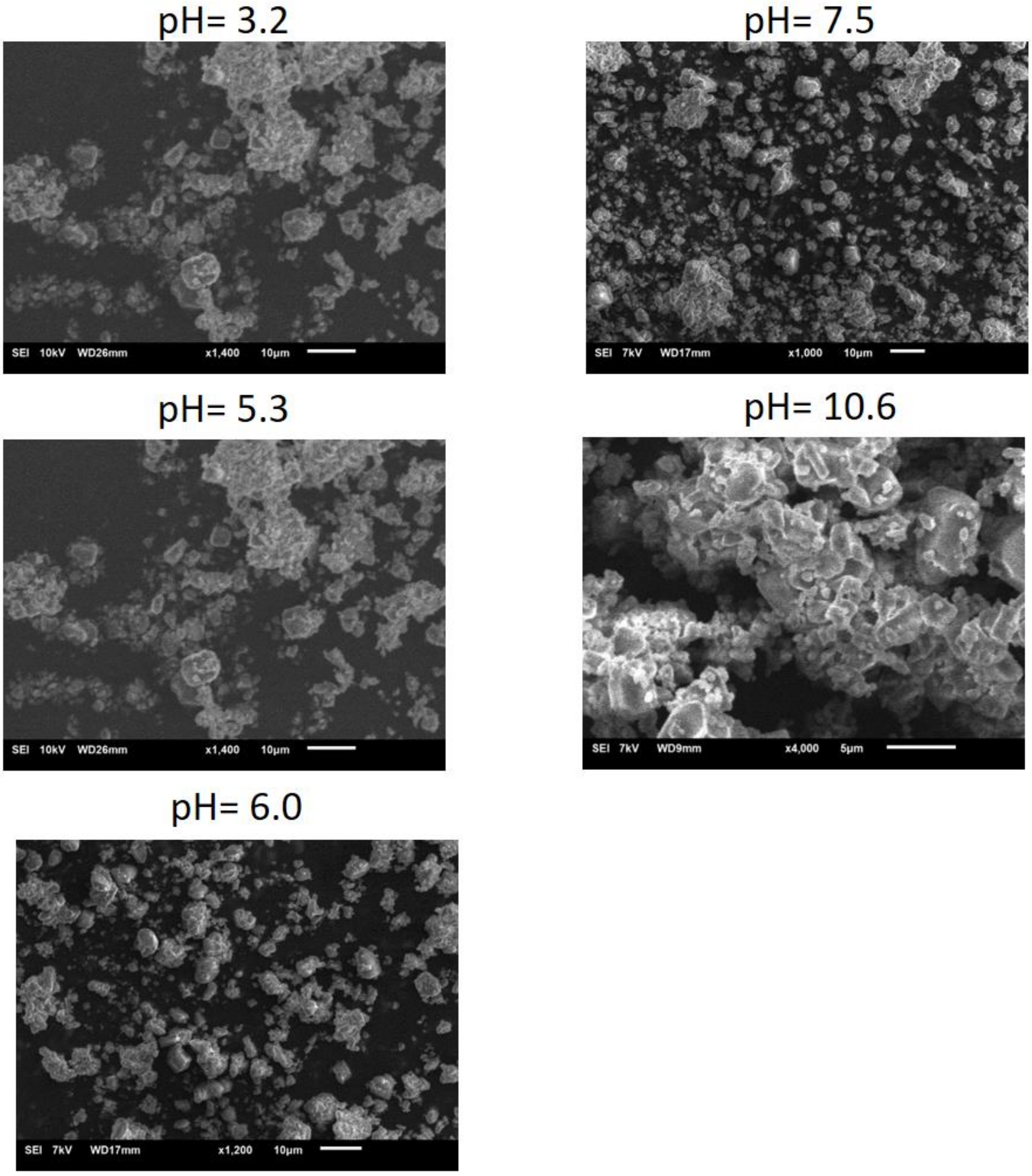
pH= 3.2

pH= 7.5

pH= 5.3

pH= 10.6

pH= 6.0

Figure A. 6. Characterization of CaOx forms via SEM at different pH values.

Based on the shape of the crystals we can guess of the crystal phases as COM, COD, and COT. The shape of our crystals is compared to literature to determine the crystal phase. Some crystals appear to be COM.[14, 15] But we could not draw conclusions on most crystals hence we cannot rule out existence of other hydrates COD and COT.

A.7. Calibration for ICP-OES

ICP-OES is using an external calibration. A multi-element standard (Merck chemicals), containing 1000 [ppm] Ca was used. From this solution, the dilutions to the proper range of calibration are done. Dilutions in 3 (m%) HNO_3. Calcium is calibrated for different wavelengths, 315.887 nm, 317.933 nm, 393.366 nm, and 396.847 nm. The certain amount of calcium chloride, sodium oxalate, and COM are dissolved in ultrapure water to check calibration of ICP-OES. The solutions were dissolved in Easymax during 1 hour at 400rpm using the same solution preparation methods. Besides that, water and diluted calcium solution are used. All samples are measured via ICP-OES at 317.9 nm. The results at chosen wavelength are presented in Table A. 15. Each values represent the average of three replications.

Known initial calcium concentrations are in agreement with ICP-OES results. We can conclude that calcium measurement at 317.9 nm by using ICP-OES are fully calibrated successfully.

Table A. 15. Different types of samples are measured via ICP-OES at 317.9 nm.

Solutions	**Average [Ca] 10^{-4} M**	**std. dev**
$0.2 \cdot 10^{-4}$ M COM	0.206	0.005
$1 \cdot 10^{-4}$ M COM	0.998	0.041
$1.5 \cdot 10^{-4}$ M COM	1.495	0.078
$15 \cdot 10^{-4}$ M Calcium Solution	14.729	0.281
$10 \cdot 10^{-4}$ M Calcium Solution	9.973	0.111
$5 \cdot 10^{-4}$ M Calcium Solution	4.941	0.072
$1.5 \cdot 10^{-4}$ M Calcium Solution	1.501	0.009
$0.5 \cdot 10^{-4}$ M Calcium Solution	0.503	0.012
$0.2 \cdot 10^{-4}$ M Calcium Solution	0.198	0.005
$0.2 \cdot 10^{-4}$ M $CaCl_2$	0.199	0.045
1x10^{-4} M $CaCl_2$	1.055	0.034
1.5x10^{-4} M $CaCl_2$	1.519	0.012
Ultrapure water	0.006	0.000
0.2x10^{-4} M NaOx	0.000	0.000
1.5x10^{-4} M NaOx	0.001	0.001
1x10^{-4} M NaOx	0.005	0.001

Appendix B for Chapter 3

Graphical abstract

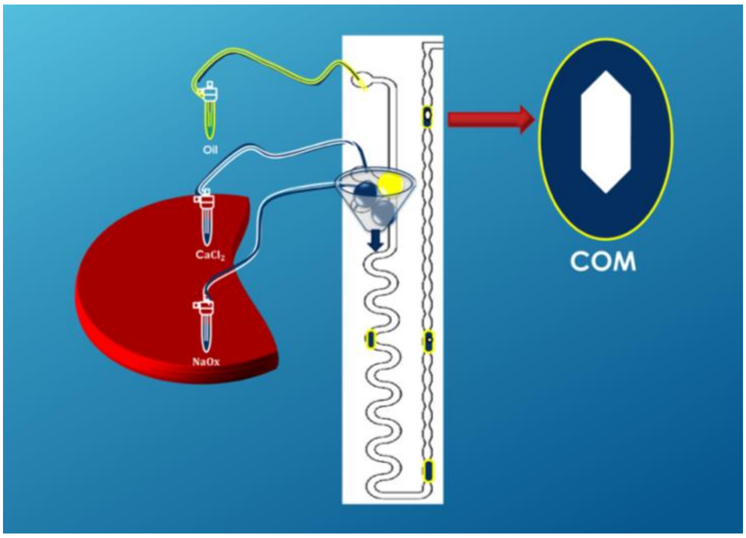

B.1. Microfluidic mold design

The microfluidic chip is designed with SolidWorks and printed via 3D printer (EnvisionTEC Micro Plus Hi-Res - 43x27mm). The printer has a resolution of 30 microns for x and y direction and a resolution of 25 microns for z-direction. The chambers` sizes are 200 µm depth, 400 µm width and 1200 µm length and narrow necks are 180 µm.

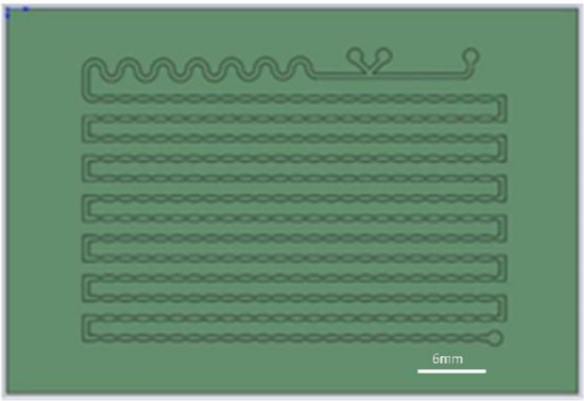

Figure B. 1. 3D printing of soft lithography mold for rapid production of PDMS microfluidic device to use for experiments. Scale bar is 6mm.

Droplets are stored in chambers in the storage part of the chip (Figure 2.1.b in the main text). Droplet volumes are measured using the images from the microfluidic chip. The average surface area of droplets is found using three droplets via publicly available software, Image J. Surface area 0.257 (±0.013)·10^{-6} m^2 is multiplied with the channel depth (2.0·10^{-4} m) to calculate the volume droplets. The droplet volume is found as 5.15·10^{-11} m^3.

The droplets always stayed in the same positions. Their sizes did not change, and the volume was stable during experiments (Even with overnight experiment trials).

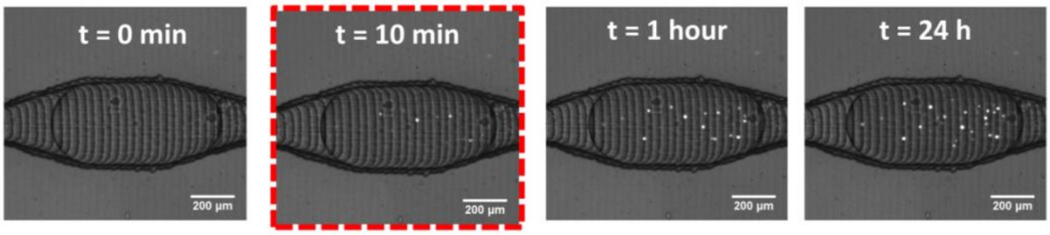

Figure B. 2. The volume of droplets does not change overnight. t=0 min, t=10 min (induction time), t=1 hour and t=24 hours are seen in figure. The droplet with $[Ca^{2+}]=[Ox^{2}]$ of 4.1·10^{-4} M.

B.2. The cumulative induction time probability distributions with Weibull

We have compared two different equations to fit the experimental data. For this reason; the data in the chapter 3, Figure 3.4, Figure 3.5,Figure 3.6 and Figure 3.7 are fitted with a single exponential function given as Equation 3.1 in Chapter 3. The data in Figure B. 3, Figure B. 4, Figure B. 5, and Figure B. 6. show the fits using the well-known Weibull function. The experimentally acquired p(t) are fitted by the Weibull function shown in Equation B. 1.

The Weibull function is commonly used to describe the probability distribution to account for measured deviations from the exponential behavior the p(t) plot.

$$p(t) = 1 - e^{-\left(\frac{t}{\tau}\right)^{k}}$$

Equation B. 1

The shape parameter k, is well suited to fit the sometimes-encountered s-shaped p(t) plots and informs us of the functional form of the nucleation rate. When k = 1 the Weibull model reduces to an exponential model. For k <1, the nucleation rate is decreasing and for $k > 1$, the nucleation rate is increasing with time under conditions of constant concentrations and temperature.[16]

Fitting Equation B. 1 to the p(t) curves enables the calculation of the effective nucleation rate, J. To calculate an effective nucleation rate with p(t) curves fitting the Weibull model, we need to consider the fact that the effective nucleation rate can be a function of time depending on the value of k, so we have to calculate a time averaged J. This can be achieved by relating the fitted characteristic crystallization time, τ, to the median induction time, t_{MED}, by $\tau = t_{MED} (\ln 2)^{1/k}$.

The colorful shading around the fitted curves represents the 95 % confidence interval of the fitting in figures of the cumulative induction time probability vs. time.

B.3. Figures and tables for added calcium concentrations in ultrapure water

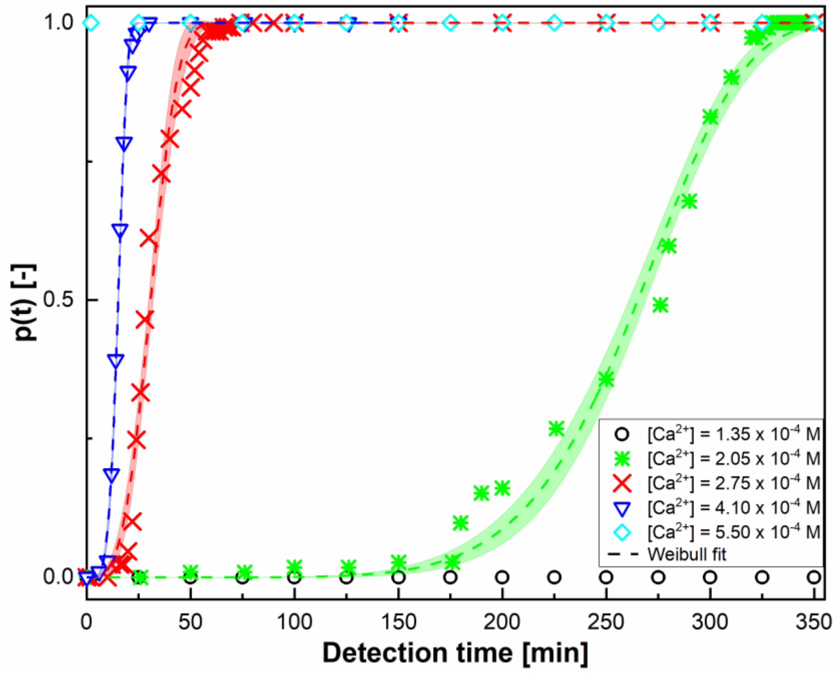

Figure B. 3. The cumulative induction time probability, p(t) as a function of the detection time, t, for different added Ca^{2+} concentrations in ultrapure water fitted with the Weibull model (Equation B. 1). The ratio of added molar concentration of Ca^{2+} and $C_2O_4^{2-}$ ions is the same for all experiments $[Ca^{2+}]/[C_2O_4^{2-}]=1$ for all solutions. The calculated initial free Ca^{2+} and $C_2O_4^{2-}$ ion concentrations, their activity coefficient and the initial supersaturation of COM in the droplets are given in Table 3.2 (in the Chapter 3).

Table B. 1. The fitted parameters with 95% confidence intervals and corresponding statistics from Weibull model without delay time for different added Calcium concentrations (for Figure B. 3)

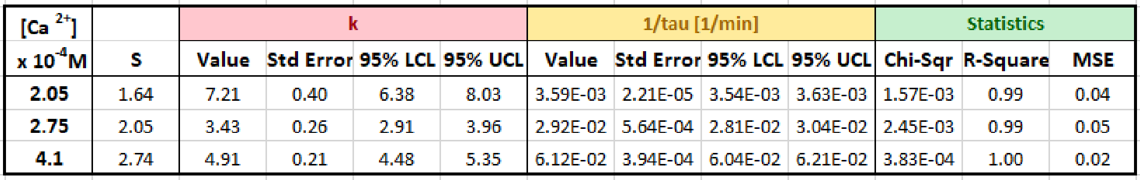

$[Ca^{2+}]$		k				1/tau [1/min]				Statistics		
$\times 10^{-4}$M	S	Value	Std Error	95% LCL	95% UCL	Value	Std Error	95% LCL	95% UCL	Chi-Sqr	R-Square	MSE
2.05	1.64	7.21	0.40	6.38	8.03	3.59E-03	2.21E-05	3.54E-03	3.63E-03	1.57E-03	0.99	0.04
2.75	2.05	3.43	0.26	2.91	3.96	2.92E-02	5.64E-04	2.81E-02	3.04E-02	2.45E-03	0.99	0.05
4.1	2.74	4.91	0.21	4.48	5.35	6.12E-02	3.94E-04	6.04E-02	6.21E-02	3.83E-04	1.00	0.02

B.4. Figures and tables for added equimolar $[Ca^{2+}]= [C_2O_4^{2-}]=4.1x10^{-4}$ calcium and oxalate concentration in different buffer solutions

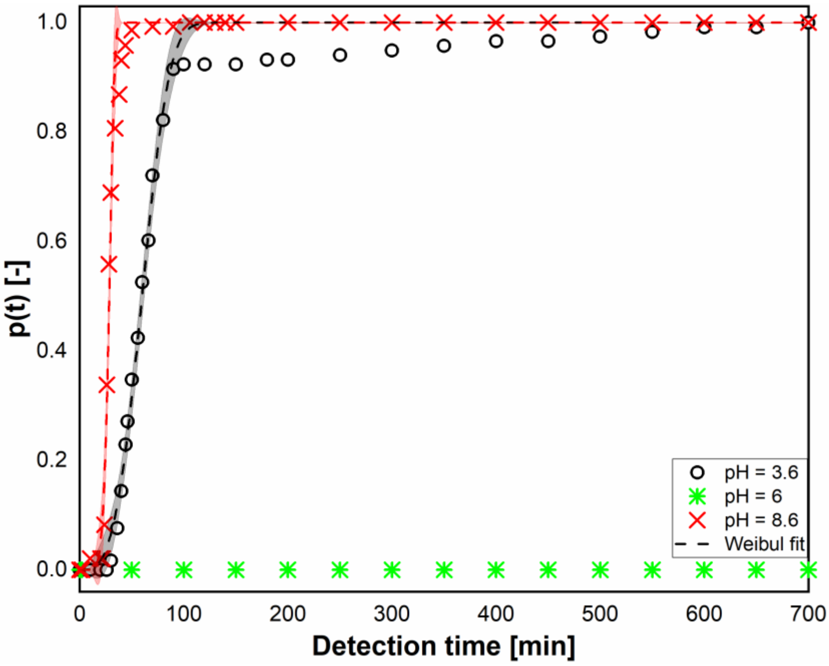

Figure B. 4. The cumulative induction time probability, p(t) curves for different pH values fitted with the Weibull model (Equation B. 1). The composition of the buffer solutions for pH values of 3.6, 6.0, and 8.6 are shown in Table 3.1 (in the Chapter 3). The added equimolar Ca^{2+} and $C_2O_4^{2-}$ concentration of $4.1·10^{-4}$ M is used in all experiments. The calculated initial free Ca^{2+} and $C_2O_4^{2-}$ ion concentrations, their activity coefficient and the initial supersaturation of COM in the droplets are given in Table 3.3 (in the Chapter 3).

Table B. 2. The fitted parameters with 95% confidence intervals and the corresponding statistics from the Weibull model without delay time for the equimolar concentration of $[Ca^{2+}]=[C_2O_4^{2-}]$ in different buffer solutions for pH values of 3.6 and 8.6 (for Figure B. 4).

		k				1/tau [1/min]				Statistics		
	S	Value	Std Error	95% LCL	95% UCL	Value	Std Error	95% LCL	95% UCL	Chi-Sqr	R-Square	MSE
pH = 3.6	1.64	3.35	0.20	2.94	3.76	0.01	2.11E-04	0.01	0.02	1.52E-03	0.99	0.04
pH = 8.6	2.53	7.55	0.80	5.93	9.18	0.03	3.85E-04	0.03	0.03	2.23E-03	0.99	0.05

B.3. Figures and tables for varying concentrations of Mg^{2+} ions are added to equimolar calcium and oxalate concentrations

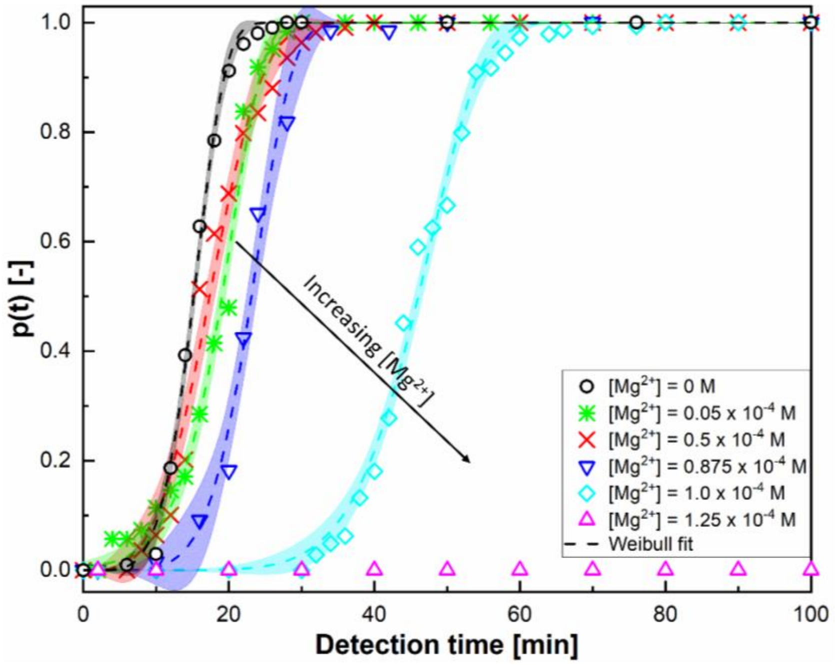

Figure B. 5. The cumulative induction time probability curves, p(t) at specific Mg^{2+} concentrations fitted with the Weibull model (Equation B. 1). The varying concentrations of Mg^{2+} ions are added to equimolar calcium and oxalate concentration of $[Ca^{2+}]=[C_2O_4^{2-}]=4.1\cdot10^{-4}$ M. The calculated initial free Ca^{2+} and $C_2O_4^{2-}$ ion concentrations, their activity coefficient and the initial supersaturation of COM in the droplets are given in

Table 3.4 (in the Chapter 3).

Table B. 3. The fitted parameters with 95% confidence intervals and the corresponding statistics from the Weibull model without delay time for the equimolar concentration of $[Ca^{2+}]=[C_2O_4^{2-}]$ with additives various amount of Magnesium (for Figure S5).

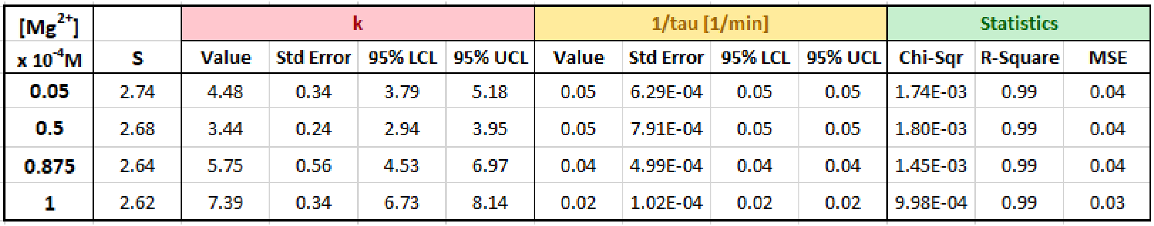

[Mg^{2+}]		k				1/tau [1/min]				Statistics		
x 10^{-4}M	S	Value	Std Error	95% LCL	95% UCL	Value	Std Error	95% LCL	95% UCL	Chi-Sqr	R-Square	MSE
0.05	2.74	4.48	0.34	3.79	5.18	0.05	6.29E-04	0.05	0.05	1.74E-03	0.99	0.04
0.5	2.68	3.44	0.24	2.94	3.95	0.05	7.91E-04	0.05	0.05	1.80E-03	0.99	0.04
0.875	2.64	5.75	0.56	4.53	6.97	0.04	4.99E-04	0.04	0.04	1.45E-03	0.99	0.04
1	2.62	7.39	0.34	6.73	8.14	0.02	1.02E-04	0.02	0.02	9.98E-04	0.99	0.03

B.5. Figures and tables are for three different osteopontin concentrations in equimolar calcium and oxalate concentrations

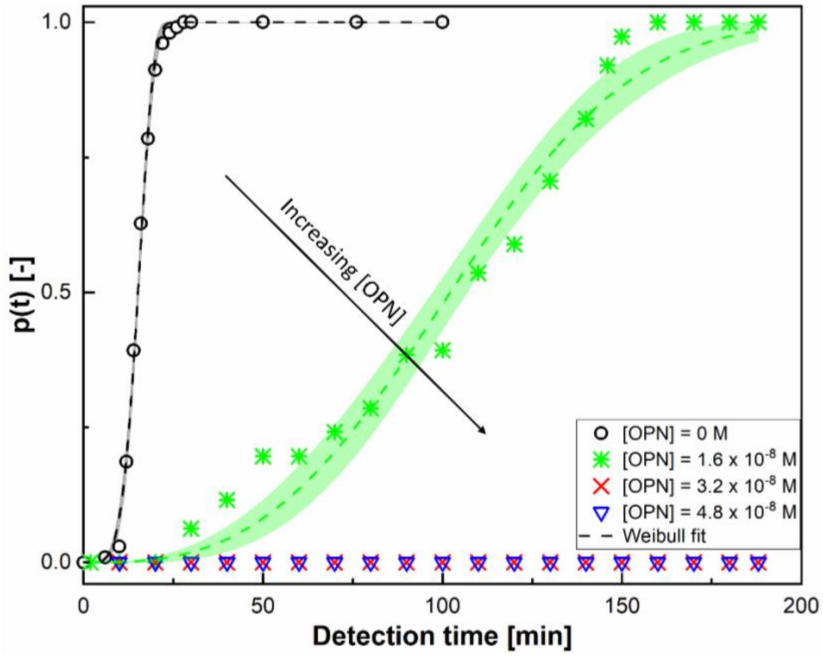

Figure B. 6. The cumulative induction time probability curves at specific osteopontin concentrations fitted with the Weibull model given in Equation B. 1. The arrow points towards the direction of increasing OPN concentration. The Ca^{2+} and $C_2O_4^{2-}$ concentrations are kept constant at $4.1 \cdot 10^{-4}$ M.

Table B. 4. The fitted parameters with 95% confidence intervals and the corresponding statistics from the Weibull model without delay time for the equimolar concentration of $[Ca^{2+}]=[C_2O_4^{2-}]$ with additive $1.6 \cdot 10^{-8}$ M Osteopontin (for Figure B. 6).

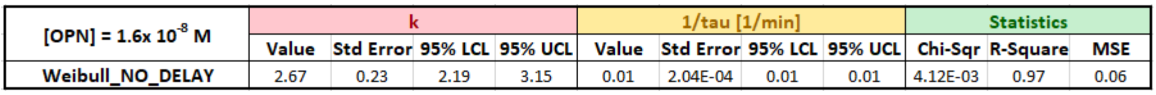

[OPN] = 1.6x 10^{-8} M	k				1/tau [1/min]				Statistics		
	Value	Std Error	95% LCL	95% UCL	Value	Std Error	95% LCL	95% UCL	Chi-Sqr	R-Square	MSE
Weibull_NO_DELAY	2.67	0.23	2.19	3.15	0.01	2.04E-04	0.01	0.01	4.12E-03	0.97	0.06

p(t) fits are performed using single exponential (Equation 3.1 in Chapter 3) and the Weibull function (Equation B. 1) comparing the results in terms of their goodness of fit statistics.

An enhancement in the goodness of fit using the Weibull function is not detected (Table B. 1, Table B. 2, Table B. 3, Table B. 4) and we conclude that single exponential (Table 3.5) described the cumulative probability curves efficiently for our purpose.

Single exponential fit allows us to evaluate effective nucleation rates, growth rate analysis and interpretation in classical nucleation theory (CNT) at different supersaturation ratios significantly.

Appendix C for Chapter 4

Graphical abstract

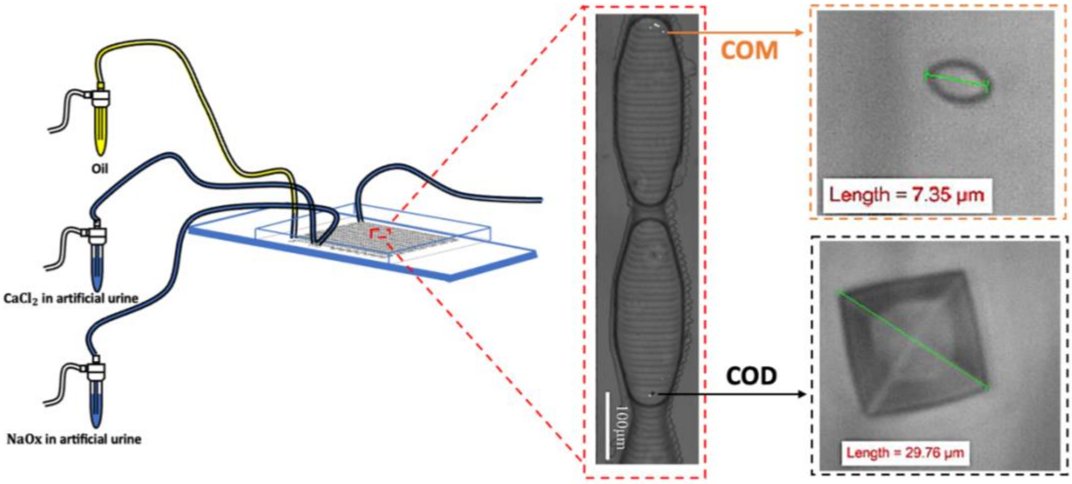

C.1. Closed microfludic system

For each experiment, a new chip is produced and used. For a closed microfluidic system, both peeling PDMS from mold and completing spin coating is quite important. For spin coating, peeled and cured PDMS (with 7:1 w/w ratio of PDMS and curing agent) chip and a new PDMS mixture are needed. For the new PDMS mixture, PDMS and curing agent at a 10:1 (w/w) ratio are prepared to coat the microscope slide (Thickness 1 mm). 0.5 ml of this new PDMS solution (see Figure S.1.a) is spin-coated at 4500 rpm on the microscope slide and semi-cured for 1 min. The pealed and cured PDMS (with 7:1 w/w ratio) chip (see Figure S.1.b) is placed on top of the microscope slide covered with the semi-cured PDMS layer (10:1) and cured for 20 minutes at 65 °C. Once the chip and spin-coated layer stick to each other, the closed device is kept in the oven 65 °C overnight to complete curing.

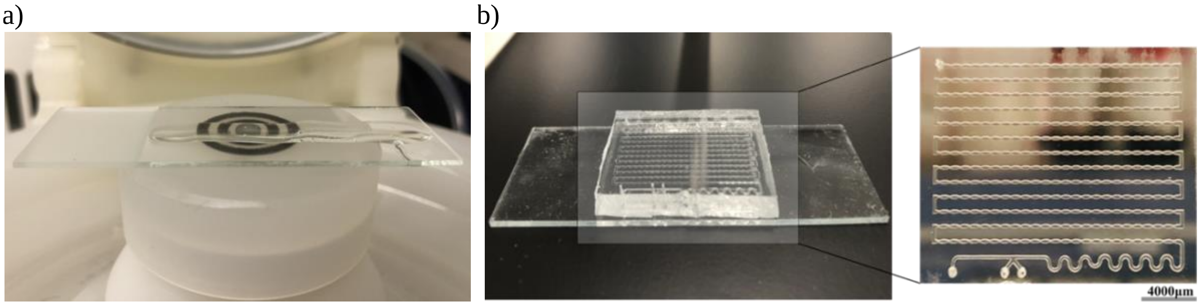

Figure C. 1. a) 0.5 ml PDMS mixing is placed glass slide to make spin coating. b) The cured and peeled PDMS chip is carefully placed on the glass slide with the semi-cured spin-coated PDMS layer.

C.2. Characterizations of pseudo-polymorphic form of the calcium oxalate stones

A visual examination of the shape of these crystals in artificial urine under a microscope was studied with ranging calcium chloride ($CaCl_2$) and sodium oxalate (NaOx) at the droplet-based microfluidic platform. Before the visual examination with a microfluidic platform, the initial experiments were done using a well-mixed reactor, Easymax (Mettler Toledo) at room temperature. The precipitated crystals were characterized by light microscopy and Raman spectroscopy to prove that the visual observations using polarized light are in line with the results obtained using Raman spectra. Therefore, the vibrational mode (or structural fingerprint) of the various CaOx phases in artificial urine is determined using Raman spectroscopy (Kaiser Optical Systems, Model Rxn2, US).

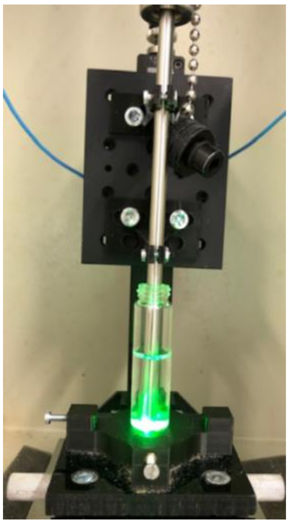

Figure C. 2. The Raman probe is detecting crystal in the glass vial.

Non-equimolar concentrations of [CaCl$_2$]=6.0 mM and [NaOx]=1.2 mM and equimolar concentrations of [CaCl$_2$]=4.3 mM and [NaOx]=4.3 mM in artificial urine solutions are used to obtain CaOx crystals which were analysed both by Raman spectroscopy (see Figure C.3) and microscope images (see Figure C.4 and C.5). Artificial urine and Calcium oxalate powder are also used to distinguish peaks clearly.

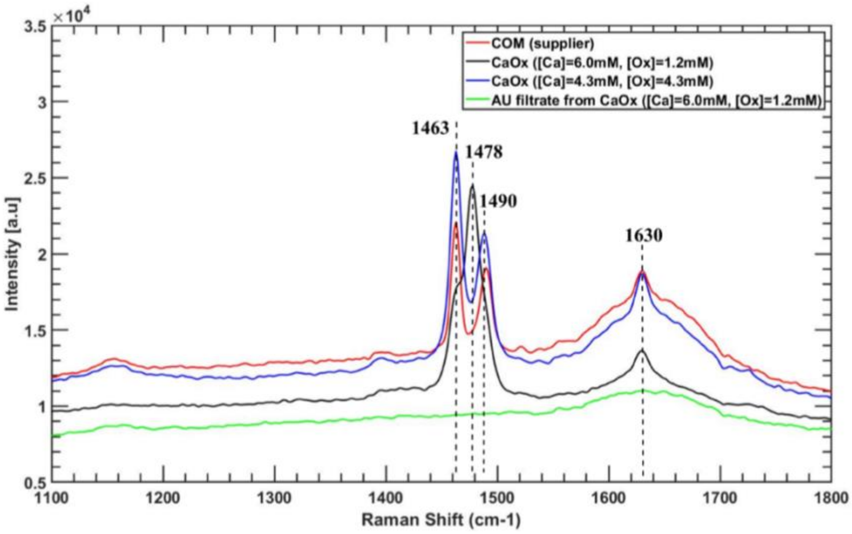

Figure C. 3. Characterization of the crystal structure of the formed crystals in artificial urine with Raman probe. The samples of the COM from supplier (red), non-equimolar solutions (black), equimolar solutions (blue), and filtrated artificial urine solution (green) are from non-equimolar solutions.

Artificial urine has various ingredients.[10] Reactions could be seen and could be caused by different products such as calcium phosphate, magnesium oxalate, etc. Raman probe was immersed in suspension to ensure that the crystals formed are only CaOx. COM and COD peaks dominate, respectively, when equimolar and non-equimolar ratios of the reactants are used. The peak results are parallel with literature values. The results are also matched with COM powder from the supplier ($CaC_2O_4 \cdot H_2O$, Sigma-Aldrich, CAS563-72-4), which has identical peak wavenumbers. The main absorption peaks for COM are observed at 1463 and 1490 (C-O) cm^{-1}.[11-13] A weak peak for COM also is observed at 1630 and is usually assigned to C-O asymmetric stretching mode.[17] Another crystal type, COD, gave the main absorption peak at 1478 which is assigned the (C-O) stretching.[12, 17] Raman spectroscopy could identify CaOx hydrates and it is seen only COM and COD in a predominant level.

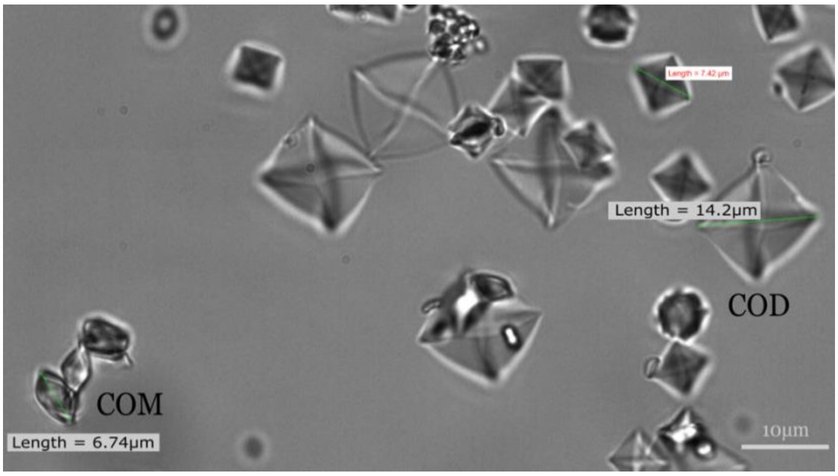

Figure C. 4. COM and COD crystals are seen in artificial urine via microscope with non-equimolar concentrations of [$CaCl_2$]=6.0 mM and [NaOx]=1.2 mM (Figure C. 3. peaks with black color). The polarizer is aligned at a 0-degree angle making it perpendicular to the analyzer.

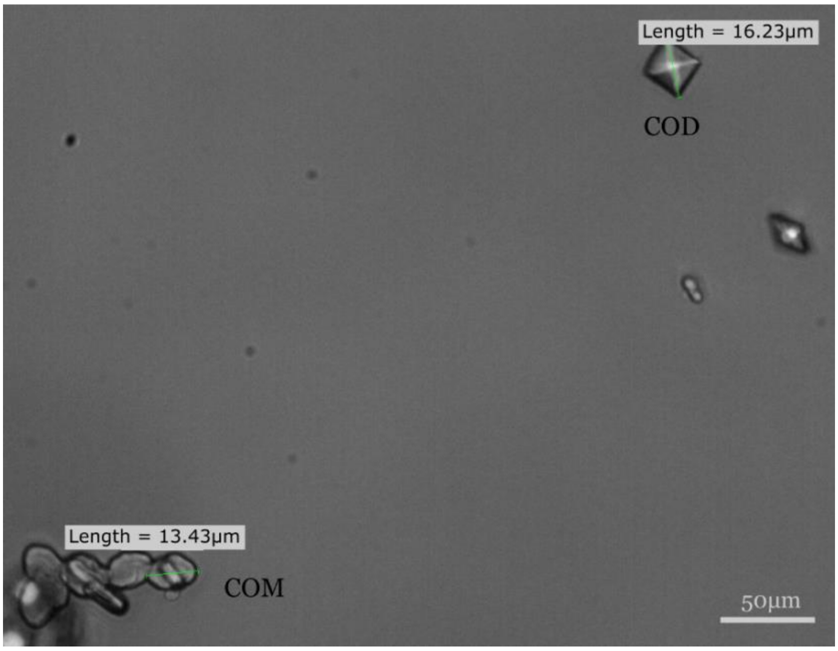

Figure C. 5. COM and COD crystals are seen in artificial urine via microscope with equimolar concentrations of [$CaCl_2$]=4.3 mM and [NaOx]=4.3 mM (Figure C. 3.peaks with blue color). The polarizer is aligned at a 0-degree angle making it perpendicular to the analyzer.

C.3. The droplet image at end of the experiment

Each image from the five hours recorded video is manually scanned to detect the first crystal emerging in each droplet. The polarized microscopy at 20° degree provided identification of the COM as bright spots while the COD appears as black spots. Figure C.6 shows the droplet has COM and COD together for five hours recording for sample has 6 mM of $CaCl_2$ and 0.85 mM of NaOx in artificial urine.

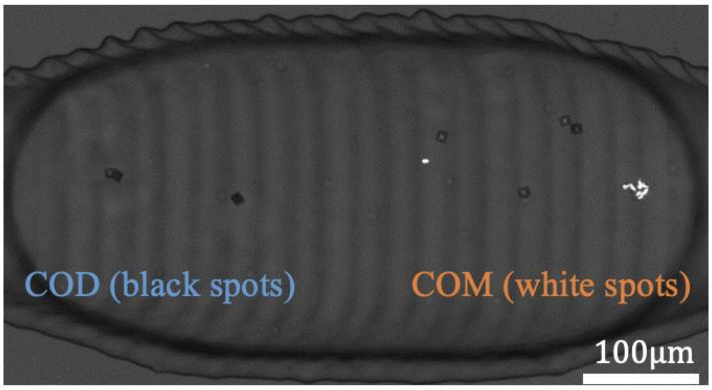

Figure C. 6. The droplet contains COD as black spots, and COM as white spots at 5. hours. The droplet has 6 mM of $CaCl_2$ and 0.85 mM of NaOx in artificial urine.

C.4. The extended tables for the single exponential model of COD and COM

The extended version of tables (Table C.1&2 in the manuscript) with %95 confidence intervals is seen below;

Table C.1. *The fitted parameters, standard errors, and the error statistics of the fits from a single exponential model with a delay time of COD and COM for the different added oxalate concentrations. MSE stands for mean squared error.*

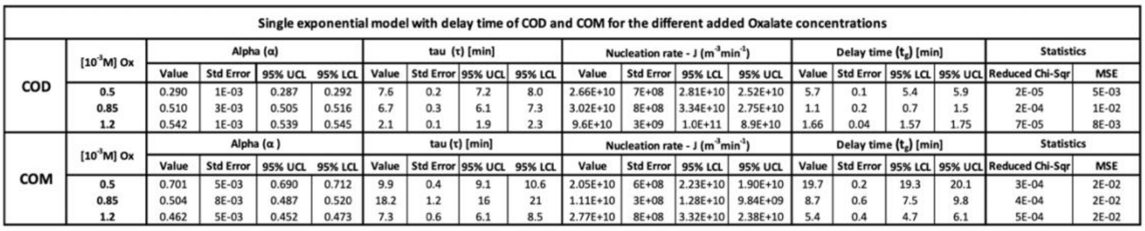

Single exponential model with delay time of COD and COM for the different added Oxalate concentrations

	[10^{-3}M] Ox	Alpha (α)				tau (τ) [min]				Nucleation rate - J ($m^{-3}min^{-1}$)				Delay time (t_g) [min]				Statistics	
COD		Value	Std Error	95% UCL	95% LCL	Value	Std Error	95% UCL	95% LCL	Value	Std Error	95% LCL	95% UCL	Value	Std Error	95% LCL	95% UCL	Reduced Chi-Sqr	MSE
	0.5	0.290	1E-03	0.287	0.292	7.6	0.2	7.2	8.0	2.66E+10	7E+08	2.81E+10	2.52E+10	5.7	0.1	5.4	5.9	2E-05	5E-03
	0.85	0.510	3E-03	0.505	0.516	6.7	0.3	6.1	7.3	3.02E+10	8E+08	3.34E+10	2.75E+10	1.1	0.2	0.7	1.5	2E-04	1E-02
	1.2	0.542	1E-03	0.539	0.545	2.1	0.1	1.9	2.3	9.6E+10	3E+09	1.0E+11	8.9E+10	1.66	0.04	1.57	1.75	7E-05	8E-03
COM	[10^{-3}M] Ox	Alpha (α)				tau (τ) [min]				Nucleation rate - J ($m^{-3}min^{-1}$)				Delay time (t_g) [min]				Statistics	
		Value	Std Error	95% UCL	95% LCL	Value	Std Error	95% UCL	95% LCL	Value	Std Error	95% LCL	95% UCL	Value	Std Error	95% LCL	95% UCL	Reduced Chi-Sqr	MSE
	0.5	0.701	5E-03	0.690	0.712	9.9	0.4	9.1	10.6	2.05E+10	6E+08	2.23E+10	1.90E+10	19.7	0.2	19.3	20.1	3E-04	2E-02
	0.85	0.504	8E-03	0.487	0.520	18.2	1.2	16	21	1.11E+10	3E+08	1.28E+10	9.84E+09	8.7	0.6	7.5	9.8	4E-04	2E-02
	1.2	0.462	5E-03	0.452	0.473	7.3	0.6	6.1	8.5	2.77E+10	8E+08	3.32E+10	2.38E+10	5.4	0.4	4.7	6.1	5E-04	2E-02

Increasing of oxalate concentrations, the ratio of Ca: Ox is decreasing, and COD shows an increase in nucleation rate (J) and a decrease delay time.

Table C.2. *The fitted parameters, standard errors and the error statistics of the fits from a single exponential model with a delay time of COD and COM for the different amount of added HA. MSE stands for mean squared error.*

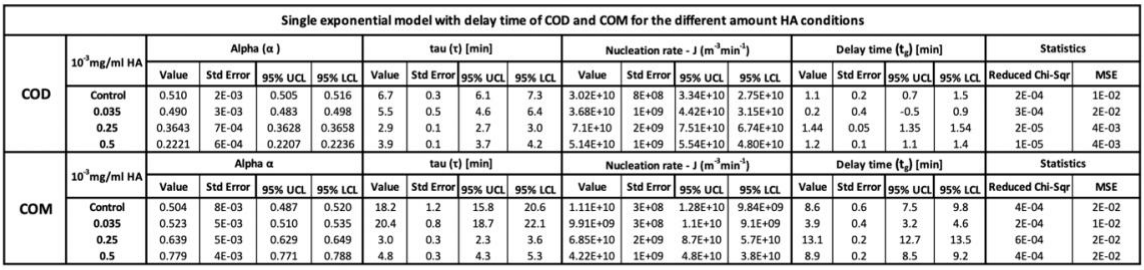

Single exponential model with delay time of COD and COM for the different amount HA conditions																			
	10^{-3}mg/ml HA	Alpha (α)				tau (τ) [min]				Nucleation rate - J ($m^{-3}min^{-1}$)				Delay time (t_g) [min]				Statistics	
		Value	Std Error	95% UCL	95% LCL	Value	Std Error	95% UCL	95% LCL	Value	Std Error	95% UCL	95% LCL	Value	Std Error	95% UCL	95% LCL	Reduced Chi-Sqr	MSE
COD	**Control**	0.510	2E-03	0.505	0.516	6.7	0.3	6.1	7.3	3.02E+10	8E+08	3.34E+10	2.75E+10	1.1	0.2	0.7	1.5	2E-04	1E-02
	0.035	0.490	3E-03	0.483	0.498	5.5	0.5	4.6	6.4	3.68E+10	1E+09	4.42E+10	3.15E+10	0.2	0.4	-0.5	0.9	3E-04	2E-02
	0.25	0.3643	7E-04	0.3628	0.3658	2.9	0.1	2.7	3.0	7.1E+10	2E+09	7.51E+10	6.74E+10	1.44	0.05	1.35	1.54	2E-05	4E-03
	0.5	0.2221	6E-04	0.2207	0.2236	3.9	0.1	3.7	4.2	5.14E+10	1E+09	5.54E+10	4.80E+10	1.2	0.1	1.1	1.4	1E-05	4E-03
	10^{-3}mg/ml HA	Alpha α				tau (τ) [min]				Nucleation rate - J ($m^{-3}min^{-1}$)				Delay time (t_g) [min]				Statistics	
		Value	Std Error	95% UCL	95% LCL	Value	Std Error	95% UCL	95% LCL	Value	Std Error	95% UCL	95% LCL	Value	Std Error	95% UCL	95% LCL	Reduced Chi-Sqr	MSE
COM	**Control**	0.504	8E-03	0.487	0.520	18.2	1.2	15.8	20.6	1.11E+10	3E+08	1.28E+10	9.84E+09	8.6	0.6	7.5	9.8	4E-04	2E-02
	0.035	0.523	5E-03	0.510	0.535	20.4	0.8	18.7	22.1	9.91E+09	3E+08	1.1E+10	9.1E+09	3.9	0.4	3.2	4.6	2E-04	1E-02
	0.25	0.639	5E-03	0.629	0.649	3.0	0.3	2.3	3.6	6.85E+10	2E+09	8.7E+10	5.7E+10	13.1	0.2	12.7	13.5	6E-04	2E-02
	0.5	0.779	4E-03	0.771	0.788	4.8	0.3	4.3	5.3	4.22E+10	1E+09	4.8E+10	3.8E+10	8.9	0.2	8.5	9.2	4E-04	2E-02

The visible trend with adding HA is the lowering of alpha values for COD and increase of alpha for COM. Yet, 0.035 mg/ml HA does not show any effect on J or alpha for any of the pseudo-polymorphs.

C.5. The Extended tables for the fraction of COD and COM crystals for control group

Two experiments were repeated for each parameter and obtaining more than 60 droplets. Control group experiment which has 6mM calcium and 1.2 mM oxalate concentration has 90 droplets. Two experiment fractions for COM and COD can be seen below in Table C.3 separately. Figure 4.3. (in Chapter 4) shows the total fraction values of COM, COD and CaOx from the Table C.3.

Table C.3. *Two experiment results, Experiment 1 and Experiment 2 for fractions of COM and COD are shown separately. The cumulative fraction values of COM, COD and CaOx show induction times for first crystals in each 90 droplet for 300 minutes.*

Time	Experiment 1		Experiment 2		Total fraction		
[minutes]	COM	COD	COM	COD	COM	COD	CaOx
0	0	0	0	0	0.00	0.00	0.00
2	0	7	0	0	0.00	0.08	0.08
4	0	14	0	19	0.00	0.37	0.37
6	1	21	5	23	0.07	0.49	0.56
8	2	22	11	23	0.14	0.50	0.64
10	2	22	15	23	0.19	0.50	0.69
12	2	23	18	24	0.22	0.52	0.74
14	4	23	20	24	0.27	0.52	0.79
16	10	24	20	24	0.33	0.53	0.87
18	19	25	21	24	0.44	0.54	0.99
20	19	25	21	24	0.44	0.54	0.99
22	19	25	21	24	0.44	0.54	0.99
24	19	25	22	24	0.46	0.54	1.00
26	19	25	22	24	0.46	0.54	1.00
28	19	25	22	24	0.46	0.54	1.00
30	19	25	22	24	0.46	0.54	1.00
32	19	25	22	24	0.46	0.54	1.00
34	19	25	22	24	0.46	0.54	1.00
36	19	25	22	24	0.46	0.54	1.00
38	19	25	22	24	0.46	0.54	1.00
40	19	25	22	24	0.46	0.54	1.00
42	19	25	22	24	0.46	0.54	1.00
44	19	25	22	24	0.46	0.54	1.00
46	19	25	22	24	0.46	0.54	1.00
48	19	25	22	24	0.46	0.54	1.00
50	19	25	22	24	0.46	0.54	1.00
52	19	25	22	24	0.46	0.54	1.00
54	19	25	22	24	0.46	0.54	1.00
56	19	25	22	24	0.46	0.54	1.00
58	19	25	22	24	0.46	0.54	1.00
60	19	25	22	24	0.46	0.54	1.00
66	19	25	22	24	0.46	0.54	1.00
74	19	25	22	24	0.46	0.54	1.00
120	19	25	22	24	0.46	0.54	1.00
180	19	25	22	24	0.46	0.54	1.00
240	19	25	22	24	0.46	0.54	1.00
300	19	25	22	24	0.46	0.54	1.00

Appendix D for Chapter 5

Crystal growth of calcium oxalate monohydrate and calcium oxalate dihydrate under laminar flow

D.1.The overview of mold and chip

The transparent Polydimethylsiloxane (PDMS) mixture is put onto the silicon wafer (see Figure D.1.a) produced microfluidic device (see Figure D.1.b) by lithography technique in the clean room.

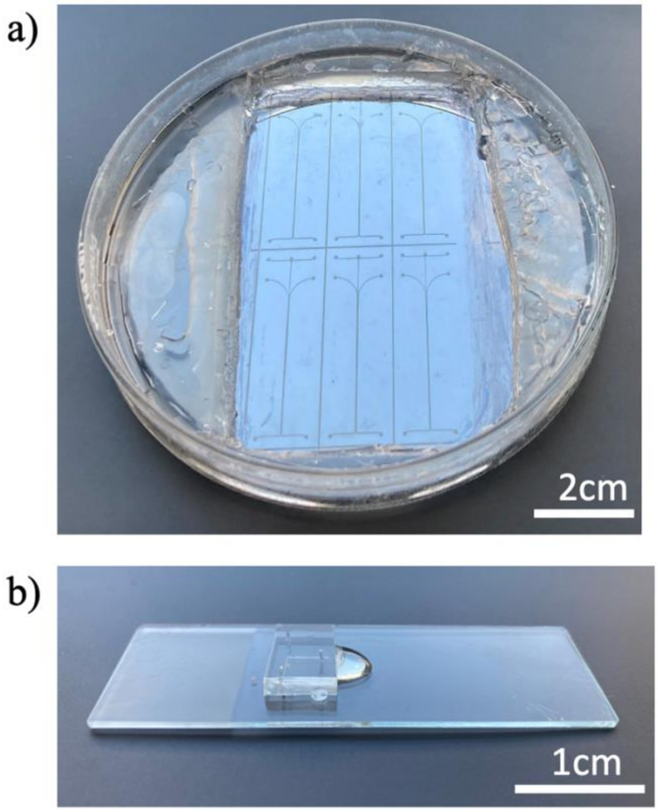

Figure D. 1. a) Silicon wafer to use in the production of PDMS chip. b) A closed microfluidic chip placed on PDMS coated glass slide after spin coating.

D.2. COMSOL Model

Velocity profiles in the channel were used in COMSOL to model concentration profiles and crystal growth. The reaction term was not included in the COMSOL model due to the reaction's limited growth kinetics. We have calculated Damköhler number (Da) as $8.11 \cdot 10^{-6}$. If Da is smaller than 1, the reaction between species is very slow compared to the diffusive mass transport of the species towards the surface.[18]

Because the Reynold number Re < 2000 (Re=6.7 at the maximum velocity of 0.075 m/s) and because the species were sparsely dissolved, a laminar flow and transport of two diluted species was chosen for the 3D analysis. Polygons and arcs were chosen in COMSOL as sketch functions to draw the geometry of the channel. While the height and width of the channel had the same size, the length of inlets is decreased from 1500 µm to 1400 µm, and the length of the main channel was reduced from 6000 to 1500 µm. In this way, the created mesh had fewer elements and it took less time to compute without dramatically affecting the results (Figure D.2). Automatically generated COMSOL microchannel mesh includes 317,354 domain, 38,130 boundary and 1,649 edge elements (in Figure D.2.b).

Once the mesh was fixed, laminar flow conditions were applied. Fully developed flows with the chosen average velocity were used for the two inlets and the outlet was set as a constant pressure boundary at 101,325 Pa.

Next, the transport equations for diluted species were solved with diffusion coefficients $0.793 \cdot 10^{-10}$ m^2/s for calcium and $0.987 \cdot 10^{-10}$ m^2/s for oxalate.[19, 20] while it was ensured that only Ox^{2-} was introduced in the upper inlet and only Ca^{2+} was introduced in the lower inlet at the channel.

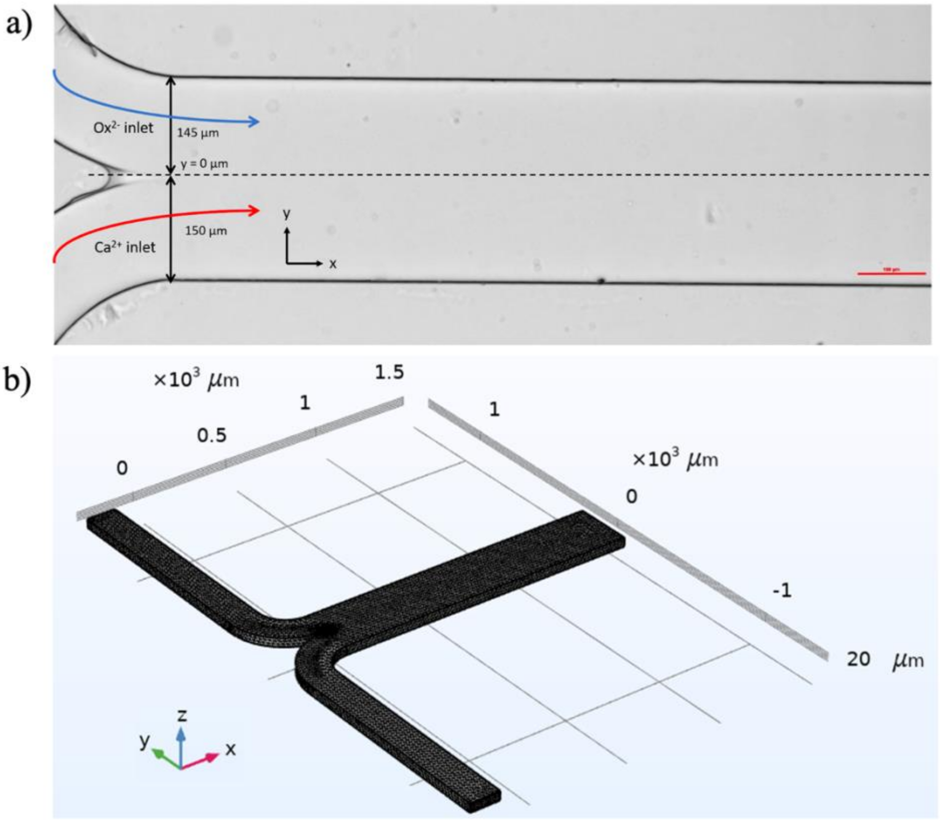

Figure D. 2. a) The view of the channel of microfluidic device. b) Automatically generated COMSOL microchannel mesh includes 317,354 domain, 38,130 boundary and 1,649 edge elements.

D.3. COMSOL Velocity Profiles in the Microchannel

The COMSOL model calculated velocity profiles are shown in several slices throughout the main channel for U = 0.075 m/s in Figure D.3.a. The v-profile at x = 800 µm is shown in Figure D.3.b as a single slice. Due to the height value (45 µm) being 6.6 times less than the width 295 µm, the majority of the xy-plane is equivalent to a situation with two “infinite” parallel plates, resulting in a parabolic Poiseuille-flow in the xz-plane (Figure D.3.c). The v-profile is plug-flow-like in the xy-plane, which is due to very small height compared to width.[21] The no-slip condition causes the velocity to decrease towards the walls. As a result, except at its edges, the v in the xy-plane is uniform (Figure D.3.d). When varying oxalate inlet concentrations and/or average velocities, similar v-profiles are seen, where the maximum velocity in the channel (U_{max}) corresponds to U as U_{max} = 3/2 U. Besides this, velocity conditions at the bottom and the top of the channel are equal because of the negligible gravity in the Navier-Stokes equations.

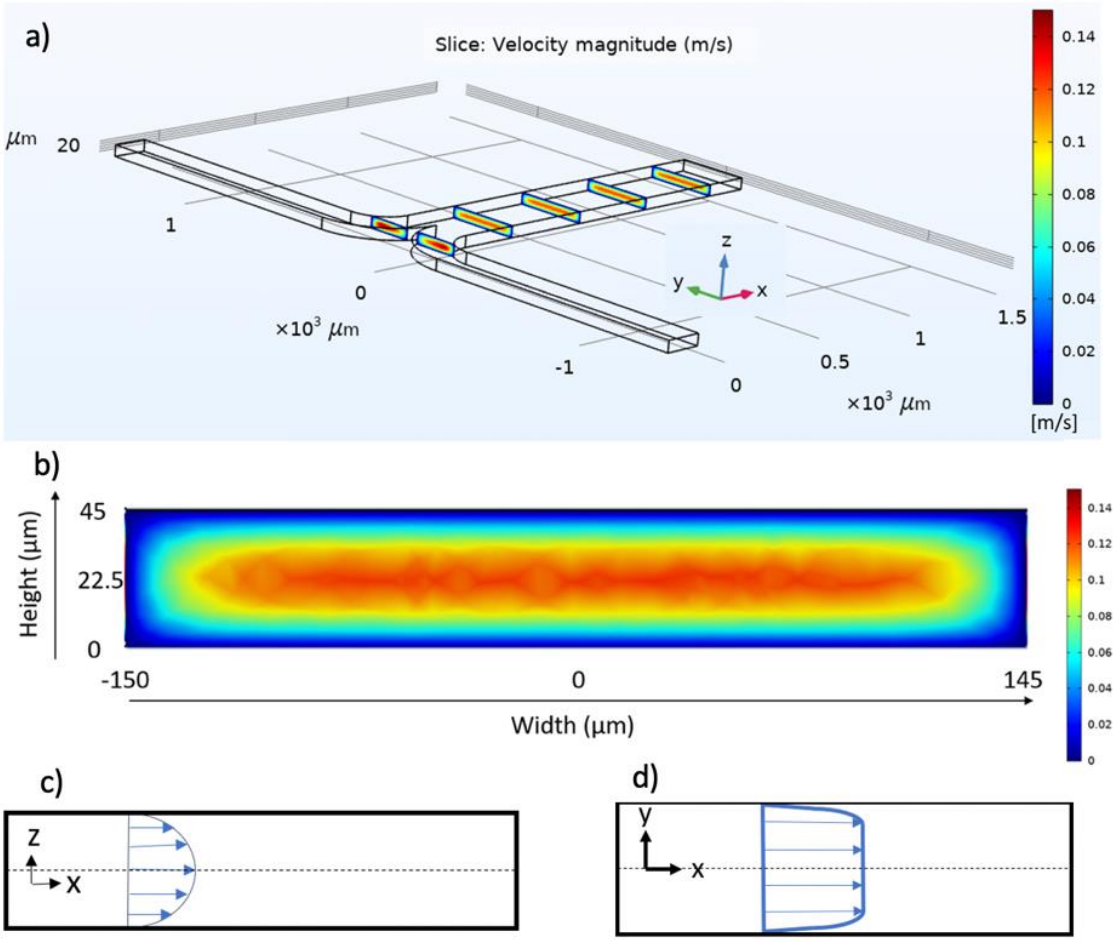

Figure D.3.a) 3D v-profiles through the main channel of the microfluidic device at different fixed length positions for sample AU3 in Figure 5.4 in Chapter 5. (b) One example of 3D plot of the v-profile as a single slice at x = 800 µm (AU3 in Figure 5.4). (c) Sketch of the parabolic v-profile in the xz-plane. (d) Sketch of the plug flow behavior of the v-profile in the xy-plane (AU3 in Figure 5.4).

D.4. Finding supersaturation (σ) values using Jess software

The initial concentration of compounds and temperature value were added to find the supersaturation values using Jess for different experiment conditions. The overview of the program is below. Jess Urine Expert program is applied to calculate supersaturation of artificial urine to estimate σ-profiles in the channel. Due to OPN and creatinine are not in Jess, we are not considering OPN to find σ-profiles.

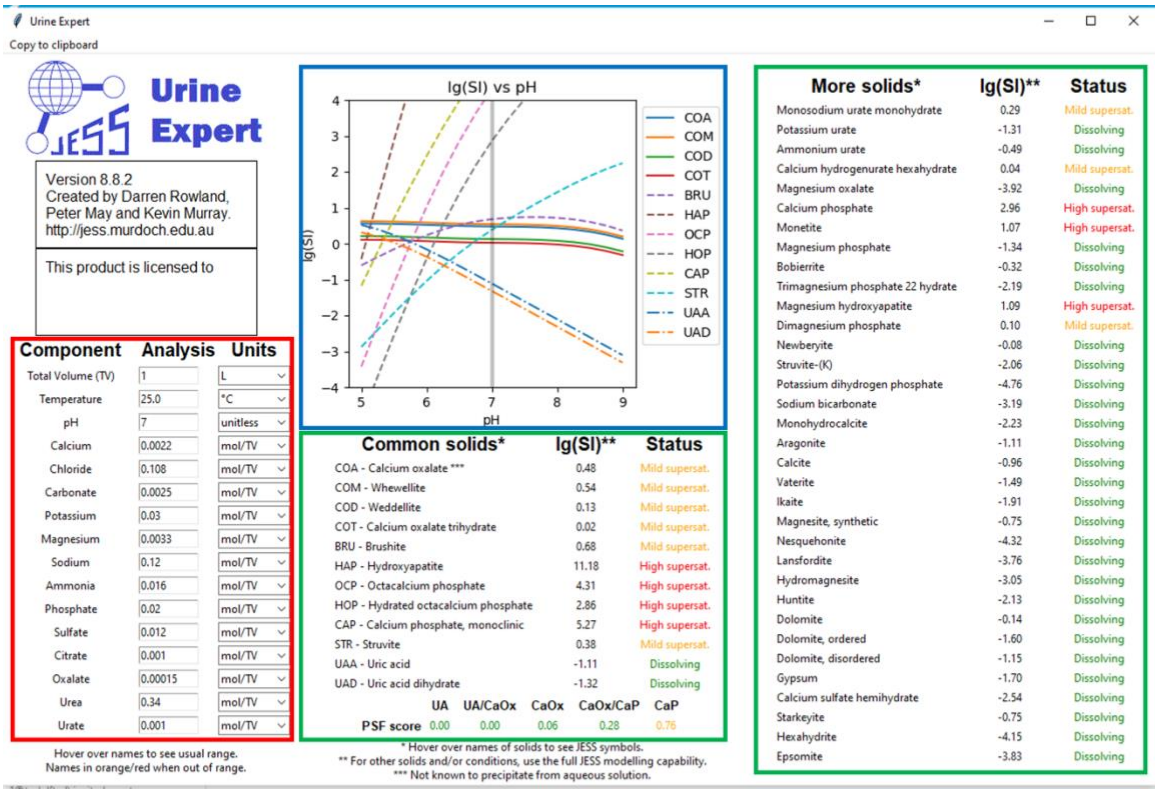

Version 8.8.2
Created by Darren Rowland,
Peter May and Kevin Murray.
http://jess.murdoch.edu.au

This product is licensed to

Component	Analysis	Units
Total Volume (TV)	1	L
Temperature	25.0	°C
pH	7	unitless
Calcium	0.0022	mol/TV
Chloride	0.108	mol/TV
Carbonate	0.0025	mol/TV
Potassium	0.03	mol/TV
Magnesium	0.0033	mol/TV
Sodium	0.12	mol/TV
Ammonia	0.016	mol/TV
Phosphate	0.02	mol/TV
Sulfate	0.012	mol/TV
Citrate	0.001	mol/TV
Oxalate	0.00015	mol/TV
Urea	0.34	mol/TV
Urate	0.001	mol/TV

Hover over names to see usual range.
Names in orange/red when out of range.

Common solids*	lg(SI)**	Status
COA - Calcium oxalate ***	0.48	Mild supersat.
COM - Whewellite	0.54	Mild supersat.
COD - Weddellite	0.13	Mild supersat.
COT - Calcium oxalate trihydrate	0.02	Mild supersat.
BRU - Brushite	0.68	Mild supersat.
HAP - Hydroxyapatite	11.18	High supersat.
OCP - Octacalcium phosphate	4.31	High supersat.
HOP - Hydrated octacalcium phosphate	2.86	High supersat.
CAP - Calcium phosphate, monoclinic	5.27	High supersat.
STR - Struvite	0.38	Mild supersat.
UAA - Uric acid	-1.11	Dissolving
UAD - Uric acid dihydrate	-1.32	Dissolving

	UA	UA/CaOx	CaOx	CaOx/CaP	CaP
PSF score	0.00	0.00	0.06	0.28	0.76

* Hover over names of solids to see JESS symbols.
** For other solids and/or conditions, use the full JESS modelling capability.
*** Not known to precipitate from aqueous solution.

More solids*	lg(SI)**	Status
Monosodium urate monohydrate	0.29	Mild supersat.
Potassium urate	-1.31	Dissolving
Ammonium urate	-0.49	Dissolving
Calcium hydrogenurate hexahydrate	0.04	Mild supersat.
Magnesium oxalate	-3.92	Dissolving
Calcium phosphate	2.96	High supersat.
Monetite	1.07	High supersat.
Magnesium phosphate	-1.34	Dissolving
Bobierrite	-0.32	Dissolving
Trimagnesium phosphate 22 hydrate	-2.19	Dissolving
Magnesium hydroxyapatite	1.09	High supersat.
Dimagnesium phosphate	0.10	Mild supersat.
Newberyite	-0.08	Dissolving
Struvite-(K)	-2.06	Dissolving
Potassium dihydrogen phosphate	-4.76	Dissolving
Sodium bicarbonate	-3.19	Dissolving
Monohydrocalcite	-2.23	Dissolving
Aragonite	-1.11	Dissolving
Calcite	-0.96	Dissolving
Vaterite	-1.49	Dissolving
Ikaite	-1.91	Dissolving
Magnesite, synthetic	-0.75	Dissolving
Nesquehonite	-4.32	Dissolving
Lansfordite	-3.76	Dissolving
Hydromagnesite	-3.05	Dissolving
Huntite	-2.13	Dissolving
Dolomite	-0.14	Dissolving
Dolomite, ordered	-1.60	Dissolving
Dolomite, disordered	-1.15	Dissolving
Gypsum	-1.70	Dissolving
Calcium sulfate hemihydrate	-2.54	Dissolving
Starkeyite	-0.75	Dissolving
Hexahydrite	-4.15	Dissolving
Epsomite	-3.83	Dissolving

Figure D.4. Overview of Jess software. Red rectangular is the workspace to add initial compositions. In the blue and green colors where are the outputs composition from program workspace.

D.5. The calculation method of Crystal Growth Rate

The image analysis tool Cellprofiler was used to analyze crystal images from experiments. From the images of channels to single crystal, the “Imagemath » Invert » Crop” module is used. Following the “IdentifyPrimaryObjects” module is to identify the crystal with a built-in thresholding system and “MeasureImageAreaOccupied”.

D.6. Evaluation supersaturated area with applying COMSOL and JESS Software

The estimated concentration values of calcium and oxalate from COMSOL were used in JESS to find supersaturation values of COM and COD in the channel. With this way from lowest to highest supersaturation values area (Figure D.5) were found and it was seen that crystals emerged between this area (Figure 5.3 in Chapter 5).

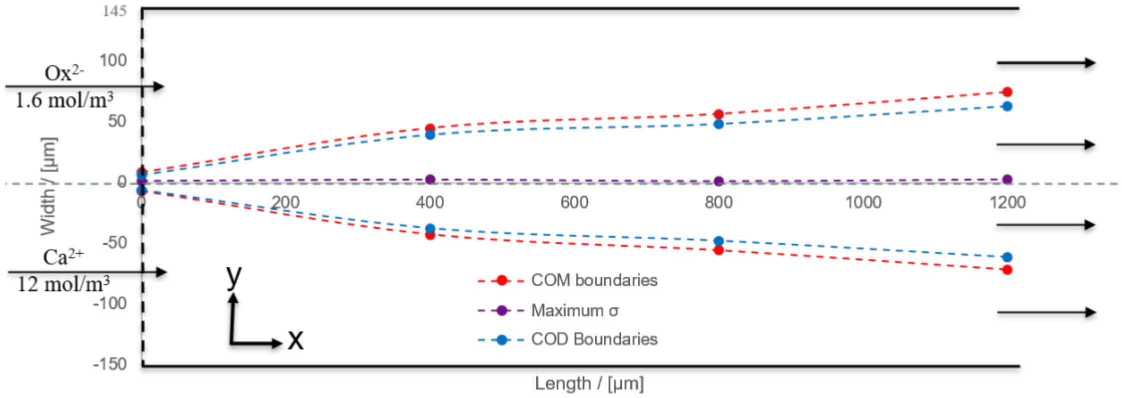

Figure D.5. 2D display of σ boundaries of COM (red dots) and COD (blue dots) at the channel bottom (z = 0 μm) in artificial urine with [Ca]=12 mmol/m^3 and [Ox]=1.6 mmol/m^3 at U=0.035 m/s as sample AU2. Highest σ is seen with purple color, it is log (σ)= 1.67 for COM and log (σ)= 1.25 for COD.

D.7. Identification of crystals via Raman spectroscopy

After completing the experiments, the crystals in the microchannels were identified using Raman Spectroscopy (Horiba Scientific Raman Spectroscope, Japan) without removing crystals from the channels. The peaks in the Raman spectrum were determined with a script which is written in Matlab in Chemical Engineering.[22] The observed peak shifts from channels were compared with literature values in Table D.1. The Raman measurement for different samples is shown in Figure D.6 in which Raman shifts associated with COM are indicated in red, COD in green, PDMS in purple, and urea in black colour circles. Calcium oxalate monohydrate ($CaC_2O_4 \cdot H_2O$, Sigma-Aldrich, CAS563-72-4, St. Louis, MO, USA) was mixed with artificial urine and sent to the chip (Figure D.6.a). The suspensions were left undisturbed for overnight to allow the crystals to sediment. The crystals were then placed on a glass slide for analysis. The Raman spectrum has COM peaks at 896, 1463, and 1490 cm^{-1} in Figure D.6.a. Another peak value at 1004 cm^{-1} is seen which represents urea present in artificial urine.[23] Only PDMS is used to find the spectrum in Figure D.6.b. It shows Raman shifts similar to literature values for PDMS, with peaks at 490, 616, 709, 1262, and 1411 cm-1. The slight difference in peaks compared to literatures values could be due to the ratio of the mixture of PDMS and the curing agent which is used to fabricate PDMS chip in Table D.1.[24]

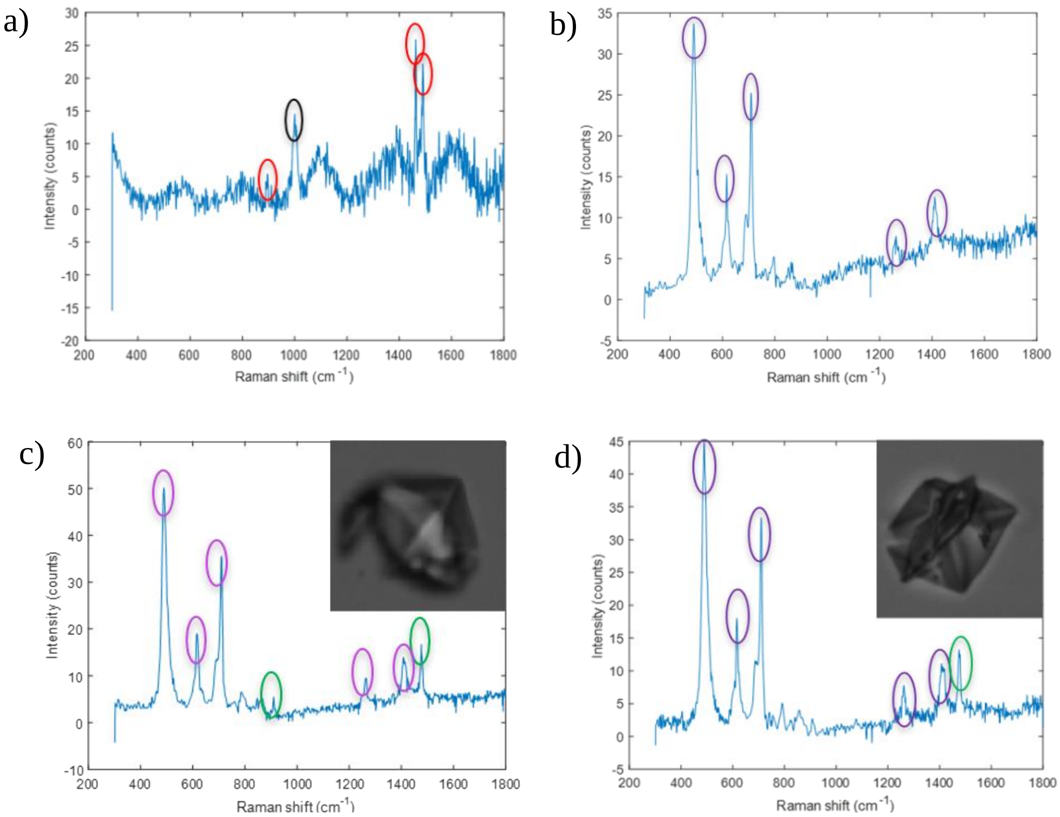

Figure D.6. The results of Raman spectroscopy to identify COM and COD crystals in the microfluidic device. Peaks encircled in black, red, green and purple are associated with urea, COM, COD and PDMS, respectively. (a) COM mixed with artificial urine and placed on glass slide, (b) PDMS material is used to identify background peaks from crystals. (c) Raman peaks from COD crystal at the right top corner. (d) Raman peaks from second COD crystal at the right top corner.

The spectrum from the tetragonal crystal image in sample AU1 (in Figure 5.4 in Chapter 5) gave peaks at 910 and 1477 cm^{-1} for COD (green) and the peaks from PDMS (purple) see Figure D.6.c. A second tetragonal crystal image from sample AU7 (Figure 5.6 in Chapter 5) showed peaks at 1474-1478, representing COD (green) among PDMS peaks (purple) see Figure D.6.d.

Table D.1. Raman shift peak values for COM, COD, and PDMS.

COM shifts [cm^{-1}][25 26 13 17]	**COD shifts [cm^{-1}]**[25 26 13, 17]	**PDMS shifts [cm^{-1}]**[27 28]
503, 504, 506	507, 508	488, 492,
896, 897	910, 912	618.5
1463	1474, 1477, 1478	688
1487, 1488, 1489, 1490, 1492	1632	707, 710, 712
1630, 1631	-	1265, 1414

References for Appendix

1. Fowler, R. M., Bright, H.A., Standardization of permanganate solutions with sodium oxalate. *Journal of Research of the National Bureau of Standards* **1935,** *15*, 493-501.

2. Ruzin, S. E. Buffers. https://microscopy.berkeley.edu/Resources/instruction/buffers.html (accessed February 2019).

3. Sigma Buffer Reference Center- Biological-buffers. https://www.sigmaaldrich.com/life-science/core-bioreagents/ (accessed May 2019).

4. Sigma Reference center - Citric. https://www.sigmaaldrich.com/life-science/core-bioreagents/biological-buffers/learning-center/buffer-reference-center.html#citric2 (accessed June 2019).

5. Robertson, W. G., Measurement of ionized calcium in biological fluids. *Clinica Chimica Acta* **1969,** *24* (1), 149-57.

6. Davies, C. W., Hoyle, B.E., 842. The interaction of calcium ions with some phosphate and citrate buffers. *Journal of the Chemical Society (Resumed)* **1953**, 4134-4136.

7. Kotrlý, S., Sucha, L., *Handbook of chemical equilibria in analytical chemistry*. 1985.

8. Ruiz-Agudo, E. Á.-L., P.; Putnis, C.V.; Rodriguez-Navarro, A.B.; Putnis, A., Influence of chemical and structural factors on the calcite–calcium oxalate transformation. *CrystEngComm* **2013,** *15* (46), 9968-9979.

9. Sillen, L. G., Martell, A.E., Bjerrum, J., Stability constants of metal-ion complexes. **1964**.

10. Streit, J., Tran-Ho, L., Königsberger, E., Solubility of the three calcium oxalate hydrates in sodium chloride solutionsand urine-like liquors. *Monatshefte für Chemie/Chemical Monthly* **1998,** *129* (12), 1225-1236.

11. Kodati, V. R.; Tomasi, G. E.; Turumin, J. L.; Tu, A. T., Raman spectroscopic identification of calcium-oxalate-type kidney stone. *Applied spectroscopy* **1990,** *44* (8), 1408-1411.

12. Frausto-Reyes, C.; Loza-Cornejo, S.; Terrazas, T.; Miranda-Beltran Mde, L.; Aparicio-Fernandez, X.; Lopez-Macias, B. M.; Morales-Martinez, S. E.; Ortiz-Morales, M., Raman spectroscopy study of calcium oxalate extracted from cacti stems. *Applied spectroscopy* **2014,** *68* (11), 1260-1265.

13. Castiglione, V.; Sacre, P. Y.; Cavalier, E.; Hubert, P.; Gadisseur, R.; Ziemons, E., Raman chemical imaging, a new tool in kidney stone structure analysis: Case-study and comparison to Fourier Transform Infrared spectroscopy. *PloS one* **2018,** *13* (8), 1-18.

14. El-Shall, H., Jeon, J.H., Abdel-Aal, E.A., Khan, S., Gower, L., Rabinovich, Y., A study of primary nucleation of calcium oxalate monohydrate: I-Effect of supersaturation. *Crystal Research and Technology: Journal of Experimental and Industrial Crystallography* **2004,** *39* (3), 214-221.

15. Sturm, E. V.; Frank-Kamenetskaya, O.; Vlasov, D.; Zelenskaya, M.; Sazanova, K.; Rusakov, A.; Kniep, R., Crystallization of calcium oxalate hydrates by interaction of calcite marble with fungus Aspergillus niger. *American Mineralogist* **2015,** *100* (11-12), 2559-2565.

16. Sear, R. P., Quantitative studies of crystal nucleation at constant supersaturation: experimental data and models. *CrystEngComm* **2014,** *16* (29), 6506-6522.

17. Edwards, H. G.; Seaward, M. R.; Attwood, S. J.; Little, S. J.; de Oliveira, L. F.; Tretiach, M., FT-Raman spectroscopy of lichens on dolomitic rocks: an assessment of metal oxalate formation. *The Analyst* **2003,** *128* (10), 1218-1221.

18. Kassemi, M.; Brock, R.; Nemeth, N., A combined transport-kinetics model for the growth of renal calculi. *Journal of Crystal Growth* **2011,** *332* (1), 48-57.

19. Nielsen, A., Transport control in crystal growth from solution. *Croatica Chemica Acta* **1980,** *53* (2), 255-279.

20. Nielsen, A. E., Theory of electrolyte crystal growth. The parabolic rate law. *Pure and Applied Chemistry* **1981,** *53* (11), 2025-2039.

21. Thompson, B. W., Secondary flow in a Hele-Shaw cell. *Journal of Fluid Mechanics* **1968,** *31* (2), 379-395.

22. Matlab Peak raman spectroscopy. http://matlab.cheme.cmu.edu/2012/08/27/peak-finding-in-raman-spectroscopy (accessed March 2021).

23. de Souza V, E. E., Bispo, J.A.M., Silveira, L.J., Fernandes, A.B., Discrimination model applied to urinalysis of patients with diabetes and hypertension aiming at diagnosis of chronic kidney disease by Raman spectroscopy. *Lasers in medical science* **2017,** *32* (7), 1605-1613.

24. Cruz-Felix, A. S.; Santiago-Alvarado, A.; Marquez-Garcia, J.; Gonzalez-Garcia, J., PDMS samples characterization with variations of synthesis parameters for tunable optics applications. *Heliyon* **2019,** *5* (12), e03064.

25. Rakotozandriny, K.; Bourg, S.; Papp, P.; Tóth, Á.; Horváth, D.; Lucas, I. T.; Babonneau, F.; Bonhomme, C.; Abou-Hassan, A., Investigating CaOx Crystal Formation in the Absence and Presence of Polyphenols under Microfluidic Conditions in Relation with Nephrolithiasis. *Crystal growth & design* **2020,** *20* (12), 7683-7693.

26. Kuliasha, C. A., Rodriguez, D., Lovett, A., Gower, L.B., In situ flow cell platform for examining calcium oxalate and calcium phosphate crystallization on films of basement membrane extract in the presence of urinary 'inhibitors'. *CrystEngComm* **2020,** *22* (8), 1448-1458.

27. Cai, D., Neyer, A., Kuckuk, R., Heise, H.M., Raman, mid-infrared, near-infrared and ultraviolet–visible spectroscopy of PDMS silicone rubber for characterization of polymer optical waveguide materials. *Journal of Molecular Structure* **2010,** *976* (1-3), 274-281.

28. Çulha, M.; Lavrik, N.; Cullum, B. M.; Astilean, S., Surface-Enhanced Raman Scattering. **2012**.

CURRICULUM VITAE

Fatma Ibis was born on 2nd February, 1990 in Izmir, Turkey. She received B.Sc. degree from Bioengineering department in Ege University in Turkey in 2014. During her undergraduate education, she studied in department of chemical engineering at Abo Akademi in Finland as an exchange student. Fatma joined to Biomedical Technologies at Izmir Katip Çelebi University to pursue a Master of science degree. As a master student she worked under supervision of Dr. Utku Kursat Ercan on the evaluation of effectiveness of cold atmospheric plasma treatment methods for prevention ventilator-associated pneumonia. Just after completing her master degree in 2016, she moved to the Netherlands to do PhD in the Crystallization group/Complex Fluid Processing at the Process and Energy department at Delft University of Technology. Fatma was supervised by Dr. Huseyin Burak Eral, Prof. dr. ir. Herman Kramer and Prof. dr. ir Antoine van der Heijden. She is investigating solubility, nucleation kinetics and growth of calcium oxalate using crystallization equipment and microfluidic platform to understand calcium oxalate kidney stone formation. In her interdisciplinary PhD project, she is combining her experience in bioengineering with the crystallization expertise of Eral lab and the microfabrication capabilities of Luigi Sasso's/ Urs Staufer's group in Precision and Microsystems Engineering in TU Delft.

PUBLICATIONS

Journal Publications included in this thesis

1. **Fatma Ibis**, Priya Dhand, Sanan Suleymanli, Antoine E.D.M. van der Heijden, Herman J. M. Kramer, Huseyin Burak Eral (2020), A coupled comparative experimental and modelling study on Calcium Oxalate Monohydrate solubility at physiologically relevant pH and temperatures, Crystals, DOI:10.3390/cryst10100924. (Chapter 2 in this thesis)

2. **Fatma Ibis**, Tsun-wang Yu, Frederico Marques Penha, Debadrita Ganguly, Manzoor Alhaji Nuhu, Antoine E.D.M. van der Heijden, Herman J. M. Kramer, Huseyin Burak Eral (2021), Nucleation kinetics of calcium oxalate monohydrate as a function of pH, magnesium, and osteopontin concentration quantified with droplet microfluidics, Biomicrofluidic, DOI: 10.1063/5.0063714. (Chapter 3 in this thesis)

3. **Fatma Ibis**, Manzoor Alhaji Nuhu, Frederico Marques Penha, Tsun-wang Yu, Antoine E.D.M. van der Heijden, Herman J. M. Kramer, Huseyin Burak Eral (2022), Antagonistic effect of hyaluronic acid on the nucleation kinetics of calcium oxalate hydrates in artificial urine quantified with droplet microfluidics, Crystal Growth and Design, DOI: 10.1021/acs.cgd.2c00198 (Chapter 4 in this thesis)

4. **Fatma Ibis**, René Smeets, Jiali Wang, Priya Dhand, Majid Mohamedhoesein, Frederico Marques Penha, Johan Grievink, Antoine E.D.M. van der Heijden†, Herman J. M. Kramer and Huseyin Burak Eral, Crystal growth of calcium oxalate monohydrate and calcium oxalate dihydrate under laminar flow (Chapter 5 in this thesis) (to be submitted)

Journal Publications not included in this thesis

5. Richard.M.B. Pleeging, **Fatma Ibis**, Daniel Fan, Luigi Sasso, H. Burak Eral, Urs Staufer (2021), Polymer Nano Manufacturing of a Biomimicking Surface for Kidney Stone Crystallization Studies, Micro and Nano Engineering, DOI: doi.org/10.1016/j.mne.2021.100094

6. Frederico Marques Penha, Ashwin Gopalan, Jochem Christoffel Meijlink, **Fatma Ibis**, and Huseyin Burak Eral (2021), Selective Crystallization of d-Mannitol Polymorphs Using Surfactant Self-Assembly, Crystal Growth & Design, DOI: 10.1021/acs.cgd.1c00243.

7. Yug C Saraswat, **Fatma Ibis**, Laura Rossi, Luigi Sasso, Burak Eral, Paola Fanzio (2020), Shape Anisotropic Colloidal Particle Fabrication using 2-Photon Polymerization, Journal of Colloid and Interface Science, DOI: 10.1016/j.jcis.2019.12.035

8. **Fatma Ibis,** Utku K. Ercan (2020), Inhibition of Biofilms on Endotracheal Tube by Cold Atmospheric Plasma Treatment for Control and Prevention of Ventilator Associated Pneumonia, Plasma Processes and Polymers, DOI:10.1002/ppap.202000065.

9. Hüseyin Akçay, Utku K. Ercan, Selen Bahçeci, **Fatma Ibis,** Şükrü Enhoş (2020), The Effect of Atmospheric Pressure Cold Plasma Application on Titanium Barriers: A Vertical Bone Augmentation, The Journal of Craniofacial Surgery, DOI: 10.1097/scs.0000000000006643.

10. Kaustub Singh, Ankur Gupta, Abel-John Buchner, **Fatma Ibis**, Joachim W. Pronk, Daniel Tam, H. Burak Eral (2019), Analysis of centrifugal homogenization and its applications for emulsification & mechanical cell lysis, Journal of Colloid and Interface Science 547, DOI: 10.1016/j.jcis.2019.03.036.

11. Burak Çelik, İsmail D. Çapar, **Fatma İbiş**, Necdet Erdilek, Utku K. Ercan (2019), Deionized water can substitute common bleaching agents for nonvital tooth bleaching when treated with non-thermal atmospheric plasma, Journal of Oral Science, Vol. 61, No. 1, 103-110, DOI: 10.2334/josnusd.17-0419.

12. Utku K. Ercan, **Fatma İbiş**, Caner Dikyol, Nesrin Horzum, Ozan Karaman, Cağla Yıldırım, Elif Cukur, Emine Afra Demirci (2018), Prevention of bacterial colonization on nonthermal atmospheric plasma treated surgical sutures for control and prevention of surgical site infections, PLoS ONE 13(9): e0202703, DOI: 10.1371/journal.pone.0202703.

13. Fatma Yilmaz, Esra Uzer Celik, Utku K. Ercan, **Fatma Ibis,** (2018), Efficacy of Plasma Activation on Bleaching, ARC Journal of Dental Science, Volume 3, Issue 2, 2018, PP 10-17 ISSN No. (Online) 2456-0030, DOI: 10.20431/2456-0030.0302003.
14. Fatma Yilmaz, Esra Uzer Celik, Utku K. Ercan, **Fatma Ibis**, (2018), Effect of Plasma-Activated Bleaching on Enamel Microhardness and Morphology, ARC Journal of Dental Science, Volume 3, Issue 2, 2018, PP 2-9 ISSN No. (Online) 2456-0030, DOI: 10.20431/2456-0030.0302002.

15. Pınar Adımcı, **Fatma Ibis**¸ Utku K. Ercan, Bora Bagis, (2018), Evaluation of effects of non-thermal plasma treatment on surface properties of CAD/CAM

material, Journal of Adhesion Science and Technology, DOI: 10.1080/01694243.2018.1493834.

16. Murat Ulu, Tugba Pekbagriyanik, **Fatma Ibis** Sukru Enhos, Utku K. Ercan, (2018), Antibiofilm Efficacies of Cold Plasma and Er:YAG Laser on Staphylococcus aureus Biofilm on Titanium for Nonsurgical Treatment of Peri-Implantitis, Brazilian Oral Research, DOI: 10.4103/njcp.njcp_261_17.

17. Nehir Arik, Alper Inan, **Fatma Ibis**, Emine A. Demirci, Ozan Karaman, Utku K. Ercan, Nesrin Horzum, (2018) Modification of electrospun PVA/PAA scaffolds by cold atmospheric plasma: alignment, antibacterial activity, and biocompatibility, Polymer Bulletin, DOI:10.1007/s00289-018-2409-8.

18. Murat Ulu, Mehmet B. Kapili. Utku K. Ercan, **Fatma Ibis**, Isıl Aydemir, Nazan Keskin, Mehmet I. Tuglu, (2018), The Evaluation of the Osteogenic Cell Activities on Titanium Surface Modified with the Atmospheric Cold Plasma, Süleyman Demirel University Journal of Natural and Applied Sciences Volume 22, Issue 1, 313-318, 2018, DOI: 10.19113/sdufbed.11302.

19. Utku Kursat Ercan, **Fatma Ibis**, (2017) Bactericidal efficacies of nebulized non-thermal atmospheric plasma-treated liquids, The European Research Journal, DOI: 10.18621/eurj.268572.

20. Hüseyin Akcay, Harun Görgülü, Utku K. Ercan, Murat Ulu, **Fatma Ibis**, Emine A. Demirci, Ozan Karaman, (2017), Evaluation of the effect of atmospheric cold plasma application on titanium mesh as In vitro, 7tepeklinik, DOI: 10.5505/yeditepe.2018.06078.

21. Ozan Karaman, Seyfi Kelebek, Emine A. Demirci, **Fatma Ibis**¸ Murat Ulu, Utku K. Ercan, (2017), Synergistic Effect of Cold Plasma Treatment and RGD Peptide Coating on Cell Proliferation over Titanium Surfaces, Tissue Eng Regen Med, DOI: 10.1007/s13770-017-0087-5.

22. Emine A. Demirci, Seyfi Kelebek, **Fatma Ibis**, Utku K. Ercan, Murat Ulu, Ozan Karaman, (2016) The Evaluation of Wettability and Cell-Surface Interactions on Modified Titanium Discs with Atmospheric Cold Plasma Application and RGD Peptide Conjugation: In Vitro Study, DOI:10.1109/BIYOMUT.2016.7849398.

23. **Fatma Ibis**, Hakan Oflaz, Utku K. Ercan, (2016), Biofilm Inactivation and Prevention on Common Implant Material Surfaces by Non-Thermal DBD Plasma Treatment, Plasma Medicine, DOI: 10.1615/PlasmaMed.2016015846.

Awards and Honors

- The scholarship for Ph.D. in Foreign Countries, from TÜBİTAK (Scientific and technological research council of Turkey) (2015).
- The scholarship for Ph.D. in UK, from TÜBİTAK (Scientific and technological research council of Turkey) and British Council (2015).
- The Scholarship for Master Thesis about Priority Areas, from TÜBİTAK (Scientific and technological research council of Turkey) (2015).
- The scholarship for Master Project, from TÜBİTAK 3501 (Scientific and technological research council of Turkey) (2014).

Acknowledgements

The most unique part of my life is finalizing with this dissertation. Five years, literally full of effort, unforgettable memories, and fun. I want to express my sincere gratitude to everyone who are involved in any point of this journey.

Firstly, I would like to start with thanking my co-promotor/supervisor H.Burak Eral for giving me the opportunity to do my PhD in your group. I am immensely thankful to you for all your input, always adding a new dimension to my work. You helped me through every point in my PhD both research and personal development. Moreover, I truly appreciate the freedom that you gave me to choose my direction, helping me to find interesting research topics and to develop myself as an independent researcher. It has been a great pleasure for me to work under your supervision and to learn from you.

Very importantly, I also would like to express my sincere gratitude to my promotor Prof.dr.ir. Johan T. Padding. You have been always very helpful, supportive, kind and patient leader in the group. I learnt from you that being kind and honest to people make life more beautiful for group members.

To my great supervisors, Prof.dr.ir. Herman Kramer and Prof.dr.ir. Antoine van der Heijden, I feel lucky to work with you. Your outstanding commitment, enthusiasm and passion for research have been a great inspiration for me. Moreover, I have always admired your modesty, kindness, and supportiveness. Thanks a lot for providing me peaceful working environment.

My dear friend, Asst. Prof. Dr. F. M. Penha, I am appreciated you for always showing interest in the presented work and for endless supporting me whenever I faced a problem that could be solved within the kidney stone project. Fred, this project improved significantly with your friendly collaboration. Thank you so much.

The collaboration with Dr. L Sasso and Dr. P. Fanzio from the Department of Precision and Microsystems Engineering initiated and tremendously significantly contributed to the quality of this work. I am very grateful for giving me the opportunity to conduct soft lithography and characterization techniques. Moreover, Paola, it was always helpful to remember your suggestion along this journey: Be strong!

I also want to thank Prof.dr.ir Andrzej Stankiewicz for his contribution with his positive energy to the initial phase of the project.

I also would like to express my gratitude to Prof.dr. Chris Bangma, Prof.dr. Ir. Wytske M. van Weerden, Prof.dr. Guido Jenster for giving me the opportunity to work on the interaction kidney stone and cells in the microfluidic device in Erasmus University Medical Center. Thank you for fruitful discussions and for your warm welcome during my stay in the Erasmus MC. I would like to thank to Wilma J. Teubel for her valuable training and help in cell culture experiments.

I am very thankful to Prof.ir. Johan Grievink to give simulation idea on kidney stone problem and for many in-depth and fruitful discussions to guide on this topic. I would also like to thank Dr. Hans Beukhof for providing patient kidney stone from hospital and guide about biologic complexity about urinary system.

Dr.ir. Peter Daudey I was always glad to listen your impressive hobby on understanding complex biological pathways which can also affect kidney stone formation. Thank you for your time.

I also would like to thank Dr. Danial Fan for all brainstorming during coffee breaks and help on Nanoscribe. I want to thank to Spiridon van Veldhoven and Patrick van Holst for their help with my many technical questions in the labs of Department of Precision and Microsystems Engineering.

Over the years, I had many colleagues within the group. They contributed to this thesis directly or indirectly in many different ways. Therefore, I would like to thank my colleagues within the Process and Energy, Nikos, Vilborg, Reza, Elyas, Sathish, Asif, Recep, Mohammed, Weiwei, Marloes, Rohid, Daniel, Sameer, Pavithra, Srushti, Karsten, Carla, Samira, Vincent, Mohamed, Uttiya, Luis, Mengmeng, Tim, Sebastian, Xuan, Mengmeng, Mara, Lalit, Vikram, Nagaraj, Yavuz, Marko, Ivan, Suriya, Mert, Heng, Pietro and Hugo.

During corona time, I realized more about the importance of having great friends, Noura, Gustavo, Stephan, Rishabh, Rumen, Simone, and Manas. Thank you very much for the fun lunches, dinners, trips, and great board games. This helped me a lot to keep my motivation high. My dear friends, Alper, Aytac, Hakan and Yildiz Gozde made a great environment to survive this tough PhD journey. You were always there to help, listen, guide and have fun time. I will always be grateful for it. I am also very grateful to my friends who helped me to recharge my energy during my first year in the Netherlands. Francesca, Anna, Sanjana, Hassan, Yash, Matteo, Johan, Pong, and Liangyuan thank you very much. A very special thank goes to Noura, I had always nice time during coffee times in the offices and all activities on the weekend. Your friendship and support are always precious for me. I would like to thank Sarah, Ezgi, Cansel, Cenk, Cevdet, Muscan, Hamit, Cigdem, and Nil for their valuable friendship and warm during our free time.

A very special thank goes to Michel van den Brink and Jaap van Raamt for always being very generous with technical support to me and my students. I should not forget to thank to the staff members who are always trying to facilitate our life at university; Leslie, Helma, Linda and Caroline and Rob for being very helpful.

Throughout this project, I had the chance to work with many students. I would like to thank my master and bachelor students who not only worked hard and made great pieces of research for themselves but also gave me the opportunity to learn from them and to teach them. You all made our lab works enjoyable. I tremendously appreciate your contributions.

Firstly, I am thankful to my master's students Manzoor and René, who never stop to work together with me in the lab during the Covid-19 lockdown. Your openness, efforts, and dedication significantly made this kidney stone project more interesting and comprehensive. I would like to thank to Tsun and Debadrita for your hardworking and the unique microfluidic design, I would not succeed on nucleation kinetics of CaOx without you. I appreciate your contribution. Priya and Sanan, you had an enormous contribution of the solubility of COM and initiated work on the growth of CaOx in microfluidics, I am very grateful to work with you who are always kind, successful, have positive energy and tolerance to problems. Jiali and Mai you had a great contribution to calcium oxalate growth, thanks a lot for that. Richard, I was always glad to work with you and appreciated your Nanoscribe-crystallization study. Besides kidney stone project, I had opportunity to work other interesting topics with Yesaswini, Manoj, Mehul, Nandalal. Thank you very much for your hard work, modest, enthusiastic and kind attitudes. Great thanks to my bachelor students, Majid, Otto, Tim, Monica and Rick for their hard works, it was always pleasure for me to work with you.

I would additionally like to thank the committee members to take their time to evaluate my dissertation.

My love, Emre, everything has become lovely in our lives since we met. Your endless support and determination helped me a lot to keep motivated during my PhD, and I am always grateful for that.

Last but definitely not least, I would like to thank my family. Annem, babam ve canım kardeşlerim, böyle güzel bir ailem olduğu için çok şanslıyım. Sevginiz, ilginiz ve destekleriniz, yorulduğum her anda bana güç verdi ve yol gosterdi. Çok teşekkür ederim, iyi ki varsınız. Sizi çok seviyorum ve bu tezi size ithaf ediyorum.